Contributions to spectral CT

Alexander M. T. Opie

A thesis presented for the degree of
Doctor of Philosophy
in
Electrical and Computer Engineering
at the
University of Canterbury,
Christchurch, New Zealand.

October 2013

Abstract

Spectral x-ray computed tomography (CT) is an important nascent imaging modality with several exciting potential applications. The research presented in this thesis separates into two primary areas with the common underlying theme of spectral CT; the first area is Compton scatter estimation and the second is interior tomography.

First, the research is framed and outputs are identified. Background on the concepts used in the thesis is offered, including x-ray imaging and computed tomography, CT scanner architecture, spectral imaging, interior tomography and x-ray scatter. The mathematical background of techniques for image reconstruction from x-ray transmission measurements are presented. Many of the tools used to perform the research, both hardware and software, are described. An algorithm is developed for estimating the intensity of Compton scattered photons within a spectral CT scan, and a major approximation used by the algorithm is analysed. One proposed interior reconstruction algorithm is briefly evaluated; while this is not directly linked to spectral CT, it is related to the work on a novel hybrid spectral interior micro-CT architecture. Conclusions are summarised and suggestions for future work are offered.

Scatter is known to cause artefacts in CT reconstructions, and several methods exist to correct data that has been corrupted by scatter. Compton scatter affects the energy of photons, therefore spectral CT measurements offer the potential to correct for this phenomenon more accurately than conventional measurements. A Compton scatter algorithm is developed and is found to match very well to Monte Carlo validation simulations, with the constraints that the object be at the micro-CT scale and that electron-binding effects are omitted. Development of the algorithm uses an approximation of the post-scatter attenuation to simplify the estimation problem and enable implementation. The consequences of this approximation are analysed, and the error introduced is found to be less than 5% in most biomedical micro-CT situations.

Interior tomography refers to the incomplete data situation caused by the truncation of some or all CT projections, and is an active research area. A recently proposed interior reconstruction algorithm is evaluated with regard to its sensitivity to input error, and is found to have mediocre performance in this respect. Published results are not found to be reproducible, suggesting some omission from the published algorithm.

A novel hybrid spectral interior architecture is described, along with an iterative reconstruction algorithm for hybrid data sets. The system combines a full field of view conventional imaging chain and an interior field of view spectral imaging chain to enable spectral measurement of a region of interest, and addresses some important limitations of spectral x-ray detectors; promising results are shown. Spectral reconstructions from interior data are shown to have sufficient information to distinguish two k-edge contrast agents (iodine and gadolinium) not only within the interior field of view but also beyond it. The architecture is further explored in the context of radiation exposure reduction, including testing of an analytical hybrid reconstruction algorithm.

Deputy Vice-Chancellor's Office
Postgraduate Office

UNIVERSITY OF CANTERBURY
Te Whare Wānanga o Waitaha
CHRISTCHURCH NEW ZEALAND

Co-Authorship Form

This form is to accompany the submission of any PhD thesis that contains research reported in co-authored work that has been published, accepted for publication, or submitted for publication. A copy of this form should be included for each co-authored work that is included in the PhD thesis. Completed forms should be included at the front (after the thesis abstract) of each copy of the thesis submitted for examination and library deposit (including electronic copy).

Please indicate the chapter/section/pages of this thesis that are extracted from co-authored work and provide details of the publication or submission from which the extract comes:

Chapter 5 is adapted from a published proceedings paper: Opie, A. M. T. and Bones, P. J. (2011), 'Sensitivity to error of the truncated Hilbert transform technique for interior reconstruction', in *'IEEE International Conference on Image Processing 2011', pp. 421–424.*

Please detail the nature and extent of contribution by the PhD candidate:

The PhD candidate did the research and wrote all sections of the published manuscript. The co-authoring supervisor suggested research directions and offered criticisms which the candidate worked into the manuscript.

Certification by co-authors: If there is more than one co-author then a single co-author can sign on behalf of them all. The undersigned certifies that:

- The above statement correctly reflects the nature and extent of the PhD candidate's contribution to this co-authored work.
- In cases where the PhD candidate was the lead author of the co-authored work, that he or she wrote the text.

Name: Philip Bones

Signature: 

Date: 23 July 2013

Deputy Vice-Chancellor's Office
Postgraduate Office

UNIVERSITY OF CANTERBURY
Te Whare Wānanga o Waitaha
CHRISTCHURCH NEW ZEALAND

Co-Authorship Form

This form is to accompany the submission of any PhD thesis that contains research reported in co-authored work that has been published, accepted for publication, or submitted for publication. A copy of this form should be included for each co-authored work that is included in the PhD thesis. Completed forms should be included at the front (after the thesis abstract) of each copy of the thesis submitted for examination and library deposit (including electronic copy).

Please indicate the chapter/section/pages of this thesis that are extracted from co-authored work and provide details of the publication or submission from which the extract comes:
Section 4.1 is adapted from a published proceedings paper: Opie, A. M. T., Butler, A. P. H., and Bones, P. J. (2012), 'Energy-resolved Compton scatter estimation for micro-CT', in *'Developments in X-Ray Tomography VIII', Vol. 8506 of* Proceedings of the SPIE*, p. 850616*

Please detail the nature and extent of contribution by the PhD candidate:
The PhD candidate did the research and wrote all sections of the published manuscript. The co-authoring supervisory team suggested research directions and offered criticisms which the candidate worked into the manuscript.

Certification by co-authors: If there is more than one co-author then a single co-author can sign on behalf of them all. The undersigned certifies that:

- The above statement correctly reflects the nature and extent of the PhD candidate's contribution to this co-authored work.
- In cases where the PhD candidate was the lead author of the co-authored work, that he or she wrote the text.

Name: Philip Bones

Signature: 

Date: 23 July 2013

Deputy Vice-Chancellor's Office
Postgraduate Office

UNIVERSITY OF CANTERBURY
Te Whare Wānanga o Waitaha
CHRISTCHURCH NEW ZEALAND

Co-Authorship Form

This form is to accompany the submission of any PhD thesis that contains research reported in co-authored work that has been published, accepted for publication, or submitted for publication. A copy of this form should be included for each co-authored work that is included in the PhD thesis. Completed forms should be included at the front (after the thesis abstract) of each copy of the thesis submitted for examination and library deposit (including electronic copy).

Please indicate the chapter/section/pages of this thesis that are extracted from co-authored work and provide details of the publication or submission from which the extract comes:
Section 6.1 is adapted from a journal paper accepted for publication: Bennett, J. R., Opie, A. M. T., Xu, Q., Yu, H., Walsh, M., Butler, A., Butler, P., Cao, G., Mohs, A., and Wang, G. (2013), 'Hybrid spectral micro-CT: System design, implementation and preliminary results', IEEE Transactions on Biomedical Engineering.

Please detail the nature and extent of contribution by the PhD candidate:
The PhD candidate assisted in operating the new scanner, reconstructed the images, and analysed the results. The manuscript was jointly prepared by the lead author and the PhD candidate.

Certification by co-authors: If there is more than one co-author then a single co-author can sign on behalf of them all. The undersigned certifies that:

- The above statement correctly reflects the nature and extent of the PhD candidate's contribution to this co-authored work.
- In cases where the PhD candidate was the lead author of the co-authored work, that he or she wrote the text.

Name: James Bennett

Signature: 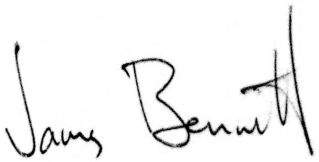

Date: 18 July 2013

Acknowledgements

First thanks belong to my primary supervisor, Professor Phil Bones, whose support and guidance have made this research possible. Additionally, our shared enthusiasm for outdoor pursuits and navigation sports has led to many off-topic discussions during our weekly meetings and meant that my substandard work hours while I organised T'Walk 2011 were not too severely admonished. Following close behind is my second supervisor, Professor Rick Millane, whose fast and comprehensive reviews of my work were much appreciated. Thanks also to my third supervisor, Dr Anthony Butler, for his valuable input and guidance on the more biomedical side of my work. I also want to thank Dr Michael Hayes for his supervisory efforts during my honours year project; although I have not worked under him during my PhD period, the quality of my English improved enormously thanks to his meticulous reviewing of my work at the time.

To my loving girlfriend Inger, thank you so much for your support through the full course of my studies, and I am truly grateful for all of your encouragement, companionship, and baking during this period.

Thank you Mum and Dad, for teaching me everything I know.

Thanks to James Bennett for working with me for the last few months. The complementary approach of a biomedical engineer was invaluable for aligning my work with realistic applications, and working "side-by-side" with someone kept motivation up. Thanks to my office-mates, especially Peter Raffensperger (thanks for not telling), Firas Al-Hasani, and Prateek Mehrotra. The encouragement to work hard paid off.

Thanks to the University of Canterbury Students' Association, to both the national body and the Canterbury branch of the Royal Society of New Zealand, to Freemasonry NZ, to the University of Canterbury, and to the MARS research group for funding me.

I am immensely grateful to Donald Knuth for TEX and to Leslie Lamport for LATEX, without which I would have been stuck at the mercy of Microsoft Word and all its evils. Instead I am able to (almost) painlessly produce this beautifully typeset document with consistent formatting, fully working hyperlinked cross-references, and good-looking equations (with numbering).

Finally, thanks to Douglas Adams for the timeless advice:

DON'T PANIC

There has been an alarming increase in the number of things I know nothing about.

Table of Contents

Chapter Zero

Introduction

The long term goal within my field of research is to identify, demonstrate, and refine the potential utility of spectral computed tomography. The specific aims for this thesis are to study scatter estimation and interior tomography techniques.

X-ray computed tomography (CT) is a radiological imaging modality of high clinical significance because it allows non-invasive diagnosis across a wide range of diseases. In 2007, 98 000 scans were performed in NZ (Stirling and Cotterill, 2009) and 72 million studies were performed in the USA, a 23-fold increase since 1980 and continuing to rise each year (Smith-Bindman et al., 2009). Widespread use of CT is attributed to the relative safety of the technique, its versatility, and short imaging times.

Spectral CT is a new CT technique that aims to provide compositional information about the tissues being imaged. In the medical world such imaging information is called functional or molecular imaging. Other functional techniques include positron emission tomography (PET) and functional magnetic resonance imaging (fMRI). An advantage of PET compared to spectral CT is its ability to measure metabolic activity, while disadvantages include the lack of contextual anatomical information and its dependence on the availability of a nearby cyclotron. An advantage of fMRI is that it does not use ionising radiation, but the financial cost of an MRI scan and the time required are much greater than that of spectral CT. Thus, if spectral CT achieves its potential it will be an imaging modality that complements these existing modalities to enable radiologists to make fast and accurate diagnoses, leading to improved patient outcomes.

My work on scatter estimation is significant to the field because image quality is adversely affected by scatter, and estimation is an important part of the correction process. Existing scatter estimation algorithms do not make use of spectral measurements, so my work in this area moves toward satisfying this need. My work on interior tomography is significant because interior tomography is a growing area of research and offers advantages unique to spectral CT. Advancement of interior tomography promises to bring forward the viability of spectral CT for clinical use.

0.1 Research environment

Most of my work was performed autonomously, but I was involved with two collaborations: with the MARS research group and with a group at Virginia Tech[1] (VT), USA. MARS (Medipix All-Resolution System) is a research group based at the University of Canterbury (UC), with members from both UC and the University of Otago. The group designs and builds experimental micro-CT scanners that use energy sensitive x-ray detectors from the Medipix[2] family. The group also performs research into all parts of the processing chain, from detector physics through to visualisation. The group includes physicists, electrical engineers, computer engineers, chemists, radiologists, mathematicians, and biologists. I was a member of the MARS research group for the full duration of my studies, and was heavily involved with the development of scanner control software for a period of several months. I also chaired fortnightly meetings of the novel reconstruction team for nearly a year. Membership of the MARS group was valuable as it enabled me to collect and use real scan data. The second collaboration, with VT, was mainly with one researcher from their team, Biomedical Engineering PhD candidate James Bennett. James first visited the MARS group in September 2011, but our work together began in earnest when I visited VT in August 2012. James also returned to NZ in February 2013. We worked closely together to design phantoms and to plan and run scans on machines both in the MARS lab and at VT. The principal outcomes of the two collaborations were, respectively, advancement of the MARS micro-CT scanner (see Chapter 3) and study of a hybrid spectral CT architecture (see Chapter 6).

Funding was obtained from several sources. My main source was the Brownlie Scholarship, which was further supplemented by the Freemasons Postgraduate Scholarship and the R.H.T. Bates Postgraduate Scholarship. The latter is awarded by the Royal Society of New Zealand (RSNZ) to a PhD candidate whose research aims to apply information/image processing to studies in medicine, the physical sciences, astronomy, or engineering. It is in honour of the late Professor Richard Bates, who contributed greatly to many fields including early research into CT. Travel to Belgium for the IEEE International Conference on Image Processing was partly funded by grants from the University of Canterbury Students' Association and the Canterbury branch of the RSNZ, and travel to the USA for the SPIE conference *Developments in X-Ray Tomography VIII* and to visit VT was partly funded by the MARS group. The balance of the funds for these trips was provided by my senior supervisor Prof. Phil Bones.

[1] In full, Virginia Polytechnic Institute and State University.

[2] Medipix are a family of energy-sensitive x-ray detectors designed at CERN. See Chapter 3 for more information.

0.2 Research outputs

My contributions to the field of spectral CT research include involvement in several published articles, presentation of progress at different conferences, collaboration both within my local research group and with the group at VT, and the supervision of a short-term research student.

0.2.1 Publications

Several manuscripts have been composed through the course of my research. These are listed below together with a summary of the paper, its significance, and my contribution to the work.

- Bones, P. J., Butler, A. P. H., Ronaldson, J. P., and Opie, A. M. T. (2010), 'Development of a CT scanner based on the Medipix family of detectors', *in* 'Developments in X-Ray Tomography VII', Vol. 7804 of *Proceedings of the SPIE*.

  A brief review of spectral imaging, Medipix detectors, and the development of the MARS micro-CT scanner. This paper identifies the state of spectral CT research and the MARS scanner, and presents further evidence of the benefits of the modality. My contribution to this paper was performing the literature review to summarise previous work on spectral CT.

- Walsh, M. F., Opie, A. M. T., Ronaldson, J. P., Doesburg, R. M. N., Nik, S. J., Mohr, J. L., Ballabriga, R., Butler, A. P. H., and Butler, P. H. (2011), 'First CT using Medipix3 and the MARS-CT-3 spectral scanner', *Journal of Instrumentation* **6**, C01095.

  A description of the improved MARS micro-CT scanner design and presentation of the first CT reconstructions of data obtained with the new Medipix3 detector. This paper updates the spectral CT community with the progress of the MARS scanner, and demonstrates the improvements to the Medipix detector. My contribution consisted of manuscript preparation, particularly the description of the new scanner design. This material is touched upon in Chapter 3.

- Opie, A. M. T. and Bones, P. J. (2011), 'Sensitivity to error of the truncated Hilbert transform technique for interior reconstruction', *in* 'IEEE International Conference on Image Processing 2011', pp. 421–424.

  An evaluation of the sensitivity to error of a recently published interior reconstruction algorithm. This paper reports an independent evaluation of a proposed algorithm, and finds that it is not very stable in the presence of input error. I performed all research and prepared the manuscript. The content of this paper is presented in Chapter 5.

- Xu, Q., Yu, H., Bennett, J., He, P., Zainon, R., Doesburg, R., Opie, A., Walsh, M., Shen, H., Butler, A., Butler, P., Mou, X., and Wang, G. (2012), 'Image reconstruction for hybrid true-color micro-CT', *IEEE Transactions on Biomedical Engineering* **59**(6), 1711–1719.

  A proposal of a new CT architecture, including results of computer simulations and physical experiments to emulate the design. The proposed architecture overcomes several limitations of current spectral x-ray detectors, offering the potential to bring spectral CT to pre-clinical and clinical use in the near future. I was involved in preparation of the mouse sample and collection of data with a MARS scanner.

- Opie, A. M. T., Butler, A. P. H., and Bones, P. J. (2012), 'Energy-resolved Compton scatter estimation for micro-CT', *in* 'Developments in X-Ray Tomography VIII', Vol. 8506 of *Proceedings of the SPIE*, p. 850616.

  The development and numerical validation of a new algorithm for the estimation of Compton scatter levels in a spectral micro-CT scan. The algorithm moves toward scatter correction optimised for spectral CT scans. I developed the algorithm, verified its results against matching Monte Carlo simulations, and prepared the manuscript. The first half of Chapter 4 presents the content of this paper.

- Bennett, J. R., Opie, A. M. T., Xu, Q., Yu, H., Walsh, M., Butler, A., Butler, P., Cao, G., Mohs, A., and Wang, G. (2013), 'Hybrid spectral micro-CT: System design, implementation and preliminary results', *IEEE Transactions on Biomedical Engineering*.

  Implementation of the CT architecture of Xu et al. (2012), with validation of the results against simulated data. This paper proves the feasibility of the architecture and shows that it can be used to collect data enabling spectral reconstruction within an interior region of interest. I assisted in operating the scanner, reconstructed the images, and analysed the results. The manuscript was jointly prepared by the lead author and me. The first part of Chapter 6 reports this work.

0.2.2 Presentations

I have presented my work six times: thrice at local bioengineering conferences, at an IEEE conference, as part of my mid-term examination, and at an SPIE conference.

- At the University of Otago Centre for Bioengineering (UO-CB) Conference in November of 2010 I spoke about the calibration processes for MARS scanners,

both mechanical and electronic. These processes are essential for maximising the spatial and energy resolutions of images reconstructed from MARS data.

- At the IEEE International Conference on Image Processing (September 2011) I presented a poster showing an evaluation of an interior reconstruction algorithm, see (Opie and Bones, 2011) above.
- At the UO-CB Conference in September of 2011 I spoke on the same evaluation.
- My mid-term examination was in November 2011. As part of this I gave a seminar on my work to date and intentions for the remainder of my research.
- At SPIE Optics+Photonics (August 2012) I spoke on a new algorithm for estimating Compton scatter levels in a spectral CT scan, see (Opie et al., 2012) above.
- At the UO-CB Conference in December 2012 I spoke about the same algorithm. For this presentation I received the Rutherford Award for best presentation.

0.2.3 Student supervision

Over the summer of 2012/2013 the MARS research group took on a Summer Research Student to investigate the incorporation of physiological monitoring equipment into the scanner. The position was filled by University of Canterbury Electrical Engineering student Ian Glass. I was charged with his immediate supervision, which involved familiarising him with the project, directing the focus of his work, and offering advice.

0.3 Terminology

Particular meanings are attached to some terms beyond their standard definitions; these are outlined here.

A "phantom" is a precisely known object, either physical or virtual. A virtual phantom is simply an image in two or three dimensions, which may be a raster or a mathematical description; a physical phantom is generally a precisely machined object made of well-defined materials. A projection algorithm can be applied to a virtual phantom to produce virtual scan data; a physical phantom can be scanned to test the calibration of the scanner and the effectiveness of algorithms on real data.

A "projection" is an x-ray image taken from a single angle. It may be a one-dimensional signal from a single row of detector pixels, but in most cases it is a two-dimensional signal from a planar array of detector pixels. Much work in the field of reconstruction algorithm development is on reconstruction of a plane from one-dimensional signals; algorithms can usually be extended to volume reconstruction

from two-dimensional signals later. My work follows this pattern; most algorithms are applied to planar reconstruction.

A "sinogram" is a set of projections over the full scan angle, so named because it appears to be the superposition of many sinusoids. A sinogram is essentially the complete input data set for a reconstruction algorithm.

The back-projection operation takes a set of projections and "smears" the values back across the image space in the direction of the original projection operation (this operation is described in more detail in Chapter 2). The term "back-projection" is used to refer to either the operation or the image thus produced — which of these is intended should be clear from the context.

A "reconstruction" is an image that is intended to represent a slice or volume of the object. This is the final output of a reconstruction algorithm. If the projections are one-dimensional, the reconstruction is a two-dimensional image; if they are two-dimensional, the reconstruction is three-dimensional. This text includes reconstructions from energy-resolved projections, thus reconstructions can also be of dimension greater than three.

In this dissertation, the term "pixel" is only used to refer to an element of an x-ray detector. To avoid ambiguity, the term "voxel" is always used to refer to an element of a reconstruction, even if the reconstruction is two-dimensional.

Summations are occasionally used without explicit limits, e.g.,

$$a = \sum_i b_i.$$

This notation means "for all values of i". Specific limits are not given in these cases because the actual values of the index are unimportant; whether the index runs from 0 to $N-1$ or 1 to N (for example) makes no difference to the result. This is intended to reduce clutter in the equations.

0.4 Dissertation structure

Chapter 1 gives the background of the concepts used in the remainder of the dissertation, including x-ray imaging and computed tomography, CT scanner architecture, spectral imaging, interior tomography and x-ray scatter. In Chapter 2 several approaches to the problem of image reconstruction from projections are described; this problem is at the core of CT imaging. Chapter 3 then describes some of the more important tools for my research, including both physical equipment and software, and my contribution to several of them. The MARS scanner is a key piece of equipment as it is the product of the MARS research group and its existence has let me work with real scan data. The majority of the content of Chapters 1 and 2 is unlikely to be new to readers experienced

in CT; however, Chapter 1 does identify the context from which I have approached the research, and an understanding of the reconstruction methods of Chapter 2 is assumed in later chapters.

Chapters 4 to 6 present my research. Chapter 4 presents the development of an algorithm for energy-resolved estimation of Compton scatter levels in micro-CT scans. The algorithm can be used directly as a means of determining the expected scatter intensity within a scan, or can be incorporated into an iterative structure to perform scatter correction. Scatter correction is important because the presence of scattered photons in CT measurements leads to artefacts in the reconstructed images such as streaks and cupping, and correcting for estimated scatter levels can reduce or remove these artefacts. The chapter also contains an extended mathematical and numerical analysis of a significant approximation used in the derivation of both the preceding algorithm and one from the literature.

Interior tomography is first explored in Chapter 5. In this chapter, a recently published interior reconstruction algorithm is considered which makes use of a small region of prior knowledge in the image. The stability of the algorithm in the face of error in the prior knowledge is evaluated. The study in Chapter 5 does not directly relate to spectral CT, but does provide some useful backing for the approaches in Chapter 6.

In Chapter 6, a new hybrid spectral interior architecture is developed, validated, and optimised. This system integrates a spectral imaging chain with an interior field of view and a conventional imaging chain with a full field of view. The design overcomes significant limitations of current spectral detectors, namely that the detectors are small and expensive and have photon counting rate limits, by reducing the required spectral detector size and only making spectral measurements in regions of attenuated flux. Image quality is maintained by the use of the full field of view conventional detector. The hybrid architecture is first described and validated against simulations, then a study on reduction of radiation exposure is undertaken.

Chapter 7 summarises the results of Chapters 4 to 6 and offers some suggestions for future work to further advance the research presented here.

Chapter One

Background

Computed tomography (CT) is an important modality of modern medical imaging. It extends standard x-ray imaging to offer three-dimensional images of the body. Evolved from tomography, CT offers radiologists the ability to view a cross section of the (x-ray) density of tissue in a patient's body, free from the superposition of neighbouring features that is found on standard x-ray images.

1.1 X-ray imaging

In November 1895, German physics professor Wilhelm Röntgen was investigating the effects of electrical discharges in vacuum tubes. He noticed fluorescence occurring on a screen painted with barium platinocyanide that was near the tube, despite the tube being in an opaque enclosure and the screen being beyond the range of cathode rays (LeVine III., 2010). After much experimentation with this phenomenon, he published a paper describing the penetration of this new type of ray which he called "X-rays" (Röntgen, 1896). This paper contained the image shown in Figure 1.1 of his wife's hand and a ring on her finger, immediately demonstrating one of the most powerful uses of this discovery: non-invasive visualisation of internal structures. Within a single year of Röntgen's initial publication, forty-nine books and over one thousand articles had been published on x-rays. In 1901 Röntgen was awarded the first Nobel Prize in Physics for his discovery. The phenomenon is still used extensively for imaging in modern medicine and industry.

A concrete definition of an "x-ray" is surprisingly difficult to find, but the term refers to a quantum of electromagnetic radiation produced by the interaction of electrons. This is in contrast, for example, to ultraviolet light, which is produced by electron transitions, or to gamma rays, produced by nuclear decay (Ball et al., 2012). The energy of an x-ray photon generally falls between 100 eV and 100 keV[(1)] but there are no hard boundaries set by any physical phenomenon.

[(1)] This range approximately corresponds to wavelengths between 10 nm and 10 pm, or frequencies between 30 PHz and 30 EHz.

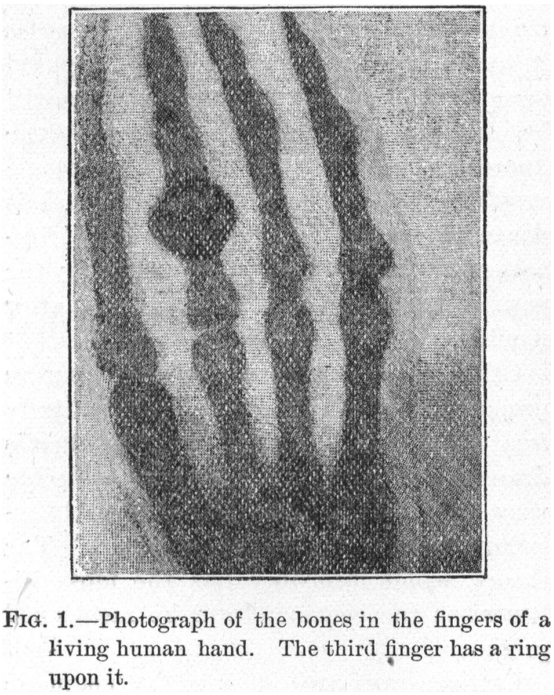

FIG. 1.—Photograph of the bones in the fingers of a living human hand. The third finger has a ring upon it.

Figure 1.1: Radiograph of Röntgen's wife's hand, from his original publication.

While x-ray imaging has the benefit of being non-invasive, its use carries risk due to the ionising nature of x-radiation. Negative effects of exposure to ionising radiation can include carcinogenesis, cataract formation, radiation sickness, and immune system suppression (Trapp and Kron, 2008); these effects are mostly caused by damage to cell DNA which results either in malfunctioning cells or in cell death (apoptosis). The risk associated with x-ray exposure is proportional to the dose; with some effects it is the severity that increases with dose, with others it is the probability of occurrence.

1.2 Computed tomography

In 1972, seventy-seven years after the discovery of x-rays, Godfrey Hounsfield built the first CT scanner (Shung et al., 1992). A CT scan offers vastly more diagnostically useful information than a standard x-ray image (radiograph), due to the ability of the reconstructed image to differentiate some soft tissues and because features from neighbouring "slices" of the body are not superimposed in the image. Although the invention of CT is attributed to Hounsfield, the reconstruction algorithm was also independently developed at the University of Canterbury by Bates and Peters (1971). They did not build a complete scanner to complement their development, but they did publish a successful reconstruction of an aluminium cylinder based on real x-ray transmission data before Hounsfield's CT publication.

CT is a process where x-ray projections of an object are acquired from many angles and then used to reconstruct a cross-section, or "slice" of that object, as illustrated

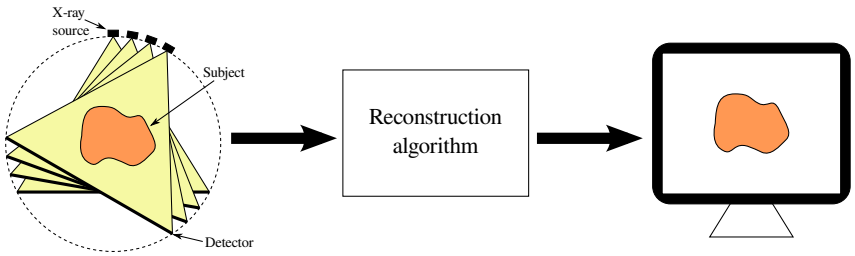

Figure 1.2: CT uses x-ray projections of an object from many angles to reconstruct an axial slice through that object.

in Figure 1.2. Theoretical development of the technique culminated in Hounsfield constructing the first scanner at EMI[(2)] in 1972 (Hounsfield, 1977). Since then, CT has been the subject of much research and development effort. Modern CT scanners are much faster than the original EMI scanner and the images they produce have much greater resolution and clarity (Cunningham and Philip, 2006).

The hazards of x-ray imaging are mentioned in Section 1.1. Because CT involves acquiring a large number of x-ray images, this modality comes with a greater risk of side-effects than a single projection x-ray examination. However, the benefit of the greater diagnostic utility of the resulting images often outweighs the risk, resulting in large numbers of scans being performed. For example, in 2007 approximately 98 000 CT scans were performed in New Zealand (Stirling and Cotterill, 2009).

CT is also used in applications outside the medical arena. Some examples include inspection of turbines, welds (Scudder, 1978), timber logs (Seeram, 2009), and ball grid arrays; geophysical characterisation (Louis et al., 2007); and astronomical imaging. The latter application uses tomographic techniques to produce images of supernovae and the solar corona, for example, and Herman (1980) introduces his book on CT with this application. For the remainder of this thesis, the term "CT" is used solely to refer to x-ray computed tomography.

1.3 X-ray generation

X-rays for CT scanning are usually produced by the bremsstrahlung process, where an electron beam is focused on a target made of a material such as tungsten, molybdenum, or copper, resulting in a beam of x-ray photons being emitted. An x-ray tube consists of a vacuum tube with a cathode and anode inside. Electrical current is passed through the cathode filament to heat it to a temperature such that electrons are boiled from its surface and these electrons accelerate toward the positively charged anode and collide with it at high speed. As the electrons decelerate rapidly in the target, their energy is

[(2)] This is the same EMI that is best known as a record company, with artists including Pink Floyd, The Beatles, Talking Heads, and The Sex Pistols.

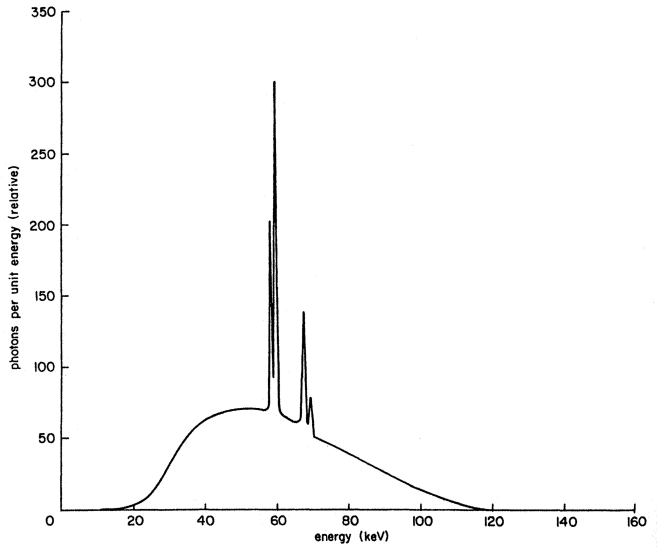

Figure 1.3: Energy spectrum of x-rays emitted from a typical 120 kVp x-ray tube with a tungsten anode. Note both the continuous bremsstrahlung and the discrete characteristic spectra.
(From Barrett and Swindell (1981)).

converted into x-rays (hence "bremsstrahlung", German for "braking radiation") which are emitted in all directions (Johns and Cunningham, 1983).

Not all electrons produce x-rays as they are stopped. In fact, at diagnostic energies over 99% of incident electrons lose all of their energy to ionising the target material, eventually producing heat. A bremsstrahlung x-ray is produced when an incoming electron is deflected (or stopped entirely) by an atomic nucleus in the target, and the deflection causes the electron to lose some energy. The amount of energy that is released as an x-ray photon varies (although it must be less than the electron's original energy), giving rise to a broad spectrum of x-ray energies being emitted by the bremsstrahlung process.

Incident electrons may also collide with an electron from the target material, dislodging it and creating a hole. When this hole is filled by an electron from an outer shell, the excess energy is released as characteristic radiation having one of a small number of specific energies determined by the band-gaps of the elements in the target material. The complete spectrum of x-rays emitted by an x-ray tube is the superposition of this characteristic radiation on the broadband bremsstrahlung spectrum, as shown in Figure 1.3.

The energy of the electrons in a cathode ray tube is determined by the strength of the electric field used to accelerate them. Using units of electron-volts (eV) makes determination of the energy trivial: with a tube voltage of 100 kV, the electrons each have energy of 100 keV. The electron energy is important because it defines the upper

limit for the energy of the x-rays that are produced, for example the spectrum in Figure 1.3 arises from a tube operating at a voltage of 120 kV.

The intensity of an x-ray beam is determined by the energy of the photons and the flux of the beam. Flux (also erroneously called flux rate) is the measure of the number of photons passing through a unit area per second, i.e., a narrow beam has a greater flux than a wider beam carrying the same number of photons per second (Hendee and Ritenour, 2002). The flux output of an x-ray tube is proportional to the current, since more electrons bombarding the anode produce more x-ray photons.

1.3.1 Other x-ray sources

X-ray tubes as described above are the most common, but certainly not the only, method of x-ray production. Synchrotron light sources are a common source of x-radiation for experimental physics, while electron-beam tomography sources and carbon nanotube field emission cathodes (CNTs) are two interesting variations on the cathode ray tube x-ray source design.

Synchrotron light sources (SLS) accelerate electrons to relativistic speeds with a synchrotron, then "wiggle" the electrons with an array of magnets. The resulting oscillating acceleration causes the electrons to emit radiation; the device can be designed such that the radiation is coherent and monochromatic. Synchrotron radiation is typically many orders of magnitude brighter than radiation from an x-ray tube (Als-Nielsen and McMorrow, 2011). The brightness and monochromaticity of a SLS make it ideal for experimental imaging tasks, but the overall size of the source makes it unsuitable for use in a CT scanner. Also, as discussed later, the development of energy-resolved x-ray detectors means that a broadband source can be of greater utility than a monochromatic one.

The x-ray sources used for electron-beam tomography (also called ultrafast or fifth generation CT) are much larger than a standard x-ray tube. In this design the tube is stationary and the x-ray focal point is swept by electromagnetically steering the beam of electrons around a tungsten anode that surrounds the object (Bharath, 2009). By also using stationary detectors to surround the object, this design has no moving parts and can thus complete a full "rotation" very quickly. This type of scanner was developed to be able to image the moving heart which can appear blurred in scans with a conventional scanner.

CNT x-ray sources use field emission (Gomer, 1993) to liberate electrons from the cathode rather than high temperature. The immediate benefits of this design are room-temperature operation, instantaneous response time, and the ability to miniaturise the source (Zhang et al., 2005). Research over the last decade by Professor Zhou's group at the University of North Carolina has resulted in the development of several CNT sources with attractive capabilities. The fast response time allows high speed gating

for small animal cardiac studies (Cao et al., 2009); they have an array source that can produce an intensity modulated beam for radiation therapy (Wang et al., 2011); and they have produced a larger array that allows the x-ray source unit to remain stationary in breast tomosynthesis (Qian et al., 2012).

1.4 X-ray statistics

Bremsstrahlung emission is a Poisson process (Buzug, 2008). The chain of emission, absorption, and detection is called a cascaded Poisson process, and the resulting number of x-ray photons detected is a Poisson-distributed random variable. The Poisson distribution arises from a limit of the binomial distribution; a large number of incident electrons each with a small probability of x-ray production limits to a Poisson distribution. The absorption and detection stages are both Bernoulli distributed, which combine with the Poisson distributed photon arrival to produce another Poisson distribution.

A Poisson random variable X has a probability distribution described by

$$P(X = x) = \frac{\lambda^x}{x!} \exp(-\lambda), \qquad x \geq 0 \tag{1.1}$$

where λ is the sole parameter of the distribution. The mean and variance of the distribution are both equal to the parameter, i.e.,

$$\mathrm{E}[X] = \mathrm{E}\left[(X - \mathrm{E}[X])^2\right] = \lambda, \tag{1.2}$$

where $\mathrm{E}[\cdot]$ represents statistical expectation and X is the number of photons being emitted, absorbed, or detected. Thus the signal-to-noise ratio of x-ray measurements, given by

$$\mathrm{SNR} = \frac{\mathrm{E}[X]}{\sqrt{\mathrm{E}\left[(X - \mathrm{E}[X])^2\right]}}, \tag{1.3}$$

is found to be

$$\mathrm{SNR} = \frac{\lambda}{\sqrt{\lambda}} = \sqrt{\lambda}. \tag{1.4}$$

In this case, λ represents the expected number of x-ray photons to be detected in the detection interval. This is proportional to the intensity of the x-ray beam, which is in turn proportional to the current in the x-ray tube. Thus the signal-to-noise ratio increases with the square root of the x-ray tube current. Note that this is only considering the quantum noise in the system.

Measured x-ray intensity data pass through several processing stages before a reconstructed image is obtained, as described in Section 2.1. Some of the steps in this chain are non-linear and one involves a logarithm; together, these steps transform the noise in such a way that the noise in the reconstructed image is not Poisson distributed.

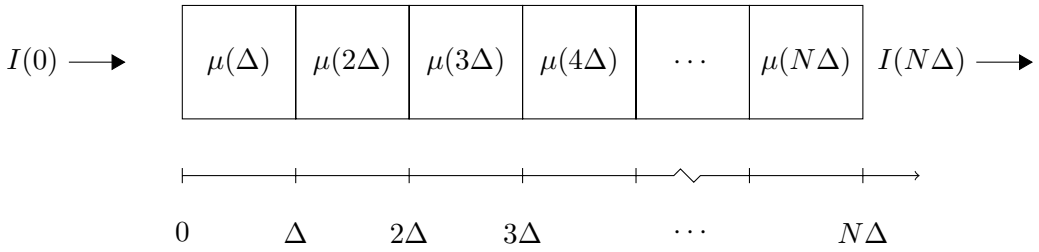

Figure 1.4: Simple representation of the attenuation of an x-ray beam passing through a series of homogeneous blocks. $\mu(x)$ is the linear attenuation coefficient at position x, and $I(x)$ is the beam flux at position x.

Algorithms such as maximum-likelihood expectation-maximisation that expect Poisson distributed values may produce suboptimal images if processed data are used instead of raw counts (Nuyts et al., 2001).

1.5 X-ray attenuation

As an x-ray photon travels through a material, there are three possibilities: it can pass through unaffected, it can be absorbed by an atom within the material by the photoelectric effect, or it can be scattered by an electron within the material (Johns and Cunningham, 1983). Photoelectric and scattering interactions can together be considered as "blocking" a photon. Each effect has its own material-dependent probability of occurrence, μ_p and μ_s, called linear attenuation coefficients, which are specified in units of inverse distance, usually cm^{-1}. These values are usually combined to form an overall coefficient $\mu = \mu_p + \mu_s$, whose value represents the probability that a photon is blocked by a thin slab of the material, normalised by the slab thickness. By the law of large numbers, in a beam with many photons the attenuation coefficient specifies the fraction of photons that are blocked. Typical values of μ are $0.3\,\mathrm{cm}^{-1}$ for soft tissues and $1.0\,\mathrm{cm}^{-1}$ for bone, at a photon energy of 40 keV (Hubbell and Seltzer, 2004). Attenuation generally decreases with increasing photon energy, with exceptions at absorption edges (see Section 1.8).

The flux of an x-ray beam that leaves an object and is measured by a detector depends on the initial beam flux and the attenuation properties of the materials comprising the object. Consider the situation illustrated in Figure 1.4. Here $I(k\Delta)$ is the beam flux after passing through material of thickness $k\Delta$, $I(0)$ is the initial beam flux incident on a series of blocks each of width Δ, and $\mu(x)$ is the linear attenuation coefficient at position x. Since each block is homogeneous, the leftmost block has linear attenuation coefficient $\mu(\Delta)$, the next block to the right has coefficient $\mu(2\Delta)$, and so forth. The fraction of flux blocked in the kth block is given by $\mu(k\Delta)\Delta$ for small Δ. So

the flux leaving the first block is given by

$$I(\Delta) = I(0)(1 - \mu(\Delta)\Delta), \tag{1.5}$$

and the flux leaving block N is

$$I(N\Delta) = I(0) \prod_{n=1}^{N} (1 - \mu(n\Delta)\Delta). \tag{1.6}$$

Rearranging (1.6) and taking logs yields

$$\ln\left(\frac{I(N\Delta)}{I(0)}\right) = \ln\left(\prod_{n=1}^{N} [1 - \mu(n\Delta)\Delta]\right), \tag{1.7}$$

$$= \sum_{n=1}^{N} \ln\left[1 - \mu(n\Delta)\Delta\right]. \tag{1.8}$$

The Taylor series expansion of the natural log is

$$\ln(1 - x) = -\sum_{k=1}^{\infty} \frac{x^k}{k!}, \tag{1.9}$$

and for sufficiently small values of x, this is well approximated by only the first term in the series,

$$\ln(1 - x) \approx -x. \tag{1.10}$$

If Δ is reduced to a differential element $\Delta \to \mathrm{d}x$, then (1.10) can be applied to (1.8) to give

$$\ln\left(\frac{I(N\Delta)}{I(0)}\right) = -\sum_{n=1}^{N} \mu(n\Delta)\Delta, \tag{1.11}$$

$$\ln\left(\frac{I(x')}{I(0)}\right) = -\int_0^{x'} \mu(x)\,\mathrm{d}x, \tag{1.12}$$

where the summation has been converted to an integral due to the use of differential elements, and using $x = n\,\mathrm{d}x$ and $x' = N\,\mathrm{d}x$. Exponentiating this equation and rearranging gives

$$I(x') = I(0) \exp\left\{-\int_0^{x'} \mu(x)\,\mathrm{d}x\right\}, \tag{1.13}$$

more commonly known as the Beer-Lambert law (Lambert, 1760; Beer, 1852).

Although this relationship is the basis of most reconstruction algorithms, it has two main shortcomings. First, the attenuation coefficient $\mu(x)$ actually varies not only

by material but also with energy and thus is more accurately written $\mu(x, E)$. The equation above can then be rewritten as

$$I(x', E) = I(0, E) \exp\left\{ - \int_0^{x'} \mu(x, E)\, \mathrm{d}x \right\}, \tag{1.14}$$

however, for this to be useful a means of measuring $I(x', E)$ and $I(0, E)$ is required; this situation is discussed more in Section 1.8. The second issue with this relationship is scatter. The law describes the intensity of a beam travelling along a single line, so it is correct to claim that scattered photons have been removed from the beam. However, it is not true that scattered photons have been blocked, rather they are only diverted. This becomes a problem when measurements are made simultaneously on many lines, which is true for all detection situations since every detector element has a non-zero size. Photons that the equation considers to be removed by scatter may in fact be picked up elsewhere; Section 1.10 and Chapter 4 address this issue.

1.6 X-ray detectors

X-ray detector technology has developed rapidly since Röntgen's discovery. The original discovery was made with a fluorescent screen and this has been the basis of most detector technologies until recently (Bushberg et al., 2012).

For simple transmission radiography, it is sufficient to use a photographic film together with a phosphor layer in an opaque enclosure (called a cassette). The light from the fluorescence of the phosphor exposes the film, which is then developed in the usual manner (Bushberg et al., 2012). A similar process can be used in general for detectors based on phosphor, also known as scintillating detectors, by replacing the photographic film with an eyeball, a video camera, an image intensifier, photodiodes, or a CCD. Fluoroscopy is the use of x-ray imaging to see internal features and instruments in real time. This requires an image intensifier to make the image from the phosphor visible under normal lighting levels (Hendee and Ritenour, 2002).

For CT, the x-ray projections need to be recorded and digitised to be used by a reconstruction algorithm. Most traditional detectors use a phosphor stage coupled with an optical sensor such as an array of photodiodes or a CCD (Yaffe and Rowlands, 1997). A related technology uses storage phosphors to capture the projection and then uses a photomultiplier tube to measure the luminescence as the phosphor is excited with a raster-scanning laser.

Flat-panel detectors are a technology that uses two layers of liquid crystals to perform x-ray detection. These detectors do not have the same problems with veiling glare as traditional phosphor detectors (Baba et al., 2002), and unlike image intensifiers they are immune to stray electric fields. The same name is given to similar systems

that stop x-rays with a selenium layer and collect the resulting charges directly with pixel electrodes (Kotter and Langer, 2002).

Direct conversion detectors, for example the Medipix (Ballabriga et al., 2007) family, are similar to the latter style of flat-panel detectors, but have a solid layer of a semiconductor such as silicon or cadmium telluride bump-bonded directly to the readout electronics. This design offers greater efficiency, resolution, and simplicity by avoiding intermediate conversion stages. This is the only design suitable for counting individual x-ray photons because any scintillating system loses the quantisation of energy deposition through the optical stage.

Alvarez (2010) suggests a useful set of notations for classifying modern detector types:

Q Measures the total energy of all photons.

N Measures the total number of photons.

NQ Measures the total number of photons and their total energy.

NK Measures the number of photons in each of **K** energy bins.

NKQ Measures the number of photons in each of **K** energy bins in addition to the total energy of all the photons.

In this lexicon **Q** includes traditional scintillating detectors while the Medipix family falls into the **NK** category, specifically **N8** or **N2** depending on the operating mode. Note that these definitions are idealised, i.e., a detector will not measure the actual total energy or number of photons, but rather the deposited energy or number of stopped photons.

The material comprising the detector layer in direct conversion detectors has a significant effect on the performance of the detector. Silicon and germanium layers have excellent charge transport properties and offer good energy resolving ability (Takahashi and Watanabe, 2001). However, these materials have low stopping power for x-rays at the higher end of the diagnostic energy range, for example a 3 mm silicon layer drops to 15% efficiency by 50 keV (Berger et al., 2010). Cadmium telluride (CdTe) layers have a much better response to harder (higher) x-ray energies: a 5 mm layer has greater than 70% efficiency for energies below 160 keV. However, these detectors suffer from considerable charge loss, reducing their effectiveness for energy-resolved detection (Siffert, 1994). Cadmium zinc telluride (CZT) layers are very similar to CdTe, but have lower leakage current and better electron transport, resulting in better spectral performance. CZT production methods are under active development to overcome problems with non-uniformities, grain boundaries, and other defects that affect the performance of the material (Del Sordo et al., 2009). Gallium arsenide (GaAs) layers

are something of a compromise, with a stopping power between that of silicon and CdTe, and better crystal homogeneity and energy resolution than CdTe (Tlustos et al., 2011) (although not as good as those of silicon).

1.7 Scanner geometries

Hounsfield's EMI scanner utilised a bank of collimated x-ray detectors and a tightly collimated x-ray source on the opposite side of the sample to the detectors. At each view angle the source scanned across the sample, illuminating each detector in turn (Hounsfield, 1977); this geometry is called parallel beam or sometimes pencil beam. Since then, scanner design has been through several generations of geometry. Most geometries can be classified as one of three fundamental types: parallel beam, fan beam, or cone beam.

1.7.1 Parallel beam

In an x-ray CT system using parallel beam geometry, a source and a detector shift linearly along opposite sides of the object (the detector need not shift if a bank of detectors is used). The source and detector then rotate around the object a small amount and repeat the scan. This is repeated until scans have been taken from many angles, usually over 180°, to obtain projections such as those illustrated in Figure 1.5.

Although the parallel beam geometry is the simplest to consider in terms of reconstruction algorithms and is least affected by scattered x-rays due to the source collimation, its slow speed of operation means that scans take much longer than those with the geometries of later generations. Also, because additional moving parts are required to enable the source (and possibly detector) to translate, scanners of this design require more maintenance and calibration.

1.7.2 Fan beam

Modern scanners do not use the parallel beam geometry but instead use what is known as fan beam (or divergent beam), as illustrated in Figure 1.6. Fan beam geometry is faster and physically simpler than parallel beam. For these reasons it superseded parallel beam as the standard design in the late 1970s (Cunningham and Philip, 2006). By removing the translation motion from the scanner operation, the gantry can be made more rigid and lighter, and by using a fan beam of x-rays and multiple detector elements, many measurements can be collected simultaneously. These changes allow shorter scan times and better mechanical stability.

Projections obtained with this geometry differ from those obtained with a parallel beam geometry. With parallel beam the magnitude of the projection of an object is always the same regardless of where the object is located between the source and

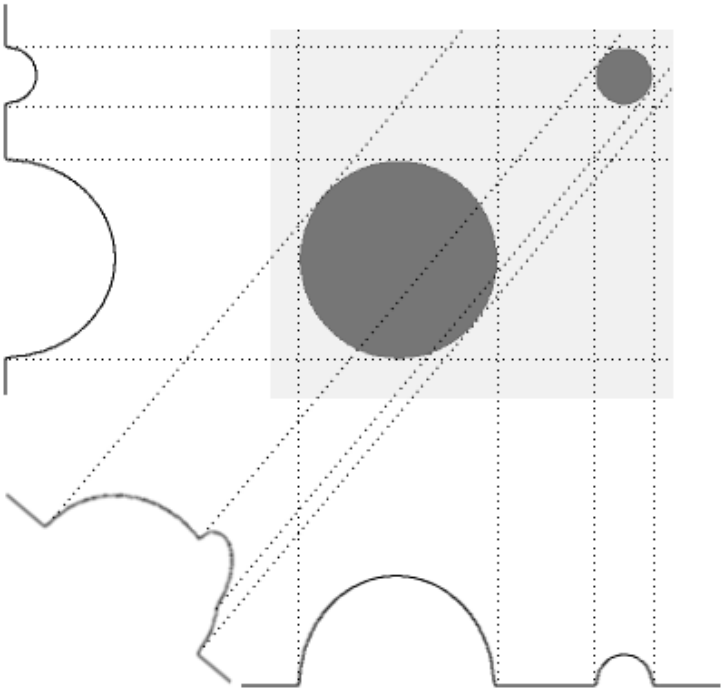

Figure 1.5: Example parallel beam projections of a simple object, taken at 0°, 40°, and 90°.

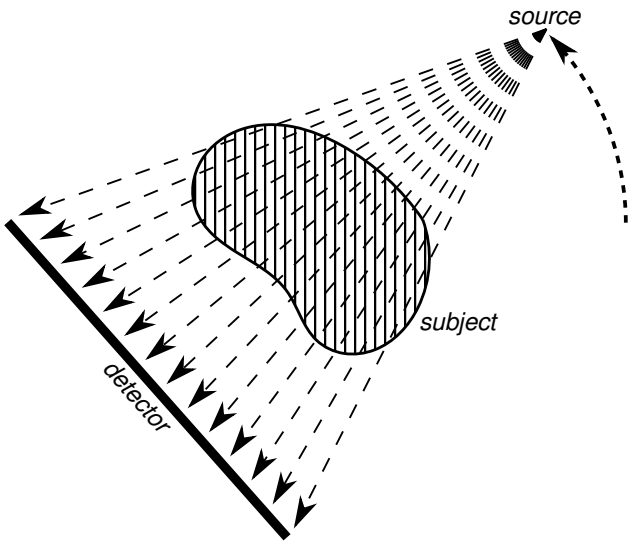

Figure 1.6: Fan beam scanner geometry.

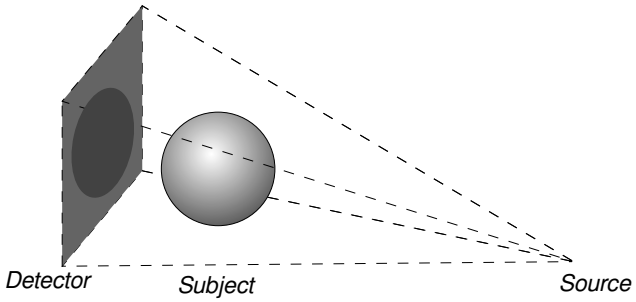

Figure 1.7: Cone beam scanner geometry.

detector; with fan beam the magnitude of the projection depends on the distance from the x-ray source to the object. This is because the x-ray flux incident on the object from a fan beam source is lower if the object is farther away. Less incident flux results in fewer x-ray photons blocked, so the object appears to have a smaller attenuation coefficient. Magnification effects are also seen on fan beam projections: an object closer to the source casts a larger shadow on the detector than it would if it were farther from the source. Another minor difference is found in the minimum scan angle. In a parallel beam system, a 180° scan yields sufficient information to reconstruct an image. However, a fan beam scan requires a scan of at least $180° + \delta$ to collect the same information, where δ is the fan spread angle (Kak and Slaney, 1987); this is called a "short scan", as compared to a full 360° scan.

There are three types of fan beam geometry, determined by the shape of the detector. Figure 1.6 shows a flat detector; the other two shapes are curved: one option is for the centre of the arc to lie at the centre of rotation, the other is for the centre of the arc to lie at the source location. A benefit of the first curve shape is that the detector can be constructed as a complete ring that does not need to rotate with the source; a benefit of the second curve shape is that the pixel spacing is equiangular as viewed from the source, giving an advantage in the formulation of the reconstruction algorithm.

1.7.3 Cone beam

The cone-beam geometry is another kind of divergent beam where the detector is not a single strip of elements but a 2D array of elements lying in a plane. X-rays are still emitted from a single point source, and the beam diverges in two dimensions (Figure 1.7). When discussing cone beam geometry, "fan angle" is used to describe the spread of the beam in the plane of the slice (the same spreading found in the fan beam geometry) whilst "cone angle" is used to describe the spread of the beam in the direction normal to the reconstruction plane. For my work I have only considered parallel and fan beam geometries. Results for fan beam can generally be extended to the cone beam case without difficulty by following methods like those presented in Feldkamp et al. (1984).

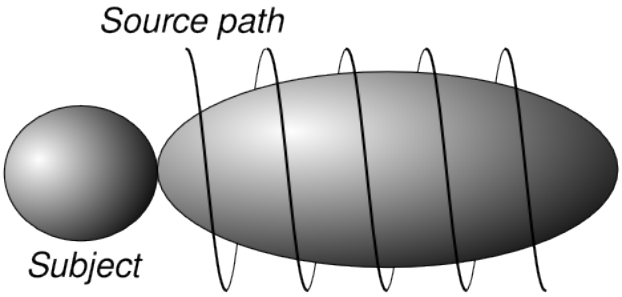

Figure 1.8: A helical scan trajectory. The detector follows a similar path to the source, but on the opposite side of the object to the source.

1.7.4 Helical trajectory

Although it is not a separate geometry in its own right, helical scanning deserves a mention here. A helical scan involves multiple rotations of the gantry whilst the object translates along the rotation axis. The effect is the same as if the object was kept still and the gantry was moved in a helical fashion as illustrated in Figure 1.8. This configuration allows reconstruction of a three-dimensional volume whilst reducing scan time and thus minimising x-ray exposure.

1.8 Spectral imaging

The x-ray attenuation properties of matter are energy dependent. Generally, the attenuation decreases monotonically with increasing photon energy although there is an important exception in k-edges[(3)] (Grodstein, 1957). This relationship is illustrated in Figure 1.9. For any given element, a k-edge occurs at the binding energy of K shell electrons within the element (Shung et al., 1992). The reason for this is that the probability of the photoelectric effect occurring is maximal when the photon energy matches the electron binding energy. As such, there is a sharp increase in the attenuation of a material when the photon energy reaches to this threshold; as the energy increases further the attenuation resumes its decreasing trend. An l-edge is caused by the same phenomenon but corresponds to the binding energy of the L shell electrons.

Traditional x-ray detectors measure the integral of the spectrum of x-ray flux. New detector designs such as the Medipix family have the ability to measure the energy of individual photons, provided two or more do not arrive simultaneously within the region associated with a single detector pixel. These detectors operate several counters so that measurements of the flux in different energy bands can be measured simultaneously. Some commercial CT scanners already offer dual-energy measurements using two source/detector pairs mounted at right angles; the latest detector in the

[(3)] Also l-edges, but these are less common within the diagnostic energy range.

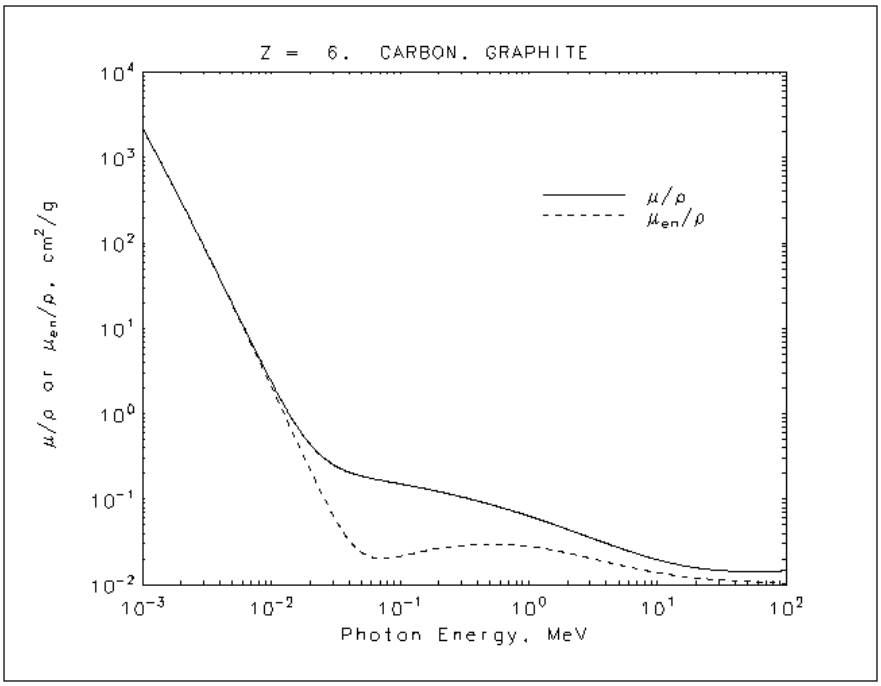

(a)

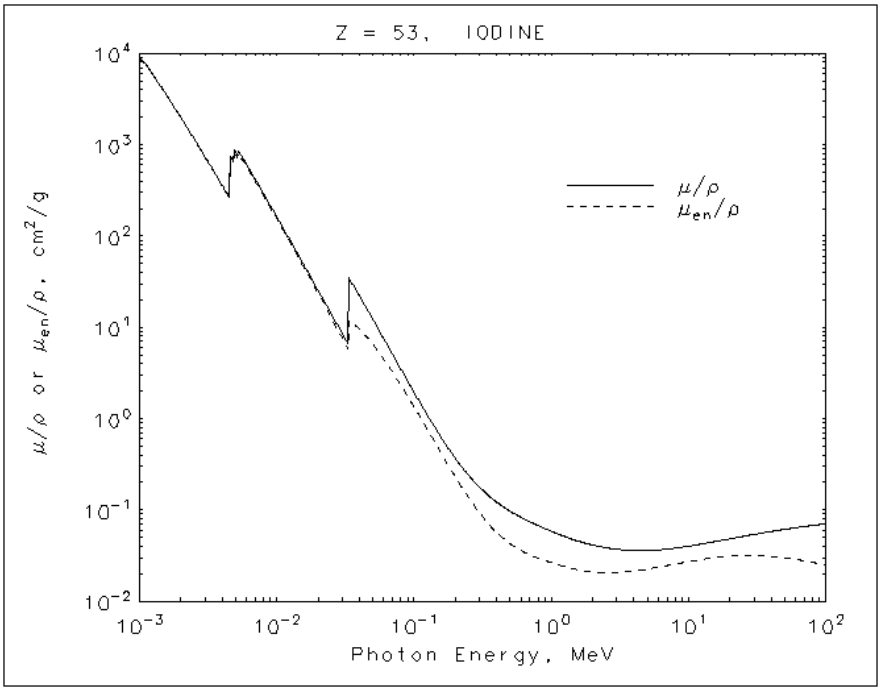

(b)

Figure 1.9: Energy dependence of x-ray attenuation coefficient for (a) carbon and (b) iodine. Note the l- and k-edges in the iodine plot.
(From Hubbell and Seltzer (2004)).

Medipix family offers the ability to measure eight energy bins simultaneously with a single detector (Ballabriga et al., 2011).

1.8.1 Benefits of spectral resolution

An image from a spectrally resolved scan has several advantages over images produced from a standard integrating detector, mostly related to material differentiation. Depending on the scan configuration, k-edges can be identified, certain substances previously indistinguishable can be discriminated, multiple contrast agents can be used concurrently, beam hardening artefacts can be avoided, and image signal-to-noise ratio (SNR) can be improved without an increased radiation dose.

1.8.1.1 Material decomposition

The seminal paper by Alvarez and Macovski (1976) discusses the theory of obtaining complete spectral information by making two independent energy spectrum measurements. They do not specify the use of any particular scanner configuration, instead they offer suggestions for methods of obtaining this data: monoenergetic radiation from two different isotope sources, filtering of a single source spectrum by two materials with different spectral absorption coefficients, or the use of pulse height analysis in photon counting systems. They suggest decomposing the attenuation coefficient spectrum into a linear sum of two functions and suggest two particular functions that respectively model absorption by the photoelectric effect and Compton scattering. They claim to have fitted these two functions to highly accurate attenuation measurements with a maximum error of one percent and an average error of a few tenths of a percent over the range of 30–200 keV.

Decomposing the attenuation coefficient into a linear combination of two or more spectral basis functions offers the ability to differentiate materials that were previously indistinguishable, provided they have different attenuation spectra. Since the attenuation spectrum of an element is determined by both its atomic number and its atomic mass, this proviso is quite reasonable in practice. There are several useful potential applications of this feature. Detection of vulnerable atherosclerotic plaques can be achieved by identifying accumulation of iron in the plaque, but with standard CT iron is indistinguishable from calcium,[(4)] which is another major component of plaques (Primak et al., 2009). Because the x-ray attenuation spectra of iron and calcium are different, this coefficient separation could enable the identification of iron even in the presence of calcification. The same approach could be used to differentiate a contrast medium such as iodine from calcified atheromas.

[(4)] Magnetic resonance imaging is also unable to differentiate iron from calcium.

Another approach to the decomposition of the attenuation coefficient is with algorithms such as principal components analysis (PCA) (Kalukin et al., 2000) or independent components analysis (ICA) (Hu et al., 2004). These methods do not rely on predetermined basis functions but instead calculate new functions tailored to the image of interest by finding basis functions which best account for the variance in the data. These methods can be used to identify the most important spectral differences in the image. Butzer et al. (2008) used PCA to analyse spectral data collected with a Medipix detector with promising results, and both PCA and ICA are used in Chapter 6.

Materials with a k-edge in the diagnostic energy range (approximately 20–140 keV) are often used as contrast media because their strong attenuation can be easily seen in the results of a scan (Shung et al., 1992). If more than one type of contrast agent were to be used for a scan, distinction between them would be impossible with a standard CT scan, whereas with a spectrally resolved image the large difference in attenuation spectra due to the k-edges should be observable. This application is explored in Chapter 6.

1.8.1.2 SNR improvement

Tapiovaara and Wagner (1985) suggest using spectral data to improve the SNR of the reconstructed image. This approach operates on the basis that energy bands with higher flux have a better measurement SNR than those with lower flux. Instead of using the energy bins separately, this method adds the measured intensities together with weighting factors proportional to the intensity in that bin. Their approach to this is to have a detector with an energy response curve matching that of the flux to be measured. A more recent result from Niederlohner et al. (2004) suggests that an improvement in SNR up to a factor of 1.4 is possible, depending on system configuration. Alvarez (2010) proposes using the decomposition into two basis functions as a means of achieving this type of SNR improvement. He claims that this allows an improvement in SNR near to the optimum predicted by Tapiovaara and Wagner, but using a detector with low energy resolution rather than their full-resolution detector.

1.8.1.3 Beam hardening reduction

A common issue in CT scans is the phenomenon known as “beam hardening”. As mentioned above, all substances attenuate lower energy photons more strongly than higher energy ones. This means that as an x-ray beam passes through an object the average energy of the beam increases, making it more penetrating or “harder”. The simple version of the Beer-Lambert law in (2.1) assumes a single x-ray energy; the violation of this assumption means the attenuation integrals (projections) are distorted.

Beam hardening causes “cupping” artefacts, where the apparent attenuation decreases toward the centre of the image (Brooks and Chiro, 1976), and streak artefacts

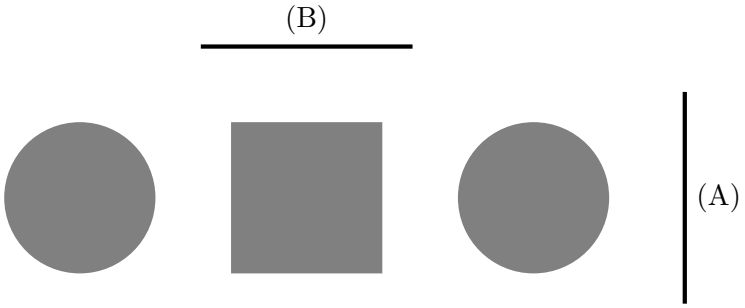

Figure 1.10: A simple example object. The two lines are example detector positions. Note that the circles are not present in the projection measured at postition (B).

behind high-density features. By measuring the attenuation across energy bands of a smaller width, spectrally sensitive detectors can avoid this problem.

1.9 Interior tomography

Interior tomography is the name given to the limited-data situation where the edges of some or all of the projections are not measured. This can happen when the detector is too small to intercept all the rays passing through the object or if the x-ray source is strongly collimated to limit the radiation dose. Figure 1.10 shows an example geometry that would result in interior-type limited data, as the circles are not imaged from all angles due to the size of the detector.

The interior problem has been shown to have no unique solution (Natterer, 1986). This can also be understood intuitively by thinking about the type of data that is collected. Consider Figure 1.10 and assume parallel beam geometry: looking from the view of detector (A), there is no way to determine how many objects are in the image. If the detector rotates around to lie at position (B), there is still insufficient information to determine how many objects are present because the detector is not long enough to image the whole scene. Although the square contributes to every projection, successful reconstruction of it requires some knowledge of the contribution of the circles to the projection at (A). In a full CT scan, this knowledge comes from a full projection from the same direction as (B), but in the case of Figure 1.10 that information is not collected.

Despite the mathematical non-uniqueness, several groups are actively researching methods of reconstructing from truncated data. The most common approach to the problem is to use prior knowledge of some region of the image being reconstructed to regularise the solution; some recent publications even claim exact reconstruction under certain circumstances. This is described in more detail in Section 2.6 and Chapter 5.

1.10 X-ray scatter

X-ray scatter can be divided into two types: Rayleigh (coherent) scatter, where the photon does not lose any energy and is usually deflected by only a small angle, and Compton (incoherent) scatter, where the photon deposits some of its energy onto the electron with which it interacts and the angle of deflection can be anywhere between zero and 180 degrees. For photon energies above 10–15 keV, Compton scatter is the dominant scatter mode in biological tissues, and above 25–50 keV Compton scatter is also more prominent than the photoelectric effect (Berger et al., 2010). The ranges specified are necessary because the actual crossover energy varies with tissue type.

1.10.1 Artefacts induced by scatter

When scattered x-rays reach the detector they increase the measured intensity and thus reduce the apparent attenuation of the material between the x-ray source and the detector. This corrupted attenuation value causes artefacts in radiographs and CT images (Joseph and Spital, 1982; Johns and Yaffe, 1982; Siewerdsen and Jaffray, 2001). In conventional x-ray imaging the effect of scatter is to reduce the contrast of the image (Seibert and Boone, 1988; Siewerdsen et al., 2006). The artefacts created in CT images are similar to those produced by beam hardening (Hunter and McDavid, 2012), namely streaks between high-density features and cupping. The magnitude of scatter-induced artefacts is proportional to the scatter-to-primary ratio (SPR) (Siewerdsen and Jaffray, 2001), which is the ratio between the amount of scattered radiation detected and the amount of primary (non-scattered) radiation that is detected. Johns and Yaffe (1982) report SPR values of up to 16% for fan-beam geometries, while Siewerdsen and Jaffray (2001) report SPR up to 140% in cone-beam geometries.

1.10.2 Magnitude of scattered radiation

The amount of scatter contributing to a radiographic projection is influenced by several factors: the geometry and collimation of the scanner; the size, shape, and composition of the object under study; and the energy spectrum of the x-ray source. The amount of scatter is greatest in a cone-beam geometry, followed by fan-beam, while pencil-beam has the least (Kalender, 1981). This is because a greater illuminated volume leads to more x-ray flux being scattered and thus detected. For the same reason, the amount of scatter increases with the cone angle in a cone-beam geometry (Kyriakou and Kalender, 2007).

Engel et al. (2008) present a study of the relative quantities of the different kinds of scatter according to object size and incident photon energy. Their results show that multiply Compton-scattered photons become increasingly predominant as the object diameter increases, and the energy spectrum of multiple Compton scatter is strongly

softened[5] compared to the incident energy spectrum. The spectrum of single Compton scatter is also softened, but not to the same extent, while the spectrum of the Rayleigh scattered radiation is the same as that of the primary radiation.

While photons are scattered by all the material within an object, the majority of scatter which is detected by a scan originates from the final few centimetres of the path (Kalender, 1981; Engel et al., 2008). There are two reasons for this. First, scattered photons originating further back in the object have greater opportunity to be absorbed after scattering, and second, the solid angle into which a photon must scatter in order to be detected is smaller for a scatter event farther from the detector, so the likelihood of detection of the scattered photon is smaller.

1.10.3 Existing techniques for addressing scatter

Current and proposed techniques for dealing with scattered radiation can be divided into hardware based methods, software based methods, and hybrid methods. Hardware techniques include antiscatter grids, air gaps, and illumination minimisation, while software techniques focus on estimating scatter intensity then subtracting this from the measured data. Hybrid techniques usually involve hardware modifications to obtain data for use in software corrections.

1.10.3.1 Hardware methods

Possibly the simplest method for reducing the amount of detected scatter is to increase the air gap between the object and the detector (Neitzel, 1992; Ardran and Crooks, 1964). This method works because primary radiation is always travelling toward the detector, so extra distance through air has negligible effect on the intensity, while scattered radiation is generally travelling at an angle with respect to the primary radiation. An extra air gap allows more of the scattered radiation to pass to the side of the detector instead of striking it. This technique is simple to implement as long as there is sufficient space inside a scanner, however a lot of scatter is still detected.

Another popular hardware solution is to place an antiscatter grid, or post-patient collimator between the object and the detector (Kalender, 1982; Wiegert et al., 2004). The grid is made up of thin blades of a highly attenuating material such as lead or molybdenum aligned parallel to the primary radiation. The grid can be either "one-dimensional" with individual blades placed parallel to each other (also known as "out-of-slice collimation"), or "two-dimensional" where an additional set of parallel blades lie perpendicular to the original set (Engel et al., 2008), creating individual boxes around each detector pixel. This method exploits the direction of travel of scattered radiation since primary radiation passes through the gaps between blades while most

[5] Softened: skewed downward in energy.

scattered radiation strikes the blades and is absorbed. The antiscatter grid approach is reasonably simple to implement and is effective, but it has two important disadvantages. First, it is not feasible to use an antiscatter grid with micro-CT as the detector pixel pitch of around 50 µm means the blades would obscure a significant portion of each pixel, severely reducing the effective detector efficiency. Second, even on standard systems the grid blocks some primary radiation. Since the signal-to-noise (SNR) of an x-ray image is proportional to the measured intensity (Buzug, 2008), this results in a reduction in the ratio between SNR and patient dose.

1.10.3.2 Software methods

An early software correction method was proposed by Joseph and Spital (1982). The method calculates "clean" projections based on the measured data according to an expression that uses a single parameter to describe level of scatter. The images in the paper are difficult to evaluate, but they do appear to show some improvement in the cupping artefact caused by scatter. Because the method does not account for scatter being a dispersive process and only uses a single parameter, they acknowledge that the algorithm is insufficient for any object more complex than a simple water cylinder phantom.

A more sophisticated approach is that of Ohnesorge et al. (1999), who calculate a scatter distribution by convolving a blurring kernel with the measured attenuation data. They then subtract the calculated estimate from the measured projections to produce an estimate of the clean data. The blurring kernel is derived to account for out-of-slice collimation and scanner geometry where necessary. Their results show an improvement in both cupping and streak artefacts on both physiological and phantom scans.

A more accurate method of scatter estimation and correction makes use of Monte Carlo simulations based on an initial reconstructed image (Jarry et al., 2006; Bertram et al., 2008). These methods, usually iterative, start with a reconstructed image then perform a Monte Carlo simulation of the x-ray projection to estimate the amount of scattered radiation that was detected. This quantity is subtracted from the original measured projection data, and a clean image is then reconstructed. Monte Carlo based methods can be very accurate and thus produce high quality results, but their main disadvantage is the computational cost. Colijn and Beekman (2004) suggest a method of accelerating Monte Carlo simulations by reducing the length of the simulation (from 10^7–10^9 simulated photon paths down to 10^5–10^6) then using a fitting algorithm to eliminate the noise in the simulated scatter projections. Depending on scan conditions, this technique can result in an acceleration factor of up to 200.

1.10.3.3 Hybrid hardware/software methods

The use of beam-stop arrays (BSAs) to directly measure scatter intensities (Wagner et al., 1989; Lo et al., 1994; Ning et al., 2004) is an example of a hybrid software/hardware technique. This approach involves installing an array of small radio-opaque (usually lead) "beam stoppers" between the x-ray source and the object under study. These small lumps block the primary radiation, but scattered photons can still arrive at the detector in the shadow of the blockers. This allows a direct measurement of the scatter intensity at several locations (determined by the arrangement of the blocker array) in the measured image. Since the spatial distribution of scatter is slowly varying (Kyriakou and Kalender, 2007), interpolation can be used to calculate the scatter at all locations in the radiograph. Another radiograph is captured without the blockers in place, then the scatter intensity is subtracted from the complete measured values to yield a "scatter-free" projection image. Since this approach operates on directly measured scatter intensities, it is very effective at correcting scatter. Unfortunately it also requires at least one, and often several, extra exposures which increases the dose delivered to the patient and the time required for a scan. The BSA technique is also used to experimentally evaluate or provide calibration data for other methods (Love and Kruger, 1987; Seibert and Boone, 1988; Rinkel et al., 2007).

Siewerdsen et al. (2006) suggest a different method using scatter measurements in primary shadows. This technique interpolates between the scatter measured in the shadows cast by the source collimator leaves. Because they do not have measurements of scatter intensity in the centre of the projections, the method relies on a long range interpolation, for which they find a quadratic to be most successful. Their published results demonstrate that the method is successful in reducing scatter-induced artefacts, although it does not eliminate them. They also note that some conditions, for example strong cylindrical asymmetry like that found in parts of the head, result in catastrophic failure and the resulting image exhibits severe streaks. They offer suggestions for fixing the algorithm when this happens. Benefits of this method are that no alterations are required of the hardware, and that the extra dose and time of the BSA method are avoided.

Another hybrid technique, proposed by Zhu et al. (2006), is called "primary modulation". This technique involves installing a checkerboard pattern of semitransparent blockers between the source and the patient. The hypothesis behind this approach is that adding high spatial frequencies to the primary beam does not result in high frequency components in the scatter distribution. This hypothesis is based on the slowly varying nature of Compton scatter contributions to radiographs. Modulating the primary beam results in the clean projection image being modulated up into the high frequency area in the Fourier domain. This allows the contribution of scatter to be calculated and subtracted from the image, which can then be demodulated to be used for

reconstruction. The published results demonstrate that this technique reduces scatter artefacts in reconstructed images, but it also heavily reduces the spatial resolution of the reconstructions. The technique has another disadvantage in that a higher dose is necessarily delivered to parts of the patient to compensate for the reduction in primary intensity caused by the semitransparent blockers.

Seibert and Boone (1988) apply a deconvolution approach to scatter correction. They derive a simplistic point-spread function (PSF) based on work by Smith and Kruger (1986) and they evaluate the parameters for the PSF using a BSA. The deconvolution is implemented in the Fourier domain after inverting the PSF numerically. Their results show that the scatter effects are reduced, but the technique involves multiple beam-stop exposures for each image, increasing the delivered dose markedly. The same authors have also published their own derivation of a PSF for scattered radiation, which they compare to a Monte Carlo simulation of a radiographic exposure (Boone and Seibert, 1988).

Rinkel et al. (2007) propose a method for correction based on the BSA technique, but avoiding the added dose and scan time. Their method uses scatter fields from scans of PMMA[(6)] of various thicknesses, measured using the BSA method, to predict the amount of scatter produced in a real patient scan. Inhomogeneities in the patient are accounted for by generating a multiplicative deformation map based on the ratio between the scatter predicted by a convolutional model and that predicted by the PMMA scans. The results show improvements in reconstructed image quality of a similar extent to those achieved by the BSA method, but without the added dose and time. However, like all of the other techniques outlined above, this approach gives no consideration to the energy-dependence of the scattering process.

In Chapter 4 a reconstruction-based scatter estimation algorithm is developed. This algorithm produces energy-resolved estimates of scatter intensity without extra measurements, and unlike other reconstruction-based algorithms it is analytical, rather than Monte Carlo-based, and thus it is fast.

[(6)] PMMA: Poly(methyl methacrylate), also known as Perspex or Lucite.

Chapter Two

Reconstruction

Reconstruction is the operation of taking measured x-ray projection data and producing an image representing a 3D region of the object. The process begins with preprocessing and then proceeds with the reconstruction proper. This chapter first describes the preprocessing step and the Radon transform, which is the basis for most analytical reconstruction techniques. The rest of the chapter is devoted to a description and explanation of the various reconstruction algorithms. All of the work in this thesis is with 2D reconstructions, so apart from the description of cone beam reconstruction in Section 2.3.3 all reconstructions are 2D slices.

2.1 Preprocessing

Preprocessing stages take the raw x-ray intensity measurements and produce line integrals of x-ray attenuation that can be used as inputs for the main reconstruction algorithm. The processes that occur may include flat-fielding, converting to attenuation, stitching, aligning, and in-painting. Which of these processes are actually applied to any given data set depends on the scanner configuration. For example, stitching is only necessary if the scanner uses a moving detector, and in-painting is only necessary if the detector has unreliable or non-responsive areas.

The detector in a scanner measures the x-ray flux that has passed through the object. However, the main reconstruction algorithms operate on attenuation data, specifically, the cumulative attenuation along a line through the object, i.e., a line integral of the object's linear attenuation coefficient. The Beer-Lambert law, derived in Section 1.5, relates the measured x-ray flux to the attenuation coefficient. Equation (1.13) can be rewritten to operate on a two-dimensional object, giving

$$I(s) = I_0(s) \exp\left(- \int_{t_{\text{source}}}^{t_{\text{detector}}} \mu(s,t)\, \mathrm{d}t \right), \tag{2.1}$$

where I is the measured x-ray intensity, I_0 is the "flatfield" intensity, $\mu(s,t)$ is the linear attenuation coefficient of the object, and (s,t) are coordinates on the rotated axes as shown in Figure 2.1. The flatfield intensity is the measured x-ray intensity when there

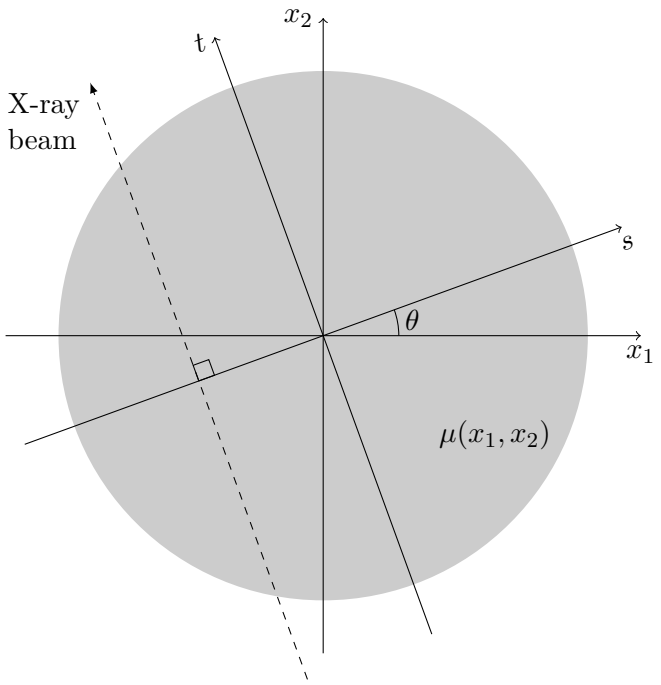

Figure 2.1: Attenuation values are integrated along rays.

is no object in the field of view. Thus the line attenuation is obtained by

$$p_\theta(s) = \int_{t_{\text{source}}}^{t_{\text{detector}}} \mu(s,t)\,\mathrm{d}t = -\ln\left(\frac{I(s)}{I_0(s)}\right). \tag{2.2}$$

The line attenuation data are referred to as the "projections" and are shown on the plots in Figure 1.5. Note that μ, I, and I_0 are all energy dependent but most reconstruction algorithms neglect this fact.

If a scanner uses multiple detectors, or multiple positions of a single detector,[(1)] then these separate measurements need to be combined into a single signal before being used for reconstruction. "Stitching" is the name given to the process of combining several signals together into one, including interpolation and averaging as necessary. If the detectors are two-dimensional, then the projections may need to be rotated slightly to align with one another as part of this process.

If a detector has pixels that give unreliable measurements, or no measurement at all, then values must be assigned to these pixels for meaningful reconstruction to take place. This can be achieved with some form of interpolation. If the system uses a movable detector then it is also possible to make overlapping measurements and thereby collect a full data set.

All of the operations mentioned above need to be applied to the raw data before they are used by the reconstruction algorithm. The conversion from raw x-ray intensity

[(1)] The MARS system measures x-ray data using multiple detector positions.

to projection data with (2.2) is always done; the data cleaning operations are only applied where necessary.

2.2 The Radon transform

To develop a means of reconstructing a slice of an object based on its projections, a mathematical expression for the projections must first be developed, then this expression needs to be inverted. The Radon transform (Radon, 1986) is a mathematical operation that describes the relationship between an N-dimensional function and its (N-1)-dimensional projections; in this thesis only the 2D→1D situation is considered. The derivation in this section is not the original approach taken by Radon; his derivations did not use the Fourier transform, but improper integrals and mathematics that are generally less accessible.

Consider the situation illustrated in Figure 2.1. Let $\mu(\boldsymbol{x}) = \mu(x_1, x_2)$ represent the x-ray linear attenuation coefficient of an object at the point (x_1, x_2). Then the cumulative attenuation along a line (ray) through the object is $p_\theta(s)$ as given by (2.2). This value varies depending on which ray is taken at which angle. Projections are considered to be one dimensional functions of s, and each angle is considered separately (Lewitt, 1983). The quantity $\mu(x_1, x_2)$ in Figure 2.1 is related to $\mu(s, t)$ in (2.1) and (2.2) by

$$x_1 = s\cos(\theta) - t\sin(\theta) \tag{2.3}$$

$$x_2 = t\cos(\theta) + s\sin(\theta), \tag{2.4}$$

so (2.2) can be rewritten

$$p_\theta(s) = \int_{-\infty}^{\infty} \mu_\theta(s,t)\,\mathrm{d}t, \tag{2.5}$$

$$= \int_{-\infty}^{\infty} \mu(s\cos\theta - t\sin\theta, t\cos\theta + s\sin\theta)\,\mathrm{d}t, \tag{2.6}$$

defining $\mu_\theta(s,t)$ to be $\mu\left(s\cos\theta - t\sin\theta, t\cos\theta + s\sin\theta\right)$, which is $\mu(\boldsymbol{x})$ rotated clockwise by θ. Taking the one dimensional Fourier transform of $p_\theta(s)$ with the conjugate variable chosen as ρ results in

$$P_\theta(\rho) = \mathcal{F}\{p_\theta(s)\} = \int_{-\infty}^{\infty} \left[\int_{-\infty}^{\infty} \mu_\theta(s,t)\,\mathrm{d}t\right] \exp(-\mathrm{j}2\pi\rho s)\,\mathrm{d}s, \tag{2.7}$$

$$= \int_{-\infty}^{\infty}\int_{-\infty}^{\infty} \mu_\theta(s,t)\exp(-\mathrm{j}2\pi\rho s)\,\mathrm{d}s\,\mathrm{d}t, \tag{2.8}$$

where $\mathcal{F}\{p\}$ represents the Fourier transform of function p.

At this point, it is beneficial to take a moment to consider the two dimensional Fourier transform (2D-FT). The 2D-FT of an image $f(x, y)$ is given by (Epstein, 2008)

$$F(X, Y) = \int_{-\infty}^{\infty} \int_{-\infty}^{\infty} f(x, y) \exp(-\mathrm{j}2\pi(Xx + Yy)) \, \mathrm{d}x \, \mathrm{d}y, \tag{2.9}$$

using X and Y as the variables conjugate to x and y respectively. If the only region of interest in the Fourier domain is the line along the X axis, then (2.9) can be written

$$F(X, 0) = \int_{-\infty}^{\infty} \int_{-\infty}^{\infty} f(x, y) \exp(-\mathrm{j}2\pi Xx) \, \mathrm{d}x \, \mathrm{d}y. \tag{2.10}$$

Comparing (2.8) and (2.10) it is clear that $P_\theta(\rho) = M_\theta(S, 0)$, where $M_\theta(S, T)$ is the 2D-FT of $\mu_\theta(s, t)$.

Rotational invariance means that the Fourier transform of a rotated image is equal to the rotated Fourier transform of the original image (Bracewell, 1986, p.246), i.e.,

$$\begin{aligned} &\mathcal{F}\{f(x\cos\theta + y\sin\theta, y\cos\theta - x\sin\theta)\} \\ &\qquad = F(X\cos\theta + Y\sin\theta, Y\cos\theta - X\sin\theta). \end{aligned} \tag{2.11}$$

From this relationship it is apparent that $M_\theta(S, T)$ is equal to $M(X_1, X_2)$ rotated clockwise by θ. As such, $P_\theta(\rho)$ represents a line through the origin of Fourier space at angle θ (measured anticlockwise from the horizontal axis). This important result is often referred to as the "central slice theorem" (Barrett and Swindell, 1981) or "Fourier slice theorem" (Kak and Slaney, 1987). By taking projections at all angles, Fourier space can be completely populated and thus there is sufficient information to reconstruct the original image. This description serves only to demonstrate that the data that is measured should theoretically be sufficient to reconstruct an image of the original object. There are a number of methods for achieving this goal in practice, some of which are covered in the following sections.

2.3 Filtered back-projection

Filtered back-projection is the most common reconstruction method used by modern scanners (Buzug, 2008, p.175). The technique closely follows the central slice theorem, and is comprised of two fundamental steps, as suggested by the name: filtering and then back-projection. The parallel beam version is the simplest, so that is presented first.

2.3.1 Parallel beam

The previous section showed that the 2D Fourier transform of the image is given by the 1D Fourier transforms of the projections laid in Fourier space according to the projection angle. Thus it is reasonable to assume that the image can be reconstructed

by applying the inverse Fourier transform to this data:

$$\mu(\boldsymbol{x}) = \int_{-\infty}^{\infty}\int_{-\infty}^{\infty} M(\boldsymbol{X}) \exp\left(\mathrm{j}2\pi(\boldsymbol{X}\cdot\boldsymbol{x})\right)\,\mathrm{d}X_1\,\mathrm{d}X_2, \tag{2.12}$$

where $M(\boldsymbol{X})$ is the Fourier domain image. Recognising that this $M(\boldsymbol{X})$ is made up of data lying along radial lines, (2.12) can be rewritten in polar coordinates as

$$\mu(\boldsymbol{x}) = \int_{0}^{2\pi}\int_{0}^{\infty} M(\rho,\theta) \exp\left(\mathrm{j}2\pi\rho(x_1\cos\theta + x_2\sin\theta)\right)\rho\,\mathrm{d}\rho\,\mathrm{d}\theta, \tag{2.13}$$

$$= \int_{0}^{2\pi}\int_{0}^{\infty} M(\rho,\theta) \exp\left(\mathrm{j}2\pi\rho(\boldsymbol{x}\cdot\boldsymbol{\alpha})\right)\rho\,\mathrm{d}\rho\,\mathrm{d}\theta, \tag{2.14}$$

where the coordinate transformation is

$$\begin{aligned} X_1 &= \rho\cos\theta, \\ X_2 &= \rho\sin\theta, \text{ and} \\ \mathrm{d}X_1\,\mathrm{d}X_2 &= \rho\,\mathrm{d}\rho\,\mathrm{d}\theta, \end{aligned} \tag{2.15}$$

and defining

$$\boldsymbol{\alpha} = (\cos\theta, \sin\theta), \tag{2.16}$$

which is the unit vector pointing along the detector. Using the property

$$M(\rho,\theta+\pi) = M(-\rho,\theta), \tag{2.17}$$

which arises due to the circular symmetry of the scan, (2.14) can be rewritten as

$$\mu(\boldsymbol{x}) = \int_{0}^{\pi}\int_{-\infty}^{\infty} M(\rho,\theta)|\rho| \exp\left(\mathrm{j}2\pi\rho(\boldsymbol{x}\cdot\boldsymbol{\alpha})\right)\,\mathrm{d}\rho\,\mathrm{d}\theta. \tag{2.18}$$

Since $P_\theta(\rho) = M(\rho,\theta)$ (from above), this expression can be decomposed into two separate operations:

$$q_\theta(s) = \int_{-\infty}^{\infty} P_\theta(\rho)|\rho| \exp\left(\mathrm{j}2\pi\rho s\right)\,\mathrm{d}\rho, \text{ and} \tag{2.19}$$

$$\mu(\boldsymbol{x}) = \int_{0}^{\pi} q_\theta\left(\boldsymbol{x}\cdot\boldsymbol{\alpha}\right)\,\mathrm{d}\theta, \tag{2.20}$$

which correspond respectively to the filtering step and the back-projection step of the algorithm. The quantity $q_\theta(s)$ is known as a "filtered projection".

The filtering step in (2.19) takes the projections and applies a filter with frequency response $|\rho|$, hence this is often called a "rho filter". This can be done either in the frequency domain by transforming the projections, multiplying by $|\rho|$, and transforming

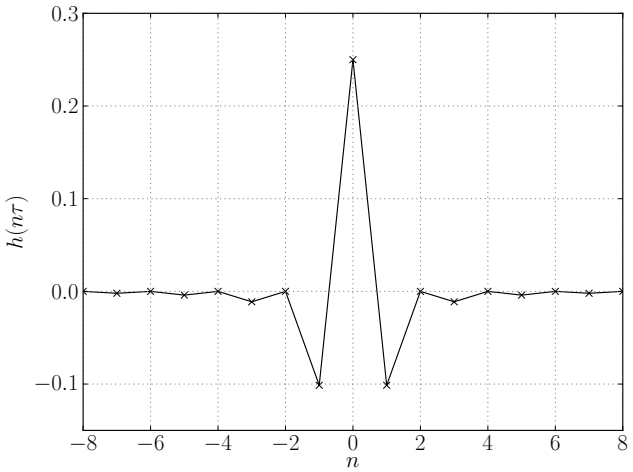

Figure 2.2: A typical rho filter kernel, based on (2.23) with $\tau = 1$.

back; or in the spatial domain using convolution:

$$q_\theta(s) = \int_{-\infty}^{\infty} p_\theta(s')\, h(s - s')\, \mathrm{d}s', \tag{2.21}$$

where $h(s)$ is the inverse Fourier transform of $|\rho|$, known as the rho filter kernel. The inverse transform of $|\rho|$ is $-1/(\pi s^2)$, which diverges at $s = 0$ and is thus not immediately useful. However, since the projection data $p_\theta(s)$ are sampled, the filter response only needs to match $|\rho|$ over a finite frequency range. If the sampling interval is τ, then the greatest frequency that can be present in the projection is $1/(2\tau)$. The inverse Fourier transform of a band-limited $|\rho|$ is given by (Kak and Slaney, 1987)

$$h(t) = \frac{1}{2\tau^2}\ \mathrm{sinc}(2t/2\tau) - \frac{1}{4\tau^2}\ \mathrm{sinc}^2(t/2\tau), \tag{2.22}$$

where $\mathrm{sinc}(t) = \sin(\pi t)/(\pi t)$, $\mathrm{sinc}(0) = 1$. Sampling this function with the same interval as the projection data yields

$$h(n\tau) = \begin{cases} \dfrac{1}{4\tau^2}, & n = 0 \\ 0, & n \text{ even} \\ -\dfrac{1}{n^2\pi^2\tau^2}, & n \text{ odd.} \end{cases} \tag{2.23}$$

This is shown in Figure 2.2 for $\tau = 1$.

In practice, the high-pass nature of the standard rho filter enhances noise in the projections, so a modified version of the filter is used which rolls off at higher frequencies. This roll-off is usually determined by a standard window function such as a Hamming or truncated sinc window applied in the frequency domain. The choice of roll-off window largely depends on the object being reconstructed: too much roll-off will blur the image,

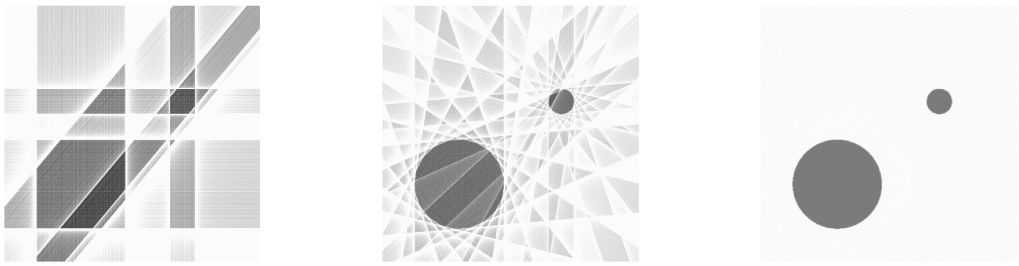

(a) **(b)** **(c)**

Figure 2.3: Example reconstructions of a simple object consisting of two circles, using parallel beam filtered back-projection. The reconstructions used projections at (a) 0°, 40°, and 90°; (b) 10 evenly-spaced angles over 180°; (c) 180 evenly-spaced angles over 180°.

but some situations can tolerate more blurring than others. For example, if bone is the primary feature of interest in a scan, then not much roll-off is required since the large difference in attenuation between bone and the tissue surrounding it means the bone can easily be distinguished from noise. Also, the large difference causes a substantial step-like change in image intensity, so the image will have larger valid components at high frequencies. Conversely, if brain matter is of interest, the difference in attenuation between white and grey matter is small (Brooks et al., 1980), so the boundaries could more easily be swamped by noise. A greater amount of roll-off would be appropriate in this case, at the expense of image sharpness.

The back-projection operation in (2.20) can be thought of as a smearing operation: each filtered projection is smeared back across the image in the direction of the rays that produced it. The results of smearing each projection are added together to produce the final image. Figure 2.3 illustrates how the back-projections of the filtered projections interact with each other to produce a quality reconstruction. Clearly, a greater number of projection angles produces a better reconstruction.

2.3.2 Fan beam

The reconstruction algorithm developed above cannot be applied directly to fan beam data. There are two options for reconstructing from fan beam data: either re-bin the projection data into a set of parallel beam projections and then apply a parallel beam reconstruction algorithm, or reformulate the reconstruction to work directly on fan beam data.

The principle behind re-binning is that each ray in a fan beam can also be described as a ray in a parallel beam data set. Figure 2.4 illustrates the relationship between the fan beam projections $R_\beta(l)$ and the equivalent parallel beam projections $p_\theta(s)$ for a flat

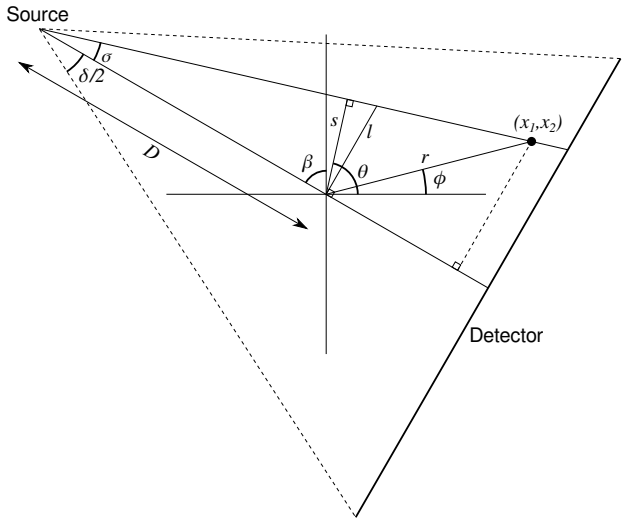

Figure 2.4: Geometrical parameters used in a fan beam algorithm. s and θ are the corresponding parallel beam parameters for any given ray.

detector:

$$\begin{aligned} s &= l\cos\sigma, & \theta &= \beta + \sigma, \\ &= \frac{lD}{\sqrt{D^2 + l^2}}, & &= \beta + \tan^{-1}\left(\frac{l}{D}\right). \end{aligned} \tag{2.24}$$

Unfortunately, the projection sample locations do not transform to lie in a regular pattern in the (s, θ) space, so interpolation is required to produce samples that are regularly spaced for input into the parallel beam reconstruction algorithm. A partial exception to this is found in the detector design that is curved such that the centre of the arc lies on the source; in this case judicious selection of the rotation angles can produce data that transform neatly onto the θ axis, although interpolation in the s axis is still required.

To avoid re-binning and operate directly on the measured fan beam data, the reconstruction formula must be rewritten to take account of the different geometry. Kak and Slaney (1987) offer a good presentation of the derivation of the reconstruction algorithms for fan beam data from two of the three detector shapes: the flat detector and the detector curved about the source. Their result for a curved detector is

$$R'_\beta(\sigma) = R_\beta(\sigma) D \cos\sigma, \tag{2.25}$$

$$g(\sigma) = \frac{1}{2}\left(\frac{\sigma}{\sin\sigma}\right)^2 h(\sigma), \tag{2.26}$$

$$Q_\beta(\sigma) = R'_\beta(\sigma) \odot g(\sigma), \tag{2.27}$$

$$\mu(\boldsymbol{x}) = \int_0^{2\pi} \frac{1}{L(\boldsymbol{x}, \beta)^2} Q_\beta(\sigma')\, \mathrm{d}\beta, \tag{2.28}$$

using $h(\sigma)$ as defined by (2.23) and where $\odot$ denotes convolution, L is the distance from the source to the voxel $\boldsymbol{x}$, and σ' is the value of σ corresponding to the ray that passes through $\boldsymbol{x}$. The projections $R_\beta(\sigma)$ are taken as a function of the angle σ to the pixel. Equation (2.25) applies a cosine weighting to the projections, (2.26) defines a modified filter kernel, (2.27) performs the filtering of the weighted projections, and (2.28) performs a weighted back-projection. Note that in this back-projection the smearing is performed in the same fan shape as the original rays, and the smeared images are divided by L^2 before being added together for the final reconstruction.

For a flat detector the geometry differs again so a separate reconstruction algorithm is derived:

$$R'_\beta(l) = R_\beta(l)\,\frac{D}{\sqrt{D^2+l^2}}, \tag{2.29}$$

$$g(l) = \frac{1}{2}h(l), \tag{2.30}$$

$$Q_\beta(l) = R'_\beta(l) \odot g(l), \tag{2.31}$$

$$\mu(\boldsymbol{x}) = \int_0^{2\pi} \frac{1}{U(\boldsymbol{x},\beta)^2} Q_\beta(l')\,\mathrm{d}\beta, \tag{2.32}$$

where l' is the value of l corresponding to the ray that passes through $\boldsymbol{x}$ and U is the distance from the source to the projection[(2)] of $\boldsymbol{x}$ onto the central ray, normalised by the distance D shown in Figure 2.4,

$$U = \frac{D + r\sin(\beta-\phi)}{D}. \tag{2.33}$$

Equations (2.29) – (2.32) have the same respective purposes as (2.25) – (2.28). In this case $R_\beta(l)$ is taken as a function of distance from the centre of the detector.

2.3.3 Cone beam

The standard method for volume reconstruction from cone beam data is simply known as FDK, an abbreviation formed from the names of the authors of the paper describing the method (Feldkamp, Davis, and Kress, 1984). This method considers the 2D projection plane as a stack of 1D projections, each like that which would be found in a fan beam data set. Each line of the projection is weighted by the cosine of its inclination angle from the mid-plane, then filtered and three-dimensionally back-projected to produce the reconstruction. The method is acknowledged to be approximate but produces good results provided the cone angle is not too large: Zeng (2007) gives a practical limit of 5°, although some variants of FDK can handle larger cone angles (Taguchi, 2003; Grass et al., 1999). Its close similarity to fan beam reconstruction algorithms leads to

[(2)] This use of the term "projection" refers to the standard mathematical operation.

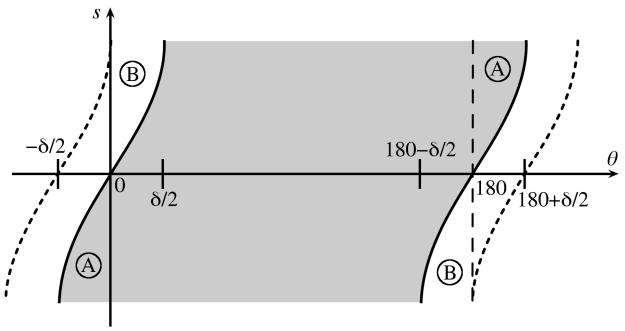

Figure 2.5: A 180° fan-beam scan covers the shaded region in Radon space. Two measurements are available in the regions marked 'A', while the regions marked 'B' contain no data. The dotted curves mark the edges of the region measured by a short scan.

the FDK method being the most widely used algorithm for cone beam reconstruction (Hsieh, 2003).

While a cone-beam geometry can be used with a circular scan, it is most often associated with a helical scan. In addition to the advantages identified in Section 1.7.4, the helical scan design also provides theoretically sufficient data for exact reconstruction of a 3D volume. Katsevich (2002) has developed an exact reconstruction strategy for helical scan data, and iterative routines such as those by Nuyts et al. (1999) and Thibault et al. (2007) can also be used.

As indicated in the first chapter, my work has focused on parallel and fan beam reconstructions, with the understanding that any results should extend to the cone beam case with relative ease. For this reason I do not dwell on cone beam reconstruction methods here, but only include a summary for completeness.

2.3.4 Short scan

The data sufficiency requirement for CT reconstruction is that all lines passing through the object, at all angles, are measured. The fan-beam back-projections in (2.28) and (2.32) use an integral over the interval of $[0, 2\pi]$ radians which satisfies this requirement, indeed it provides more than enough measurements. By considering the relationships given in (2.24) between the parallel-beam $p_\theta(s)$ and the fan-beam $R_\beta(l)$ parameters, the amount of measurement duplication can be found.

Figure 2.5 shows how a fan-beam scan populates the (s, θ) Radon space. A complete set of data fills the area between the s-axis and the dashed vertical line, but a 180° fan-beam scan acquires some measurements twice whilst missing others. To obtain sufficient data for reconstruction, a fan-beam scan must therefore be over an angular range of at least $180° + \delta$, where δ is the fan angle (see Figure 2.4). This is known as a short scan (Kak and Slaney, 1987).

While a short scan will provide sufficient data, the double measurement of some parts of Radon space means that direct reconstruction produces an image with streaks and gradients. One solution is to re-bin the fan-beam data into parallel-beam form, but it is possible to retain the use of a direct fan-beam reconstruction algorithm by weighting some measurements. The requirements are that the weights for two measurements of the same line must sum to 1, and the weighting function should be smooth to avoid introducing high frequencies that will be enhanced by the rho-filter. Parker (1982) derives these conditions and a suitable window, which is given by

$$w_\beta(\sigma) = \begin{cases} \sin^2\left(45^\circ \dfrac{\beta}{\delta/2 - \sigma}\right), & 0 \le \beta \le \delta - 2\sigma, \\ 1, & \delta - 2\sigma \le \beta \le 180^\circ - 2\sigma, \\ \sin^2\left(45^\circ \dfrac{180^\circ + \delta - \beta}{\delta/2 + \sigma}\right), & 180^\circ - 2\sigma \le \beta \le 180^\circ + \delta, \end{cases} \tag{2.34}$$

where δ, β, and σ are as shown in Figure 2.4. Applying this window to the short-scan data before reconstruction removes the artefacts mentioned above.

2.4 Rho-filtered layergram

This method, introduced by Bates and Peters (1971), works on similar principles to those of filtered back-projection but reverses the main operations. The method begins by back-projecting the (unfiltered) projections then performs two-dimensional filtering on the resulting image to form the final reconstruction.

Let $q(\boldsymbol{x}) = q(x_1, x_2)$ be the result of back-projecting the projections, so

$$q(\boldsymbol{x}) = \int_0^\pi p_\theta\left(\boldsymbol{x} \cdot \boldsymbol{\alpha}\right) \, \mathrm{d}\theta, \tag{2.35}$$

where $\boldsymbol{\alpha}$ is defined in (2.16). By the central slice theorem,

$$p_\theta(s) = \int_{-\infty}^{\infty} M(\rho\cos\theta, \rho\sin\theta) \exp\left(\mathrm{j}2\pi\rho s\right) \, \mathrm{d}\rho, \tag{2.36}$$

and substituting (2.36) into (2.35) yields

$$q(\boldsymbol{x}) = \int_0^\pi \int_{-\infty}^{\infty} M(\rho\cos\theta, \rho\sin\theta) \, \exp\left(\mathrm{j}2\pi\rho\left(\boldsymbol{x} \cdot \boldsymbol{\alpha}\right)\right) \, \mathrm{d}\rho \, \mathrm{d}\theta. \tag{2.37}$$

Comparing this to the polar 2D Fourier transform, it can be seen that

$$M\left(\rho\cos\theta, \rho\sin\theta\right) = |\rho| \, Q(\rho\cos\theta, \rho\sin\theta), \tag{2.38}$$

where Q is the 2D Fourier transform of q. From this point all that is required is to apply the inverse Fourier transform to obtain a reconstruction. So the overall method

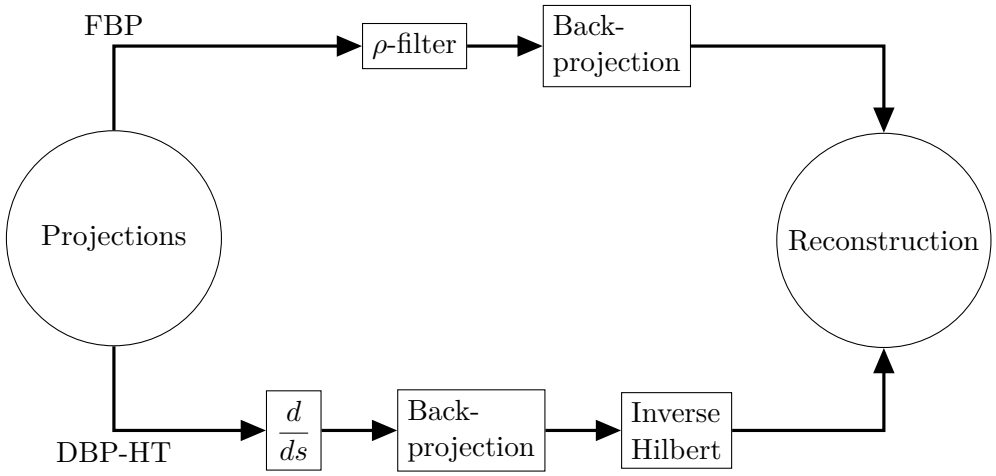

Figure 2.6: Alternative data flows of the FBP and Hilbert transform reconstruction techniques.

is to back-project the projection data, take the 2D Fourier transform, multiply by $|\rho|$, and take the inverse 2D Fourier transform.

Lewitt (1983) notes that the method suffers from some practical problems, including the fact that both q and Q are infinite in extent so they must be truncated in practice. He also suggests that the method is suited to optical implementation.

2.5 Differentiated back-projection, Hilbert transform (DBP-HT)

This reconstruction algorithm, recently presented by Noo et al. (2004), decomposes the Radon inversion into operations that are different from those in FBP. This technique differentiates the projection data, back-projects the result, then applies an inverse Hilbert transform along certain lines in the resulting image. The DBP-HT and FBP methods are compared in Figure 2.6.

2.5.1 The Hilbert transform

The Hilbert transform is the integral operator

$$g(y) = \mathcal{H}f(x) = \frac{1}{\pi} PV \int_{-\infty}^{\infty} \frac{f(x)}{y - x}\, \mathrm{d}x, \tag{2.39}$$

where PV indicates that the improper integral is to be treated in the Cauchy principal value sense (Bracewell, 1986). The inverse operator is simply

$$f(x) = \mathcal{H}^{-1}g(y) = \frac{1}{\pi} PV \int_{-\infty}^{\infty} \frac{g(y)}{y - x}\, \mathrm{d}y, \tag{2.40}$$

so that $\mathcal{H}\mathcal{H}f(x) = -f(x)$. The Hilbert transform is a convolutional operator with the convolution kernel $1/(\pi x)$; the inverse kernel is simply $-1/(\pi x)$. The Fourier transform of the Hilbert kernel is $-\mathrm{j}\,\mathrm{sgn}(X)$.

The DBP-HT reconstruction makes use of the concept of a Hilbert transformed image. Since the Hilbert transform is a one-dimensional operator, an image is said to be Hilbert transformed when all lines of the image in some direction are independently Hilbert transformed. For an angle of zero, we get the image transformed along the vertical lines of the image, i.e.,

$$\mathcal{H}_0 f(\boldsymbol{x}) = \frac{1}{\pi}\int_{-\infty}^{\infty} \frac{f(x_1, x_2')}{x_2 - x_2'}\,\mathrm{d}x_2', \tag{2.41}$$

where the subscript on $\mathcal{H}$ refers to the angle of the lines. In terms of the Fourier transform of the image,

$$\mathcal{H}_0 f(\boldsymbol{x}) = \int_{-\infty}^{\infty}\int_{-\infty}^{\infty} -\mathrm{j}\,\mathrm{sgn}(X_2) F(\boldsymbol{X}) \exp(\mathrm{j}2\pi \boldsymbol{x}\cdot\boldsymbol{X})\,\mathrm{d}X_1\,\mathrm{d}X_2, \tag{2.42}$$

where $\boldsymbol{X} = (X_1, X_2)$ is the conjugate variable of $\boldsymbol{x} = (x_1, x_2)$.

The concept of a Hilbert transformed image can be generalised to any angle θ measured anti-clockwise from the vertical axis:

$$\mathcal{H}_\theta f(\boldsymbol{x}) = \frac{1}{\pi}\int_{-\infty}^{\infty} \frac{f(\boldsymbol{x} - s\boldsymbol{\lambda})}{s}\,\mathrm{d}s \tag{2.43}$$

$$= \int_{-\infty}^{\infty}\int_{-\infty}^{\infty} -\mathrm{j}\,\mathrm{sgn}(\boldsymbol{X}\cdot\boldsymbol{\lambda}) F(\boldsymbol{X}) \exp(\mathrm{j}2\pi \boldsymbol{x}\cdot\boldsymbol{X})\,\mathrm{d}X_1\,\mathrm{d}X_2, \tag{2.44}$$

where $\boldsymbol{\lambda} = (-\sin\theta, \cos\theta)$ is the unit vector in the direction of the Hilbert lines.

2.5.2 DBP-HT reconstruction

The DBP-HT reconstruction method begins by differentiating the projections, giving

$$p_\theta'(s) = \frac{\partial p_\theta(s)}{\partial s}, \tag{2.45}$$

which are then back-projected to give

$$b(\boldsymbol{x}) = \int_0^\pi p_\theta'(\boldsymbol{x}\cdot\boldsymbol{\alpha})\,\mathrm{d}\theta, \tag{2.46}$$

where $\boldsymbol{\alpha} = (\cos\theta, \sin\theta)$. The quantity $b(\boldsymbol{x})$ is known as the differentiated back-projection (DBP). Differentiation in the spatial domain corresponds to multiplying by $2\pi\mathrm{j}\rho$ in the Fourier domain, so that

$$p_\theta'(s) = 2\pi\int_{-\infty}^{\infty} \mathrm{j}\rho P_\theta(\rho)\exp(\mathrm{j}2\pi\rho s)\,\mathrm{d}\rho, \tag{2.47}$$

and (2.46) can be rewritten as

$$b(\boldsymbol{x}) = 2\pi \int_0^{\pi} \int_{-\infty}^{\infty} \mathrm{j}\rho P_\theta(\rho) \exp(\mathrm{j}2\pi\rho(\boldsymbol{x}\cdot\boldsymbol{\alpha}))\,\mathrm{d}\rho\,\mathrm{d}\theta \tag{2.48}$$

$$= 2\pi \int_0^{\pi} \int_{-\infty}^{\infty} \mathrm{j}\,\mathrm{sgn}(\rho) P_\theta(\rho) \exp(\mathrm{j}2\pi\rho(\boldsymbol{x}\cdot\boldsymbol{\alpha}))|\rho|\,\mathrm{d}\rho\,\mathrm{d}\theta. \tag{2.49}$$

For $\theta \in [0, \pi]$, the signum term can be rewritten as $\mathrm{sgn}(\rho) = \mathrm{sgn}(\rho \sin\theta) = \mathrm{sgn}(\rho\alpha_2)$, and from the central slice theorem, $P_\theta(\rho) = M(\rho, \theta)$, where $M(\rho, \theta)$ is the Fourier transform of $\mu(\boldsymbol{x})$. Using these results gives

$$b(\boldsymbol{x}) = 2\pi \int_0^{\pi} \int_{-\infty}^{\infty} \mathrm{j}\,\mathrm{sgn}(\rho\alpha_2) M(\rho, \theta) \exp(\mathrm{j}2\pi\rho(\boldsymbol{x}\cdot\boldsymbol{\alpha}))|\rho|\,\mathrm{d}\rho\,\mathrm{d}\theta, \tag{2.50}$$

which gives, after a change of variables from polar to rectangular,

$$b(\boldsymbol{x}) = 2\pi \int_{-\infty}^{\infty} \int_{-\infty}^{\infty} \mathrm{j}\,\mathrm{sgn}(X_2) M(\boldsymbol{X}) \exp(\mathrm{j}2\pi(\boldsymbol{x}\cdot\boldsymbol{X}))\,\mathrm{d}X_1\,\mathrm{d}X_2, \tag{2.51}$$

where $\boldsymbol{X} = (X_1, X_2) = \rho\boldsymbol{\alpha}$ is the new coordinate system. Comparing this to (2.44) yields the relationship

$$b(\boldsymbol{x}) = -2\pi\mathcal{H}_0\mu(\boldsymbol{x}), \tag{2.52}$$

so that the image $\mu(\boldsymbol{x})$ can be found from the inverse Hilbert transform of $b(\boldsymbol{x})$.

This equation is limited to vertical Hilbert lines only; a more useful relationship would operate with any angle. To this end, (2.46) is altered to define

$$b_\phi(\boldsymbol{x}) = \int_\phi^{\phi+\pi} p'_\theta(\boldsymbol{x}\cdot\boldsymbol{\alpha})\,\mathrm{d}\theta. \tag{2.53}$$

Now recall that $p_\theta(s)$ has period 2π in θ and satisfies the relationship $p_{\theta+\pi}(s) = p_\theta(-s)$. The derivative then satisfies $p'_{\theta+\pi}(s) = -p'_\theta(-s)$, and so

$$b_\phi(\boldsymbol{x}) = \int_\phi^{\pi} p'_\theta(\boldsymbol{x}\cdot\boldsymbol{\alpha})\,\mathrm{d}\theta + \int_\pi^{\phi+\pi} p'_\theta(\boldsymbol{x}\cdot\boldsymbol{\alpha})\,\mathrm{d}\theta, \tag{2.54}$$

$$= \int_\phi^{\pi} p'_\theta(\boldsymbol{x}\cdot\boldsymbol{\alpha})\,\mathrm{d}\theta + \int_0^{\phi} -p'_\theta(\boldsymbol{x}\cdot\boldsymbol{\alpha})\,\mathrm{d}\theta, \tag{2.55}$$

$$= \int_0^{\pi} \mathrm{sgn}\left(\sin(\theta-\phi)\right) p'_\theta(\boldsymbol{x}\cdot\boldsymbol{\alpha})\,\mathrm{d}\theta, \tag{2.56}$$

noting that there is no minus sign in the argument of the second $p'_\theta(s)$ term in (2.55) because $\boldsymbol{\alpha}$ is also negated with the variable change $\theta \to \theta - \pi$. The $\sin(\cdot)$ term is introduced to allow any value of ϕ to be used, rather than restricting it to $[0, \pi]$. If $b_\phi(\boldsymbol{x})$ is used in place of $b(\boldsymbol{x})$ for the sequence of equations (2.46) to (2.52), then (2.50)

becomes

$$b_\phi(\boldsymbol{x}) = 2\pi \int_0^\pi \int_{-\infty}^\infty \mathrm{j}\,\mathrm{sgn}(\rho\,\boldsymbol{\alpha}\cdot\boldsymbol{\lambda}) M(\rho,\theta)\exp(\mathrm{j}2\pi\rho(\boldsymbol{x}\cdot\boldsymbol{\alpha}))|\rho|\,\mathrm{d}\rho\,\mathrm{d}\theta, \tag{2.57}$$

$$= 2\pi \int_{-\infty}^\infty \int_{-\infty}^\infty \mathrm{j}\,\mathrm{sgn}(\boldsymbol{X}\cdot\boldsymbol{\lambda}) M(\boldsymbol{X})\exp(\mathrm{j}2\pi(\boldsymbol{x}\cdot\boldsymbol{X}))\,\mathrm{d}X_1\,\mathrm{d}X_2, \tag{2.58}$$

where $\boldsymbol{\lambda} = (-\sin\phi, \cos\phi)$ like in (2.44). Comparing this to (2.51) generalises (2.52) to

$$b_\phi(\boldsymbol{x}) = -2\pi\mathcal{H}_\phi\mu(\boldsymbol{x}), \tag{2.59}$$

where ϕ can be chosen to suit the application.

The final reconstruction step is to recover the image $\mu(\boldsymbol{x})$ using the inverse Hilbert transform:

$$\mu(\boldsymbol{x}) = -\mathcal{H}_\phi^{-1}\left\{\frac{b_\phi(\boldsymbol{x})}{2\pi}\right\}. \tag{2.60}$$

The Hilbert transform of the image theoretically has infinite extent, which at first may appear to be a problem for inversion. However, Mikhlin (1957) showed that if a function $g(s)$ is known to have finite support, i.e., $g(s) = 0$ for $|s| > R - \epsilon$ for some small positive ϵ, then that function can be exactly reconstructed from its Hilbert transform on $[-R, R]$, with

$$g(s) = \frac{-1}{\sqrt{r^2 - s^2}}\left(\frac{1}{\pi}\int_{-R}^R \sqrt{R^2 - t^2}\,\frac{\mathcal{H}g(t)}{s-t}\,\mathrm{d}t + C\right). \tag{2.61}$$

This result is known as the finite Hilbert inversion formula, and is applicable to the DBP-HT algorithm because the image $\mu(\boldsymbol{x})$ has finite support. Provided the projections are complete, the DBP will be known for the full support of the image, and thus (2.60) can be evaluated.

The advantage of this decomposition scheme is found in reconstruction from truncated data, a topic discussed further in Section 2.6 and Chapter 5. Because differentiation is a local operation (in contrast to the convolutional filtering operation), the truncation of projection data does not affect the whole back-projected image, leaving most of it intact. The second step in the reconstruction then operates independently on lines in $b_\phi(\boldsymbol{x})$, requiring only that lines are valid on a region at least covering the object support. Figure 2.7 shows an example of a situation that can still be partially reconstructed despite some projections being truncated.

2.6 Interior tomography

A limited-data situation where the object is not completely imaged from all angles in the scan is described in Section 1.9. Theoretically, this type of scan does not collect

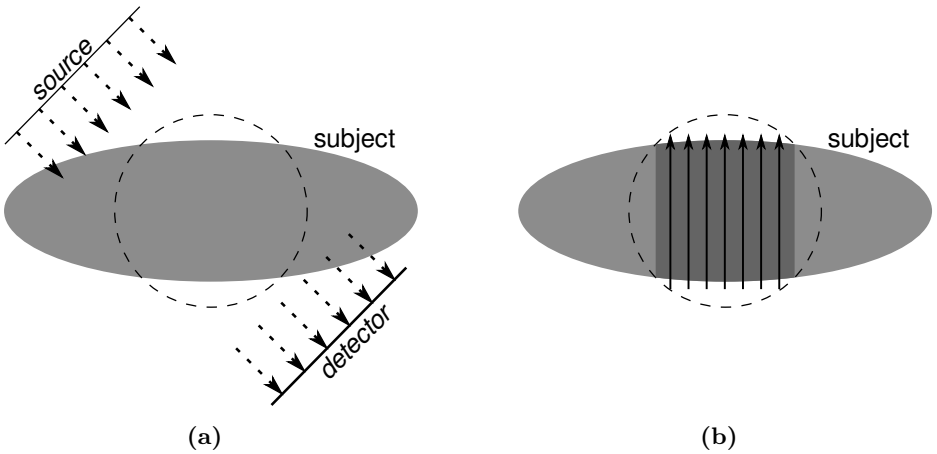

Figure 2.7: A scan producing truncated projections. In (a), the detector width is not sufficient to collect data over the full object; however, the dark region in (b) can be reconstructed along the indicated lines using the Hilbert transform technique.

sufficient information to uniquely reconstruct an image of the object. However, despite the theoretical non-uniqueness, some recent results (Clackdoyle et al., 2004; Noo et al., 2004; Courdurier et al., 2008) suggest that having prior knowledge of some small part of the field of view (FOV)[(3)] might allow a unique solution to be found. The FOV is the region of the image that contributes to all projections; in Figure 1.10 this would approximately be the square, in Figure 2.7 it would be the region inside the dashed circle. According to these publications, prior knowledge can be used to condition the reconstruction to produce a unique result.

Reconstruction is achieved in these papers using the Hilbert transform method described in Section 2.5. For Noo et al. (2004) the prior knowledge consists only of the image support, so that the known subregion is the (possibly small) area of air outside the object, known to have attenuation of zero. In the remainder of the works, the configuration is more challenging, not meeting the conditions required for the finite Hilbert inversion, so an iterative approach is taken. Many of the papers use projections onto convex sets (POCS) for the iterative Hilbert inversion, while Yu et al. (2008) use singular value decomposition (SVD) for the inversion. One of these algorithms is explained in more detail in Chapter 5, where an evaluation of its performance is presented.

2.7 Iterative reconstruction methods

Iterative reconstruction methods reconstruct an image by constraining it to match the measured projections. The set of iterative techniques can be divided into algebraic

[(3)] Several publications use the term “region of interest” (ROI) instead of FOV.

reconstruction techniques (ART) and statistical iterative reconstructions (SIR); the former are based on solving a set of linear equations while the latter consider the statistics of the underlying physics of the x-ray interaction process.

Advantages of iterative techniques include improved noise properties in the reconstructed image, the ability to incorporate prior knowledge, and better low-contrast detectability with low-dose imaging (Nelson et al., 2011). Part of the reason for the improved noise characteristics of iterative techniques is that no rho-filter is used, so noise is not enhanced by the filtering operation. The improvement in low-dose contrast enables the x-ray exposure to patients to be reduced (Leipsic et al., 2010).

One of the main disadvantages of iterative techniques is the extra computational effort required for reconstruction. Because the process involves many calculations of both forward- and back-projections, it can take much longer to produce a reconstruction. For example, many systems can reconstruct an image using filtered back-projection in 30 ms, whereas a high-quality iterative technique could take 10 minutes (Nelson et al., 2011). For this reason iterative reconstruction techniques are not yet suitable for scanning patients in acute situations.

Notation in this section differs slightly from the rest of the chapter. For the iterative techniques, the image is always considered as a raster of discrete voxels. For this reason image voxels are written $\mu_{i,j}$ or μ_k, where the subscript on the former version indicates the row and column of the voxel, and that on the latter version indicates an index into the complete set of voxels. The notations can be interchanged by $k = iJ + j$, where J is the image width and i, j, k are all 0-based indices.

2.7.1 Algebraic reconstruction technique

The basic premise of algebraic techniques for CT reconstruction is that each measurement can be represented as

$$p_i = \sum_j a_{i,j}\mu_j, \tag{2.62}$$

where p_i is the integral of the object attenuation coefficient along the ray between the source and detector pixel position i (also referred to simply as ray i), μ_j is the attenuation coefficient in voxel j, and $a_{i,j}$ is the intersection area of ray i with voxel j. This relationship is usually written as

$$A\boldsymbol{\mu} = \boldsymbol{p}, \tag{2.63}$$

where $\boldsymbol{\mu} = (\mu_1, \mu_2, \ldots, \mu_M)^T$ is the image vector, $\boldsymbol{p} = (p_1, p_2, \ldots, p_N)^T$ is the measurement vector, and $A = \{a_{i,j}\}$ is the system (geometry) matrix. The values M and N in

these vector subscripts represent the number of image voxels and the number of x-ray measurements, respectively.

There are several ways to calculate the $a_{i,j}$ values. In many early versions of the algorithm, the coefficients were approximated by 1's and 0's according to whether the centre of the voxel j was within ray i (Kak and Slaney, 1987). Other methods include those outlined in Section 3.2.1, as well as ray tracing algorithms borrowed from the field of 3D graphics rendering.

For a suitably small system, the reconstructed image could be obtained by a straightforward matrix inversion; however, a realistic scan system has an image of at least $256 \times 256 = 65\,536$ voxels and 256 measurements at each of 200 view angles, giving $51\,200$ measurements. The A matrix in this (minimal) scenario would be $51\,200 \times 65\,536$ in dimension. Despite the sparseness of the matrix it is not feasible to directly invert it.

Since the solution cannot be calculated directly, an iterative approach is taken: this method was originally known as the Kaczmarz method (Kaczmarz, 1993). In each iteration the current estimate $\boldsymbol{\mu}^{(k)}$ is projected onto the hyperplane defined by (2.62) for the next value of i, so

$$\boldsymbol{\mu}^{(k+1)} = \boldsymbol{\mu}^{(k)} + \frac{p_i - \boldsymbol{\mu}^{(k)} \cdot \boldsymbol{a}_i}{\boldsymbol{a}_i \cdot \boldsymbol{a}_i} \boldsymbol{a}_i, \tag{2.64}$$

where $i = k \bmod N + 1$ and $\boldsymbol{a}_i$ is the i-th row of A. $\boldsymbol{\mu}^{(0)}$ is arbitrary, but common choices are 0, white noise, or an image reconstructed by another means such as FBP. Equation (2.64) can be interpreted thus: forward-project the current estimate along ray i; subtract this value from the measured line integral p_i; and add the back-projection of this difference to the current estimate.

2.7.1.1 SART

Andersen and Kak (1984) present an algorithm called simultaneous ART, or SART. This algorithm is based on the existing ART method, with three main changes. First, the method of calculating ray sums is improved to give better approximations in the forward-projection step. Second, the image is updated by all rays in a view simultaneously. Finally, a heuristic Hamming weight is applied to the back-projected update lines.

The second change listed above is the most significant one and is the source of the algorithm name. The update equation becomes

$$\mu_j^{(k+1)} = \mu_j^{(k)} + \frac{\displaystyle\sum_i \frac{p_i - \boldsymbol{\mu}^{(k)} \cdot \boldsymbol{a}_i}{\displaystyle\sum_{j'} a_{i,j'}} a_{i,j}}{\displaystyle\sum_i a_{i,j}}, \tag{2.65}$$

where the summations with respect to i are over the rays from the current view that intersect voxel j. This new equation can be interpreted thus: forward-project the current estimate along each ray i within the current view angle; subtract these values from their respective measured line integrals; back-project the normalised errors; normalise each voxel of the back-projection by the sum of ray intersections with that voxel; and add this normalised back-projection to the current estimate. The convergence of this alternative technique was proved by Jiang and Wang (2003).

The main advantage of SART over ART is that it reduces the amount of "salt-and-pepper noise" in the reconstructed image. This artefact arises because in ART the completion of a single iteration can result in a noticeable stripe along the particular ray; repeating this for all the different rays in the system can produce a noisy appearance in the final image (Andersen and Kak, 1984). By merging the ray updates from each view angle into a smooth update image, SART reduces the artefacts.

Some later versions of SART have dropped the limitation of considering only the rays within a single view in each iteration, for example Wang et al. (1996) and Pan et al. (2010). Instead, the algorithm merges the updates for all rays in the system before applying the update image. The mathematics for this version are the same as in (2.65), but the values of i considered in the summations are no longer limited to those from only one view angle.

2.7.1.2 OS-SART

The full-scan version of SART was refined further by Wang and Jiang (2004) to make use of the ordered subsets (OS) concept. This approach differs in that it generates an update image from a subset of the view angles rather than all at once, iterating through the subsets until all view angles have been considered. The advantage of this approach over full-scan SART is faster convergence. This can be seen in an intuitive sense by considering the similarity between projections at neighbouring view angles. Take the two subset case as an example: the image that can be reconstructed from every other view angle will be of a lower quality, but very similar to the image that could be reconstructed from all view angles. With the assumption that processing time is proportional to the number of views being processed, this image will only take half as long to create, and still be reasonable, giving a good starting point for the second sub-iteration. Thus after considering all views once, in a comparable time, OS-SART will have produced an image of better quality than that of full-scan SART. By this reasoning, OS-SART converges faster.

It seems likely that SART was extended to use all view angles simultaneously by a misreading of Andersen and Kak (1984) or a misunderstanding of the mathematics within that paper. OS-SART is actually a shift back toward the original definition of

SART; indeed, the original definition is actually a particular case of OS-SART where the number of subsets is equal to the number of view angles.

2.7.2 Statistical iterative reconstruction

The aim of SIR is to reconstruct the original attenuation image by finding the maximum *a posteriori* (MAP) estimate of the attenuation image, $P(\boldsymbol{\mu}|\boldsymbol{I})$, where $\boldsymbol{I} = (I_1, I_2, \ldots)^T$ is the complete set of x-ray measurements. This means finding the value of $\boldsymbol{\mu}$ that has the greatest probability given the measured data, or

$$\boldsymbol{\mu}^* = \arg\max_{\boldsymbol{\mu}} P(\boldsymbol{\mu}|\boldsymbol{I}), \tag{2.66}$$

$$= \arg\max_{\boldsymbol{\mu}} \frac{P(\boldsymbol{I}|\boldsymbol{\mu})P(\boldsymbol{\mu})}{P(\boldsymbol{I})}, \tag{2.67}$$

by Bayes' law. The maximisation can be simplified by instead minimising the negative logarithm:

$$\arg\max_{\boldsymbol{\mu}} P(\boldsymbol{\mu}|\boldsymbol{I}) = \arg\min_{\boldsymbol{\mu}} -\ln P(\boldsymbol{\mu}|\boldsymbol{I}), \tag{2.68}$$

$$= \arg\min_{\boldsymbol{\mu}} \{-\ln P(\boldsymbol{I}|\boldsymbol{\mu}) - \ln P(\boldsymbol{\mu}) + \ln P(\boldsymbol{I})\}, \tag{2.69}$$

$$= \arg\min_{\boldsymbol{\mu}} \{-\ln P(\boldsymbol{I}|\boldsymbol{\mu}) - \ln P(\boldsymbol{\mu})\}, \tag{2.70}$$

where the final term of (2.69) is dropped because it is not a function of $\boldsymbol{\mu}$. A reconstructed image is found by solving (2.70). This is thus a minimisation task, with the objective function

$$\Phi(\boldsymbol{\mu}) = -\ln P(\boldsymbol{I}|\boldsymbol{\mu}) - \ln P(\boldsymbol{\mu}). \tag{2.71}$$

As described in Section 1.4, x-ray flux measurements follow the Poisson distribution

$$P(I_i|\boldsymbol{\mu}) = \frac{\lambda_i^{I_i} \exp(-\lambda_i)}{I_i!}, \tag{2.72}$$

where I_i is the measured number of counts at detector pixel position i and $\lambda_i = I_{0i} \exp(-\mathcal{P}_i(\boldsymbol{\mu}))$ is the expected number of counts given the open beam flux I_{0i} and the line integral (forward projection) $\mathcal{P}_i(\boldsymbol{\mu})$ of the attenuation image $\boldsymbol{\mu}$. Since individual

pixels make independent measurements[4], the joint probability distribution is given by

$$P(\boldsymbol{I}|\boldsymbol{\mu}) = \prod_i P(I_i|\boldsymbol{\mu}), \tag{2.73}$$

$$= \prod_i \frac{\lambda_i^{I_i} \exp(-\lambda_i)}{I_i!}, \tag{2.74}$$

and the log-likelihood function is thus

$$\ln P(\boldsymbol{I}|\boldsymbol{\mu}) = \sum_i \left[I_i \ln \lambda_i - \lambda_i - \ln(I_i!)\right], \tag{2.75}$$

$$= \sum_i \left[I_i \ln(I_{0i} \exp(-\mathcal{P}_i(\boldsymbol{\mu}))) - I_{0i} \exp(-\mathcal{P}_i(\boldsymbol{\mu})) - \ln(I_i!)\right], \tag{2.76}$$

$$= \sum_i \left[I_i \ln I_{0i} - I_i \mathcal{P}_i(\boldsymbol{\mu}) - I_{0i} \exp(-\mathcal{P}_i(\boldsymbol{\mu})) - \ln(I_i!)\right]. \tag{2.77}$$

Following Xu et al. (2011) and treating the $\ln(P(\boldsymbol{\mu}))$ term in (2.71) as a regularisation term $R(\boldsymbol{\mu}) = -\ln(P(\boldsymbol{\mu}))$, substituting (2.77) into (2.71), and dropping terms not dependent on $\boldsymbol{\mu}$ gives

$$\Phi(\boldsymbol{\mu}) = \sum_i \left[I_i \mathcal{P}_i(\boldsymbol{\mu}) + I_{0i} \exp(\mathcal{P}_i(\boldsymbol{\mu}))\right] + R(\boldsymbol{\mu}). \tag{2.78}$$

Using a second-order Taylor's series expansion, the expression inside the brackets can be approximated as (Xu et al., 2011)

$$I_i \ln\left(\frac{I_{0i}}{I_i}\right) + I_i + \frac{1}{2} I_i \left[\mathcal{P}_i(\boldsymbol{\mu}) - \ln\left(\frac{I_{0i}}{I_i}\right)\right]^2, \tag{2.79}$$

and after omitting terms not dependent on $\boldsymbol{\mu}$ this yields the objective function

$$\Phi(\boldsymbol{\mu}) = \sum_i \frac{I_i}{2} \left(\mathcal{P}_i(\boldsymbol{\mu}) - p_i\right)^2 + R(\boldsymbol{\mu}), \tag{2.80}$$

where $p_i = \ln\left(I_{0i}/I_i\right)$ is the measured projection at detector pixel i.

Minimisation of (2.80) can be implemented by alternately minimising the data fidelity term and the regularisation term. A possible method of implementation developed by Erdoğan (1999) optimises a surrogate function instead of the actual fidelity term, where the surrogate is an additively separable function and thus can be easily optimised with respect to the individual voxel values μ_j. The update equation in this

[4] The independence assumption can in fact be violated by charge sharing; however, for the development of this algorithm this is ignored. In addition, the charge summing mode of Medipix detectors is intended to mitigate the effects of charge sharing.

case is

$$\mu_j^+ = \mu_j - \frac{\mathcal{B}_j(I_i(\mathcal{P}_i(\boldsymbol{\mu}) - p_i))}{\mathcal{B}_j(I_i\mathcal{P}_i(1))}, \tag{2.81}$$

where μ_j^+ is the improved estimate, and $\mathcal{B}_j(\cdot)$ is the back-projection to voxel j. The term $\mathcal{P}_i(1)$ should be interpreted as the forward projection of a constant unity image of the same size as $\boldsymbol{\mu}$; this is the length of the line being integrated.

Total variation (TV) can be used for the regularisation term $R(\boldsymbol{\mu})$. This part of the reconstruction can then be performed with a common search technique such as the Gauss-Seidel method (Sauer and Bouman, 1993) or with soft-threshold nonlinear filtration as recently described by Yu and Wang (2010). The latter method filters the current image estimate to reduce the gradient between adjacent voxels, and is the method used in the SIR implementation of Chapter 6.

For the description of soft-threshold nonlinear filtration, voxels are now indexed according to their row j and column k. For a current image estimate $\boldsymbol{\mu}$ with voxels $\mu_{j,k}$, and for some threshold w,

- Calculate

$$d_{j,k} = \sqrt{(\mu_{j,k} - \mu_{j+1,k})^2 + (\mu_{j,k} - \mu_{j,k+1})^2} \tag{2.82}$$

  for each voxel.

- Where $d_{j,k} < w$, adjust the values of $\mu_{j,k}$, $\mu_{j+1,k}$, and $\mu_{j,k+1}$ to make $d_{j,k} = 0$; and otherwise adjust these values so that $d_{j,k}$ is reduced by w. The equations to implement this are

$$\mu_{j,k} = \frac{1}{4}(2\mu_{j,k}^a + \mu_{j,k}^b + \mu_{j,k}^c), \tag{2.83}$$

$$\mu_{j,k}^a = \begin{cases} \dfrac{2\mu_{j,k} + \mu_{j+1,k} + \mu_{j,k+1}}{4}, & \text{if } d_{j,k} < w, \\ \mu_{j,k} - \dfrac{w(2\mu_{j,k} - \mu_{j+1,k} - \mu_{j,k+1})}{4d_{j,k}}, & \text{if } d_{j,k} \geq w, \end{cases} \tag{2.84}$$

$$\mu_{j,k}^b = \begin{cases} \dfrac{\mu_{j,k} + \mu_{j-1,k}}{2}, & \text{if } d_{j-1,k} < w, \\ \mu_{j,k} - \dfrac{w(\mu_{j,k} - \mu_{j-1,k})}{2d_{j-1,k}}, & \text{if } d_{j-1,k} \geq w, \end{cases} \tag{2.85}$$

$$\mu_{j,k}^c = \begin{cases} \dfrac{\mu_{j,k} + \mu_{j,k-1}}{2}, & \text{if } d_{j,k-1} < w, \\ \mu_{j,k} - \dfrac{w(\mu_{j,k} - \mu_{j,k-1})}{2d_{j,k-1}}, & \text{if } d_{j,k-1} \geq w. \end{cases} \tag{2.86}$$

Inspection of these equations suggests that each voxel is set to an average of three separate adjustments, where each of these adjustments operates to bring the voxel value

closer to that of its neighbours. The resulting filtered image will have a reduced total variation. The equations are derived in full by Yu and Wang (2010).

The complete reconstruction algorithm is thus to alternately apply (2.81) and (2.83) to the current image estimate $\boldsymbol{\mu}$. These steps are repeated either for a fixed number of iterations or until the amount of change in $\boldsymbol{\mu}$ between iterations drops below some threshold. The former stopping condition is used in my implementations as it was found to produce adequate results.

Chapter Three

Tools

Through the course of my research I have used a variety of tools, both tangible and virtual; some of these tools are of my own creation, and I have contributed to the development of others. This chapter describes the MARS scanner, the reconstruction software I have written and used, and the Monte Carlo simulation package that I used and contributed to.

3.1 MARS scanner

MARS scanners are experimental, spectral, micro-CT scanners developed by the MARS research group at the University of Canterbury (Walsh et al., 2011; Butler et al., 2011*b*), one of which is shown in Figure 3.1. MARS stands for Medipix All-Resolution System, so named because the scanners use Medipix detectors which enable resolution of x-ray photon energies. The key component of the scanners is the MARS x-ray camera, which uses an x-ray detector chip from the Medipix family (Ballabriga et al., 2007) to acquire energy resolved x-ray photon count images. The latest version of Medipix chip is 3.2 (a.k.a. 3RX), which supersedes the 3.1, 3.0, and 2.0 (a.k.a. MXR) (Ballabriga et al., 2011; Llopart et al., 2002). Figure 3.2 shows the construction of a Medipix chip. The detector layer material that is bonded to the Medipix chip is silicon, cadmium telluride (CdTe), cadmium zinc telluride (CZT), or gallium arsenide (GaAs). The electronics layer uses pulse height analysis (Amsel et al., 1967) to compare the energy of individual photons against up to eight programmable energy thresholds. In this way, each energy bin accumulates a count of the number of incident photons above its respective threshold energy, which enables measurement of the photon flux across the spectrum.

The scanners contain an x-ray source manufactured by Source-Ray, Inc. (Ronkonkoma, New York, USA), either the SB-120-350 with a maximum tube voltage and current of 120 kV and 350 µA respectively, or the SB-80-1k with maximum tube voltage and current of 80 kV and 1000 µA. The 80 kV tube is used with silicon detectors, while the 120 kV tube is used with the harder materials.

Figure 3.1: MARS spectral micro-CT scanner.

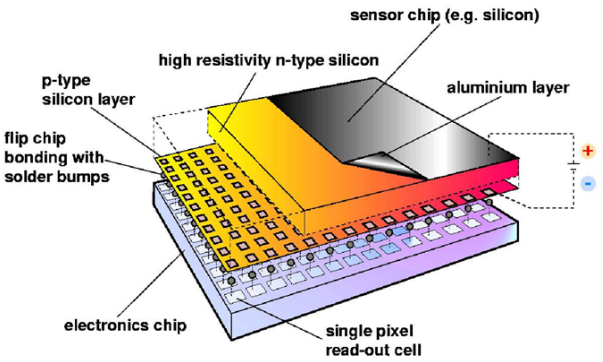

Figure 3.2: Exploded diagram of the construction of a Medipix x-ray detector chip.
(From Anton et al. (2009)).

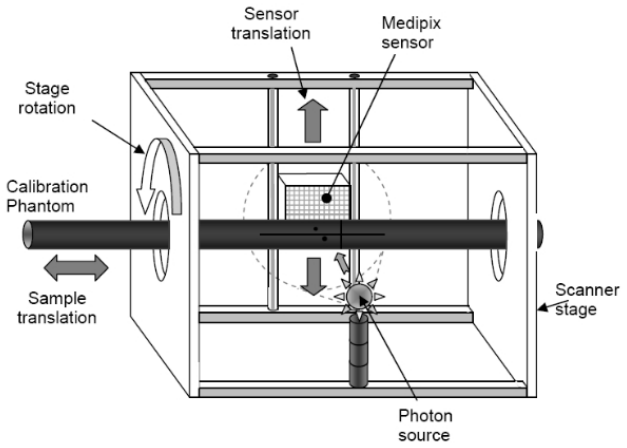

Figure 3.3: Diagram of the gantry of a MARS scanner. Motors control the sample longitudinal position, gantry rotation angle, camera translation, and camera and source radial position. The latter two drives are not shown in this diagram, as it is from an older mechanical version.
(From Ross (2008)).

The current scanner design uses motors to set the sample longitudinal position, gantry rotation angle (0–360°), x-ray source magnification, camera magnification, and camera offset. Figure 3.3 illustrates these drives. The camera offset control is used to enable scanning of larger objects, since the detector chips are only 14 mm × 14 mm in size and the largest detector configuration is currently 2 × 3 chips. The next scanner design, which is currently being built and tested, adds motorised shutters to the x-ray source, three degrees of freedom for source positioning, and most importantly the gantry is wired through slip rings to allow for unconstrained rotation. The entire assembly is housed in a wheeled cabinet that measures 1245 mm × 1420 mm × 750 mm (H × W × D), and can scan samples up to 100 mm in diameter and 280 mm in length.

My principal contribution to the MARS research group is in software development for the MARS micro-CT scanner. This includes a major overhaul of the graphical user interface (GUI), packaging of the software to simplify the installation and update processes, and creation of a driver for an x-ray source. In addition, I supervised a summer student working on physiological gating to enable cardiac imaging of live animals.

3.1.1 Software system

As shown in Figure 3.4, the software running on the MARS scanners falls into a defined hierarchy. The MARS hardware contains, depending on the version, one or two microprocessors which control the hardware according to instructions received from a main PC. Communication with the camera uses ethernet, allowing fast transfer of captured image data back to the PC. The motor controller communication uses RS-232

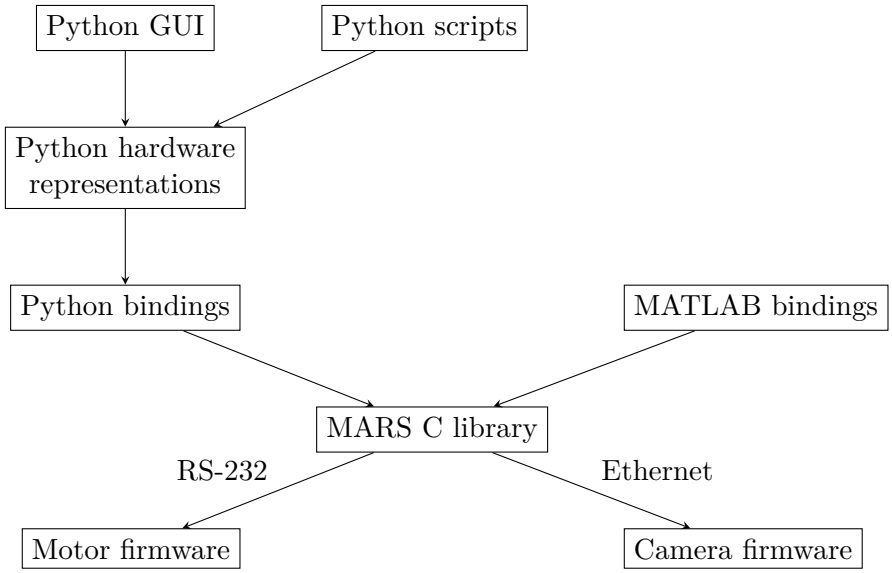

Figure 3.4: The hierarchy of the software running on the MARS scanners. The label "motor firmware" includes both motor and x-ray source control.

as it does not send or receive large quantities of data and the protocol is simple to implement.

3.1.2 GUI multithreading

The GUI for configuring and running scan and maintenance scripts was originally written as a small convenience layer but gradually grew much larger. Because it had not been designed with proper GUI design principles, it did not scale well and many problems began to appear in the operation of the scanner. There was no separation of logic between the code to control the graphical elements and the code to interact with the scanner hardware library. Combined with a lack of multithreading, this resulted in the interface often becoming unresponsive and many strange bugs emerging due to the convoluted information flow paths.

To repair the system, it was changed to a better application model and threaded operation was introduced. A new layer of abstraction was created, consisting of objects that represented the system hardware and which had no user interface logic within them. All hardware control logic was moved out of the GUI code and into this new layer, so that the GUI code only needed to keep track of the state of the GUI, leaving the new layer to track the hardware state.

A comprehensive threading module was created which allowed the GUI to continue to operate normally whilst hardware operations were being executed. This module includes mutual exclusion (mutex) locking of objects so that inconsistencies do not arise due to multiple threads manipulating the same object simultaneously. The module defines several "decorators" (Eby, 2005), which are a feature of Python that allows

methods and functions to be modified without altering the existing function definitions. For example, there are decorators that mark methods as “readers” or “writers” which determine the type of mutex locking they apply to their respective objects. This approach makes it easy for programmers who are not trained in threaded design to develop further functionality and removes a lot of code duplication.

In the previous design, the code to conduct a circular CT scan was embedded into the core of the GUI. The new system was set up so that scans are created separately as scripts and run as a separate thread in the application. A problem encountered here was that a scan may need to be interrupted, but Python does not offer a simple interface for interrupting a thread once it has started execution. To overcome this issue, a new thread class was written that allows threads to be safely interrupted. This includes the option to have failsafe finalising code, e.g., to switch off the x-ray source and return the gantry to its loading position.

3.1.3 Packaging

The packaging and installation process was first simplified with a script that produced a single executable that would perform the install. Following this, the necessary infrastructure was written to build the software as a package that integrates with the Debian package management system. This was done because the scanner computers run the Ubuntu Linux operating system, which uses the Debian package management system. Using packages for installation allows for easy tracking of library versions and updates.

The code base was split into two repositories, one for the drivers written in C, the other for the interface code written in Python and Matlab. The install script for the driver code evolved into three Debian packages, one for the camera drivers, one for the remaining drivers, and one for the Python bindings to the libraries. The drivers were split into two packages because the MARS group supplies not only scanner systems but also standalone x-ray cameras, which have no need for the gantry and x-ray source drivers. The interface code is provided in a fourth package, with the intention that alternative interface systems may be developed in the future, for example a command-line interface or a web-based interface.

3.1.4 Hamamatsu x-ray source

The hybrid scanner of Chapter 6 uses a MARS camera, but with gantry and x-ray source hardware different from the usual MARS scanner equipment. The sample stage is controlled by proprietary Xradia software while the camera is controlled by a custom Python script using the MARS library. Synchronisation between these two systems is crudely performed by careful timing of the rotation system and appropriate waits in

the scan script. Two problems with this configuration were radiation damage to the detector and calibration of the camera.

The x-ray source for the spectral imaging chain is a Hamamatsu L10101[(1)] and was originally controlled by a simple Windows based interface. The source was switched on before beginning a scan and then off afterwards, even though photons were not being captured for a large portion of the scan time. The calibration and response of the MARS camera changes over time with radiation exposure, so this unnecessary irradiation resulted in the camera response changing considerably during the scan.

The MARS system has support for calibrating the camera, which is the process of mapping digital threshold values to their corresponding photon energy. This is achieved by varying the x-ray source voltage and adjusting the thresholds to find the response edge (Panta et al., 2013). However, because the hybrid scanner does not use an x-ray source usually found in MARS scanners, it was not possible to calibrate the camera while it was in the hybrid scanner.

These two problems were solved by developing a driver for the Hamamatsu x-ray source, allowing it to be directly controlled by the MARS software. Based on the serial interface documentation for the x-ray source, C code was written to hook into the MARS library framework. The driver includes functions to probe for the presence of a Hamamatsu x-ray source, set tube current and voltage, switch the tube on and off, read tube current and voltage, and interpret error codes in response messages. With this functionality implemented, the source can be controlled directly from the MARS control interface, and source control can be scripted.

The Hamamatsu source has broader functionality than the SourceRay sources usually used in MARS scanners, including automatic conditioning, timed warm-up periods, and self testing. These features were not incorporated when the MARS library framework was originally developed. For example, there is no means to report to a higher level that the tube cannot switch on yet because it is being conditioned. If this source or another like it were to be fully supported by MARS, the library would need to be extended. However, because it was only being used on a single scanner which runs a dedicated scan script, these problems could be worked around with extra manual checks.

3.1.5 Physiological gating

Cardiac scanning of live animals is a challenge because the specimen is in motion during the scan. The usual solution to this problem is to have electrocardiogram and respiration sensors attached to the specimen and to trigger the image acquisitions to occur at the same phase in both the cardiac and breathing cycles (Badea et al., 2004). This technique is known as “gating”, in particular prospective gating. In comparison, retrospective

[(1)] `http://www.hamamatsu.com/jp/en/L10101.html`

gating involves acquiring images normally but also storing the phase of the heart and lungs cycles with the image. This requires more images to be acquired, and thus exposes the specimen to more radiation, but allows reconstruction of a time-resolved volume (Achenbach et al., 2000).

Over the summer period between 2012 and 2013 I supervised undergraduate student Ian Glass, who was supported by a University of Otago Summer Research Scholarship. The aim of his project was to perform initial planning for, and incorporation of, physiological gating into the MARS scanner. This included software and hardware interfacing of ECG, respiratory, temperature, and oxygen monitoring signals from a Model 1025T Monitoring and Gating System manufactured by Small Animal Instruments, Inc. (Stony Brook, New York, USA). The project concluded with full development plans and some preliminary software for handling the monitoring signals and generating trigger signals. Ian is continuing the work as a research project for the Honours year of his Bachelor of Engineering degree, during which he will implement both prospective and retrospective gating for MARS scanners.

3.2 Reconstruction

Almost all of the reconstructions during the course of this research were performed in Python, using my own functions, with the exception of the work in Chapter 6, which was perfomed in Matlab. Array processing functionality in the NumPy (Dubois et al., 1996) and SciPy (Oliphant, 2007) packages was used to simplify and optimise the functions. My library includes functions for simulating projection data and for reconstructing images from projections. For simulations there are forward projection functions for both parallel and fan beam geometries, and there is a function to generate the Shepp-Logan phantom (Shepp and Logan, 1974), which can also be used to generate the superposition of an arbitrary set of ellipses. For reconstruction there is a ρ-filter function, and back-projection functions for both parallel and fan beam geometries. Finally, there is a function to perform the short scan weighting given by Parker (1982) in the fan beam function set.

The initial implementations were for parallel beam, using pixel-driven projection and back-projection (see Section 3.2.1), and performing ρ-filtering in the frequency domain. Later versions use the distance-driven projection method, include fan beam operations, and perform ρ-filtering using convolution to avoid wrap-around effects. The embarrassingly parallel[(2)] nature of forward- and back-projection (Hofmann et al., 2011) has been exploited to speed up the functions using Python's multiprocessing package.

[(2)] A programming problem is embarrassingly parallel if it naturally divides into many independent sub-problems. Etymology of the term is unclear, but I have seen a suggestion that it is similar to the term "an embarrassment of riches".

3.2.1 Projection methods

Most of the algorithms described in Chapter 2 use equations of the form

$$\mu(\boldsymbol{x}) = \int_0^{\pi} q_\theta \left(\boldsymbol{x} \cdot \boldsymbol{\alpha}\right) \, \mathrm{d}\theta, \tag{3.1}$$

to perform back-projection, where μ is the back-projected image, $\boldsymbol{x}$ is the image location being reconstructed, θ is the view angle, $\boldsymbol{\alpha}$ is the unit vector along the detector, and q_θ is the function being back-projected. However, these equations operate on continuous functions while projections are always discrete in implementation: the reconstructed image is an array of voxels, and the projections themselves originate from a pixelated detector.

In addition to back-projection, forward projection (also known as re-projection or simply projection) is also an important operation. Forward projection is used to synthesise x-ray image data to test reconstruction algorithms and is an integral part of iterative reconstruction algorithms. Back-projection implementations also have matching forward projection implementations, together these are here referred to simply as "projection methods". There are several published projection methods. This section describes the three principal classes: ray-driven (Crawford, 1986), pixel-driven (Peters, 1981), and a recently developed method called distance-driven (De Man and Basu, 2004*a*). The names generally refer to the focus of the main loop within an implementation.

3.2.1.1 Ray-driven

In a ray-driven implementation, each detector pixel within each view angle is considered in turn. A line is drawn connecting the pixel location to the source location and each image voxel intersected by the line is incremented by a weighted version of the pixel value. The process is

- For each view angle θ:
  - Set source location $\boldsymbol{x}_s$
  - For each detector pixel, at location $\boldsymbol{x}_d$:
    - Find all voxels along the line between $\boldsymbol{x}_s$ and $\boldsymbol{x}_d$ ($\star$)
    - Determine weights w_j for each of these voxels ($\star$)
    - Add the pixel value to each voxel, weighted by w_j

There are several methods for determining the intersected voxels and corresponding weight factors (steps marked ($\star$) above) and a selection of them are described here. For these descriptions, consider the situation illustrated in Figure 3.5 where the pixel marked i is under consideration, and the line connecting it to the x-ray source is shown, as are the voxels that the line intersects.

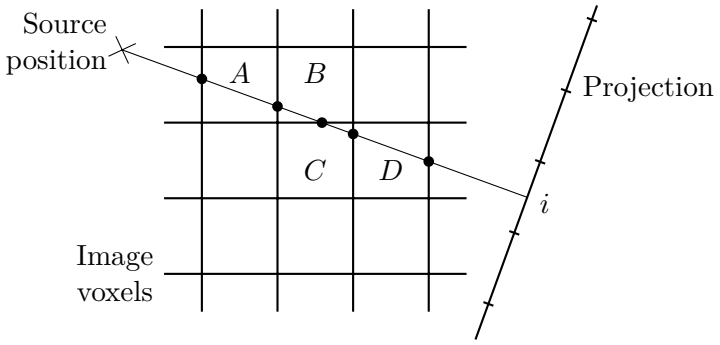

Figure 3.5: Ray-driven back-projection. A, B, C, and D are the (square) image voxels that receive a contribution from projection pixel i. The dots represent the intersections of the ray with the voxel boundaries.

A linear interpolation technique would calculate the weights by finding where the line intersects each column in the image, then calculating the linear interpolation coefficients for the voxels whose centres lie immediately above and below the intersection point. For example, voxel B would have a slightly larger coefficient than voxel C since the line intersects the middle column slightly above the boundary between B and C.

A bilinear interpolation technique starts by choosing equally spaced sample points along the line. For each sample, the bilinear interpolation coefficients are calculated for the four nearest voxels, and these coefficients determine the back-projection weights for those voxels.

Siddon's method (Siddon, 1985) operates by finding where the line intersects voxel boundaries, shown by the dots in Figure 3.5. From these intersections the length of the line within each voxel can be calculated, and this length is used to determine the weights. This method is popular because it scales well with image size and can produce accurate weight values.

More accurate weight values can be obtained by considering the ray not as a line, but as a beam with finite width. Methods of this nature are more complicated, as they tend to involve the calculation of approximate area intersections. However, a similar effect can be obtained by considering artificial pixels that are smaller than the real ones, then using one of the line based methods and combining the results for several small pixels to evaluate each real pixel.

Ray-driven forward-projection follows similar principles, except in this case it is the projection pixel's value being determined. The line is drawn, and the value assigned to the projection pixel is calculated as a weighted sum of the values of the voxels intersected by the line; the methods for determining the weights are the same.

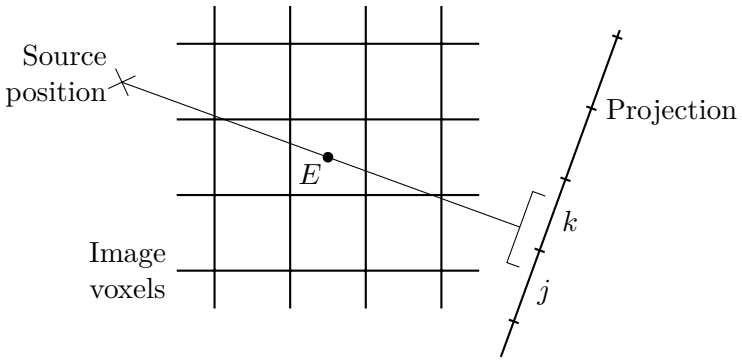

Figure 3.6: Pixel-driven back-projection. The contribution to voxel E can be determined by interpolating between the values of projection pixels j and k.

3.2.1.2 Pixel-driven

The pixel-driven implementation is the natural complement to the ray-driven technique. Following the terminology of this dissertation, the technique ought to be called "voxel-driven", but the name is left as it is to align with the literature. In this case, it is the voxels within the image that are considered independently for every view. For each voxel, a line is drawn that runs from the source location through the centre of the voxel to the detector (see Figure 3.6). The contribution to the voxel is determined by interpolating between the values on the detector pixels adjacent to where the line meets the detector. The process is as follows:

- For each view angle θ:
  - Set the source location $\boldsymbol{x}_s$
  - For each voxel, at location $\boldsymbol{x}_v$:
    - Find the location $\boldsymbol{x}_d$ where the line from $\boldsymbol{x}_s$ through $\boldsymbol{x}_v$ intersects the detector
    - Interpolate projection values to calculate the contribution to the voxel ($\star$)

Again, there are several implementation methods. Any one-dimensional interpolation can be used for the step marked ($\star$), with nearest neighbour and linear interpolation being the simplest. A more sophisticated technique, called "splatting", involves projecting not just the centre of the voxel onto the detector, but the complete shadow of the voxel. The contribution to the voxel can then be calculated according to the amount of shadow that falls on each detector pixel.

The principle for forward projection is again similar to that for back-projection. In this case, the value on each image voxel is added to the detector pixels nearest to where the ray through the voxel meets the detector. In Figure 3.6 the value on E would be

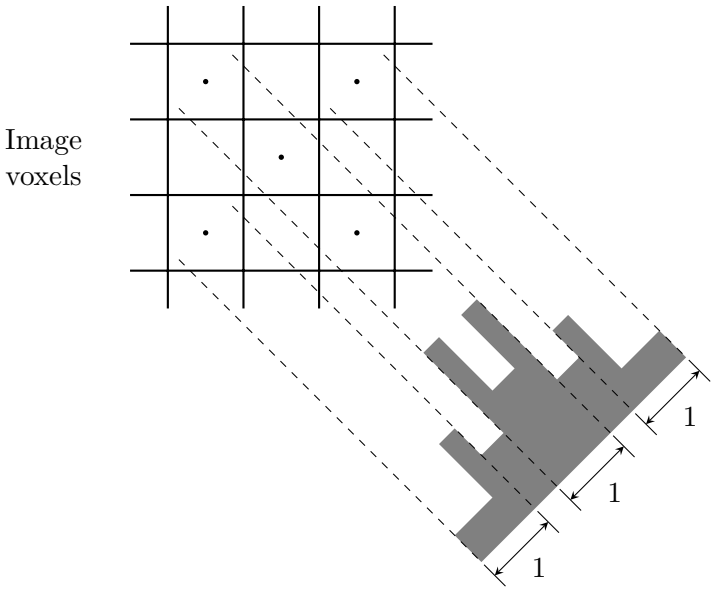

Figure 3.7: If pixel-driven projection is used with constant voxel shadow widths, even a perfectly smooth object produces an uneven projection at view angles other than multiples of 90°. The dashed lines show the shadows of the voxels marked with a dot at their centre, while the complete projection is from all nine voxels.

added to pixels j and k, with the same weighting scheme as linear interpolation would generate.

3.2.1.3 Distance-driven

While the ray- and pixel-driven methods often consider the x-ray beam as a set of infinitesimally narrow lines, the distance-driven method breaks it down into finite-width rays. It does this by considering the boundaries of voxels and pixels rather than the centres. The distance-driven algorithm is a recent development, presented by De Man and Basu (2002) with further expansion by De Man and Basu (2004*a*,*b*) and Basu and De Man (2006). The authors claim that the new method both operates faster and produces fewer artefacts than the ray- and pixel-driven approaches. The speed is due to the algorithm making use of sequential memory access and low arithmetic complexity. The algorithm achieves better artefact behaviour because it maps the relationship between image voxels and detector pixels such that there are no gaps between them. In contrast, pixel-driven projection casts a shadow of each voxel onto the detector line, usually of a predetermined width. At all angles other than horizontal and vertical these shadows do not abut, and so the overall effective shadow of the object on the detector is uneven, as shown in Figure 3.7. This tends to introduce high-frequency artefacts into the calculated projections. Likewise, ray-driven *back*-projection finds a line between the centre of each detector pixel and the x-ray source, then finds the voxels that this line

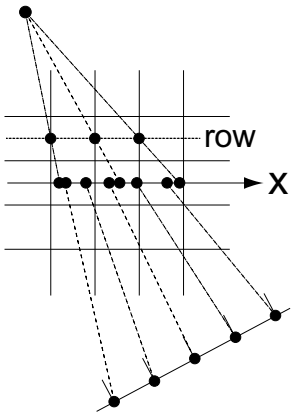

Figure 3.8: Distance-driven projection mapping onto the x-axis.
(From De Man and Basu (2002)).

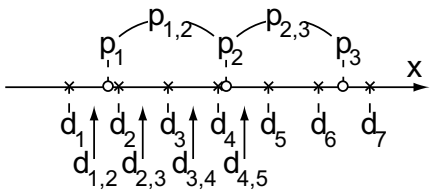

Figure 3.9: An example of the mapped boundaries showing the transfer from voxel values to pixel values. Here p_i correspond to voxel boundaries, $p_{j,k}$ correspond to voxel values, and $d_i/d_{j,k}$ follow a similar pattern for the detector pixels.
(From De Man and Basu (2002)).

intersects. In this case, the "shadow" of the pixels can overlap in places, also resulting in high-frequency artefacts, generally observed as moiré patterns in the reconstruction.

It is possible to avoid these problems by using a ray-driven projector function and a pixel-driven back-projector function. However, the distance driven algorithm has the advantage of being self-adjoint and is at least as fast as the other operations. The self-adjoint property has two main effects: errors introduced in iterative routines by repeated forward- and back-projections are minimal, and the code for the two forms of the algorithm are almost identical, which simplifies development, debugging, and maintenance. Another solution to the artefact problems is to adjust the shadowing widths; while this solves the problem, it increases the computational complexity. For these reasons I have used the distance-driven algorithm for my implementations.

Figure 3.8 shows how the mapping is performed by the distance driven algorithm for a single view angle with a fan-beam geometry. For a given view angle, the algorithm operates thus:

- Map the detector boundaries onto the x-axis.
- For each row in the image:

- Map the pixel boundaries onto the x-axis.
- Calculate the overlaps between voxels and pixels. ($\star$)
- Multiply the overlap amounts by the ray length through the voxel, to give the weight for the voxel/pixel pair.

For implementation of the step marked ($\star$), consider Figure 3.9. Omitting the ray length, the quantities back-projected into the voxels shown are

$$p_{1,2} = \frac{(d_2 - p_1)d_{1,2} + (d_3 - d_2)d_{2,3} + (d_4 - d_3)d_{3,4} + (p_2 - d_4)d_{4,5}}{p_2 - p_1}, \tag{3.2}$$

$$p_{2,3} = \frac{(d_5 - p_2)d_{4,5} + (d_6 - d_5)d_{5,6} + (p_3 - d_6)d_{6,7}}{p_3 - p_2}. \tag{3.3}$$

I found implementation of this algorithm to be relatively straightforward and flexible. Furthermore, I was able to modify my parallel beam implementation to operate on fan beam data without changing much code.

3.3 BEAMnrc Monte Carlo system

For the scatter estimation research reported in Chapter 4, the output of my algorithm needed validation. However, it is impossible to separate scattered photons from primary photons in real scan data, so Monte Carlo simulations were used to generate realistic radiograph data that could be separated into primary and scattered photons. The particular Monte Carlo package used is named BEAMnrc (Rogers et al., 2006).

BEAMnrc is designed to model radiotherapy systems, and is based on the EGSnrc package that models electron and photon propagation. Both systems are maintained by the National Research Council of Canada. EGSnrc was first released in February 2000 with BEAMnrc following in February 2002, and revisions are generally released annually. Simulations are configured through a graphical interface that has superseded the original text file configuration. The physical phenomena simulated by EGSnrc include photoelectric, Compton, and Rayleigh interaction events, as well as relativistic spin effects and atomic relaxations during and after these events. Several radiation sources can be simulated with BEAMnrc, and simple phantoms can be configured. The simulation output individually describes all the photons that reached the detector plane, including tags identifying whether the photon interacted within the target. As such, the package is suitable for simulating x-ray transmission imaging.

Simulations are compiled from Fortran source into an executable which can be executed directly. Multiple instances of the program can be run in parallel, allowing a job to be easily split across multiple CPU cores of a single computer or across many nodes in a cluster or supercomputer. I ran my simulations on the cluster[(3)] in the

[(3)] The ECE Dept. cluster has 100 compute nodes coordinated by GridEngine. The resources available to each node vary slightly, but a typical node has a 2.0 GHz AMD Opteron processor and 4 GB of RAM.

Department of Electrical and Computer Engineering, and on my desktop PC with a quad-core Intel i7 CPU (2.8 GHz). Running on the cluster was faster because up to 50 processor cores could be used simultaneously. However, most simulations were run on my PC because the cluster did not have enough hard disk space to store the large data sets produced by BEAMnrc. The simulation run-time varied according to the number of photons being simulating, from 1 minute for 20×10^6 photons up to 11 hours for 15×10^9 photons[4] on my desktop PC.

While BEAMnrc on the whole worked well, I did find a few problems. Fortunately, the package is open source so I was able to identify the bugs in the code, fix them, and send the patches back to the maintainers, although this required me to learn Fortran. The two main bugs were:

- One of the x-ray source modules had a variable that was being used uninitialised under certain conditions. While the conditions were rare, they occurred occasionally, and when they did, the program would either abort with a segmentation fault or would get trapped in an infinite loop. Because of the fatal consequences of this bug, I spent a week working through assembly code in core dumps to isolate the cause.

- The batch processing includes a timeout to kill the simulation if it runs for too long. This timeout was incorrectly implemented and thus I sometimes had a four day simulation terminated after 36 hours.

I also fixed a problem that prevented me from defining new materials for the simulation, and fixed some sources of compiler warnings. The maintainers have applied my patches and they are in the latest release of the package.[5]

[4] I also had simulations that ran for several days. However, the log files from these larger simulations (along with the raw output data) were lost due to a hard disk failure, so I cannot report accurate photon numbers or run-times for these simulations.

[5] The latest BEAMnrc source package can be obtained from `http://irs.inms.nrc.ca/software/beamnrc/download.html`

Chapter Four

Compton scatter

In the first half of this chapter an algorithm is developed for estimating spectrally-resolved scatter levels that can be used in a scatter correction framework (Opie et al., 2012). The second half of the chapter is an analysis of a key approximation used in the derivation of the estimation algorithm.

4.1 The IBLESS algorithm

IBLESS (Image Based Low-order Estimation of Spectral Scatter) is an algorithm I developed for compensating projection data for scatter. The algorithm performs an analytical calculation of the scatter intensity that is expected at the detector based on an estimate of the imaged volume. IBLESS differs from existing analytical methods in that it can produce an estimate for each of the energy bins being measured by an energy resolving x-ray detector, and thus it can be used in a spectral CT reconstruction. It uses the known energy-spreading characteristics of Compton scatter (Johns and Cunningham, 1983) to calculate which energy bin to attribute scatter to.

4.1.1 Introduction

The detection of scattered x-rays in a CT scan causes cupping and streaking artefacts in the reconstructed image (Johns and Yaffe, 1982). Hardware and software techniques exist to reduce or compensate for scatter, however hardware techniques are not suitable for micro-CT, and most software techniques do not account for energy-dependent scatter behaviour.

Many methods have been proposed for reducing the effect of scatter, as discussed in Section 1.10.3. Hardware methods such as antiscatter grids and air gaps are simple and can be effective, but they increase patient dose and space requirements, respectively. In addition, the detector pixel pitch used in micro-CT scanners is generally of the order of 50 µm so an antiscatter grid would be unsuitable because the blades would obscure a significant portion of each pixel (Colijn and Beekman, 2004). Reconstruction-based correction methods operate iteratively by reconstructing a volume, calculating a scatter

estimate based on that volume, correcting for the scatter, then repeating the steps (Rührnschopf and Klingenbeck, 2011). They tend to be Monte Carlo driven methods, which can be computationally expensive. This section describes a reconstruction-based method with a much smaller computational expense.

All of the post-acquisition scatter compensation techniques referred to in Section 1.10.3 are designed to operate on data produced by traditional detectors. However, like primary radiation, scatter also varies with energy, and taking this variation into consideration should result in improved scatter compensation. The fact that Compton scattering of a photon reduces the energy of that photon also suggests that considering the energy of scatter should be valuable.

IBLESS estimates the scatter contribution to each energy bin of each pixel, based on a reconstructed volume. The intention is for IBLESS to be used in an iterative framework like that described by Rührnschopf and Klingenbeck (2011). The algorithm aims to offer the accuracy of reconstruction-based estimation methods whilst being faster than a Monte Carlo simulation. Micro-CT has been chosen as the target of IBLESS for two main reasons. First, current energy-resolved detectors are mainly deployed in experimental micro-CT scanners, including the MARS scanner (Bones et al., 2010), and second, micro-CT is not amenable to the use of antiscatter grids or large air gaps.

Section 4.1.2 contains a derivation of the mathematical model used by IBLESS and some comments on its implementation. Section 4.1.3 describes the simulations used to validate IBLESS, Section 4.1.4 shows the results of this validation against a Monte Carlo system, then Section 4.1.5 explains these results and discusses their implications. Section 4.1.6 offers concluding thoughts and an outline of future work required for the algorithm.

4.1.2 Algorithm

IBLESS calculates single Compton scatter quantities, neglecting multiple and Rayleigh scatter. This simplification is justified because most of the scatter affecting micro-CT systems is single scatter (Kyriakou and Kalender, 2007), and omitting the complexity of multiple scatter makes implementation of the algorithm feasible. IBLESS could be extended to include Rayleigh scatter but Compton scatter is the focus due to its energy-shifting characteristic.

A derivation of the model used by IBLESS is now presented. First, the model for the total scatter intensity is derived, then the model is extended to include energy-shifting effects. Several of the quantities described are illustrated in Figure 4.1. For this work a parallel beam geometry is assumed, irradiating a thin slice of the object (Figure 4.1(a)).

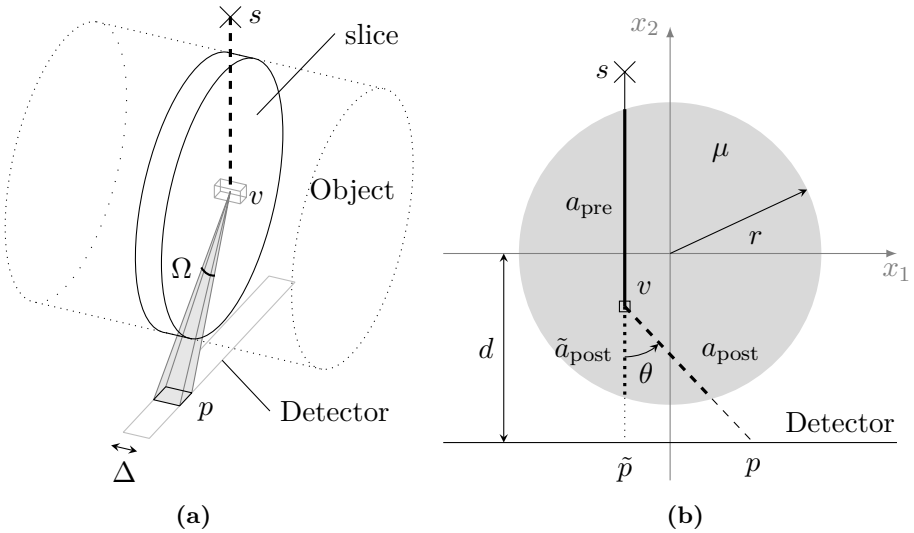

Figure 4.1: Illustrations of the geometry and variables used in the text. (a) shows a slice of the 3D object that is illuminated by the x-ray beam, and (b) shows this slice and the variables used for the model. An example scatter path is shown, along with the corresponding unscattered path. a_{post} is the actual post-scatter attenuation, while $\tilde{a}_{\text{post}}$ is the post-scatter attenuation assumed by the ZAA (see Section 4.2). p is the detector location where the scattered photons would be measured, $\tilde{p}$ is the detector location where the primary photons through v would be measured. Ω is the solid angle of the detector element at p as seen from v.

4.1.2.1 Total intensity model

Let v be an arbitrary voxel within the volume being imaged, and let $\tilde{p}$ be the location of the detector pixel such that a line between $\tilde{p}$ and the source passes through v. Let I_0 be the incident open-beam intensity at the detector, $A_{\tilde{p}}$ be the area of $\tilde{p}$, I_v be the incident intensity on v, and A_v be the cross-sectional area of v. With no material between the source and v, I_v can be expressed as

$$I_v = \frac{A_v}{A_{\tilde{p}}} I_0(\tilde{p}), \tag{4.1}$$

which can be understood by considering Figure 4.2: with a parallel beam of x-rays, the number of photons incident on the surface A_v is the same as the number incident on the shaded region of the pixel. With even coverage of the pixel, the ratio between the number of photons incident on the shaded area and the total number incident on the pixel is $A_v/A_{\tilde{p}}$, leading directly to (4.1). Let $a_{\text{pre}}(v)$ be the attenuation, equal to the inverse of the transmission, of the x-ray beam between the source (at s) and v. Then

$$I_v = \frac{1}{a_{\text{pre}}(v)} \frac{A_v}{A_{\tilde{p}}} I_0(\tilde{p}), \tag{4.2}$$

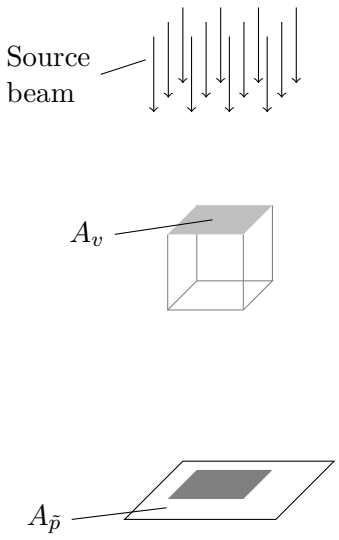

Figure 4.2: Illustration of the origin of (4.1). The dark shaded region is the shadow cast by the voxel onto the pixel.

with

$$a_{\text{pre}}(v) = \exp\left\{\int_s^v \mu(l,\alpha)\,\mathrm{d}l\right\}, \tag{4.3}$$

where l represents distance along the photon path (from s to v), $\mu(l,\alpha)$ is the total linear attenuation coefficient of the material at l, and α is the incident photon energy normalised by the electron rest energy (511 keV). Let $\mu_c(v,\alpha)$ be the linear attenuation coefficient due to Compton scattering. The proportion of the incident intensity that is scattered within voxel v due to the Compton process is then

$$1 - \exp\left\{-\mu_c(v,\alpha)\Delta x(v)\right\}, \tag{4.4}$$

where $\Delta x(v)$ is the path length through v and $\mu_c(v,\alpha)$ is assumed to be constant within v. This expression follows directly from the Beer-Lambert law (see Section 1.5). Thus the total scattered intensity leaving v is given by

$$\frac{1}{a_{\text{pre}}(v)}\frac{A_v}{A_{\tilde{p}}} I_0(\tilde{p})\left(1 - \exp\left\{-\mu_c(v,\alpha)\Delta x(v)\right\}\right). \tag{4.5}$$

The next step is to evaluate the *distribution* of this scatter. For this the Compton differential cross-section is used, $\frac{\mathrm{d}\sigma_c}{\mathrm{d}\Omega}(\theta,\alpha)$, which describes the probability that an incident photon will be deflected into the elemental solid angle $\mathrm{d}\Omega$ when passing through an attenuator containing one scattering centre per unit area (Barrett and Swindell, 1981). Integrating this value over the solid angle subtended at v by a detector pixel p gives the probability that a photon will be scattered toward that pixel. From

Barrett and Swindell (1981),

$$\frac{\mathrm{d}\sigma_c}{\mathrm{d}\Omega}(\theta,\alpha) = \frac{r_0^2}{2}\left[1 + \frac{\alpha^2(1-\cos\theta)^2}{(1+\cos^2\theta)\left[1+\alpha(1-\cos\theta)\right]}\right]\frac{1+\cos^2\theta}{\left[1+\alpha(1-\cos\theta)\right]^2}, \tag{4.6}$$

where θ is the angle of deflection of the photon and r_0 is the classical electron radius, $r_0 = 2.818 \times 10^{-13}\,\mathrm{cm}$ (Mohr et al., 2008).

To obtain the spatial scatter distribution, the value of the Compton differential cross-section in (4.6) is normalised by the complete Compton scattering cross section σ_c,

$$\sigma_c = \sigma_0\, f_{\mathrm{KN}}(\alpha), \tag{4.7}$$

where

$$f_{\mathrm{KN}}(\alpha) = \frac{3}{4}\left[\frac{2(1+\alpha)^2}{\alpha^2(1+2\alpha)} + \frac{\ln(1+2\alpha)}{\alpha}\left(\frac{1}{2} - \frac{1+\alpha}{\alpha^2}\right) - \frac{1+3\alpha}{(1+2\alpha)^2}\right] \tag{4.8}$$

is the Klein-Nishina function (Klein and Nishina, 1928), and the Thompson scattering cross-section σ_0 is given by $\sigma_0 = 8\pi r_0^2/3$. Thus the proportion of scattered radiation from v that is directed toward a particular detector pixel p is given by

$$P(v,p) = \frac{\int_\gamma \frac{\mathrm{d}\sigma_c}{\mathrm{d}\Omega}(\theta,\alpha)\,\mathrm{d}\Omega}{\sigma_0\, f_{\mathrm{KN}}(\alpha)}, \tag{4.9}$$

where γ is the surface of detector pixel p, $\mathrm{d}\Omega$ is the incremental solid angle from v to a point within γ, and θ is the deflection angle from v to the same point within γ.

The scattered radiation is also attenuated between v and p. Let $a_{\mathrm{post}}(v,p)$ be this attenuation, defined in a similar manner to $a_{\mathrm{pre}}(v)$, i.e.,

$$a_{\mathrm{post}}(v,p) = \exp\left\{\int_v^p \mu(l,\alpha')\,\mathrm{d}l\right\}, \tag{4.10}$$

where l again represents position along the photon path (this time from v to p) and α' is the energy of the scattered photon (see Section 4.1.2.2). The intensity of radiation scattered from v and detected at p is then

$$\begin{aligned} I_s(p,v) = &\left(\frac{1}{a_{\mathrm{pre}}(v)}\frac{A_v}{A_{\tilde{p}}}I_0\right)\left[1-\exp\{-\mu_c(v,\alpha)\Delta x(v)\}\right] \\ &\times\left(\frac{\int_\gamma \frac{\mathrm{d}\sigma_c}{\mathrm{d}\Omega}(\theta,\alpha)\,\mathrm{d}\Omega}{\sigma_0\, f_{\mathrm{KN}}(\alpha)}\right)\frac{1}{a_{\mathrm{post}}(v,p)}. \end{aligned} \tag{4.11}$$

To simplify the problem, the method of Rinkel et al. (2007) is followed in assuming the

attenuation factor $a_{\text{post}}(v,p)$ is equal to that of photons scattered at $\theta = 0$, i.e.,

$$a_{\text{post}}(v,p) \approx \tilde{a}_{\text{post}}(v) = \exp\left\{\int_v^{\tilde{p}} \mu(l,\alpha)\,\mathrm{d}l\right\}, \tag{4.12}$$

where $\tilde{p}$ is the detector pixel "behind" v (see Figure 4.1(b)). A detailed analysis of this approximation, which I have named the "zero-angle approximation", is presented in Section 4.2. The approximation enables the simplification

$$a_{\text{pre}}(v)\tilde{a}_{\text{post}}(v) = \exp\left\{\int_s^{\tilde{p}} \mu(x,\alpha)\,\mathrm{d}x\right\} = \frac{I_0(\tilde{p})}{I(\tilde{p})}, \tag{4.13}$$

where I is the primary (scatter-free) x-ray intensity and the second equality arises from the Beer-Lambert law. The approximation also includes the assumption that the attenuation experienced by a scattered photon is the same as if it had its original energy; this part of the approximation is discussed later.

Since the Compton differential cross-section is approximately constant across the small area of a pixel, the integral over γ can be simplified to

$$\int_\gamma \frac{\mathrm{d}\sigma_c}{\mathrm{d}\Omega}(\theta,\alpha)\,\mathrm{d}\Omega \approx \frac{\mathrm{d}\sigma_c}{\mathrm{d}\Omega}(\theta,\alpha)\cdot\Omega(p,v), \tag{4.14}$$

where $\Omega(p,v) = \int_\gamma \mathrm{d}\Omega$ is the solid angle subtended by p at v. Substituting (4.13) and (4.14) into (4.11) yields

$$I_s(p,v) = \frac{I(\tilde{p})}{I_0(\tilde{p})}\frac{A_v}{A_{\tilde{p}}} I_0(\tilde{p})\left[1-\exp\left\{-\mu_c(v,\alpha)\Delta x(v)\right\}\right]\frac{\frac{\mathrm{d}\sigma_c}{\mathrm{d}\Omega}(\theta,\alpha)\cdot\Omega(p,v)}{\sigma_0\, f_{\text{KN}}(\alpha)} \tag{4.15}$$

for the contribution of scatter from one voxel to one pixel. The complete scatter field at any pixel p for an incident beam energy α can then be calculated as

$$I_s(p) = \sum_v I_s(p,v) \tag{4.16}$$

$$= \sum_v I(\tilde{p})\frac{A_v}{A_{\tilde{p}}}\left(1-\exp\left\{-\mu_c(v,\alpha)\Delta x(v)\right\}\right)\frac{\frac{\mathrm{d}\sigma_c}{\mathrm{d}\Omega}(\theta,\alpha)\cdot\Omega(p,v)}{\sigma_0\, f_{\text{KN}}(\alpha)}. \tag{4.17}$$

4.1.2.2 Energy change

As well as being deflected, Compton scattered photons lose energy. This energy loss means that in addition to being detected by a different pixel from the one in the original path, scattered photons may be detected in a different energy bin by an energy-resolving detector. The relationship between original and scattered photon energy is (Barrett and Swindell, 1981)

$$\alpha' = \frac{1}{1/\alpha + (1-\cos\theta)}, \tag{4.18}$$

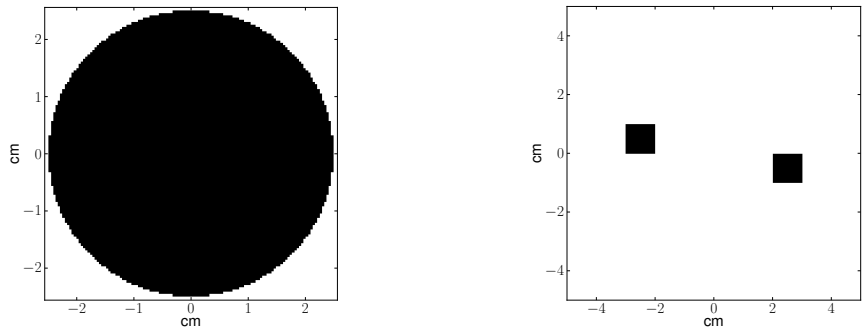

(a) **(b)**

Figure 4.3: The two phantoms used for testing. (a) is a PMMA cylinder, (b) comprises two blocks of cortical bone.

where α is the photon's original energy and α' is its energy after scattering through angle θ. This equation can be inverted to give

$$\alpha(\alpha', \theta) = \frac{1}{1/\alpha' - (1 - \cos\theta)}, \tag{4.19}$$

which can be used in (4.17) to fully model the energy-shifting effect of Compton scattering:

$$I_s(p, \alpha') = \sum_v I(\tilde{p}, \alpha(\alpha', \theta)) \frac{A_v}{A_{\tilde{p}}} \left(1 - \exp\left\{-\mu_c\left(v, \alpha(\alpha', \theta)\right) \Delta x(v)\right\}\right) \times \frac{\frac{\mathrm{d}\sigma_c}{\mathrm{d}\Omega}(\theta, \alpha(\alpha', \theta)) \cdot \Omega(p, v)}{\sigma_0 \, f_{\mathrm{KN}}(\alpha(\alpha', \theta))}. \tag{4.20}$$

The model (4.20) has been implemented in Python (using NumPy), but it could be accelerated considerably by converting it to a language such as C or C++ and applying optimisations. This has not been done because the principal aim of this project is to evaluate the effectiveness and utility of IBLESS, not a particular implementation of it.

The implementation currently estimates the amount of scatter generated within a single slice of an object. The mathematics given here are not limited to this case, and the program could be extended to operate on cone-beam data where scatter is a much greater problem (Kyriakou and Kalender, 2007). The single-slice operation has been retained as it makes results simpler to interpret and reproduce, and reduces the time required to run Monte Carlo simulations for validation.

4.1.3 Simulations

The output of IBLESS was compared to the scatter predicted by the Monte Carlo simulator BEAMnrc (Rogers et al., 2006). Rayleigh scatter and Compton electron-

binding effects were disabled in the configuration of BEAMnrc so that the results could be directly compared. Two simulated phantoms were used for the testing; a cross section of each is shown in Figure 4.3. IBLESS was tested by simulating a parallel beam source illuminating the phantoms from above.

The first phantom, shown in Figure 4.3(a), is a 2.5 cm radius PMMA[(1)] cylinder. The gap between the bottom of the cylinder and the detector is 1.5 cm. The purpose of this phantom is to test the operation on a simple homogeneous structure. The second phantom, shown in Figure 4.3(b), comprises two blocks of cortical bone, each with a 1 cm square profile, vertically offset by 1 cm and with a 4 cm gap between them horizontally. The detector is located 4 cm below the bottom edge of the lower block. This phantom is intended to test the operation on an object with inhomogeneities. Different materials are simulated for the two phantoms to test the operation of IBLESS on materials with different Compton cross-sections.

Simulations were performed for each of two monochromatic x-ray sources, 50 keV and 30 keV, and energy bins of 4 keV width, with the source energy in the middle of the highest energy bin. A monochromatic source was simulated so that the results would be simpler to interpret, and 30 and 50 keV were chosen as they fall within the diagnostic energy range. He et al. (2012) found that a bin width of approximately 4 keV is optimal for spectral scans of objects containing k-edge materials. This is also around the greatest resolution achievable by current detectors. The Compton cross-sections and complete attenuation coefficients used by IBLESS were obtained from the database distributed with BEAMnrc which in turn originates from the online XCOM program (Berger et al., 2010); the values are given in Table 4.1.

4.1.4 Simulation results

Figure 4.4 shows the intensities predicted for the PMMA cylinder. All scatter intensities shown in this and subsequent figures have been normalised by the total flatfield (open beam) intensity to facilitate comparison. For the 48–52 keV energy bin the form of the profile produced by IBLESS closely matches that of the Monte Carlo simulation, and the magnitude matches well for most of the detector width. In the lower energy bin, 44–48 keV, the output of IBLESS matches that of BEAMnrc reasonably well, apart from the central region of the detector where IBLESS estimates zero scatter but BEAMnrc

[(1)] PMMA: Poly(methyl methacrylate), also known as Perspex or Lucite.

Table 4.1: Total (μ) and Compton (μ_c) linear attenuation coefficients of phantom materials (Berger et al., 2010). Units: cm^{-1}.

	μ_c(30 keV)	μ(30 keV)	μ_c(50 keV)	μ(50 keV)
PMMA	0.321	0.334	0.206	0.236
Cortical bone	0.356	2.423	0.334	0.761

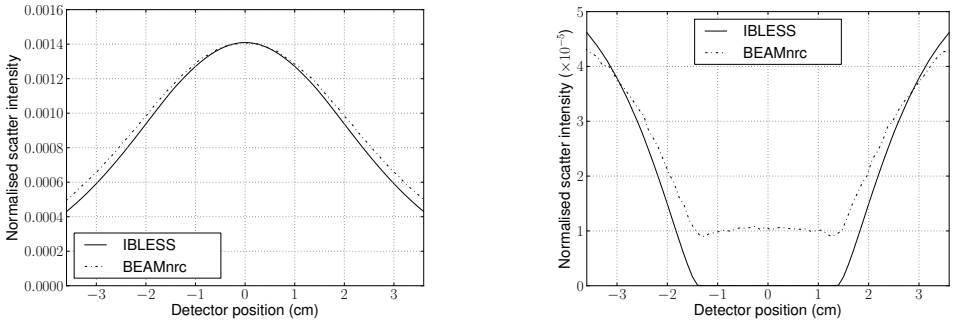

(a) **(b)**

Figure 4.4: Normalised scatter intensity with the PMMA cylinder phantom, 50 keV source. (a) is the scatter in the 48–52 keV bin, (b) is in the 44–48 keV bin.

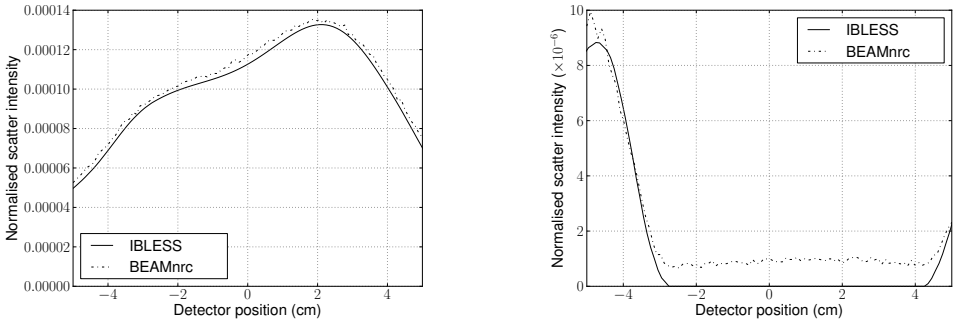

(a) **(b)**

Figure 4.5: Normalised scatter intensity with the bony phantom, 50 keV source. (a) is the scatter in the 48–52 keV bin, (b) is in the 44–48 keV bin.

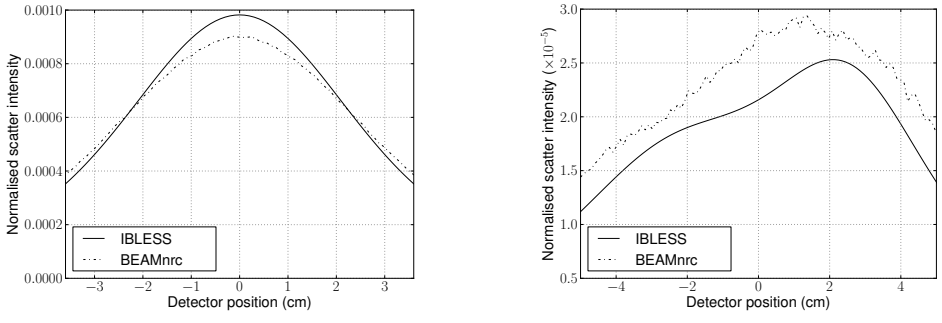

(a) **(b)**

Figure 4.6: Normalised scatter intensity with the PMMA cylinder phantom and with a 30 keV source, in the 28–32 keV bin. (a) is the scatter from the PMMA cylinder, (b) is from the bones.

does not. Inspection of the scales on the y-axes shows that the vast majority of scattered radiation remains in the 48–52 keV bin. Plots are not shown for bins lower than 44 keV as the modelled intensity levels are zero.

Figure 4.5 shows the intensities predicted for the bony phantom. In the upper energy bin IBLESS again closely matches the profile of the Monte Carlo output but predicts a slightly smaller magnitude. The estimate for the lower energy bin again matches BEAMnrc reasonably well toward the edges of the detector but falls to zero in the centre while BEAMnrc does not. The overall scatter intensity from this phantom is smaller than that of the PMMA cylinder, as could be expected given the much smaller volume of material.

To confirm that IBLESS works across the diagnostic energy range, the simulations were repeated with a 30 keV source. Figure 4.6(a) shows that IBLESS still agrees with the amount produced by BEAMnrc although the form of the scatter does not match quite as closely as it does at 50 keV. Conversely, Figure 4.6(b) shows that for the bony phantom the estimate has a good shape but is smaller in magnitude. In fact it was possible to reproduce the profiles generated by BEAMnrc very closely by running IBLESS with slightly different coefficients, however these results are not shown as this experiment is intended to evaluate the operation of IBLESS without any empirical calibration.

IBLESS is much faster to run than a BEAMnrc simulation. Calculating the scatter intensity for a single view angle of the cylinder phantom with IBLESS took 3.8 seconds on a single processor, while the BEAMnrc simulation took a little over 4 hours using 8 processors.

4.1.5 Discussion

The results in the preceding section show that IBLESS performs well at the micro-CT scale. Apart from missing some scatter near the centre of the detector for energy bins below the source energy, both the form and magnitude agree either reasonably or very well with the output of BEAMnrc. The scatter in the 44–48 keV bin is made up of photons that have lost enough energy to "bin-hop". I conjecture that the intensity predicted by BEAMnrc through the central detector region for this bin comprises photons which have been multiply scattered; such photons are not modelled by IBLESS. The basis for this claim is that for a photon to lose enough energy to bin-hop, it must either scatter at a large angle[(2)] or experience multiple scatter events. Since scatter reaching the centre of the detector can only have been deflected by a small angle, it must have been scattered more than once to appear in a lower energy bin. This phenomenon means that IBLESS is only applicable to micro-CT: larger objects produce a greater level of multiple scatter, which is not modelled by IBLESS.

[(2)] For example, to lose energy from 50 keV to 48 keV requires a deflection of 55°, according to (4.18).

The results presented here suggest that the amount of scatter that hops between energy bins of a practical size is not significant enough to warrant inclusion in an estimation scheme. Accurate estimation of intra-bin scatter is much more important for effective scatter compensation, and IBLESS performs well at this task. Removal of the logic that accounts for inter-bin scatter would simplify and accelerate the software slightly.

While estimating inter-bin scatter is of low importance, this should not be confused with estimating the amount of scatter produced at different energies within a polychromatic (broadband) spectrum. Comparison of the scatter quantities at the two energies tested in this paper shows that different amounts of scatter are produced at each energy. This leads to the conclusion that scatter estimation and compensation on a bin-by-bin basis is worthwhile for spectral CT. IBLESS has the ability to do this and can work with the spectral variation of the Compton scattering cross-section. This type of spectrally-aware compensation can be applied independently to each bin if inter-bin scatter is neglected.

IBLESS requires knowledge of both μ and μ_c to operate. An estimate of μ can be obtained from an initial reconstruction, as is the case with other reconstruction-based iterative algorithms. My suggested method of obtaining μ_c is simply to scale the value for μ based on a simple segmentation procedure. This involves using thresholding to distinguish between air, soft tissue, and bone, then multiplying μ by a predetermined scaling factor according to the type of tissue comprising each voxel. This works because soft tissues all have a similar ratio of μ_c to μ (about 79% at 50 keV), and bone and air similarly have known ratios. It is possible to tailor the particular scaling factors according to the type of scan being performed, since the types of tissue likely to be encountered are usually known. For example, when performing a chest CT it is usually safe to assume the presence of lung tissue and ribs, so the soft-tissue ratio can be biased toward that of inflated lung while the bone ratio can be set to that of rib tissue.

Several approaches can be taken to apply these findings to scans that use contrast agents, e.g., iodine or gadolinium. With an intravenous contrast agent, the volume of contrast agent is small compared to the rest of the body, so it should be acceptable to treat contrast agent voxels as bone (since they will be segmented as such due to their higher attenuation). In the case of orally administered contrast agent, the bolus may be present in a larger volume. This could be addressed by choosing the scaling factor for 'bone' to be closer to that of the contrast agent. It may also be feasible to include contrast agent as a separate segmentation target.

4.1.6 Conclusions and future work

An algorithm was derived for energy-resolved estimation of Compton scatter based on a reconstruction of a micro-CT scan. The algorithm was implemented and its results

have been verified against the output of the BEAMnrc Monte Carlo simulator. The program was found to be effective at estimating single scatter. For micro-CT, single scatter is the dominant process, although multiple scatter is more prominent in energy bins below the source energy. A further finding was that very little scatter crosses bin boundaries with realistically sized energy bins, so this phenomenon could possibly be omitted from the model. The amount of scatter varies with the energy of the incident radiation, so energy-resolved CT reconstruction will benefit from the use of a scatter compensation technique that accounts for this behaviour. IBLESS is suitable for this task, and is much faster than running a Monte Carlo simulation.

There are three main improvements required to make IBLESS a more useful tool. First, the program needs to account for electron-binding effects in Compton scatter so that the amount of Compton scatter can be more accurately estimated. Next, Rayleigh scatter should be included in the model. This would require the use of another scaling factor to obtain the linear attenuation coefficient due to Rayleigh scattering, μ_{R}, based on the reconstructed μ. Finally, the geometry assumed by the program should be converted to cone-beam. The first detector style to be implemented would be flat-panel as that is the style used in the MARS scanner, but consideration should also be given to the curved detector styles.

4.2 Analysis of the zero-angle approximation

The derivation of IBLESS, above, uses what I call a zero angle approximation (ZAA), whereby the post-scatter attenuation is assumed to be equal to that of photons that are not scattered, after Rinkel et al. (2007). However, there appears to have been no analysis of the accuracy of this approximation. The objective of this section is to analyse the ZAA and its consequences for IBLESS and the scatter estimation algorithm of Rinkel et al. Section 4.2.1 describes the ZAA and an analysis of its effects. Numerical simulations of these effects are presented in Section 4.2.2. The overall results and their implications are given in Section 4.2.3.

4.2.1 Theory

Consider a 3D object illuminated by a parallel beam of x-rays that passes through a slice of the object as shown in Figure 4.1(a). The scattered radiation from this slice that falls on a linear detector of width Δ (Figure 4.1(a)) is considered here. For simplicity and to match previous work, a cylindrical slice of radius r (Figure 4.1(b)) is assumed. A photon is emitted from the source at s and travels uneventfully until it reaches the location marked v, where it undergoes Compton scattering through a deflection angle θ toward the location marked p (Figure 4.1(b)). The photon path is completely defined by the scattering voxel v and the ultimate detector pixel p. The object here is a homogeneous

cylinder with linear attenuation coefficient μ and the attenuation coefficient outside the object is zero. The total attenuation experienced by a photon beam along this path is given by

$$a(v,p) = a_{\text{pre}}(v)\, a_{\text{post}}(v,p), \tag{4.21}$$

where the a values are defined in (4.3) and (4.10). The ZAA substitutes $\tilde{a}_{\text{post}}$ for a_{post}, where

$$\tilde{a}_{\text{post}}(v) = \exp\left(\int_v^{\tilde{p}} \mu \,\mathrm{d}l\right). \tag{4.22}$$

The point $\tilde{p}$ is on the detector and is collinear with s and v. Note that in the above equations, s and $\tilde{p}$ are determined by the location of v since the parallel beam geometry is being used.

The motivation for the ZAA is that the approximate attenuation $\tilde{a}(v,p)$ is simply expressed in terms of the primary radiation transmission, thus

$$\begin{aligned}
\tilde{a}(v) &= a_{\text{pre}}(v)\, \tilde{a}_{\text{post}}(v), && (4.23)\\
&= \exp\left(\int_s^{v} \mu \,\mathrm{d}l\right) \exp\left(\int_v^{\tilde{p}} \mu \,\mathrm{d}l\right), && (4.24)\\
&= \exp\left(\int_s^{\tilde{p}} \mu \,\mathrm{d}l\right), && (4.25)\\
&= \frac{I_0(\tilde{p})}{I(\tilde{p})}, && (4.26)
\end{aligned}$$

where I is the primary x-ray intensity measured by the detector, and I_0 is the flat-field (incident) intensity. This relationship simplifies the scatter estimation algorithm significantly.

The approximation clearly introduces an error into the scatter model. The justification given by Rinkel et al. (2007) for the ZAA is that "the most significant contribution to the detected scattered radiation is from photons scattered at small angles". This is because for photon energies in the range used by x-ray radiography and CT, the Compton differential cross-section decreases rapidly with increasing deflection angle θ (Barrett and Swindell, 1981).

As presented in Section 4.1.2.1, the scatter intensity for any scatterer location v and any detector pixel location p is given by

$$I_s(v,p) = \frac{1}{a_{\text{pre}}(v)\, a_{\text{post}}(v,p)} \frac{A_v}{A_{\tilde{p}}} I_0(\tilde{p}) \left\{1 - \exp\left[-\mu_c(v,\alpha)\Delta x\right]\right\} \frac{\frac{\mathrm{d}\sigma_c}{\mathrm{d}\Omega}(\theta,\alpha)\, \Omega(p,v)}{\sigma_0 f_{\text{KN}}(\alpha)}, \tag{4.27}$$

which is (4.15) after reverting the effect of (4.13). Then the total scatter intensity at

the pixel p is, as before, simply

$$I_s(p) = \sum_v I_s(v,p). \tag{4.28}$$

With a homogeneous specimen and assuming uniform incident intensity, (4.28) can be written as

$$I_s(p) = K \sum_v \frac{1}{a(v,p)}\, w(v,p), \tag{4.29}$$

where

$$K = \frac{A_v}{A_{\tilde{p}}} \frac{I_0 \left\{1 - \exp\left[-\mu_c(\alpha)\Delta x\right]\right\}}{\sigma_0 f_{\mathrm{KN}}(\alpha)} \tag{4.30}$$

represents the terms that do not depend on v or p (v has been dropped from the dependencies of μ_c for this reason), and

$$w(v,p) = \frac{\mathrm{d}\sigma_c}{\mathrm{d}\Omega}(\theta,\alpha)\, \Omega(p,v) \tag{4.31}$$

contains all the terms that depend on v or p except the attenuation $a(v,p)$. The quantity $w(v,p)$ is therefore unaffected by the ZAA.

4.2.1.1 Homogeneous phantom

With the geometry as shown in Figure 4.1(b) and denoting the coordinates of v by (x_1, x_2) such that the origin is at the centre of the circle, the true path length within the phantom is given by

$$L(v,p) = \underbrace{\sqrt{r^2 - x_1^2} - x_2}_{L_{\mathrm{pre}}(v)} + \underbrace{x_2\cos\theta - x_1\sin\theta + \sqrt{r^2 - (x_1\cos\theta + x_2\sin\theta)^2}}_{L_{\mathrm{post}}(v,p)}, \tag{4.32}$$

where the post-scatter length $L_{\mathrm{post}}(v,p)$ can be rewritten as

$$L_{\mathrm{post}}(v,p) = \frac{x_2 d + x_2^2 - x_1 p_1 + x_1^2}{\sqrt{(p_1 - x_1)^2 + (d + x_2)^2}} + \sqrt{r^2 - \frac{(x_1 d + x_2 p_1)^2}{(p_1 - x_1)^2 + (d + x_2))^2}}, \tag{4.33}$$

where p_1 is the horizontal coordinate of p. In contrast, the approximate post-scatter length is given by

$$\tilde{L}_{\mathrm{post}}(v) = \sqrt{r^2 - x_1^2} + x_2, \tag{4.34}$$

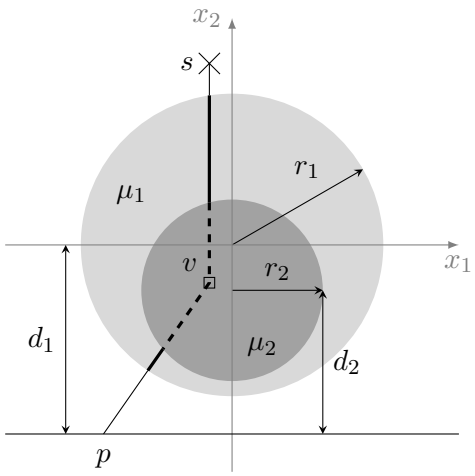

Figure 4.7: Example of a phantom composed of one homogeneous cylinder embedded inside another, and the geometrical parameters used by the equations in the text. L_2 is the length of the heavy dashed line and L_1 is the sum of the lengths of the heavy solid lines. The lighter shaded region has attenuation coefficient μ_1, while the darker shaded region has attenuation coefficient μ_2.

and thus the true and approximated attenuations are given by

$$a(v,p) = \exp\left[\mu L_{\text{pre}}(v)\right] \exp\left[\mu L_{\text{post}}(v,p)\right], \tag{4.35}$$

$$\tilde{a}(v,p) = \exp\left[\mu L_{\text{pre}}(v)\right] \exp\left[\mu \tilde{L}_{\text{post}}(v)\right]. \tag{4.36}$$

The arguments of the exponentials do not contain integrals in this case because the phantom is homogeneous. The relative error introduced by the ZAA can now be calculated by

$$e(p) = \frac{\left|I_s(p) - \tilde{I}_s(p)\right|}{I_s(p)}, \tag{4.37}$$

$$= \frac{\left|\sum_v \left\{[a(v,p)]^{-1} - [\tilde{a}(v,p)]^{-1}\right\} w(v,p)\right|}{\sum_v [a(v,p)]^{-1} w(v,p)}. \tag{4.38}$$

4.2.1.2 Piecewise homogeneous phantom

The analysis is extended now to the case of a piecewise homogeneous phantom that contains a smaller homogeneous cylinder with a different attenuation coefficient inside the cylindrical object (Figure 4.7). In this case the path length L_2 through the interior circle is calculated by substituting r_2 for r in (4.32) and shifting the origin to lie at the centre of the interior circle. For v located in the outer region, L_2 is calculated as

$L_2 = L_{2,\text{pre}} + L_{2,\text{post}}$, where

$$L_{2,\text{pre}} = \begin{cases} 2\sqrt{r_2^2 - x_1^2}, & x_2 < 0 \text{ and } |x_1| < r_2, \\ 0, & \text{otherwise}, \end{cases} \tag{4.39}$$

$$L_{2,\text{post}} = \begin{cases} 2\sqrt{r_2^2 - \widehat{x}_1^2}, & \widehat{x}_2 > 0 \text{ and } |\widehat{x}_1| < r_2, \\ 0, & \text{otherwise}, \end{cases} \tag{4.40}$$

where

$$\widehat{x}_1 = x_1 \cos\theta + x_2 \sin\theta, \tag{4.41}$$

$$\widehat{x}_2 = x_2 \cos\theta - x_1 \sin\theta. \tag{4.42}$$

The path length through the outer region is then

$$L_1 = L - L_2, \tag{4.43}$$

where L is the total path length through the phantom. The attenuation is

$$a(v,p) = \exp\left[\mu_1 L_1(v,p) + \mu_2 L_2(v,p)\right], \tag{4.44}$$

where the inner circle has attenuation coefficient μ_2 and the outer region has attenuation coefficient μ_1. A similar expression gives the approximate attenuation $\tilde{a}(v,p)$.

The grouping of terms into K and $w(v,p)$ is different for the piecewise homogeneous case. The term $\{1 - \exp[-\mu_c(v,\alpha)\Delta x]\}$ must be included in $w(v,p)$ since μ_c is no longer constant across all voxels. Thus the modified expression for the relative error introduced when studying this piecewise homogeneous object is

$$e(p) = \frac{\left|\sum_v \left\{[a(v,p)]^{-1} - [\tilde{a}(v,p)]^{-1}\right\} \widehat{w}(v,p)\right|}{\sum_v [a(v,p)]^{-1} \widehat{w}(v,p)}, \tag{4.45}$$

with

$$\widehat{w}(v,p) = \frac{\mathrm{d}\sigma_c}{\mathrm{d}\Omega}(\theta,\alpha)\, \Omega(p,v) \left\{1 - \exp\left[-\mu_c(v,\alpha)\Delta x\right]\right\}. \tag{4.46}$$

4.2.2 Simulation results

The ZAA error was evaluated in four simulated scenarios. The first two simulated a homogeneous cylinder phantom, one at micro-CT size and one at human CT size. The third and fourth simulations used dual-material phantoms at micro-CT size. All simulations used a grid of 500×500 voxels, a 1 mm detector width, and 150 detector pixels spanning 110% of the phantom diameter. The detector was located 2 cm from the edge of the micro-CT phantoms and 12 cm from the edge of the human sized phantom.

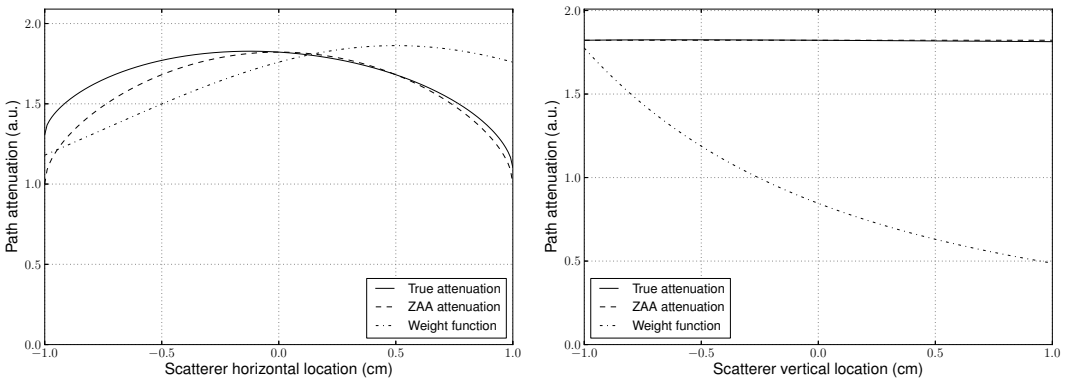

(a) **(b)**

Figure 4.8: True and ZAA attenuation for selected scatterer locations in the 1 cm radius homogeneous phantom, scattering to the detector at $p = 0.5$. (a) is for scatterers lying on the horizontal axis, and (b) is for scatterers lying on the vertical axis. The weighting function $w(v, p)$ for the same (v, p) set is also shown on the same axes.

To analyse the effects of the approximation in a micro-CT setting, the approximation was studied with a homogeneous cylindrical phantom with radius 1 cm as shown in Figure 4.1. To observe the interactions of the terms in (4.38), the quantities $a(v, p)$, $\tilde{a}(v, p)$, and $w(v, p)$ were independently calculated for two sets of v locations. Then the total scatter was calculated according to (4.29) (neglecting K) along with the corresponding error (4.38) for the full range of detector positions.

The individual components are plotted in Figure 4.8 for the values $p = 0.5\,\text{cm}$ and $\mu = 0.3\,\text{cm}^{-1}$. The plots show the variation in the components as the scattering voxel location is varied. For v on the horizontal (x_1) axis, Figure 4.8(a) shows that the attenuation with the ZAA matches the true value reasonably well over an interval where the scatterer horizontal coordinate is close to that of the detector pixel, and tends to underestimate the attenuation outside of this range. The weight function is greatest around the best matching region and is lower in the region with the greatest error. For the scatterer on the vertical (x_2) axis, Figure 4.8(b) shows that the ZAA produces a very good match. Although not evident on the plot, the ZAA slightly underestimates the attenuation near the bottom of the phantom and slightly overestimates it near the top. The weight function is greatest for scatterers nearest to the detector and drops off significantly with increasing distance from the detector.

The total scatter profile at the detector is shown in Figure 4.9(a) as a function of detector position. The ZAA causes a slight overestimation of the scatter intensity, with the error being greatest at the centre of the detector. The relative error is shown in Figure 4.9(b), showing that the maximum error is about 2.3% at the centre of the detector and drops to below 1.5% at the edges.

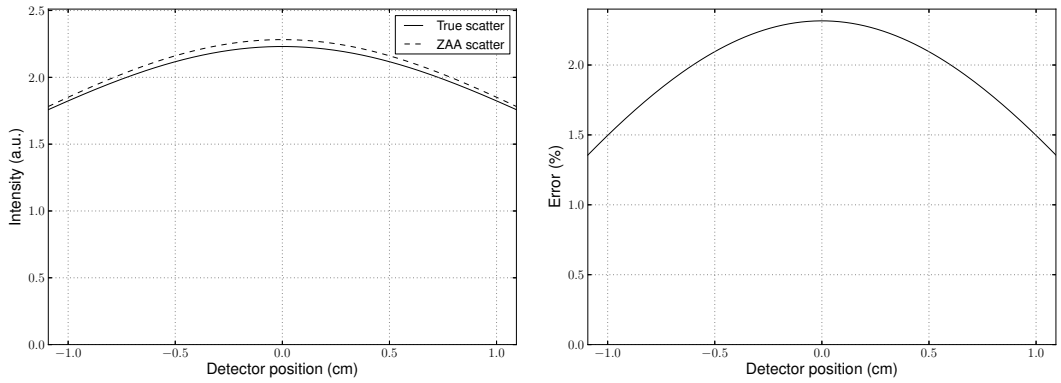

(a) **(b)**

Figure 4.9: Total scatter intensity at the detector for the 1 cm radius homogeneous phantom of Figure 4.1(b). (a) shows the true scatter and the scatter under the ZAA, and (b) shows the relative error introduced by the ZAA.

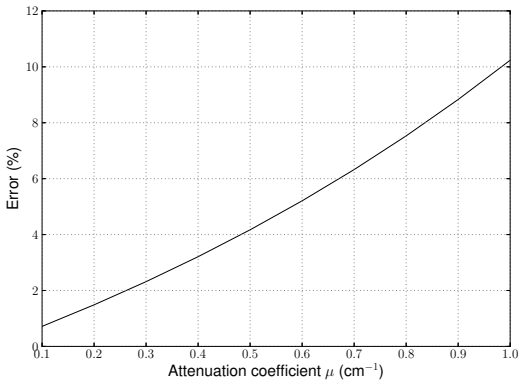

Figure 4.10: Peak relative error caused by the ZAA for the 1 cm radius homogeneous phantom.

Since $a(v,p)$ and $\tilde{a}(v,p)$ depend on μ, the error also varies with attenuation. At a photon energy of 40 keV, the attenuation coefficients of soft tissue and bone are approximately 0.3 cm^{-1} and 1.0 cm^{-1} respectively (Hubbell and Seltzer, 2004). Using the homogeneous phantom with 1 cm radius, the error at the centre of the detector was calculated for μ varying from 0.1 cm^{-1} to 1.0 cm^{-1} and is shown in Figure 4.10 versus μ. The error rises from 1% for $\mu = 0.1\,\text{cm}^{-1}$ to about 10% for $\mu = 1.0\,\text{cm}^{-1}$.

The error in the ZAA increases with the difference in attenuation experienced by the scattered and unscattered photons. The error therefore increases with the size of the object for a fixed attenuation coefficient. To study this effect, the simulation was repeated with the phantom enlarged to a radius of 18 cm, representative of the size of a human abdomen. The attenuation coefficient μ was kept at 0.3 cm^{-1}. Figure 4.11 shows that at this size the approximation ceases to track the actual scatter intensity, overestimating it by up to 1500%. Clearly, therefore, the ZAA is not appropriate for

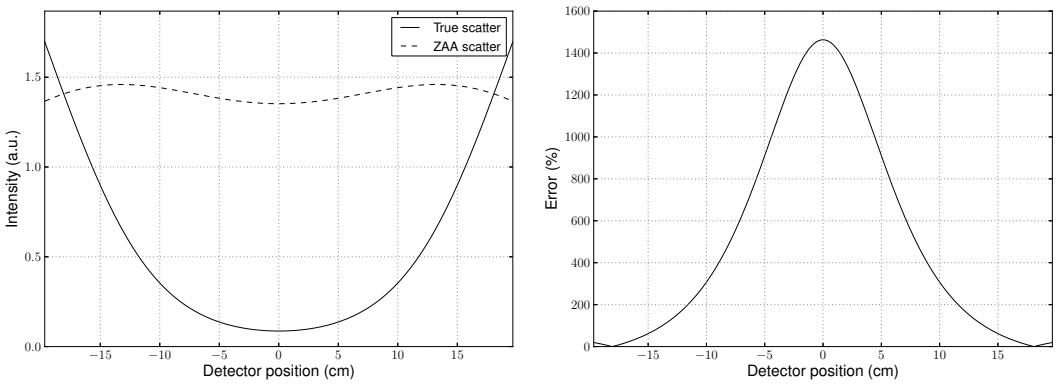

(a) **(b)**

Figure 4.11: Total scatter intensity at the detector for the homogeneous phantom of Figure 4.1(b) of radius 18 cm. (a) shows the true scatter and the scatter under the ZAA, and (b) shows the relative error introduced by the ZAA.

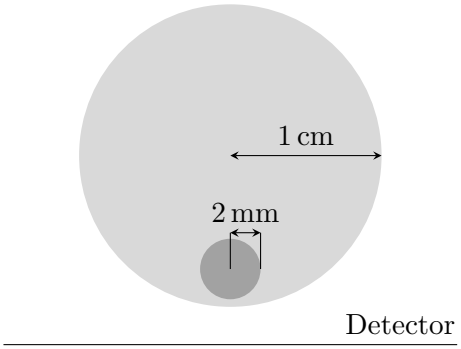

Figure 4.12: The first piecewise homogeneous phantom at micro-CT scale represents the inclusion of a spine in a simple soft tissue phantom. The small, darker, circle near the bottom represents the spinal column, with $\mu = 0.73\,\mathrm{cm}^{-1}$, while the rest of the phantom has $\mu = 0.30\,\mathrm{cm}^{-1}$ to represent soft tissue.

use in human scale scans.

Returning to the micro-CT scale, the effect of two common inhomogeneities in the object, a spine and a skull, were studied. The phantom shown in Figure 4.12 was used to represent a small specimen such as a mouse, with an overall diameter of 2 cm and a spine of diameter 4 mm. The values of μ and μ_c, given in Table 4.2, were obtained from the XCOM program (Berger et al., 2010) using the chemical compositions of liver and vertebral bone given by Schneider et al. (1996). The errors calculated for this phantom are shown in Figure 4.13. The true and approximate scatter as a function of detector position shown in Figure 4.13(a) are similar to those for the homogeneous phantom of the same size (c.f. Figure 4.9(a)). However, Figure 4.13(b) shows that the relative error has increased to a maximum of about 3.2% at the centre of the detector, dropping to 1.5% at the edges. Calculations for view angles with the spine in other locations gave

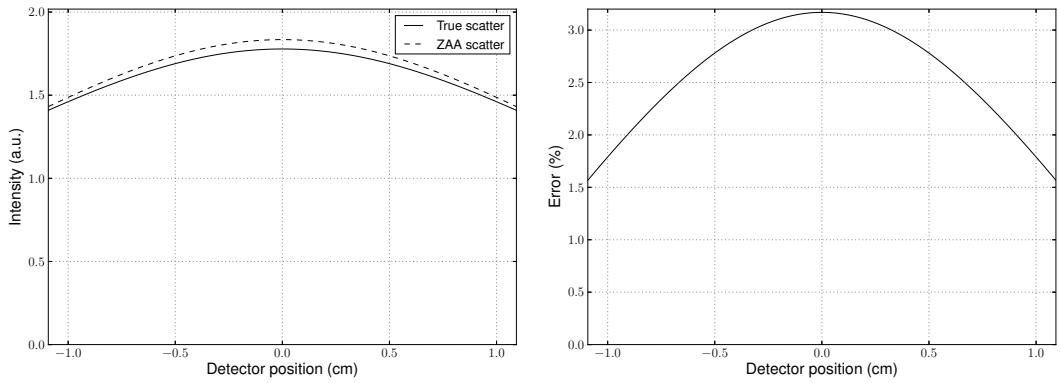

(a) **(b)**

Figure 4.13: Total scatter intensity at the detector for the abdomen phantom of Figure 4.12 with 1 cm radius. (a) shows the true scatter and the scatter under the ZAA, and (b) shows the relative error introduced by the ZAA.

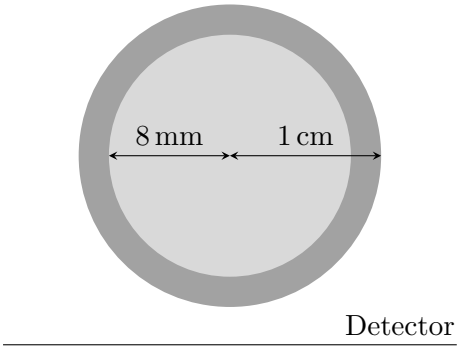

Figure 4.14: The second piecewise homogeneous phantom at micro-CT scale represents a ring of dense tissue around a softer core, for example a cranial scan. The darker region around the edge represents bone, with $\mu = 0.95\,\mathrm{cm}^{-1}$, while the core of the phantom has $\mu = 0.29\,\mathrm{cm}^{-1}$ to represent brain tissue.

peak errors of 2.3% with the spine at the top and 2.1% with the spine at one side (3 or 9 o'clock position).

A second piecewise homogeneous phantom, shown in Figure 4.14, was used to represent a soft core surrounded by a shell of denser material, as is found in a cranium. Values for μ and μ_c, shown in Table 4.2, are taken from the XCOM program using chemical compositions for brain tissue and cranial bone from Schneider et al. (1996). The results in Figure 4.15 are similar to those for the spine phantom (Figure 4.13), with the true and approximated scatter profiles being comparable, and a peak error of about 3.2% in the centre of the detector. In contrast to the spine phantom, the skull has radial symmetry, therefore the error does not change depending on rotation of the object.

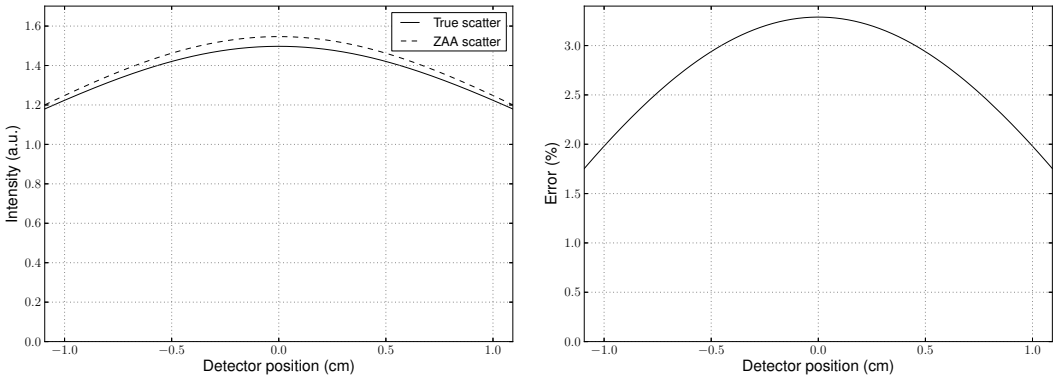

(a) **(b)**

Figure 4.15: Total scatter intensity at the detector for the skull phantom of Figure 4.14 with 1 cm radius. (a) shows the true scatter and the scatter under the ZAA, and (b) shows the relative error introduced by the ZAA.

4.2.3 Discussion

The validity of the zero angle approximation depends on the size and composition of the scanned specimen. For micro-CT sized objects the error introduced by the ZAA is acceptable, with peak error less than 5% for specimens composed primarily of soft tissue. Denser specimens, such as a bone sample, will have greater error, in this study reaching 10%. At human size, the error introduced can be on the order of 1500%, which is clearly unacceptable.

For small objects, there are some scatterer/detector pairings which can result in the approximation introducing significant error, both by under- and over-estimating the photon path length. However, the total scatter intensity reaching any detector pixel is the result of a sum over the whole object, and as such some of the under- and over-estimations cancel out, reducing the error. It is instructive to see in Figure 4.8(a) that the weight function $w(v, p)$ is smallest where the error is largest. This helps to reduce the final error in the weighted sum (4.29). The form taken by the weight function $w(v, p)$ validates the claim of Rinkel et al. (2007) that scatter through small angles constitutes the greatest contribution to the detected scattered radiation.

The results shown here suggest that the ZAA is more reasonable than might be

Table 4.2: Total (μ) and Compton (μ_c) linear attenuation coefficients used for the piecewise homogeneous phantom tissues in Figure 4.12 and Figure 4.14 at 40 keV. Units: cm^{-1}.

Tissue type	Liver	Vertebral bone	Brain	Cranial bone
μ	0.30	0.73	0.29	0.95
μ_c	0.20	0.26	0.20	0.29

anticipated, as long as scanned samples are at the scale of micro-CT, as is the case for Opie et al. (2012) (as presented in Section 4.1). The algorithm reported by Rinkel et al. (2007) is not limited to samples of this size. One explanation for the the validity of their results may be that their approach is to take the analytically derived scatter function and deform it to match the measured results.

The error profiles shown in Figures 4.9(b) and 4.13(b) are simple to model, which offers a possible method for reducing ZAA-induced errors in a micro-CT setting. Scaling scatter estimates by a function based on these profiles could potentially be a suitable heuristic technique for mitigating the errors. This approach would need to be tailored to the specimen being scanned, for example a mouse abdomen scan would use a function based on Figure 4.13(b), while a relatively homogeneous phantom would call for a function based on Figure 4.9(b).

It is worth noting that there is a trade-off between sample size and attenuation. This section has studied biologically relevant attenuations and found that the ZAA is only reasonable up to the micro-CT scale. However, for a material with a very low attenuation, for example in an atmospheric fog, the ZAA could apply with a low error over a relatively large region. Similarly, if a sample were to be composed entirely of a denser substance, the size for which the error is acceptable will be smaller.

4.2.4 Conclusion

The error introduced by the zero angle approximation used by Rinkel et al. (2007) and Opie et al. (2012) is expected not to exceed 5% in most micro-CT situations applied to biological specimens, while in human sized scans the approximation introduces unacceptable error. The simple profile of the error for small specimens suggests that it might be possible to apply a heuristic correction to the scatter levels estimated by an algorithm using the ZAA, by scaling the scatter profile by the analytical error presented here. If this were to be implemented, the scaling profile would need to be made dependent on the object being studied.

Chapter Five

Interior reconstruction algorithm evaluation

Interior tomography refers to the reconstruction of a region of an image where the outer parts of some or all of the projections are not collected, as discussed in Section 1.9. It has become an active research pursuit because of its ability to reduce dose and detector size in pre-clinical and clinical scenarios that require diagnostic images of a region of interest (ROI), for example in cardiac imaging. A narrow ROI can also be useful to avoid saturation of the detector, which can occur when the exposure needed to penetrate the core of an object causes the flux at and beyond the edges of the object to be too high for the detector to handle. By only measuring the flux penetrating the centre of the object, these outer regions with high flux are outside the detector.

Figure 5.1 shows the poor result of reconstructing from truncated projections of the Shepp-Logan phantom with standard FBP (approximately 50% of each projection has been retained). In addition to being unsuited to standard reconstruction techniques, the interior CT problem has been shown to be non-unique (Lewitt and Bates, 1978*a*; Clackdoyle and Defrise, 2010). Consider the scanning geometry depicted in Figure 5.2. Even though line-integral data may be available for all angles for points in region A, that does not allow a unique solution to be found for region A when there exists another disjoint region (B) within the object for which line-integral data is only available over less than the full set of angles. It is therefore necessary to introduce some form of extra prior knowledge to achieve a useful and accurate solution.

Despite the somewhat negative tone of the previous paragraph, a series of recent results have suggested what nature of prior knowledge might enable a unique solution to be found for the interior CT problem. In particular, knowledge of a small part of region A has been shown to enable a solution in principle (Clackdoyle et al., 2004). A key part of the approach has been to re-formulate the inverse Radon transform to the form described in Section 2.5, where the projection data are differentiated before back-projection, then the image so formed is Hilbert transformed along certain lines (Noo et al., 2004). In the final step of the algorithm, an estimate $\hat{\mu}(\boldsymbol{x})$ of the unknown density $\mu(\boldsymbol{x})$ is formed by performing an inverse Hilbert transform of $b_\phi(\boldsymbol{x})$ along lines

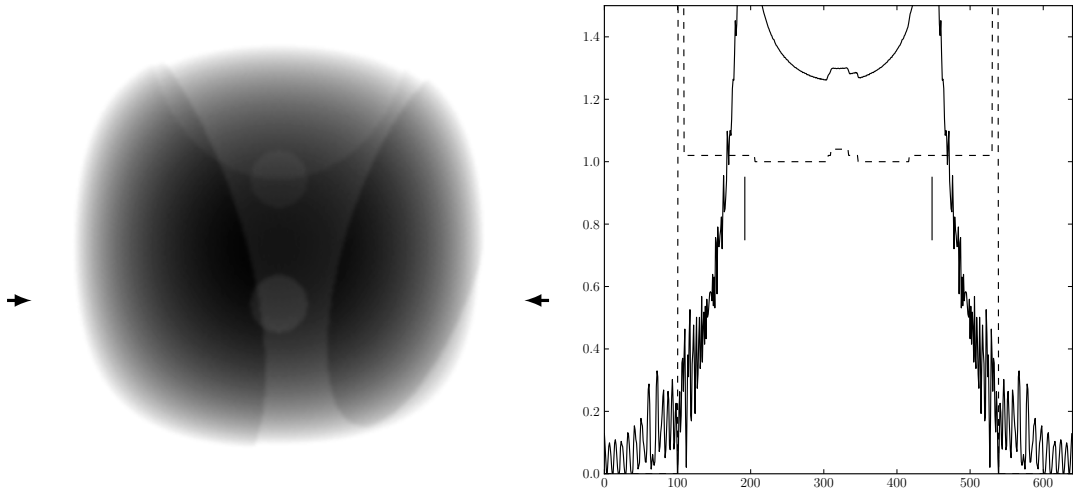

(a) **(b)**

Figure 5.1: FBP reconstruction of truncated projection data of the Shepp-Logan phantom with parallel beam geometry. Reconstruction of the ROI is shown in (a); the profile in (b) is taken between the arrows on (a). The solid line shows the reconstructed image, the dashed line shows the actual image, and the vertical bars indicate the edge of the the ROI. Approximately 50% of each projection has been retained, following the same truncation configuration as later in the chapter.

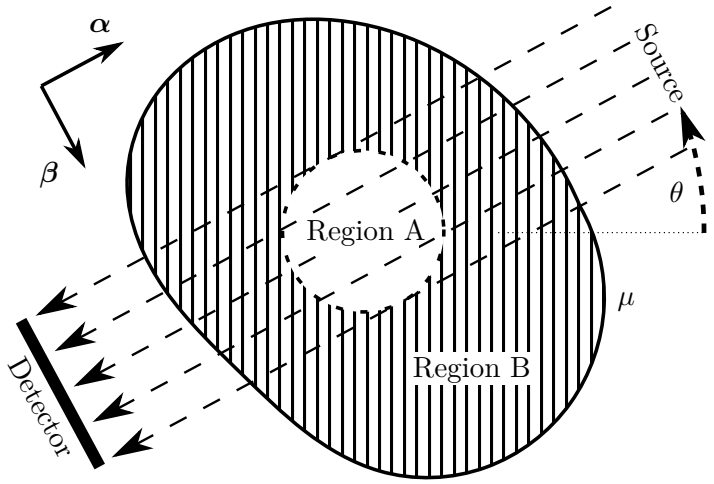

Figure 5.2: Geometry for the scanning operation showing truncated line integral data gathered at angle θ and the corresponding regions A and B within the object.

at angle ϕ (from (2.60)),

$$\hat{\mu}(\boldsymbol{x}) = -\mathcal{H}_{\phi}^{-1}\left\{\frac{b_{\phi}(\boldsymbol{x})}{2\pi}\right\}, \tag{5.1}$$

where $b_{\phi}(\boldsymbol{x})$ is the back-projection of the differentiated projection data (a.k.a. DBP, for differentiated back-projection),

$$b_{\phi}(\boldsymbol{x}) = \int_{\phi}^{\phi+\pi} p'_{\theta}(\boldsymbol{x}\cdot\boldsymbol{\alpha})\,\mathrm{d}\theta, \tag{5.2}$$

where $\boldsymbol{\alpha} = (\cos\theta, \sin\theta)$, and ϕ is selected to align the Hilbert transform lines as required (from (2.53)). For this to work, however, the lines along which the Hilbert transform is applied must not encounter region B (Clackdoyle and Defrise, 2010). In the general interior case, this condition is not satisfied, so an alternative approach must be taken which makes use of some prior knowledge of the region to be reconstructed.

A number of authors have recently reported encouraging results from simulation studies of the differentiated back-projection/Hilbert transform (DBP-HT) reconstruction method described in Section 2.5. These papers have sought to demonstrate that the DBP-HT approach, with prior knowledge of the image in a small region and using projections onto convex sets (POCS) for the Hilbert transform inversion, can lead to an accurate reconstruction (Kudo et al., 2008; Courdurier et al., 2008; Ye et al., 2007; Defrise et al., 2006). In this chapter I revisit aspects of their work and investigate the sensitivity of the reconstructions to various errors in the "known" part of the image, henceforth referred to as the "truth". Specifically, I investigate the sensitivity of the algorithm to errors in the mean of the truth, to noise on the truth, and to the case where only the mean density of the truth is known.

5.1 The DBP-POCS algorithm

The reconstruction algorithm used in this chapter is the DBP-POCS algorithm described by Kudo et al. (2008), which is a modified version of the algorithm described by Defrise et al. (2006) and uses the DBP-HT algorithm of Section 2.5. The core steps of the method are:

- Select the Hilbert lines. Lines should be chosen such that all lines intersect the region of known density.
- Calculate the truncated Hilbert transforms. The Hilbert transform within region A of the chosen lines can be calculated according to (5.2).
- Invert the truncated Hilbert transforms. The truncated Hilbert transform on each of the lines chosen in the first step can be inverted using the POCS method.

Within the algorithm, the Hilbert lines are reconstructed independently, so the following description outlines the approach taken for a single line $\mu(t)$ of the image $\mu(\boldsymbol{x})$. The POCS method aims to find $\hat{\mu}(t)$ which belongs to the intersection of the following five convex sets:

$$\begin{aligned}
C_1 &= \left\{ \hat{\mu}(t) \in L^2(\mathbb{R}) \,\middle|\, \mathcal{H}\hat{\mu}(t) = b(t) \;\text{ for } t \in \Lambda_H \right\} \\
C_2 &= \left\{ \hat{\mu}(t) \in L^2(\mathbb{R}) \,\middle|\, \hat{\mu}(t) = 0 \;\text{ for } t \notin \Lambda \right\} \\
C_3 &= \left\{ \hat{\mu}(t) \in L^2(\mathbb{R}) \,\middle|\, \hat{\mu}(t) = \mu_K(t) \;\text{ for } t \in \Lambda_K \right\} \\
C_4 &= \left\{ \hat{\mu}(t) \in L^2(\mathbb{R}) \,\middle|\, \int_\Lambda \hat{\mu}(t)\,\mathrm{d}t = p_\Lambda \right\} \\
C_5 &= \left\{ \hat{\mu}(t) \in L^2(\mathbb{R}) \,\middle|\, \hat{\mu}(t) \geq 0 \;\text{ for } t \in \mathbb{R} \right\},
\end{aligned} \tag{5.3}$$

where Λ_H, Λ, and Λ_K denote the supports of the truncated Hilbert transform, the full object, and the known region respectively, following the notation of Kudo et al. (2008). $\mathcal{H}$ denotes the Hilbert transformer operator, $\mu_K(t)$ the image value in the known region, and $b(t)$ the value of $b_\phi(\boldsymbol{x})$ from (5.2) on the line. The quantity p_Λ is the measured value of the projection along the line.

In each iteration of the algorithm, the current estimate $\hat{\mu}^{(i)}(t)$ is projected onto each of the above sets, as

$$\hat{\mu}^{(i+1)} = P_5 P_4 P_3 P_2 P_1 \hat{\mu}^{(i)}(t), \tag{5.4}$$

where the initial estimate $\hat{\mu}^{(0)}(t)$ is zero, and P_n is the operator for projecting onto set C_n. The operator P_1 is defined by

$$P_1\hat{\mu}(t) = \mathcal{H}^{-1} M \mathcal{H} \hat{\mu}(t), \tag{5.5}$$

$$Mh(t) = \begin{cases} b(t), & t \in \Lambda_H, \\ h(t), & t \notin \Lambda_H, \end{cases} \tag{5.6}$$

where the Hilbert transformer $\mathcal{H}$ and its inverse $\mathcal{H}^{-1}$ are defined in (2.39) and (2.40) respectively. The M operator can be understood as simply forcing the Hilbert transform of $\hat{\mu}(t)$ to be equal to the function $b(t)$ calculated with (5.2) within the region where that function is valid. Operators P_2 and P_3 are defined as

$$P_2\hat{\mu}(t) = \begin{cases} \hat{\mu}(t), & t \in \Lambda, \\ 0, & t \notin \Lambda, \end{cases} \tag{5.7}$$

$$P_3\hat{\mu}(t) = \begin{cases} \mu_K(t), & t \in \Lambda_K, \\ \hat{\mu}(t), & t \notin \Lambda_K, \end{cases} \tag{5.8}$$

which enforce a support constraint and set the density in the known region equal to the known values, respectively. The definition of P_4 is

$$P_4\hat{\mu}(t) = \begin{cases} \hat{\mu}(t) + \dfrac{p_\Lambda - \int_\Lambda \hat{\mu}(t')\,\mathrm{d}t'}{\int_\Lambda \mathrm{d}t'}, & t \in \Lambda \setminus \Lambda_K, \\ \hat{\mu}(t), & t \notin \Lambda \setminus \Lambda_K, \end{cases} \tag{5.9}$$

which forces the integrals of the Hilbert lines to match the measured projection data. Finally, P_5 is defined as

$$P_5\hat{\mu}(t) = \begin{cases} \hat{\mu}(t), & \hat{\mu}(t) \geq 0, \\ 0, & \hat{\mu}(t) < 0, \end{cases} \tag{5.10}$$

which enforces a positivity constraint since the solution is an attenuation coefficient image, and thus always non-negative. The definitions of P_1 and P_4 above are given by Kudo et al. (2008). POCS is guaranteed to converge to the intersection of these sets (Bauschke and Borwein, 1993), but there is no guarantee on the speed of convergence.

The convexity of C_2 to C_5 is easily shown, but that of C_1 is less obvious and thus briefly demonstrated here. A set is convex if all points on the line between any two members of the set is also in the set itself, i.e.,

$$p_3 \in C, \tag{5.11}$$

$$p_3 = \alpha p_1 + (1-\alpha)p_2, \qquad \alpha \in [0,1], \tag{5.12}$$

for any $p_1, p_2 \in C$. Here, a "point" is a line $\hat{\mu}(t)$, and the set C is those lines $\hat{\mu}(t)$ where

$$\mathcal{H}\hat{\mu}(t) = b(t), \qquad \text{for } t \in \Lambda_H. \tag{5.13}$$

If $f(x)$ and $g(x)$ are two members of C, then C is convex if $e(x) = \alpha f(x) + (1-\alpha)g(x)$ also satisfies (5.13). Using the definition of $\mathcal{H}$ in Section 2.5.1,

$$\mathcal{H}e(y) = \frac{1}{\pi} PV \int_{-\infty}^{\infty} \frac{e(x)}{x-y}\,\mathrm{d}x, \tag{5.14}$$

$$= \frac{1}{\pi} PV \int_{-\infty}^{\infty} \frac{\alpha f(x) + (1-\alpha)g(x)}{x-y}\,\mathrm{d}x, \tag{5.15}$$

$$= \alpha \frac{1}{\pi} PV \int_{-\infty}^{\infty} \frac{f(x)}{x-y}\,\mathrm{d}x + (1-\alpha)\frac{1}{\pi} PV \int_{-\infty}^{\infty} \frac{g(x)}{x-y}\,\mathrm{d}x, \tag{5.16}$$

$$= \alpha\mathcal{H}f(y) + (1-\alpha)\mathcal{H}g(y), \tag{5.17}$$

$$= \alpha b(y) + (1-\alpha)b(y), \qquad \text{for } t \in \Lambda_H, \tag{5.18}$$

$$= b(y), \qquad \text{for } t \in \Lambda_H, \tag{5.19}$$

so $e(y)$ belongs to C and therefore C is convex.

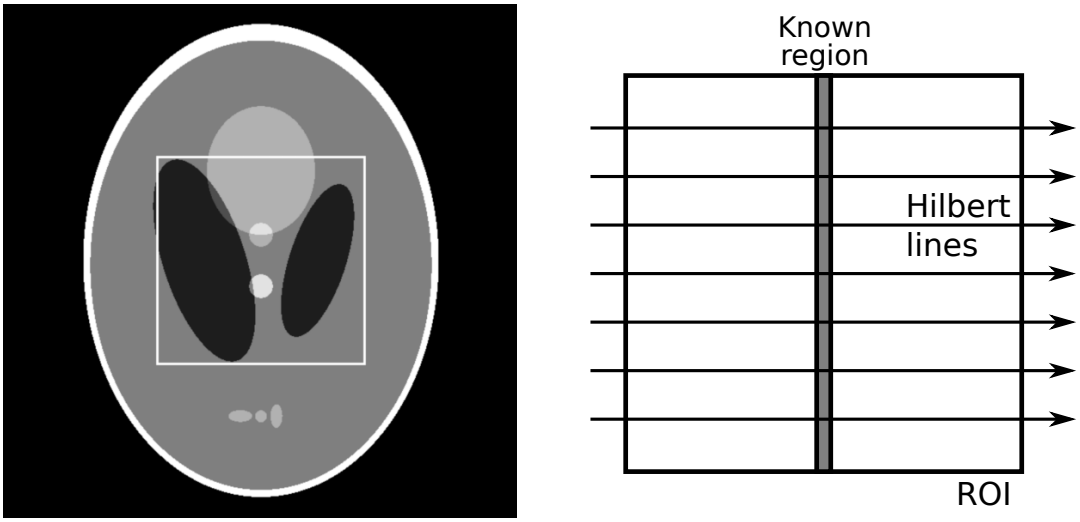

(a) (b)

Figure 5.3: The phantom and the region of interest. (a) shows the Shepp-Logan phantom with the square region of interest overlaid in white. The greyscale range is [0.994,1.046]. (b) shows the configuration of the region of interest.

5.2 Results

Simulated data were used to test the reconstruction algorithm. The data were obtained by simulating parallel beam projections at 1200 angles on $[0,\pi)$, with detector pixel width equal to the width of the image voxels. The standard Shepp-Logan phantom (Shepp and Logan, 1974) shown in Figure 5.3(a) was used, sampled such that the region of interest (ROI) was of dimension 256×256 voxels and the full image size was 640×640 voxels.

A truncated data set was created by removing projection data corresponding to rays that did not pass through the ROI. As illustrated in Figure 5.3(b), the known region was a narrow strip down the centre of the ROI, twelve voxels wide. Each reconstruction used 500 iterations of the POCS method. This configuration was selected to follow Kudo et al. (2008) and to allow the Hilbert lines to be chosen to be simply the horizontal lines of the image. For the same reasons, the region of interest was chosen to be a square, rather than the more realistic shape of a circle, and an ellipse 20% larger than the true boundary was used as the support Λ for the reconstruction. The algorithm was exercised with perfect truth data, then with three different forms of error in the *a priori* data to evaluate its sensitivity to each. A single trial was also performed using a different known region.

Using error-free data in the known region produces a good reconstruction as seen in Figure 5.4(a). The plot in Figure 5.4(b) is a profile of the reconstruction along the line

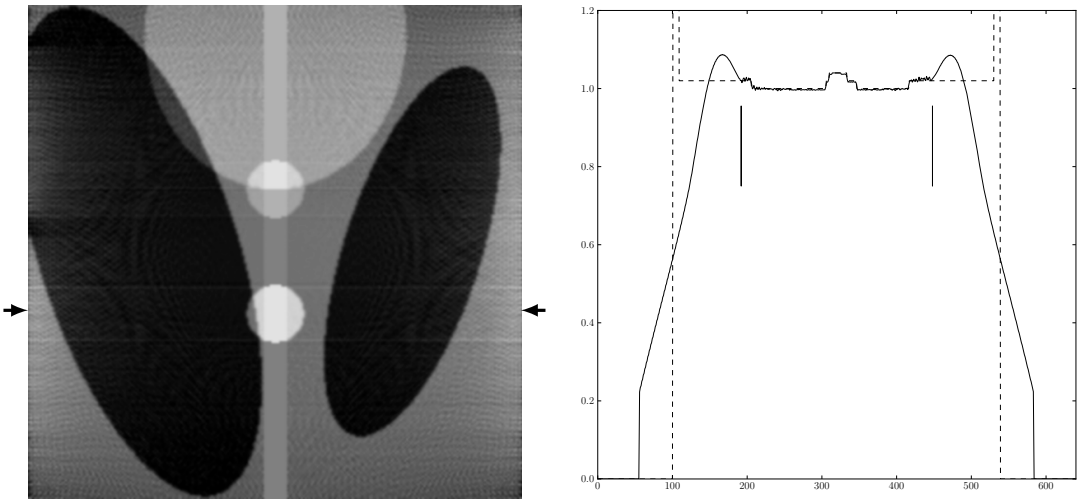

(a) **(b)**

Figure 5.4: ROI reconstructed with no error in the *a priori* data. The ROI image is shown in (a), with arrows indicating the source of the profile plot in (b). The greyscale range is [0.994, 1.046]. (b) shows profiles of the reconstruction (solid) and of the original image (dashed). The solid vertical bars in (b) indicate the extent of the ROI.

between the arrows shown on Figure 5.4(a) and shows the accuracy of the reconstruction within the ROI, denoted in Figure 5.4(b) by the vertical bars.

Three trials were performed with a constant added to the truth, specifically $+0.1$, -0.1, and $+0.04$, which constitute approximately $\pm 10\%$ and 4% error in the mean. Figure 5.5 shows that a constant error of -0.1 in the known region causes the reconstruction to suffer from negative cupping along the Hilbert lines. Also present, more obvious in the profile than in the image, is a negative constant error on the whole ROI. When the known region has a constant $+0.1$ error the reconstruction has similar but opposite artefacts: positive cupping on the Hilbert lines and a positive constant error on the whole ROI (Figure 5.6). Figure 5.7 shows the reconstruction obtained when the known data has a smaller constant error. The positive cupping and positive constant offset can be seen clearly.

The presence of noise in the known data was the next form of error trialled. The noise added was Gaussian with standard deviation 0.02, which is of the same order as the features in the ROI. Figure 5.8 shows that the reconstruction contains considerably more noise than the results of the other trials. However, it does not suffer from any significant cupping or constant shifts.

Kudo et al. (2008) suggest that good reconstruction may be achievable with knowledge of only the mean density on some region. They present an example of a reconstruction obtained with the mean over the known region substituted for the true data, which appears to work well. However, the region they used for this was relatively featureless,

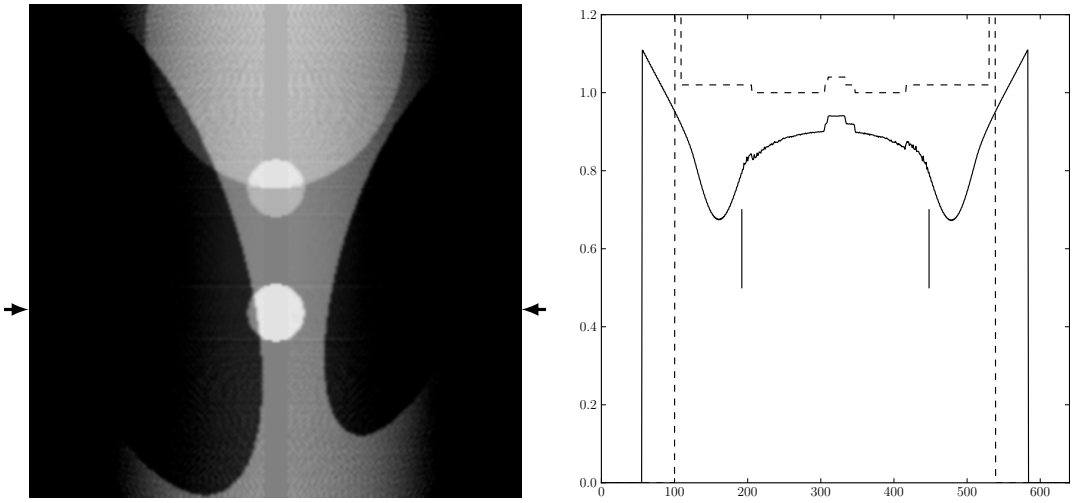

(a) **(b)**

Figure 5.5: Result due to a constant offset error of -0.1 in the known region. The greyscale range in (a) is [0.894, 0.946] and the profile in (b) is from between the arrows on (a).

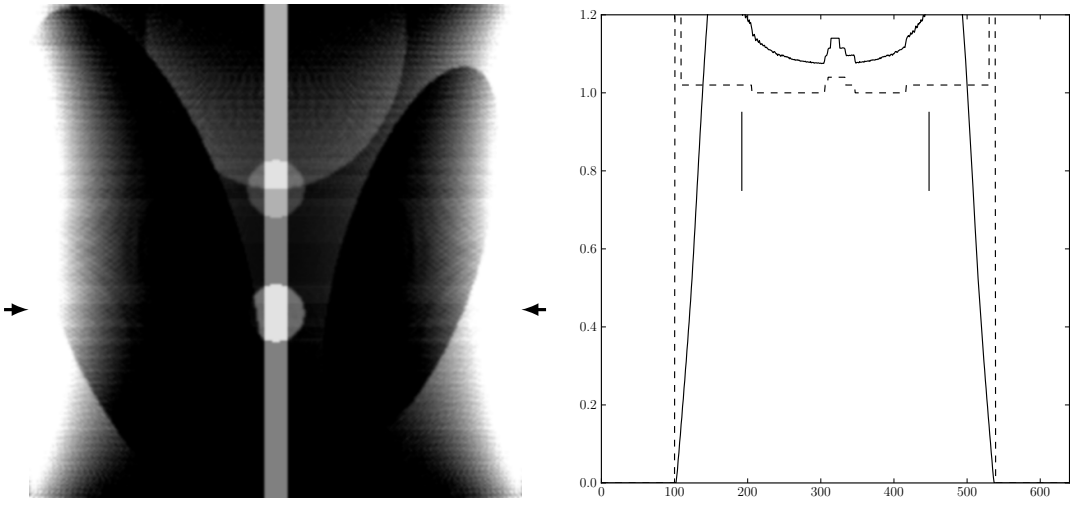

(a) **(b)**

Figure 5.6: Result due to a constant offset error of $+0.1$ in the known region. The greyscale range in (a) is [1.094, 1.146] and the profile in (b) is from between the arrows on (a).

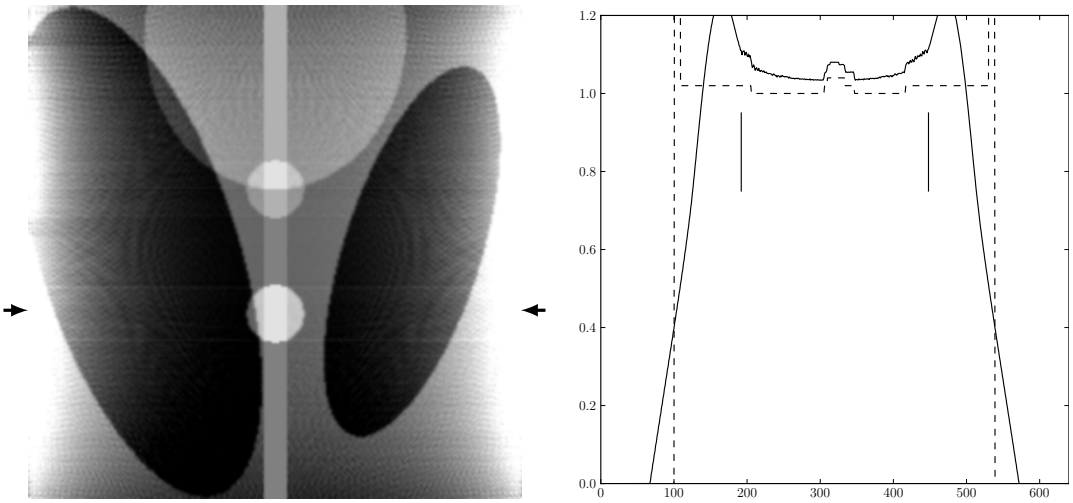

(a) **(b)**

Figure 5.7: Result due to a constant offset error of +0.04 in the known region. The greyscale range in (a) is [1.034, 1.086] and the profile in (b) is from between the arrows on (a).

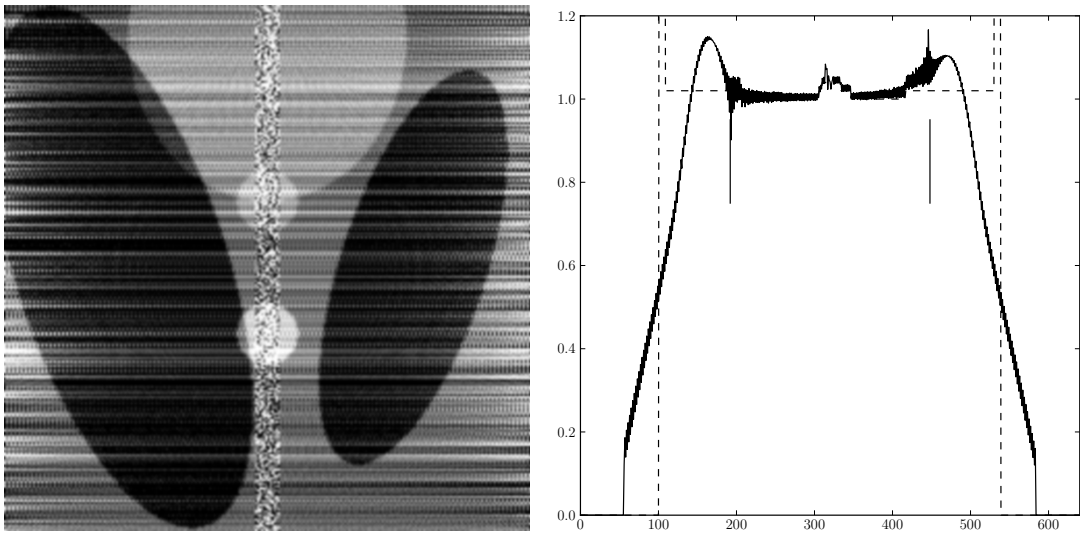

(a) **(b)**

Figure 5.8: Result when noise is present in the known region. The greyscale range in (a) is [0.994, 1.046] and the profile in (b) is from between the arrows on (a).

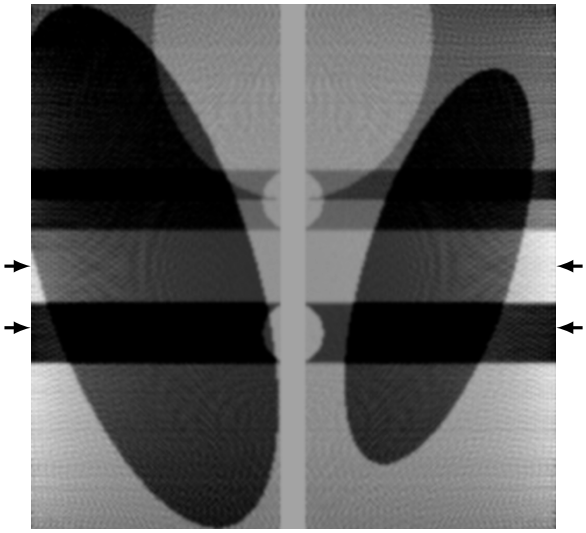

(a)

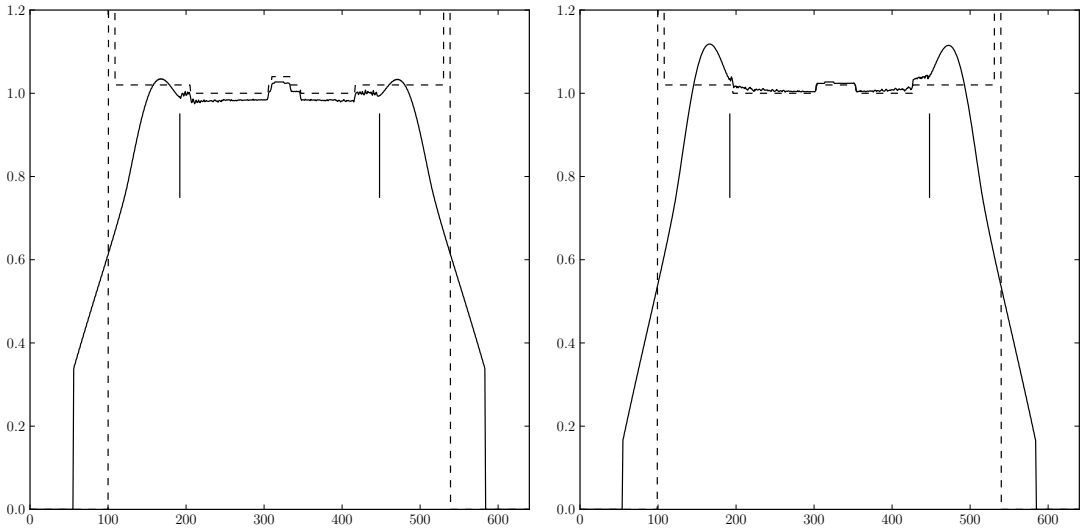

(b) **(c)**

Figure 5.9: The truth value is taken as the mean over the known region. Greyscale range in (a) is [0.994, 1.046], the profiles in (b) and (c) are from between the lower and upper arrows, respectively.

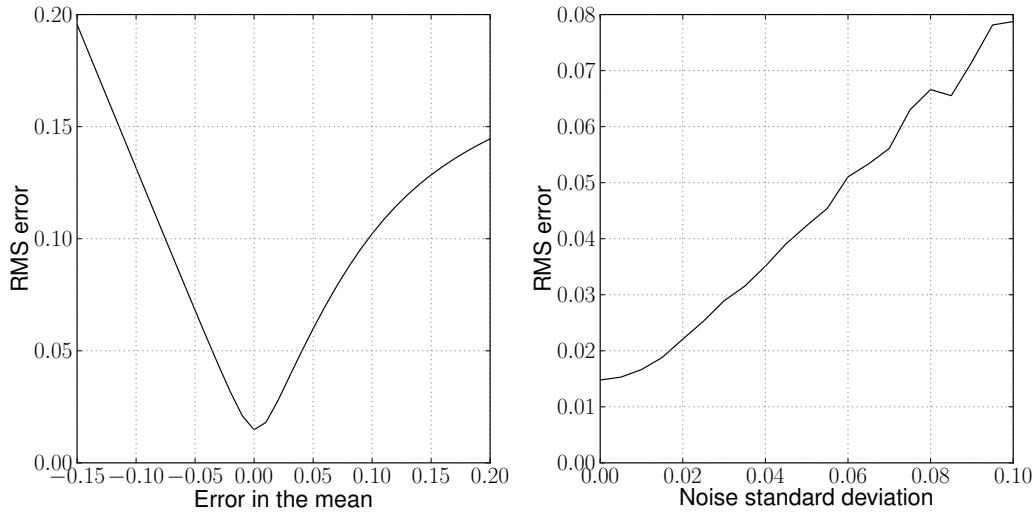

Figure 5.10: RMS error introduced into the ROI by two forms of corruption in the *a priori* data: (a) shows the effect of error in the mean of the truth (samples shown in Figures 5.5 to 5.7), and (b) shows the effect of Gaussian noise in the truth (see Figure 5.8).

and so the mean would not have been very different from the actual truth. Figure 5.9 illustrates the outcome when the mean of the known region is used as the truth when that region contains features. Clearly, attempting to use a mean value when the "known" region contains features does not produce a good quality image.

The overall sensitivity to the two main types of error used above is shown in Figure 5.10. Figure 5.10(a) shows that the algorithm is sensitive to errors in the mean, and that more error is introduced when the known data is too low than when it is too high. In both cases the RMS error introduced appears to be similar to the absolute mean error. Figure 5.10(b) shows that the RMS error increases approximately linearly with the standard deviation of the noise on the known region. The error introduced appears to be similar to the noise standard deviation. Both plots show that there is a small amount of error even with exact knowledge of the image in the known region.

In addition to studying the effect of error in the known region, the algorithm was tested once with a different known region, this time at the left-hand edge of the ROI (Figure 5.11(a)). No noise or mean error was added to the truth. Kudo et al. (2008) demonstrate good results with this configuration, but Figure 5.11 shows that the reconstruction is severely degraded by this change in configuration.

5.3 Discussion

The DBP-POCS algorithm was tested with different errors present in the *a priori* data. The effect of error in the mean of the data is to alter the mean of the reconstructed

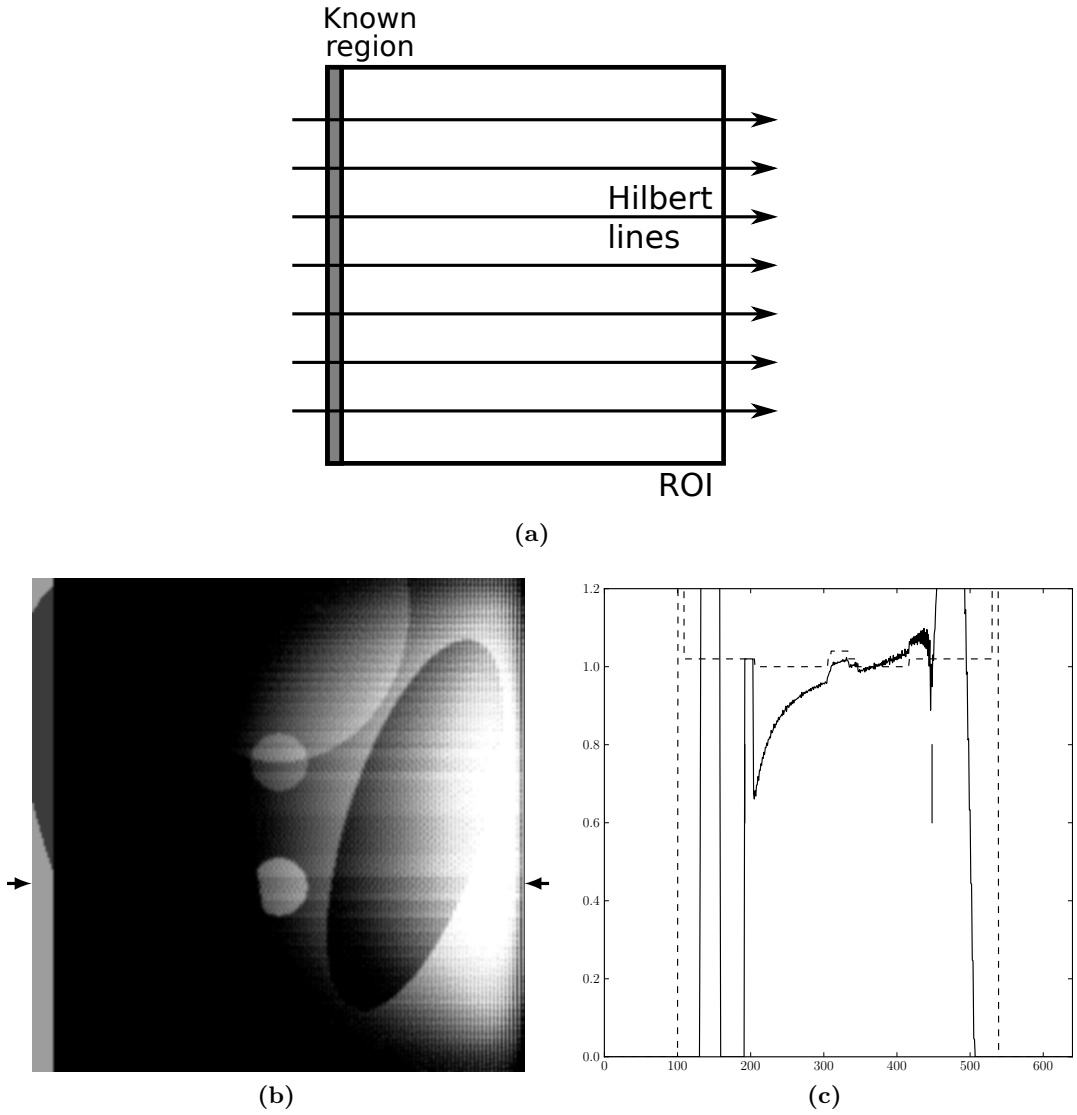

Figure 5.11: Result of the known region being located on the left-hand side of the RHS instead of in the centre. (a) illustrates the new ROI configuration, the greyscale range in (b) is [0.988, 1.040], and the profile in (c) is between the arrows on (b).

density as well as to introduce cupping artefacts. The effect of noise on the data is to spread noise across the resulting reconstruction, as seen in Figure 5.8.

Errors in the mean cause considerable harm to the reconstruction, as seen in Figures 5.5 to 5.7. This is because the main function of the known region in the algorithm is to regularise the low frequencies of the reconstructed image. The features in the image are already reasonably well described by the Hilbert transform lines (obtained via DBP), so the details of the image in the known region is of less importance than its mean value. As long as the truth used in the algorithm has approximately the correct mean on each of the Hilbert lines, the algorithm should produce a good estimate of the original object. Figure 5.10(a) shows that the error introduced increases more sharply when the mean is underestimated than it does for an overestimated mean. This suggests that the method used to obtain the estimate of the truth should be biased slightly toward producing a higher mean.

The 10% offset error assumed in generating Figures 5.5 and 5.6 is relatively large. In practice any scanning process used to obtain an estimate for the truth needs to be able to distinguish the features in the image. Since the features in this image are of the order of 4%, it is reasonable to expect the scanning process to have an accuracy better than 4% and thus obtaining a truth estimate with less than 10% error should be possible. The same observation applies to noise: the noise introduced in the measurement of the known region ought to be less than the extent of the features in the image.

Figure 5.9 suggests that knowing only the mean density across a region is insufficient to produce a good reconstruction. If the approximate mean density is known across a relatively homogeneous region, the liver for example, the prior knowledge may still be sufficient. If, however, the mean density across a heavily featured region is known, the results indicate that this is insufficient to achieve a useful reconstruction with the DBP-POCS algorithm.

The poor quality reconstruction in Figure 5.11 does not follow the results of Kudo et al. (2008). The algorithm in that paper has been faithfully implemented as described, which suggests some details of the original implementation are omitted from the paper. Attempts to communicate with the authors have been unsuccessful, thus further study of the algorithm is warranted to identify the omitted details. The results presented here should be revisited if the algorithm can be improved such that the original results are reproducible.

In contrast to the DBP-POCS algorithm studied here, Chapter 6 demonstrates two interior reconstruction algorithms that are not only stable within the interior FOV but also beyond it. These algorithms do use a different, and greater, set of data than DBP-POCS, so a direct comparison is not fair, but the results here do provide motivation to find a better technique for interior reconstruction.

5.4 Conclusion

The interior reconstruction method examined in this chapter appears to be sensitive to both errors in the mean of the prior knowledge and noise in the prior knowledge. Therefore, to obtain reliable reconstructions on an interior region of interest from truncated line integral data using this method, one must ensure that the density data applied as prior knowledge have a reliable mean and limited noise. Identification of the difference between this implementation and the original is desirable, and the conclusions drawn from these results may be altered if such a difference is found.

Chapter Six

Hybrid spectral interior architecture

This chapter is devoted to the development and study of a hybrid spectral interior scanner architecture. The scanner design was proposed by Xu et al. (2012) and built by James Bennett at Virginia Tech[(1)] (VT), USA. James is a Biomedical Engineering PhD candidate at VT, and he and I worked closely together to perform scans and analyse the data produced. The first part of this chapter covers the design, implementation, and validation of the hybrid architecture. The second part presents an analysis of the efficacy of three techniques for reduction of radiation exposure.

The results are based on studies with two physical contrast agent phantoms, shown in Figures 6.4 and 6.10, which are referred to as Phantom A and Phantom B respectively. Phantom A is used for the study in Section 6.1, while Phantom B is used for the study in Section 6.2; the details for each phantom are provided in their respective sections.

6.1 Design, implementation, and validation

The benefits of spectral imaging are outlined in Section 1.8. However, the use of current spectral x-ray detectors has several critical limitations, primarily cost, size, radiation dose, and flux. Current spectral detectors are both small and expensive. Radiation dose is a concern for any x-ray based system, and energy bins for each spectral channel require a higher total exposure relative to an energy-integrating (conventional) detector to maintain image quality. Furthermore, the maximum x-ray flux detectable by photon counting detectors is limited by the speed of the electronics and by pulse pile-up, and current technology is too slow for clinical use by an estimated three orders of magnitude (Taguchi et al., 2009).

To overcome these limitations, Xu et al. (2012) proposed to combine a spectral imaging chain with a conventional imaging chain, as illustrated in Figure 6.1. The latter provides wide-beam ("global") greyscale projections of the object, while the former provides narrow-beam (interior) spectral projections covering a small field of view (FOV). Furthermore, Xu et al. (2012) proposed a reconstruction method whereby the

[(1)] In full, Virginia Polytechnic Institute and State University.

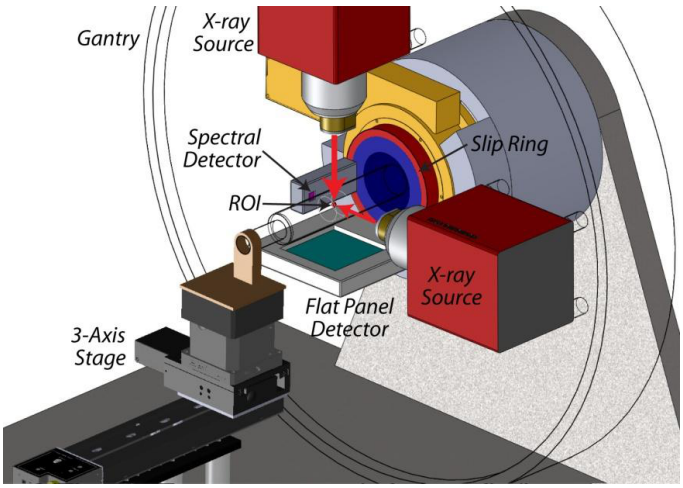

Figure 6.1: Artist's rendering of the hybrid spectral interior architecture as proposed by Xu et al. (2012).
(From Xu et al. (2012)).

greyscale image from the global imaging chain is reconstructed by statistical iterative reconstruction with total variation minimisation (SIR-TV), and the interior image for each energy bin is reconstructed by a compressed sensing-based statistical interior tomography (CS-SIT) method (Xu et al., 2011; Yu and Wang, 2009). The spectral images are processed with principal component analysis (PCA) and the results are colour mapped together with the global reconstruction to produce high resolution hybrid spectral images.

There are several merits to this approach. First, the radiation dose is lower for a hybrid architecture than for a full FOV spectral micro-CT/CT scanner, as only the interior ROI receives the higher exposure necessary for equivalent spectral contrast resolution. Second, spectral flux can be increased because the x-ray beam is restricted to the paths traversing the core of the object, avoiding pulse pile-up that would occur at the object periphery with a full FOV spectral detector (Schmidt and Pektas, 2011). Third, the hybrid architecture maintains a conventional energy-integrating imaging chain, which is important for obtaining "scout" views to locate and centre the interior ROI prior to a full scan. Fourth, the global imaging chain provides necessary prior information about the interior ROI for exact interior spectral reconstruction. Fifth, the system cost would be lower than the cost of a full FOV spectral detector because energy-integrating detectors are vastly more mature and less expensive than spectral detectors. Finally, the most obvious and important benefit of a hybrid architecture is that it brings spectral CT closer to wide-spread use in the near-term.

In the following study, a first-of-its-kind hybrid spectral micro-CT prototype system is implemented. There are three goals for this study: firstly, to demonstrate the hybrid spectral micro-CT architecture with a prototype system implementation, phantom scan and reconstruction; secondly, to numerically simulate the hybrid prototype phantom

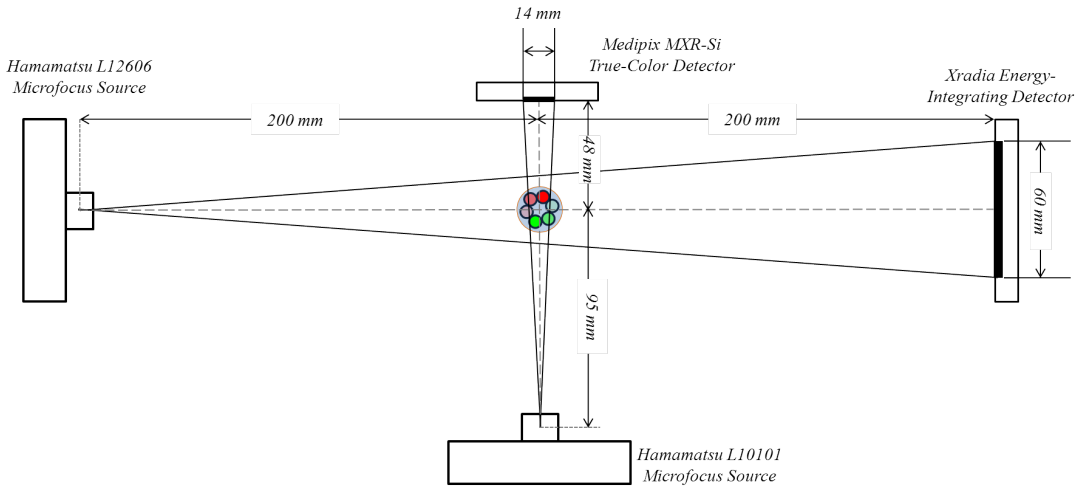

Figure 6.2: Hybrid spectral micro-CT design schematic.

scan; and finally, to validate the prototype system by comparing the prototype results to those of the matching simulation. Section 6.1.1 describes the hybrid scanner design and configuration, Section 6.1.2 describes the operation of the system simulation, Section 6.1.3 contains a description of Phantom A and an explanation of the data collection and processing methods used in the study, Section 6.1.4 presents the results from the first hybrid spectral micro-CT system and simulation studies, Section 6.1.5 discusses the results and their interpretation, and Section 6.1.6 summarises the findings of the study.

6.1.1 Hybrid scanner design

The hybrid architecture proposed by Xu et al. (2012) incorporates spectral interior and conventional global imaging chains into a rotating gantry configuration. The benefit of a rotating gantry design, compared to a rotating sample stage, for biomedical researchers is that it allows *in vivo* scans (e.g., of small rodents) to be performed. However, a rotating gantry configuration requires specialised mechanical components, such as a rotation slip ring, and many parts must be custom manufactured. Furthermore, it is more difficult to make alignment and configuration (e.g., source-to-detector positions, etc.) changes with a rotating gantry design. Thus, a rotating sample configuration was instead chosen for the first prototype of this hybrid architecture. While a rotating sample design may only be useful for micro-CT, it still has significant biomedical applications and the resulting data should support further development of a rotating gantry system for *in vivo* application.

The design for the first prototype of a hybrid spectral micro-CT has undergone several revisions to reach its final form. The original design required building both the global and spectral imaging chains from scratch, along with a new sample rotation

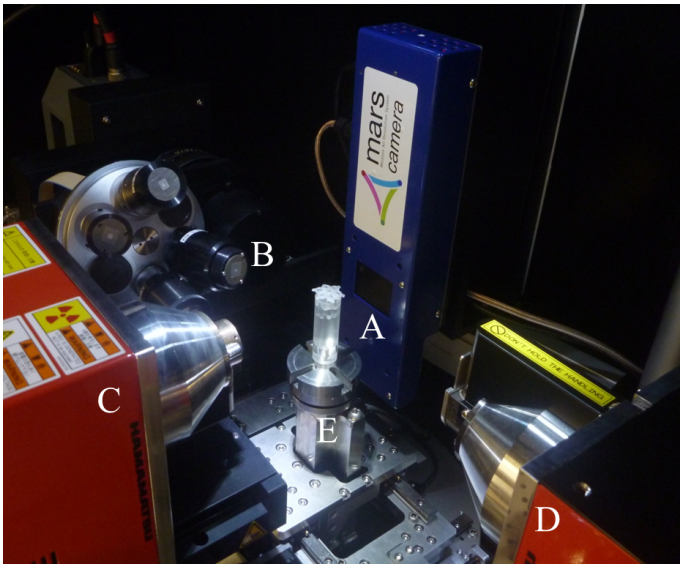

Figure 6.3: Hybrid spectral micro-CT prototype system. Hardware component labels: (A) Medipix MXR-Si detector; (B) Xradia conventional detector; (C) Hamamatsu L10101 X-ray source for spectral imaging chain; (D) Hamamatsu L12606 X-ray source for Xradia global imaging chain; (E) Xradia sample rotation stage with contrast agent phantom A.

Table 6.1: Hybrid spectral micro-CT hardware component specifications.

		Global imaging chain	Spectral imaging chain
X-ray source	Tube voltage	80 kVp	80 kVp
	Tube current	100 µA	200 µA
	Output window	100 µm Be	150 µm Be
	Focal spot size	15 µm	7 µm
	Distance to centre of rotation	200 mm	95 mm
X-ray detector	Number of pixels	512	256
	Pixel size	109.2 µm	55 µm
	FOV diameter	30 mm	9.3 mm
	Distance to centre of rotation	200 mm	48 mm
	Detector type	Scintillator + CCD camera	Medipix2 (MXR), 300 µm silicon layer

system. After completing the preliminary system build, it was realised that the spectral imaging chain could be reconfigured to fit within an existing Xradia XCT micro-CT scanner (Xradia, Pleasanton, CA). There are several advantages to this approach: the Xradia micro-CT is an existing, well-known, and tested scanner with a very high precision rotating sample stage; the Xradia greyscale detector has high resolution and a large FOV (up to approximately 40 mm at the object) with existing control hardware and software integration; and use of the Xradia micro-CT eliminated the need to build and test two of the three major components required by the original hybrid spectral micro-CT design.

The global imaging chain relies on the native Xradia hardware: a Hamamatsu L12606 (Hamamatsu, Japan) micro-focus x-ray source and 6 cm scintillator with a high resolution CCD camera. The Xradia source and detector positions are controlled by proprietary Xradia software and hardware. The spectral imaging chain consists of a Hamamatsu L10101 micro-focus x-ray source and a MARS x-ray camera with a silicon layer on a Medipix MXR detector. The L10101 source is mounted on a linear translation stage, while the Medipix detector is mounted in a permanent position after alignment. The sample rotation stage consists entirely of the Xradia hardware, which allows for sub-micron position accuracy in three linear dimensions plus rotation. The hardware component details are outlined in Table 6.2, a design schematic is shown in Figure 6.2, and a photo of the prototype system is shown in Figure 6.3.

6.1.2 Simulation

The prototype hybrid system was validated by comparing its results to those of a matching simulation. Within the simulation, the energy spectrum of a source with a tungsten anode is generated with Spektr (Siewerdsen et al., 2004), the material-dependent linear attenuation coefficients of the phantom are calculated as functions of incident photon energy using NIST tables (Hubbell and Seltzer, 2004), and the efficiency of the spectral detector is calculated according to Redus (2002). The phantom is specified as a set of ellipses. The energy spectrum, from 10 keV[(2)] to the x-ray tube voltage, is discretised into 1 keV steps and the numbers of flatfield and transmitted photons at each energy is computed. Energy bins in Medipix detectors accumulate a count of all photons with energies above the respective bin threshold (recall Section 3.1), so the outputs of the simulation of the spectral imaging chain are sums of photons at all energies above each of the bin energies. The same procedure is used for the global imaging chain, except that the output is the sum of photons at all energies above 10 keV and the detector efficiency is assumed to be uniform across the spectrum. The operation of the simulation is summarised in Algorithm 1. Parameters were chosen to match the prototype system scan, including source spectrum and flux, source-to-object distance,

[(2)] The source spectrum calculated by Spektr goes to zero below 10 keV.

Input : Set of ellipses A
(material, location, semi-major/semi-minor axes, rotation);
Set of energy thresholds $E_1, \ldots, E_N$.
Output : Flatfield photon counts $F_n(s,\theta), \quad n = 1, \ldots, N$;
Transmitted photon counts $T_n(s,\theta), \quad n = 1, \ldots, N$.

1 Let E_{kVp} be the x-ray tube voltage.
2 Let $I_0(s,\theta,E)$ be the number of photons with energy E detected by the pixel at s and projection angle θ when no phantom is present (flatfield).
3 Let $I(s,\theta,E)$ be the number of photons with energy E transmitted by the phantom and detected by the pixel at s and projection angle θ.
4 Let D be the thickness of the detector layer.
5 Let m_d be the detector layer material, e.g., Si or GaAs.
6 Let m_a be the material of ellipse a.
7 Let Spektr(E) represent calculation of the intensity of the source at energy E.
8 Let NIST(m,E) represent extraction of the linear attenuation coefficient of material m at energy E from NIST tables.
9 Let $\mathcal{F}(A,\theta)$ be a function to calculate fan-beam line integrals through ellipse set A at angle θ (i.e., forward projection).
10 Let Poisson$\{\lambda\}$ extract a sample from the Poisson distribution with mean λ.
11 **For** $E \leftarrow [10\,\text{keV}, \ldots, E_{\text{kVp}}]$ **do**
12 $\quad \nu(E) \leftarrow \text{Spektr}(E)$ `/* Source intensity */`
13 $\quad \eta(E) \leftarrow 1 - \exp\left[-D \times \text{NIST}(m_d, E)\right]$ `/* Detector efficiency */`
14 $\quad$ **For each** ellipse $a \in A$ **do**
15 $\quad\quad \mu_a(E) \leftarrow \text{NIST}(m_a, E)$ `/* Ellipse material attenuation */`
16 $\quad$ **For each** θ **do**
17 $\quad\quad I_0(s,\theta,E) \leftarrow \nu(E) \times \eta(E)$
18 $\quad\quad I(s,\theta,E) \leftarrow \nu(E) \times \exp\left[-\mathcal{F}(A,\theta)\right] \times \eta(E)$
19 **For** $n \leftarrow [1, \ldots, N]$ **do**
20 $\quad F_n(s,\theta) \leftarrow \sum_{E=E_n}^{E_{kVp}} I_0(s,\theta,E)$
21 $\quad T_n(s,\theta) \leftarrow \text{Poisson}\left\{\sum_{E=E_n}^{E_{kVp}} I(s,\theta,E)\right\}$ `/* Add Poisson noise */`
22 **Return** $\{F_n(s,\theta)\}$ and $\{T_n(s,\theta)\}$

Algorithm 1: Algorithm for simulation of a CT scan. Line 18 represents noise-free transmission, while Poisson noise is added to the measurements on line 21. For global simulation, $N = 1$, and $E_1 = 10\,\text{keV}$. The outputs are equivalent to those of a Medipix detector, so further processing is necessary to produce narrow energy bins. Section 6.1.2 gives a more detailed description of the simulation.

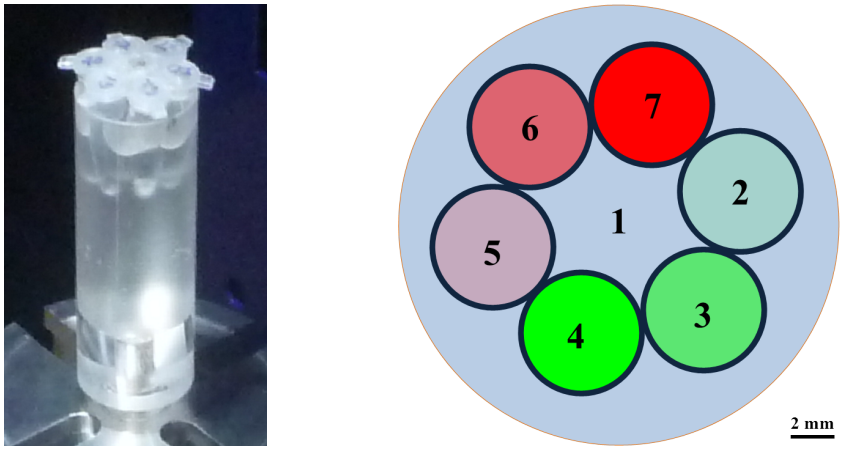

(a) (b)

Figure 6.4: Contrast agent phantom 'A'. (a) Photo of the phantom mounted on the sample stage (excerpt from Figure 6.3). (b) Axial schematic of the phantom at the reconstructed slice location used for Figures 6.5 and 6.6: blue indicates water, red indicates gadolinium, and green indicates iodine. See Table 6.2 for concentrations.

Table 6.2: Contrast agent concentrations. Region numbers refer to those in Figure 6.4(b).

Region	Contrast agent	Concentration
1	Ultra-filtered water	Pure
2	Iodine	0.005 M
3	Iodine	0.05 M
4	Iodine	0.5 M
5	Gadolinium	0.005 M
6	Gadolinium	0.05 M
7	Gadolinium	0.5 M

source-to-detector distance, projection angles, spectral detector material, detector pixel size, and energy thresholds.

6.1.3 Methods

Preliminary experiments were performed with Phantom A on the prototype hybrid spectral micro-CT system. Two common contrast agent types, gadolinium-based Magnevist (gadopentetate dimeglumine, Berlex Laboratories, Wayne, NJ, USA) and iodine-based Omnipaque 300 (iohexol, GE Healthcare, Princeton, NJ, USA), were mixed with pure water to three concentrations each. The contrast agent samples were contained in polyethylene centrifuge tubes which were themselves suspended inside a pure water filled cylinder. A schematic of Phantom A is shown in Figure 6.4(b) and the corresponding contrast agent concentrations are listed in Table 6.2.

The phantom was alternately scanned on the prototype system with the global and spectral imaging chains to prevent contamination by cross-scatter (Kyriakou and Kalender, 2007). The interior spectral chain x-ray source was set to 80 kVp and 200 µA without filtration, and the silicon Medipix detector captured data at 12 energy thresholds uniformly distributed between 10 and 38 keV and at 360 uniformly distributed angles over a total scan angle of 192°. The global greyscale chain x-ray source was set to 80 kVp and 100 µA without filtration, and the energy-integrating detector captured 1500 projections uniformly distributed over a total scan angle of 192°. Simulations according to Section 6.1.2 of both the spectral and global imaging chains were performed with the same parameters. Narrow energy bins were created by subtracting the measurement at each threshold from the one below it, e.g., an energy bin covering 15 to 18 keV was formed by subtracting the measurement at 18 keV from the measurement at 15 keV. This was done independently for the flatfield intensity $F_n(s,\theta)$ and for the transmitted intensity $T_n(s,\theta)$; the resulting data could then be used for reconstruction (the notations $F_n(s,\theta)$ and $T_n(s,\theta)$ are to match Algorithm 1).

Image reconstructions of the spectral interior projections were performed with CS-SIT, with both the global greyscale image and zero as an initial estimate. CS-SIT is the name given by Xu et al. (2012) to the interior reconstruction technique of Xu et al. (2011) that follows the same process as total-variation regularised statistical iterative reconstruction (SIR-TV, described in Section 2.7.2) except that it uses an existing reconstruction as the initial image estimate. In this case the existing reconstruction comes from the global imaging chain. The method is summarised here for convenience:

- Reconstruct the global image $\boldsymbol{\mu}_G$ with SIR-TV (initialised with zero);
- Reconstruct each energy bin image with CS-SIT, using $\boldsymbol{\mu}_G$ as the initial image;
- Apply PCA to the set of reconstructed images to produce $\{\hat{\boldsymbol{\mu}}_s\}_{s=1}^{S}$, where $\hat{\boldsymbol{\mu}}_s$ is component s of the PCA result set, and S is the number of PCA components;
- Create a colour image by mapping the first two principal components and the global reconstruction image into the HSV colour space (Nishad, 2013).

The reconstructed images from the spectral imaging chain are processed with PCA because it is a simple but effective method to identify the primary differences in spectra across the image (Anderson et al., 2010). PCA operates to find orthogonal basis functions that best describe the variance of a data set: the first component is chosen such that it describes as much of the multidimensional data as possible with a single coefficient per voxel; the second component is chosen to describe as much of the residual image as possible, again with a single coefficient per voxel; and the remaining components continue in this manner until all the data is accounted for (Kalukin et al.,

2000). This process produces a set of components $\{\hat{\boldsymbol{\mu}}_c\}$ and a separating matrix W that satisfy

$$\begin{Bmatrix} (\hat{\boldsymbol{\mu}}_1)^T \\ (\hat{\boldsymbol{\mu}}_2)^T \\ \vdots \\ (\hat{\boldsymbol{\mu}}_N)^T \end{Bmatrix} = W \begin{Bmatrix} (\boldsymbol{\mu}_1)^T \\ (\boldsymbol{\mu}_2)^T \\ \vdots \\ (\boldsymbol{\mu}_M)^T \end{Bmatrix}, \tag{6.1}$$

where $\boldsymbol{\mu}_n$ is a column vector representing all the image voxels in the reconstruction of energy bin n, $\hat{\boldsymbol{\mu}}_c$ is a column vector representing the set of image voxels in the decomposed component c, and the superscript T denotes the transpose operation. There are M energy bins and N decomposed PCA components; in many cases (including this one) $M = N$, but (6.1) holds without this equality. The rows of W are the basis functions mentioned above. Because PCA finds components that account for the maximum variance in the multidimensional image data at each step, most of the spectral information is represented by the first few components.

6.1.4 Experimental results

Evaluation of the prototype hybrid micro-CT system was performed by simulating a scan of Phantom A and comparing with the prototype scan results.

6.1.4.1 Reconstruction

Figure 6.5 shows three reconstructions of each of the simulated and actual prototype data sets, and demonstrates the improvement obtained by incorporating a global projection data set. Figure 6.5 (a) and (d) show the global greyscale image reconstructed by SIR-TV for the simulated and prototype system, respectively; these images demonstrate the expected high spatial resolution of a high-end micro-CT scanner with full FOV. Figure 6.5 (e) is the Medipix spectral image reconstructed by CS-SIT without *a priori* global greyscale data, processed with PCA and colour mapped; Figure 6.5 (b) is the result from the corresponding simulation data. Figure 6.5 (c) and (f) are the spectral images reconstructed from the hybrid interior spectral and global greyscale data sets; these images benefit from both the spectral resolution of the interior spectral chain and the spatial resolution of the global greyscale chain.

To allow fair comparison between the reconstructions, the basis sets obtained from the PCA of the hybrid reconstructions were also used to decompose the interior reconstructions. The same windows and levels were used for image display for the same reason. Figure 6.5 (b) and (e) lack spatial resolution and Figure 6.5 (c) and (f) demonstrate better spectral homogeneity inside the FOV (delineated by the black

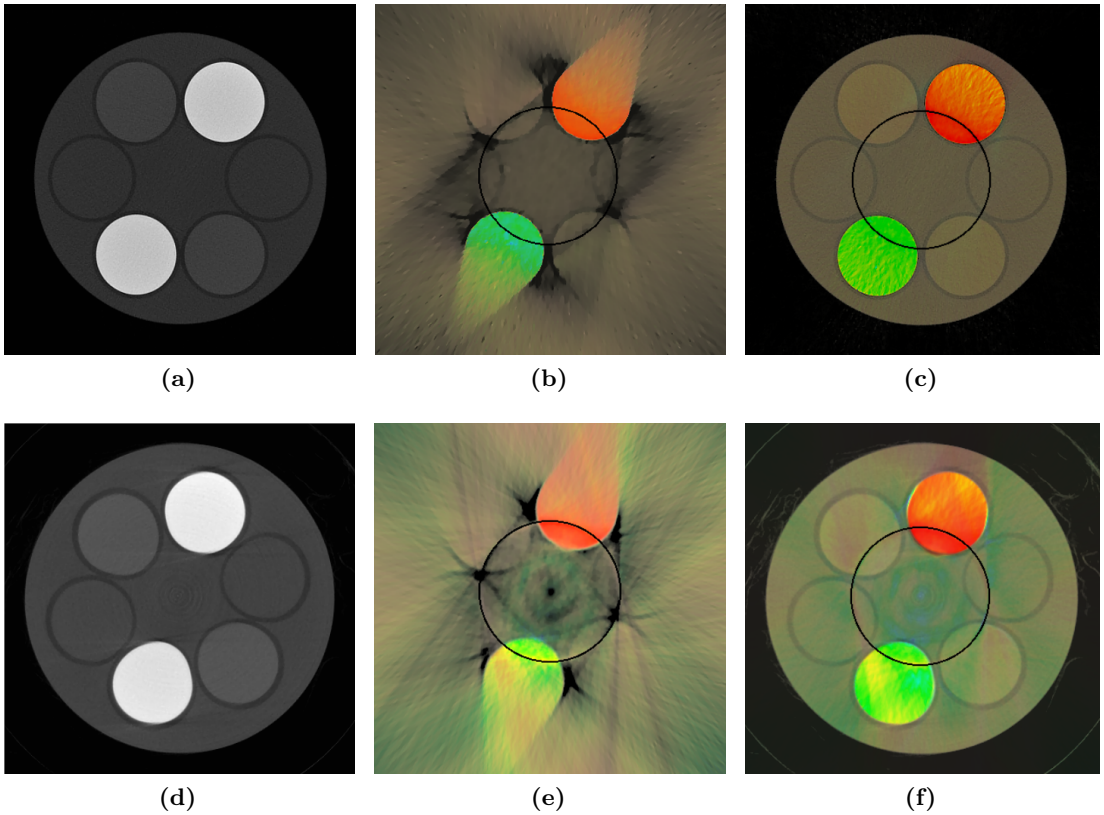

Figure 6.5: Hybrid spectral micro-CT reconstruction results of the simulated (first row) and real prototype (second row) scans of Phantom A: (a, d) are the SIR-TV reconstructions of the global greyscale projections; (b, e) are the CS-SIT reconstructions of the interior spectral projections without the global greyscale image; (c, f) are the reconstructions of the interior spectral and global greyscale projection data using CS-SIT. The black circles denote the interior FOV.

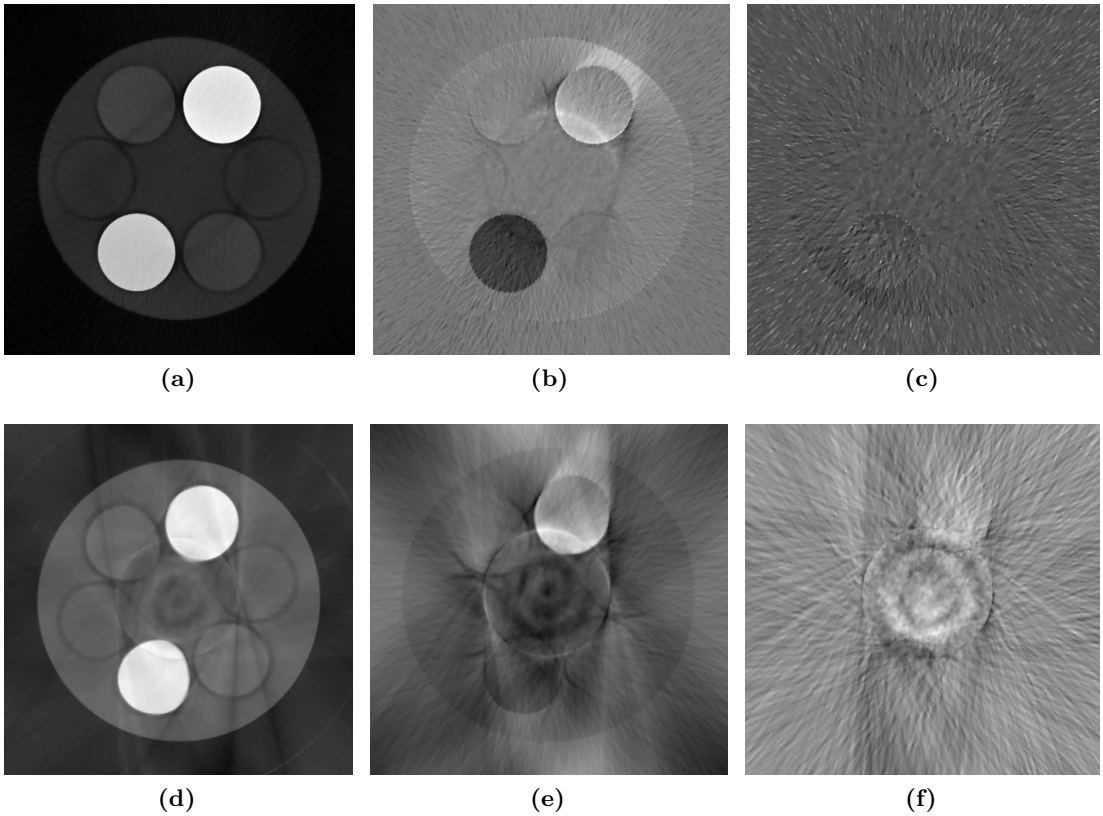

Figure 6.6: PCA decomposition of the simulated (first row) and real prototype (second row) hybrid spectral reconstructions: (a, d), (b, e) and (c, f) are the first, second and third principal components, respectively.

circle) than Figure 6.5 (b) and (e). Also observe that Figure 6.5 (c) and (f) show better spectral homogeneity outside the FOV.

Figure 6.4(b) shows which contrast agent solution is in each tube. The global greyscale reconstruction does not differentiate between iodine and gadolinium, but all spectral reconstructions (Figure 6.5(b,c,e,f)) allow differentiation between the two contrast agents. The regions of medium concentration (0.05 M) are not readily distinguished from the surrounding water on the interior images of Figure 6.5 (b) and (e), while the improved reconstructions in Figure 6.5 (c) and (f) show greater contrast. Neither imaging chain could distinguish the 0.005 M concentrations. Further, the interior spectral reconstructions do not clearly show spatial details such as the plastic centrifuge tube containing the contrast agent, nor the slight interior bulge in tube 4, both of which are apparent in the global and hybrid spectral reconstructions (Figure 6.5 (d) and (f)).

6.1.4.2 Quantitative analysis

Figure 6.6 shows the first three components from PCA decomposition of the simulated and prototype hybrid spectral reconstructions. Figure 6.7 shows the proportion of data

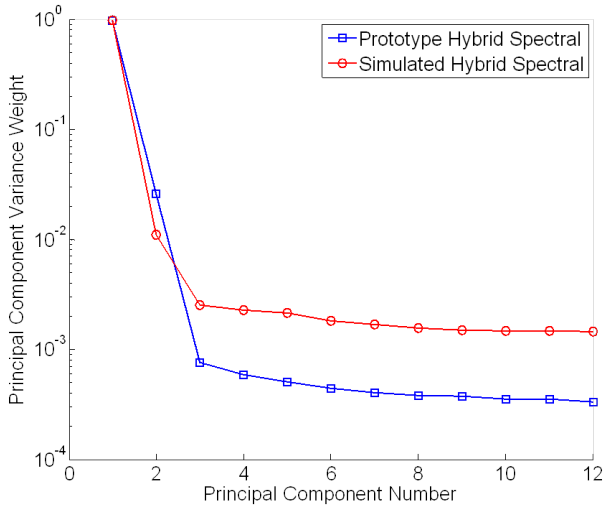

Figure 6.7: Semi-log plot of the proportional variance weight of each principal component for real and simulated hybrid spectral reconstructions.

variance represented by each principal component on a semi-log plot. It is clear that the variance diminishes significantly after the second principal component in both simulated and prototype reconstructions; this observation is supported by the images in Figure 6.6: the first two principal components ((a) and (d), (b) and (e)) clearly contain relevant information, whereas the third component ((c) and (f)) does not show any relevant information.

Another critical element of Figure 6.6 is the differentiation between gadolinium and iodine. The first principal component (Figure 6.6 (a) and (d)) does not show any appreciable difference between the contrast agent types, yet it is visually obvious that only the gadolinium is enhanced in the second principal component (Figure 6.6 (b) and (e)). The second principal component produces the colourisation of the different

Table 6.3: Attenuation, contrast, and noise analysis. $\bar{\mu}_{Gd}$ and $\bar{\mu}_{I}$ are the mean values in the gadolinium and iodine ROIs, respectively; σ is the noise measured in the water ROI; SDNR is the signal difference to noise ratio between the iodine and gadolinium ROIs in the reconstruction. The ROIs are shown in Figure 6.8.

	Simulation			Prototype		
	Global	PCA comp. 1	PCA comp. 2	Global	PCA comp. 1	PCA comp. 2
$\bar{\mu}_{Gd}$	1.204	3.857	0.465	1.804	6.236	1.808
$\bar{\mu}_{I}$	1.195	3.825	-0.446	1.870	6.063	0.526
σ	0.019	0.029	0.027	0.021	0.258	0.105
SDNR	0.47	1.1	33.7	3.11	0.67	12.21

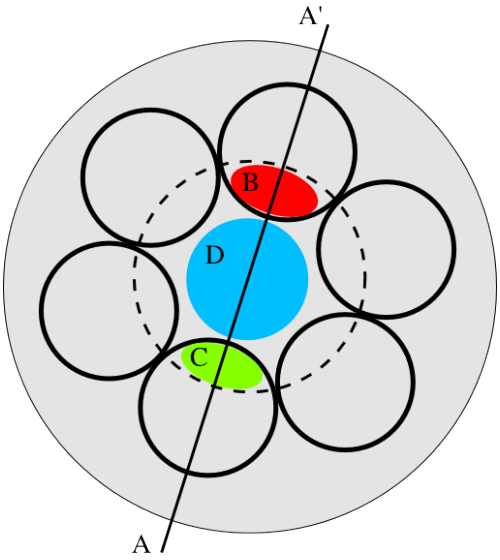

Figure 6.8: Schematic of the ROIs used for quantitative analysis. Line segment A-A' is used for spatial resolution measurements; B, C and D denote the sampled gadolinium, iodine and water regions, respectively; the dashed circle shows the interior FOV.

materials shown in Figure 6.5 (b), (c), (e), and (f), and thus enables distinction of elements that would otherwise be indistinguishable with conventional greyscale imaging (Figure 6.5 (a) and (d)). This phenomenon is due to the k-edge property of the contrast agents with respect to the photon energy (see, e.g., Figure 1.9). The signal difference to noise ratio (SDNR) was calculated as described by He et al. (2012) to quantify the contrast improvement between materials,

$$\text{SDNR} = \frac{|\bar{\mu}_I - \bar{\mu}_{Gd}|}{\sigma}, \tag{6.2}$$

where $\bar{\mu}_{Gd}$ and $\bar{\mu}_I$ are the mean values in the gadolinium and iodine ROIs, respectively, and σ is the noise measured in the water ROI. Figure 6.8 shows the location and extent of these ROIs; the contrast agent ROIs were chosen to be the largest ellipses to fit in the intersection of the interior FOV with the region of highest concentration of the respective contrast agent, while the water ROI was chosen as the largest circle to contain only water. The results in Table 6.3 clearly demonstrate the improved contrast resolution with spectral hybrid reconstruction and PCA: the SDNR in PCA component 2 is far superior to that of the other images. The difference between the values found for the simulation and the prototype scan arises because the simulation only accounts for quantum noise and not for other defects and distortions in the response of the Medipix detector, therefore the actual scan data has greater noise. An ideal phantom for this type of experiment would have contrast agent concentrations such that the reconstructed attenuations of the two different contrast agents are identical in the global image; this would produce an SDNR of zero for the global reconstruction. Table 6.3 shows that the

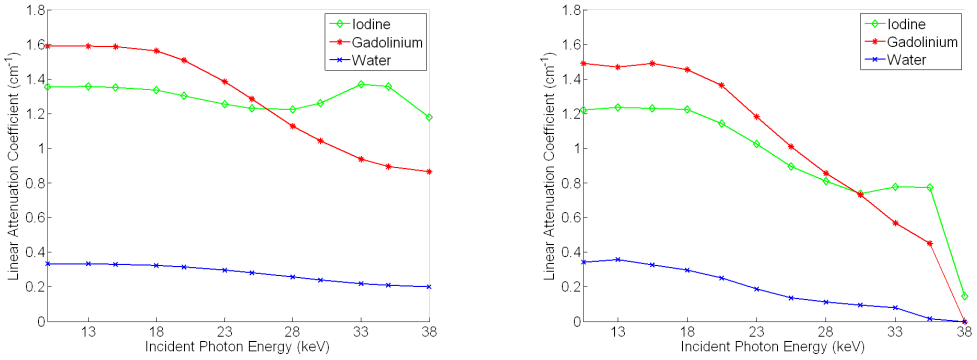

(a) **(b)**

Figure 6.9: Reconstructed attenuation spectra of the (a) simulated and (b) real phantom. The plots show the average linear attenuation coefficient in the three ROIs described in Figure 6.8 as a function of the twelve spectral energy bins in the simulated hybrid reconstructions. Note the increased attenuation above 33 keV caused by the k-edge of iodine.

actual phantom was not ideal in this sense, but the values were close enough to enable a measurement; the difference between the values listed for the simulated and prototype scans is due to imperfect modelling of the contrast agents within the simulation.

Figure 6.9 shows the reconstructed linear attenuation coefficient as a function of the twelve spectral energy bins for both the simulated hybrid data and the actual prototype hybrid data. The attenuations are averages within the ROIs described in Figure 6.8. There are two prominent features in the hybrid prototype plot, the most critical being the expected increase in attenuation at 33 keV from the k-edge of iodine. Secondly, there is a signal drop-off after roughly 35 keV for all three ROIs which corresponds to the limited efficiency of the silicon detector above this energy, thus the detected counts are too low for accurate reconstructions.

The spatial resolution of each reconstruction (greyscale, interior, and hybrid) was calculated for the prototype data via the edge spread function (Bentzen, 1983), which gives a measure of the amount of blurring applied to a sharp edge. First, a line profile was sampled at 1 µm intervals through the segment A–A' as shown in Figure 6.8. The edge spread function was produced by selecting the line profile regions passing through the contrast agent–polyethylene boundary (border between the contrast agent and the polyethylene centrifuge tubes). The line spread function was produced by calculating the derivative of the edge spread function, and the spatial resolution was calculated from the full width at half maximum (FWHM) value of the line spread function at the boundary. The FWHM values are 106 µm, 339 µm, and 124 µm for the greyscale, interior, and hybrid reconstructions respectively. These values show spatial resolution improvement in the hybrid reconstruction relative to the original interior reconstruction. Note that this difference in spatial resolution suggests that the noise levels quoted earlier

are not directly comparable; however, since the noise level is lower where the resolution is greater, the conclusions are still meaningful.

6.1.5 Discussion

The results from the prototype and simulated hybrid scans match well, showing that reconstructions from hybrid data exhibit the strengths of both imaging chains. This finding confirms the viability of the architecture and offers encouragement for further development.

PCA has worked well as a means of dimensional reduction, as suggested by Butler et al. (2011*a*). Figure 6.7 shows that essentially all useful information in the attenuation spectra is encompassed by the first two components, and inspection of the decomposed images in Figure 6.6 shows that these two components approximately correspond to integrated attenuation and contrast agent type, respectively. The second component has one contrast agent brighter than the background and one darker, and it is interesting to note that the gadolinium is enhanced by this component, despite its k-edge (50.2 keV) being beyond the range of energy thresholds. However this is merely a result of the unguided nature of PCA, and the important result to observe is that the different contrast agents were separated. The dominance of the first two components in this experiment suggests that a carefully chosen dual energy CT system may be capable of producing similar results. However, this would not be true, in general, for the hybrid configuration with a harder detector layer (e.g., CdTe or GaAs) because more k-edges could be measured yielding more than two PCA components containing significant information. The results in Section 6.2 confirm this assertion.

In the original paper proposing the hybrid architecture, Xu et al. (2012) observe that useful spectral information is reconstructed beyond the FOV boundary. This study also exhibits this result: parts (c) and (f) of Figure 6.5 have better homogeneity outside the FOV than parts (b) and (e). However, this degree of improvement may not be equally impressive in cases of more complex shapes and contrast in the exterior region. Further study is required to establish the conditions that lead to this phenomenon.

The k-edge of iodine can be seen in the reconstructed attenuation spectra from both the simulated and real data (Figure 6.9). It should be noted that the attenuation curves do not appear as ideal curves (c.f. NIST (Hubbell and Seltzer, 2004)) for several reasons: energy bin width, charge sharing, spectral response of the silicon detector, source spectrum, and unavoidable noise all combine to make the measured attenuation plots differ from ideal ones. For example, a sharp attenuation jump at the iodine k-edge like that seen in Figure 1.9(b) is not observed either in the real prototype or the simulated plots because the relatively wide energy bins are not exactly positioned on either side of the k-edge. Thus, the increased attenuation at energies above the iodine k-edge is averaged, but it is still clearly visible in Figure 6.9. The spectral detector also

has defects and distortions that cause data degradation beyond that of the expected noise. For example, Figure 6.9 shows that the attenuation spectra reconstructed from the prototype data drops away faster than the corresponding simulated spectra; this is conjectured to be due to partial saturation of the detector layer during flatfield measurements, which does not occur in the simulation. The increased level of variance in the reconstructed images can also be seen in the noise values of Table 6.3. Despite these problems, the key result is that the Medipix detector produced adequate data for the reconstruction of meaningful attenuation spectra.

The simulation used for this study is reasonably comprehensive, including source spectrum, detector efficiency, and energy-dependent material attenuation. The close correlation of the results from the prototype and simulated systems suggests that the most important effects are represented. However, there are some physical phenomena that are not modelled such as charge sharing, residual threshold dispersion, pulse pile-up, and scatter. The simulation could be further improved by including these effects in a future version of the simulation; for example, an expansion of the IBLESS algorithm in Chapter 4 could be used for modelling the scatter content of the measurements.

6.1.6 Conclusion

The experimental results from the hybrid spectral micro-CT prototype demonstrate the feasibility and the merits of this particular system architecture. There is a synergy between the high spatial resolution of the greyscale imaging chain and the energy resolution of the spectral imaging chain. The described reconstruction technique utilises the respective strengths of each imaging chain to produce images with both high spatial and contrast resolution. This concept was shown theoretically by Xu et al. (2012), and the results from the prototype system implementation in this section support the assertions made in that publication.

6.2 Radiation exposure reduction

A primary benefit of the interior spectral imaging chain in the hybrid architecture is the reduction of exposure to radiation while maintaining the benefits of spectral CT imaging. This is because the x-ray beam path is collimated, which reduces exposure relative to a full FOV spectral detector. Further exposure reduction for hybrid spectral micro-CT can be achieved by reducing the width of the interior FOV, the number of interior projections, and the number of global projections. Fewer projections also allows for shortened scan time which can be critical for *in vivo* biomedical applications. However, it is important that these reductions do not significantly degrade the spatial or spectral fidelity of the reconstructed images.

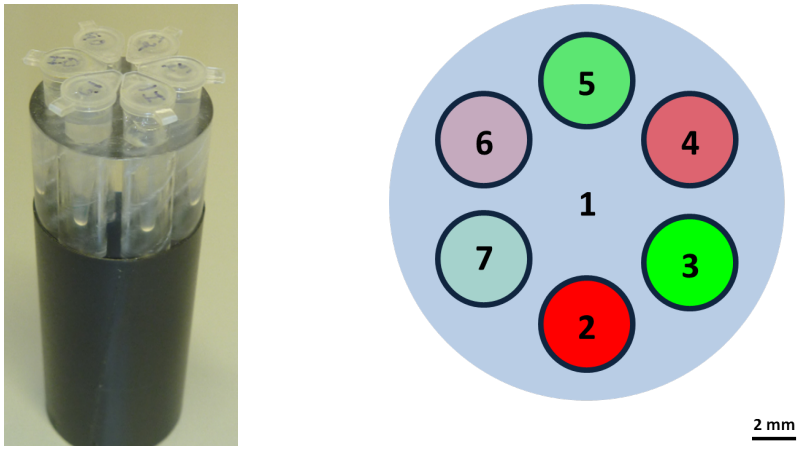

(a) (b)

Figure 6.10: Contrast agent phantom 'B'. (a) Photo of the phantom. (b) Axial schematic of the phantom at the reconstructed slice location: region 1 is PMMA; regions 2, 4, and 6 are 0.5M, 0.05M, and 0.005M gadolinium solutions, respectively; regions 3, 5, and 7 are 0.5M, 0.05M, and 0.005M iodine solutions, respectively.

The goal of this study is to evaluate the effects of the interior FOV, number of projections (both interior and global), and reconstruction method on the spectral fidelity of reconstructions in simulated and real experimental settings. The remainder of the section is organised as follows: Section 6.2.1 describes the hybrid scan protocol for real and simulated scans along with evaluation metrics; Section 6.2.2 contains the results of the spectral fidelity evaluation on real and simulated reconstructions; Section 6.2.3 provides a discussion of the results and suggestions for future studies; and Section 6.2.4 concludes the chapter.

6.2.1 Methods

Three hybrid scan protocol elements, namely interior FOV width, number of spectral projections, and number of global projections, were independently decreased to reduce radiation exposure. The effects of decreasing these elements are evaluated with each of three data sets: a physical scan of Phantom B, a matching simulated scan of Phantom B, and a further simulated scan of a virtual thorax phantom. The processes for collecting, reconstructing, and evaluating these data sets are described below.

6.2.1.1 Phantoms

A simple contrast agent phantom (Phantom B) was designed, crafted, and then scanned with a hybrid system; numerical simulations were also performed. The phantom is shown in Figure 6.10. The phantom body comprises a 25 mm diameter poly(methyl

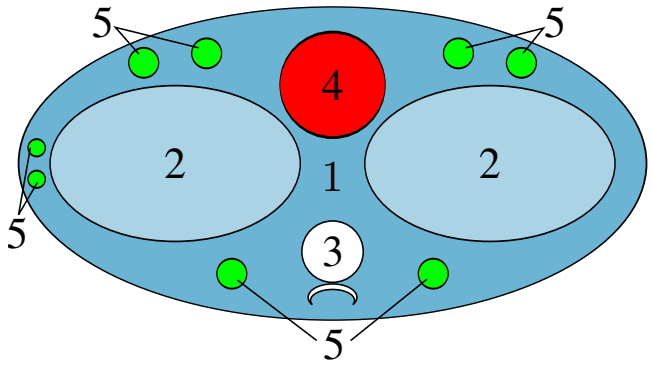

Figure 6.11: Schematic of the simulated thorax phantom. Region 1 is soft tissue, region 2 is two partially inflated lungs, and region 3 is the spine (bone). The heart (region 4) contains a mixture of muscle tissue and gadolinium (0.3M), while the blood vessels (regions 5) contain a mixture of blood and iodine (0.3M).

methacrylate) (PMMA) cylinder with six equally spaced 6 mm diameter cylindrical cavities. Each cavity contains one of six polyethylene centrifuge tubes containing various concentrations of clinical contrast agents: gadolinium-based Magnevist (gadopentetate dimeglumine, Berlex Laboratories, Wayne, NJ) and iodine-based Omnipaque 300 (iohexol, GE Healthcare, Princeton, NJ). Phantom B is thus similar to Phantom A used in Section 6.1 but with solid PMMA instead of water, and with a 25 mm diameter instead of 20 mm. The actual phantom and an axial schematic are shown in Figure 6.10.

In addition, a simulated thorax phantom was created to evaluate the hybrid scanning method on a sample with more complexity than Phantom B; a schematic is shown in Figure 6.11. Several contrast agent regions were specifically positioned away from the sample centre to ensure that the regions were completely outside the interior spectral FOV. The "spine" region was designed with a slender bone protrusion that represents fine structure lacking in Phantom B. In the remainder of this section, the term "background" is used to refer to the soft tissue of the thorax phantom and the PMMA of Phantom B.

6.2.1.2 Real and simulated hybrid scans

The real hybrid spectral micro-CT scan of Phantom B was performed using two separate systems: a MARS spectral micro-CT scanner and an Xradia XCT conventional micro-CT scanner (Xradia, Pleasanton, CA). The phantom was intentionally designed to be physically static, allowing the scans to be performed in two separate locations. The study in Section 6.1 demonstrated the quality of the hybrid spectral micro-CT architecture; however, those facilities were unavailable for this study, and hence the two scans were performed separately and exposure reduction parameters were evaluated by directly modifying the reconstruction inputs. In other words, full FOV and maximum projection

Table 6.4: Hybrid spectral micro-CT hardware component specifications for the exposure reduction study.

		Global imaging chain	Spectral imaging chain
X-ray source	Tube voltage	80 kVp	120 kVp
	Tube current	100 µA	150 µA
	Output window	100 µm Be	Glass (1.8 mm Al equiv.) + 127 µm Be
	Distance to centre of rotation	100 mm	119 mm
X-ray detector	Number of pixels	512	973
	Pixel size	109.2 µm	55 µm
	Energy range(s)	Integrated, 0–80 keV	28–38, 45–55 keV
	Energy bin width	N/A	4 keV
	Counts per exposure	$\sim$ 25 000	$\sim$ 4000
	Distance to centre of rotation	65 mm	66 mm
	Detector type	Scintillator + CCD camera	Medipix 3.1, 300 µm GaAs layer

number data sets were separately collected for global and spectral imaging chains, and then truncated or decimated to emulate various hybrid scanner configurations. The reference values for the number of projections were selected from the manufacturer recommended scan protocols: 360 and 1500 projections for spectral and global imaging chains, respectively.

Fan-beam projections for the two phantoms were generated with the simulation in Section 6.1.2. The simulation scan parameters mirrored the real hybrid scanner settings shown in Table 6.4. The simulation differed in the number of energy thresholds, where eight thresholds were simulated compared to the 76 real thresholds. This difference is explained in Section 6.2.2.1.

6.2.1.3 Reconstruction and decomposition

Two different algorithms were used to reconstruct the hybrid data sets. One is compressed sensing based statistical interior tomography (CS-SIT) as reported by Xu et al. (2011) and as used in Section 6.1; the other uses the greyscale data to estimate spectral projection data outside the interior FOV and reconstructs images using conventional filtered back-projection (FBP). CS-SIT has proven to be effective at hybrid reconstructions by Xu et al. (2012) and in Section 6.1, but is considerably slower than FBP. Both algorithms were applied to the data sets to determine which is best suited for hybrid spectral reconstruction.

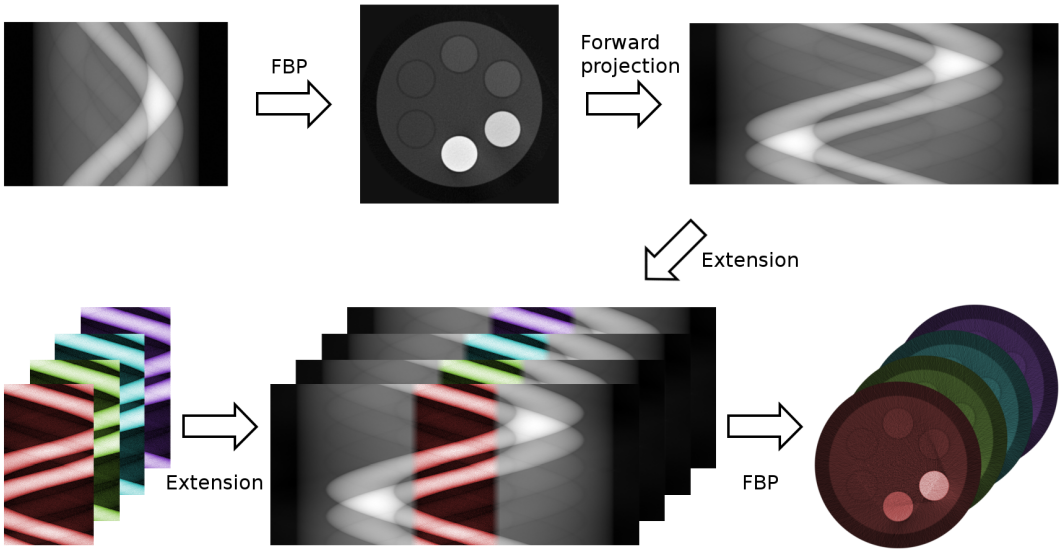

Figure 6.12: For the FBP reconstruction method, the truncated spectral sinograms (lower left) are completed using data from the full FOV greyscale image, then FBP reconstruction proceeds as normal. Note that the colours are illustrative only, and are not related to the colours of reconstructions shown elsewhere in this section.

Figure 6.12 illustrates the FBP based reconstruction process, which was inspired by Lewitt and Bates (1978*b*) and is closely related to the approach taken by Schmidt and Pektas (2011). The global reconstruction is first forward-projected (reprojected) using the geometry of the spectral imaging chain. The new global sinogram exactly matches the spectral sinograms except that it covers the full object, and thus the edges of the global sinogram can be used as approximations to the truncated parts of the spectral sinograms. The global sinogram values are scaled to match the values at the edges of the sinogram for each energy bin, and the data are blended over 10 pixels to avoid any sudden jumps in the combined (hybrid) sinogram. The hybrid sinograms are then used to perform reconstruction with conventional fan-beam FBP; this hybrid reconstruction method is referred to simply as FBP in this section.

Decomposition of the reconstructed hybrid spectral image set is performed with independent components analysis (ICA) (Hyvärinen and Oja, 2000). ICA is a statistical multivariate data processing technique developed for blind source separation which is used here to decompose the set of spectral reconstructions $\{\mu_s(\boldsymbol{x})\}$ into components

$\{\hat{\mu}_\alpha(\boldsymbol{x})\}$ such that

$$\begin{Bmatrix} \mu_1(\boldsymbol{x}) \\ \mu_2(\boldsymbol{x}) \\ \vdots \\ \mu_S(\boldsymbol{x}) \end{Bmatrix} = M \begin{Bmatrix} \hat{\mu}_1(\boldsymbol{x}) \\ \hat{\mu}_2(\boldsymbol{x}) \\ \vdots \\ \hat{\mu}_N(\boldsymbol{x}) \end{Bmatrix} \tag{6.3}$$

where M is the mixing matrix estimated by ICA, N is the number of independent components, the images are denoted $\mu_s(\boldsymbol{x})$ to be interpreted as row vectors indexed by voxel coordinates $\boldsymbol{x} = (x_1, x_2)$, $\hat{\mu}_\alpha(\boldsymbol{x})$ are row vectors containing components, and $N \leq S$. ICA operates in a manner similar to PCA, but unlike PCA it is not restricted to finding orthogonal basis functions; instead it seeks statistically independent underlying functions which can be a powerful technique for numerous applications (Hyvärinen and Oja, 2000). In this study, ICA is applied to the attenuation spectra found in the set of reconstructed hybrid image voxels. While PCA has previously been used successfully to decompose spectral reconstructions by Xu et al. (2012), Butler et al. (2011*a*), and in Section 6.1, ICA was chosen because it offers the potential for better separation of individual materials since statistical independence is a stronger property than uncorrelatedness; the results below confirm that ICA indeed outperforms PCA (see Section 6.2.2.1 and Figure 6.15). The particular ICA implementation used is a fixed-point iteration scheme known as FastICA (Hyvärinen, 1999), written for Matlab. Default parameters were used for this function, except that output was limited to three components and only four eigenvalues were retained. These values were found to be suitable through simple trials. The ICA algorithm was trained with images reconstructed by each of the reconstruction algorithms from full FOV spectral data, and then the appropriate separation matrix was applied to the hybrid reconstructions.

After applying ICA to the hybrid spectral image set, the resulting component images (or just "components") were compared to distinguish iodine from gadolinium. As shown in Section 6.2.2, ICA produced three components of meaningful data: one component enhanced iodine, another enhanced gadolinium, and a third contained residual PMMA density. It is important to note that this separation is fortuitous rather than expected: ICA does not perform pure targeted decomposition where each component contains only the contribution of a specific material, as would be expected from a scheme such as that of Roessl and Proksa (2007) or Schlomka et al. (2008). While targeted decomposition is a worthwhile goal, the data from the current MARS spectral x-ray detector is not amenable to this type of analysis because charge sharing (Korn et al., 2007), pulse pile-up, and residual energy dispersion (Walsh et al., 2011) nonlinearly corrupt the measured transmission spectrum such that it can no longer be decomposed into a simple sum of material transmission spectra. Regardless, the results of Schlomka et al. (2008) show that features of other materials leak into the contrast agent component images

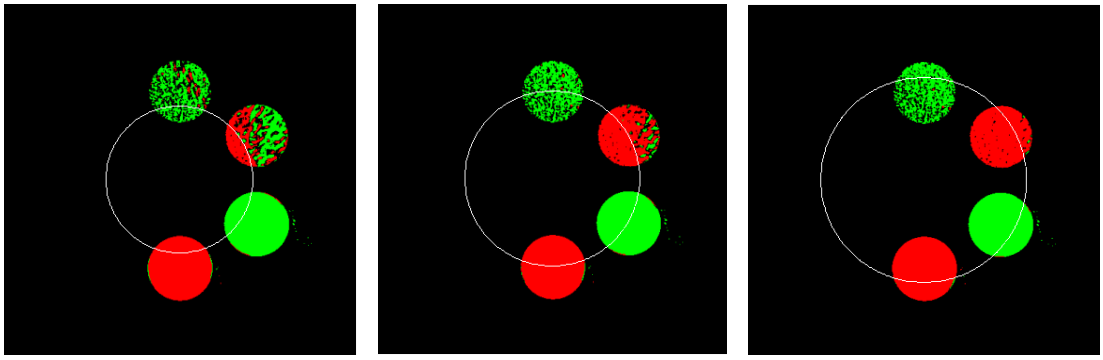

(a) (b) (c)

Figure 6.13: Hybrid spectral reconstructions after ICA and colour-mapping of simulated projection data with interior FOVs of (a) 50%, (b) 60% and (c) 70% of full FOV.

even with targeted decomposition, so the output of blind separation is not significantly inferior.

Contrast agent identification in the reconstructed image is achieved as follows: the ICA separation produces one component that enhances iodine and a second component that enhances gadolinium, as illustrated in Figure 6.15; these images are henceforth referred to as the iodine component and the gadolinium component. The average background value is subtracted from each of these images and then the images are compared voxel-wise. Voxels with a greater value in the iodine component are marked as iodine, and likewise with the gadolinium component; a small dead-zone is included in the comparison to reduce noise in the identification result where the two components have comparable values. Thus

$$f_I(\boldsymbol{x}) = \begin{cases} 1, & \hat{\mu}_I(\boldsymbol{x}) - \hat{\mu}_{Gd}(\boldsymbol{x}) > \epsilon, \\ 0, & \text{otherwise}, \end{cases} \tag{6.4}$$

$$f_{Gd}(\boldsymbol{x}) = \begin{cases} 1, & \hat{\mu}_{Gd}(\boldsymbol{x}) - \hat{\mu}_I(\boldsymbol{x}) > \epsilon, \\ 0, & \text{otherwise}, \end{cases} \tag{6.5}$$

where $f_I(\boldsymbol{x})$ and $f_{Gd}(\boldsymbol{x})$ are binary images showing the voxels identified as iodine and gadolinium respectively, $\hat{\mu}_I(\boldsymbol{x})$ and $\hat{\mu}_{Gd}(\boldsymbol{x})$ are the iodine and gadolinium components, respectively, and ϵ is the dead-zone. The dead-zone is chosen to be 1% of the maximum value found between $\hat{\mu}_I$ and $\hat{\mu}_{Gd}$. Examples of $f_I(\boldsymbol{x})$ and $f_{Gd}(\boldsymbol{x})$ are shown in Figure 6.13 for three interior FOVs. The images show both $f_I(\boldsymbol{x})$ and $f_{Gd}(\boldsymbol{x})$, with $f_I(\boldsymbol{x})$ mapped to green and $f_{Gd}(\boldsymbol{x})$ mapped to red; inspection of eqs. (6.4) and (6.5) shows that it is impossible for a voxel to have a value of 1 in both binary images.

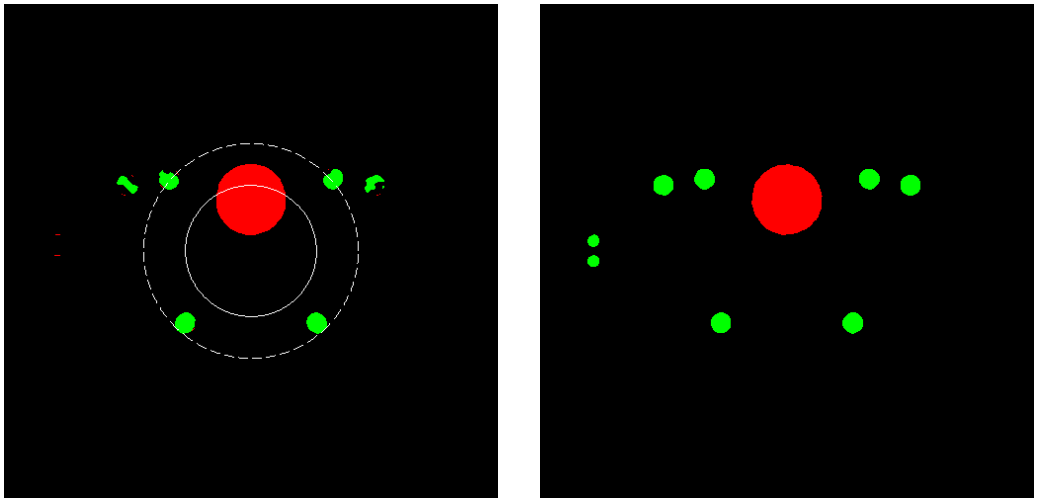

(a) (b)

Figure 6.14: Illustration of the EFOV metric. (a) is created in the same way as Figure 6.13 but based on thorax phantom data. The solid white circle marks the boundary of the measured FOV, while the dashed white circle marks the boundary of the EFOV. Note that inside the EFOV the contrast agent separation is reliable but outside the EFOV it is not, e.g., the iodinated vessels on the left are not identified. (b) shows the true decomposition for comparison.

6.2.1.4 Measurements and metrics

Several metrics are used to evaluate the effect of exposure reduction on hybrid reconstructions: Effective FOV (EFOV) is calculated for interior FOV reduction; EFOV and contrast-to-noise ratio (CNR) are used to evaluate reduction of interior spectral projections; and CNR is used to evaluate the reduction of global projections. The meaning and calculation of these metrics are explained below.

Previous studies of the hybrid architecture have suggested that useful spectral information extends beyond the spectral interior FOV (Xu et al. (2012) and Section 6.1). In this study, a measure of this "spectral dispersion" was sought by way of the EFOV, defined as the region where the spectral fidelity is sufficient to correctly distinguish between the two contrast agents in the phantom with at least 90% of the accuracy of the full FOV spectral reconstruction. The accuracy is measured as a function of radius from the centre of the phantom by calculating the proportion of correctly identified voxels within concentric rings 1.5 mm thick. Thus

$$a(r) = \frac{\sum_{\boldsymbol{x}=\Gamma(r)} \Big[f_I(\boldsymbol{x}) g_I(\boldsymbol{x}) + f_{Gd}(\boldsymbol{x}) g_{Gd}(\boldsymbol{x}) \Big]}{\sum_{\boldsymbol{x}=\Gamma(r)} \Big[g_I(\boldsymbol{x}) + g_{Gd}(\boldsymbol{x}) \Big]} \tag{6.6}$$

where $a(r)$ is the accuracy at radius r, $\Gamma(r)$ is the set of image voxels in the ring of

width 1.5 mm with central radius r, and $g_I(\boldsymbol{x})$ and $g_{Gd}(\boldsymbol{x})$ are equal to 1 in the known regions of iodine and gadolinium, respectively, and zero elsewhere. Equation (6.6) can be interpreted as counting the number of voxels at radius r from the image centre that were identified correctly, and dividing by the total number of contrast agent voxels at that radius. The EFOV is calculated by finding the radius where the accuracy of the hybrid reconstruction first drops to 90% of the accuracy found in the full FOV spectral reconstruction. In cases where the accuracy is better than 90% over the full phantom, the EFOV is set to the maximum radius that contains contrast agent: 83% for Phantom B and 95% for the thorax phantom. A larger EFOV means spectral fidelity remains high over a larger region. For most interior reconstruction algorithms, the reconstruction quality and stability deteriorate toward the boundary of the FOV (Courdurier et al., 2008; Clackdoyle and Defrise, 2010). However, with hybrid reconstructions the image quality remains high beyond the FOV, so the EFOV can be expected to be larger than the measured FOV. The significance of an EFOV being larger than the measured FOV is that the amount of radiation exposure required to obtain spectral information on a given ROI can be reduced.

When evaluating the effect of a reduction in the number of spectral projections, CNR is calculated separately for each of the gadolinium and iodine component images, and for each contrast agent region within these images. The contrast is measured against the average attenuation of the background, and the noise is measured in the background region. For example,

$$\mathrm{CNR}_{k|\alpha} = \frac{\bar{\mu}_{k|\alpha} - \bar{\mu}_{\mathrm{BG}|\alpha}}{\sigma_{\mathrm{BG}|\alpha}}, \tag{6.7}$$

where $\bar{\mu}$ denotes the mean image value in a region, σ denotes the image standard deviation in a region, and the subscript identifies the measured region. $k|\alpha$ denotes region number k (see Figure 6.10(b)) in the α component (either gadolinium or iodine), and $\mathrm{BG}|\alpha$ similarly denotes the background region in the α component. Ideal results would show a high CNR for the gadolinium component image in the gadolinium regions (2, 4, and 6) and zero CNR in the iodine regions (3, 5, and 7), and vice versa.

The CNR measurement for a varying number of global projections is only calculated in region 2 (0.5M gadolinium, see Figure 6.10(b)). Thus

$$\mathrm{CNR} = \frac{\bar{\mu}_{2|G} - \bar{\mu}_{\mathrm{BG}|G}}{\sigma_{\mathrm{BG}|G}}, \tag{6.8}$$

where the subscript "$|G$" denotes that the respective value is measured on the global reconstruction. The gadolinium region is used in this calculation because it has the greatest attenuation of the contrast agent regions.

6.2.2 Experimental results

Exposure reduction was effected through decreasing the spectral FOV, the number of spectral projections, and the number of global projections in turn. The results from each parameter are presented in a separate section below. Within each section, representative hybrid reconstructions are provided (Figures 6.18, 6.20, and 6.23) to illustrate the effect of the particular technique, using both FBP and CS-SIT/SIR-TV. These images are created by colour mapping the gadolinium component to red, the iodine component to green, and the remaining (PMMA) component to blue in the RGB colour space. Regions 4 and 5 can be harder to make out in these images, and this is often easier on a computer screen than on paper. Spectral FOV width and EFOV width are measured as a percentage of the phantom diameter.

6.2.2.1 Decomposition

The reconstructed images of the real phantom spectral scan were decomposed using both ICA and PCA to compare the performance of these methods. The images in Figure 6.15 demonstrate that ICA decomposes the three phantom materials into separate components, whereas PCA does not clearly decompose each material. For example, the gadolinium in region 2 is partially enhanced in both the second and third PCA components while the gadolinium in region 4 cannot be distinguished in any of the first three PCA components. These results confirm the anticipated benefits of ICA, and subsequent results are processed only with ICA. Computational costs for each of the methods were comparable: ICA and PCA required an average of 7.5 seconds and 18 seconds, respectively, to decompose the real phantom data. Note that the PCA implementation in Matlab does not have the option to stop processing after a given number of components, and thus the cost quoted here is greater than would be necessary in an optimised environment. Decomposition of the thorax phantom reconstructions (Figure 6.16) shows that ICA successfully separates the contrast agents when bone is present in the object. In this case the soft tissue appears to spread more evenly between the components, rather than collecting mainly in one component like PMMA does in the Phantom B results.

While not shown here, repeating ICA decomposition with the same data does not always produce the same separation order; i.e., sometimes the first component enhances iodine, while other times the second component does so. This non-deterministic behaviour is due to the statistical nature of ICA, and that FastICA seeds its iterative routine with a pseudo-random mixing matrix (Hyvärinen, 1999). This means that the order of two similarly strong components depends on which is nearer to the random initial matrix. This behaviour had no effect on the decomposition of the hybrid images because the separating matrix was frozen after training it with full FOV spectral data and did not change between image sets.

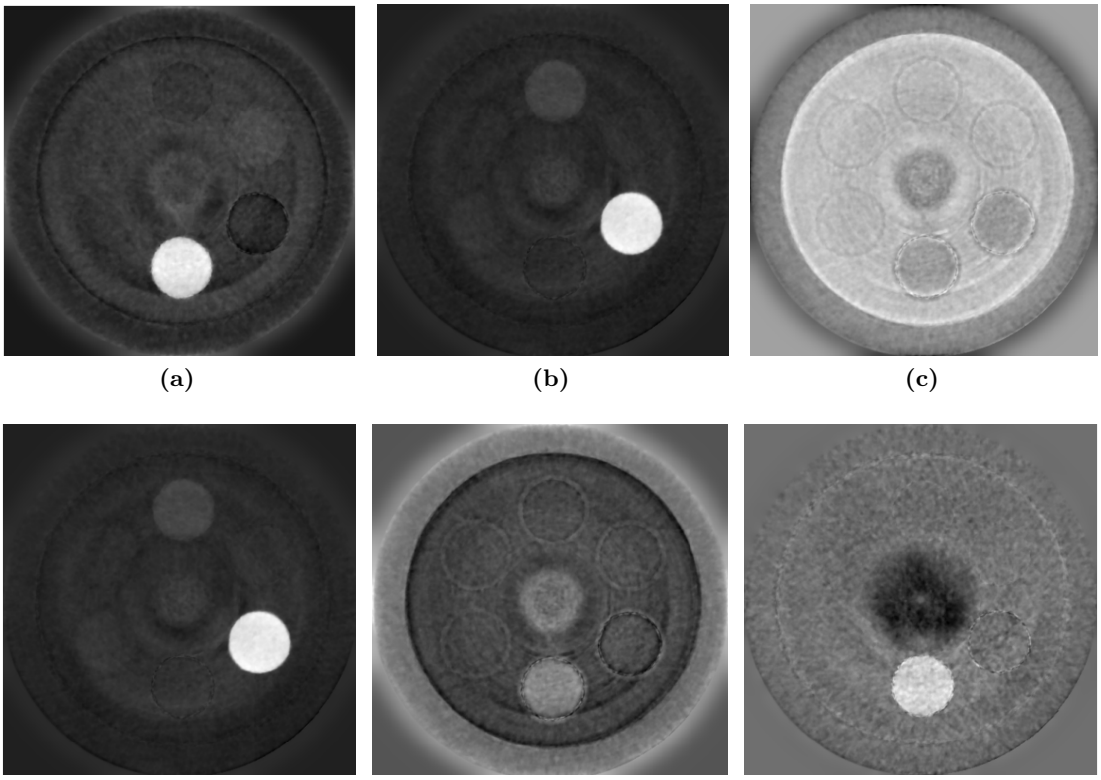

(a) **(b)** **(c)**

(d) **(e)** **(f)**

Figure 6.15: In the top row: first (a), second (b), and third (c) ICA components of the full FOV CS-SIT reconstructions of prototype spectral data. These images enhance iodine, gadolinium, and PMMA, respectively. In the second row: first (d), second (e), and third (f) PCA components of the full FOV CS-SIT reconstructions of prototype spectral data. Note that the gadolinium in region 2 appears in both (e) and (f) with a lower brightness than in (a), and the gadolinium in region 4 cannot be seen in any of the PCA components.

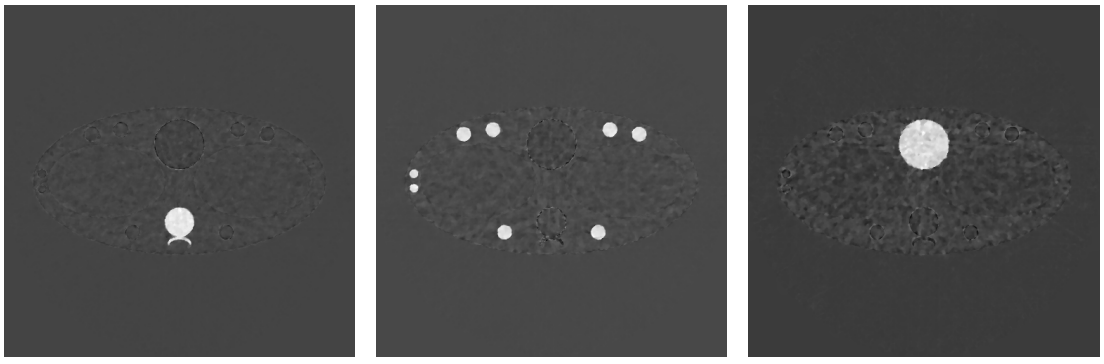

(a) **(b)** **(c)**

Figure 6.16: The first three component images from ICA applied to spectral CS-SIT reconstructions of the simulated thorax phantom. The second (b) and third (c) components enhance iodine and gadolinium respectively, while bone appears in the first component (a). Soft tissue contributes to all three components.

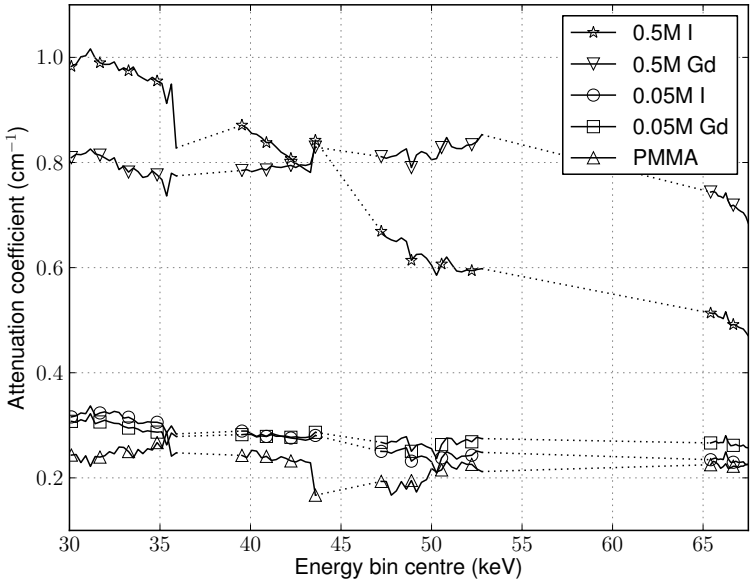

Figure 6.17: Attenuation spectra reconstructed from the prototype scan of Phantom B. The centre of the high energy bins is taken to be midway between the threshold energy and 80 keV (which is where the efficiency of 300 µm GaAs is less than 15%). Note the lack of any obvious k-edges. The values are averages taken over the known regions within the phantom. Markers are shown sparsely to aid readability, and the dotted lines indicate where no measurements were made.

The number of energy bins considered by the decomposition routines differed between the real and simulated data sets. Real projection data was collected at every discrete energy threshold within the ranges of 28–38 keV and 45–55 keV, totalling 76 thresholds (thresholds were discretised to 0.27 keV steps). Energy bins of approximately 4 keV width (as suggested by He et al. (2012)) were created by subtracting appropriate thresholds, then each energy bin was reconstructed independently. The mean attenuation within several regions was found and is plotted in Figure 6.17. This plot shows that neither of the two k-edges are clearly resolved by the data. The principal cause of this poor resolution is believed to be charge sharing (Korn et al., 2007), and studies by other members of the MARS group have found that charge-summing mode[(3)] greatly enhances the measured spectrum. Because of the poor spectral resolution, the reconstructed prototype data can not be separated unless all energy bins are considered. In contrast, since the simulation does not model charge sharing and assumes the detector pixels all have equivalent energy response, the reconstructed spectra of the simulated data are much better and good quality decomposition is possible with eight energy thresholds chosen to measure both sides of each k-edge. Eight are used to match the number of counters in a Medipix3 detector.

6.2.2.2 Interior FOV

The effect of reducing the spectral interior FOV was studied. Simulated hybrid reconstructions of Phantom B with two representative truncation levels are shown in Figure 6.18. The loss of spectral fidelity, especially outside the FOV, can be seen in the top images (small FOV) compared to the bottom row (larger FOV). As can be expected, reduced spectral FOV causes reduced spectral fidelity. To quantify this effect, EFOV values were calculated for the simulated and real Phantom B data, along with simulated thorax phantom data, and are plotted in Figure 6.19. The line of identity in each of the plots in Figure 6.19 marks where the EFOV is equal to the actual FOV; where the plot is above this line, the EFOV is larger than the actual FOV. Figure 6.19(a) shows that the EFOV generally rises with the FOV and is greater than the FOV over the whole range of truncation levels apart from two instances of the prototype data. The CS-SIT reconstructions exhibit slightly greater EFOV values than the corresponding FBP reconstructions in most cases, although this claim is weakened by the fact that the worst individual data point on the plot belongs to CS-SIT. Figure 6.19(b) shows that the EFOV somewhat plateaus when the interior FOV contains most of the contrast agent volume (FOV $\approx 50\%$), suggesting that the truncated spectral accuracy is dependent on the structure of the sample.

[(3)] A mode of operation for Medipix3 chips whereby arbitration is performed between neighbouring pixels to counteract charge sharing.

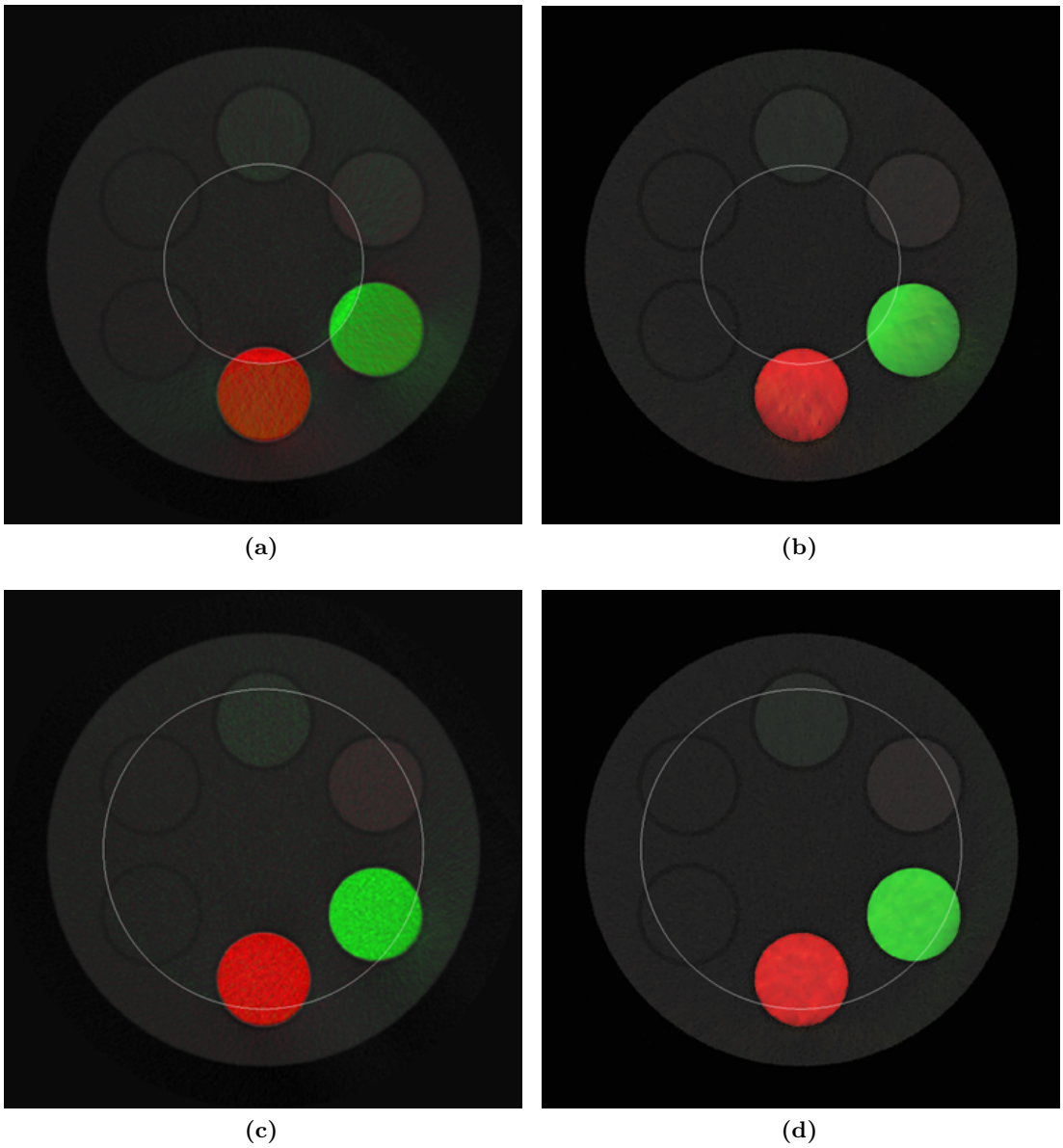

(a) **(b)**

(c) **(d)**

Figure 6.18: Hybrid spectral reconstructions after ICA and colour-mapping of simulated projection data. Top row shows 46% FOV, bottom row shows 74% FOV. Left shows FBP reconstructions, right shows CS-SIT reconstructions. Observe that the contrast agents are identified beyond the FOV (marked with a white circle), and that the accuracy of this identification reduces with distance beyond the FOV. In (a), for example, many of the voxels that ought to be bright red (gadolinium) are in fact green (iodine). The

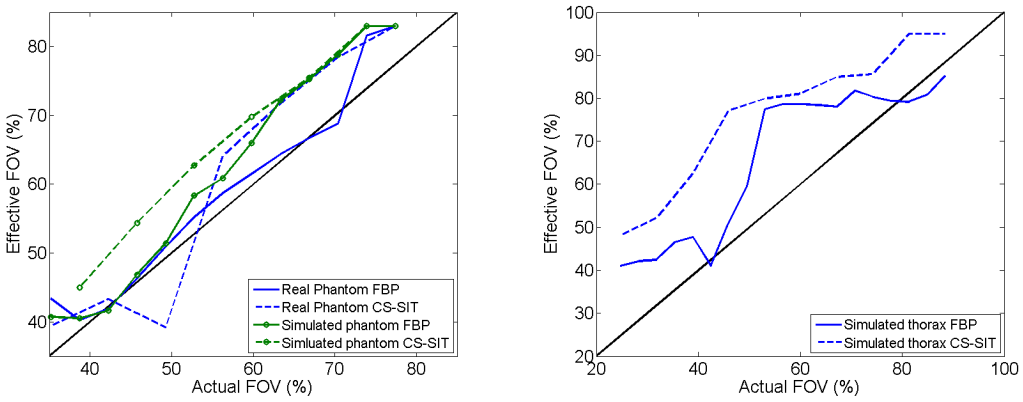

(a) **(b)**

Figure 6.19: EFOV versus actual FOV for hybrid reconstructions of (a) the simulated and prototype Phantom B data sets, and (b) simulated thorax phantom data.

The plots in Figure 6.19(a) suggest that the EFOV is generally not much larger than the actual FOV. However, Figure 6.18 shows that contrast agent identification remains possible (albeit less reliable) outside the EFOV boundary and is dependent not only on radius but also on contrast agent concentration. The higher concentration contrast agent regions (2 and 3 in Figure 6.10) are reliably decomposed even with a narrow FOV, while the regions of medium concentration (4 and 5 in Figure 6.10) more rapidly lose spectral fidelity. The lowest concentrations can not be decomposed even with full FOV spectral data, and thus are not considered. The plots of Figure 6.19(b) demonstrate somewhat better EFOV versus actual FOV than those of Figure 6.19(a). A possible reason for this is that the thorax phantom does not have contrast agent concentrations as low as Phantom B; a second possibility is that the structure of the thorax phantom leads to more reliable decomposition. In summary, EFOV is larger than the FOV in general and the relationship between EFOV and FOV is object dependent.

6.2.2.3 Number of interior projections

Next, the number of interior spectral projections was studied to evaluate its effect on CNR and EFOV. Hybrid reconstructions are shown in Figure 6.20 with two representative numbers of interior projections and an interior FOV of 60%. For the small number of projections (40) on the top row, CS-SIT shows better noise suppression while FBP shows slightly better homogeneity. The results in Figure 6.21 demonstrate that using a larger number of interior projections produces higher CNR, whereas Figure 6.22 shows that the EFOV appears to remain relatively constant once the number of projections surpasses some threshold between about 120 and 180 projections. The EFOV exhibits large fluctuations below this threshold for the simulated data set. Again the difference

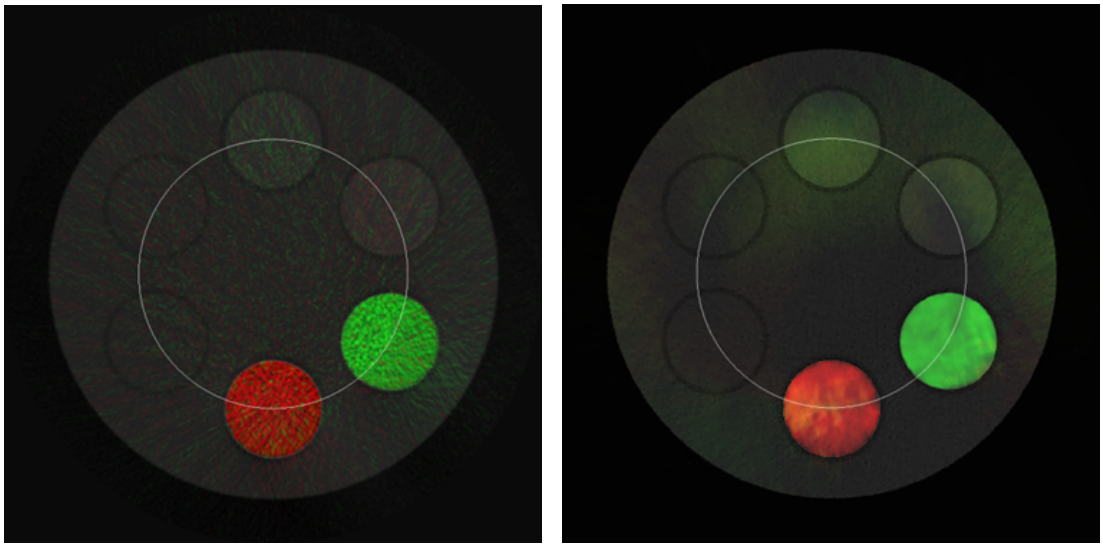

(a) (b)

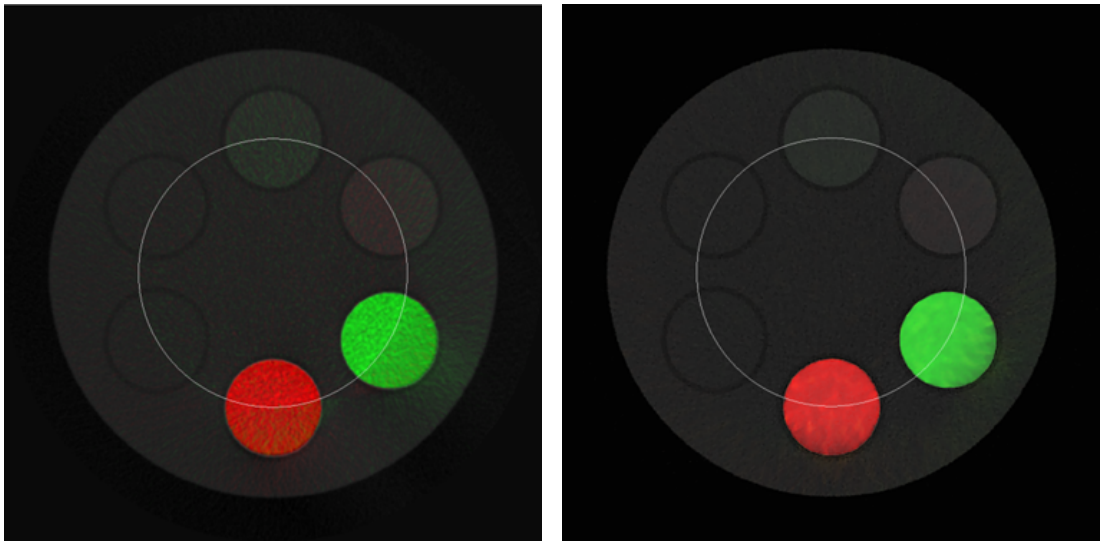

(c) (d)

Figure 6.20: Hybrid spectral reconstructions of Phantom B simulation data with FOV of 60%, after ICA and colour-mapping, showing the effect of decreasing the number of interior projections. Top row shows 40 spectral projections, bottom row shows 240 spectral projections. Left shows FBP reconstructions, right shows CS-SIT reconstructions. Observe the lower image quality in the top row: (a) exhibits greater noise and (b) shows lower homogeneity than the corresponding images in the bottom row.

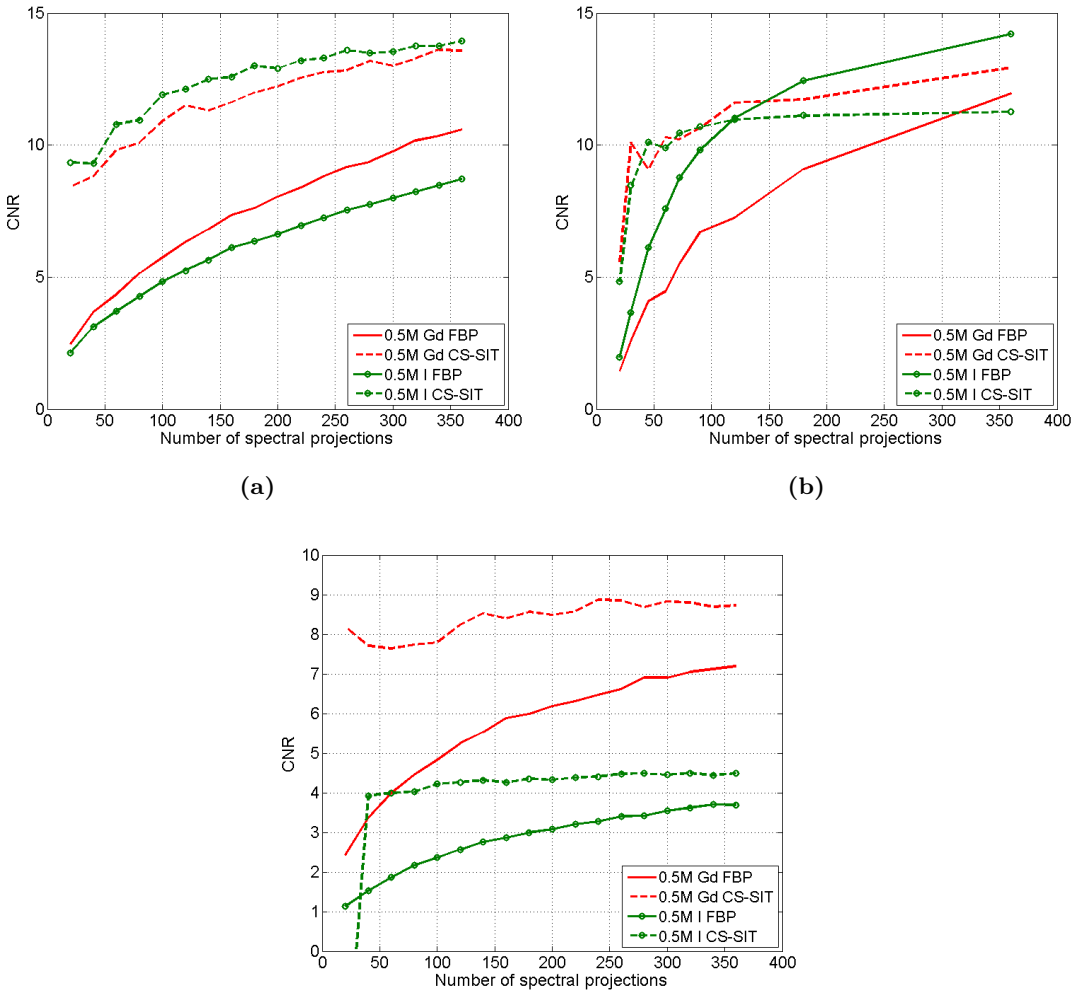

Figure 6.21: CNR versus number of interior spectral projections for the (a) simulated Phantom B, (b) real Phantom B, and (c) simulated thorax phantom reconstructions.

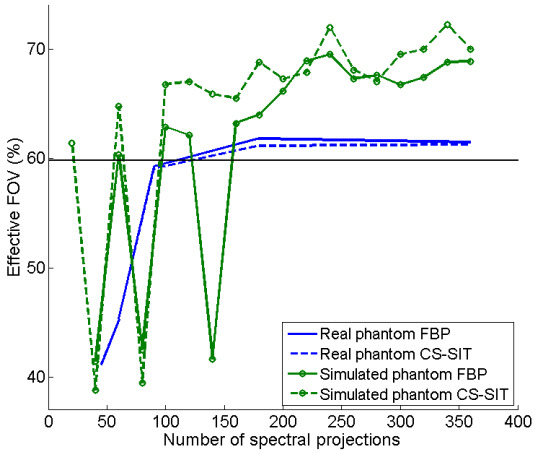

Figure 6.22: Effective FOV versus number of interior spectral projections for simulated and real Phantom B reconstructions. The black horizontal line marks the actual FOV for these measurements.

between CS-SIT and FBP is greatest in the simulated results (Figures 6.21(a) and 6.21(c)) whereas very little difference appears in the EFOV plots for the real scan data (Figure 6.21(b)). The greater EFOV results with simulated data are conjectured to be due to the simulated attenuation spectra having less distortion than the real measured attenuation spectra. CS-SIT reconstructions also appear to have a higher CNR than FBP reconstructions in most of the reconstructed data sets. It is interesting to observe that for the prototype and thorax data sets, the CS-SIT CNR stays approximately constant over most of the plot, while for the simulated Phantom B data set (Figure 6.21(a)) the CNR of the CS-SIT reconstructions follows a curve similar in shape to that of the FBP reconstructions. The cause of this difference in behaviour is unclear.

6.2.2.4 Number of global projections

Finally, the number of global projections was studied to determine its effect on the reconstructed greyscale CNR. Reconstructions for two representative numbers of global projections and with a spectral FOV of 60% are shown in Figure 6.23. The visible effect of reducing the number of global projections differs between the reconstruction methods: with FBP, having few projections causes streaks to appear and the noise level to increase, while in CS-SIT the image becomes “patchier” in homogeneous regions. My understanding is that this is due to the smoothing effect of TV minimisation operating on the greater noise level. CNR values in Figure 6.24 show that CS-SIT slightly outperforms FBP in the simulated and real studies of Phantom B. However, the FBP method performs better for the thorax phantom. In all cases both reconstruction methods show a very similar relationship between the number of global projections and

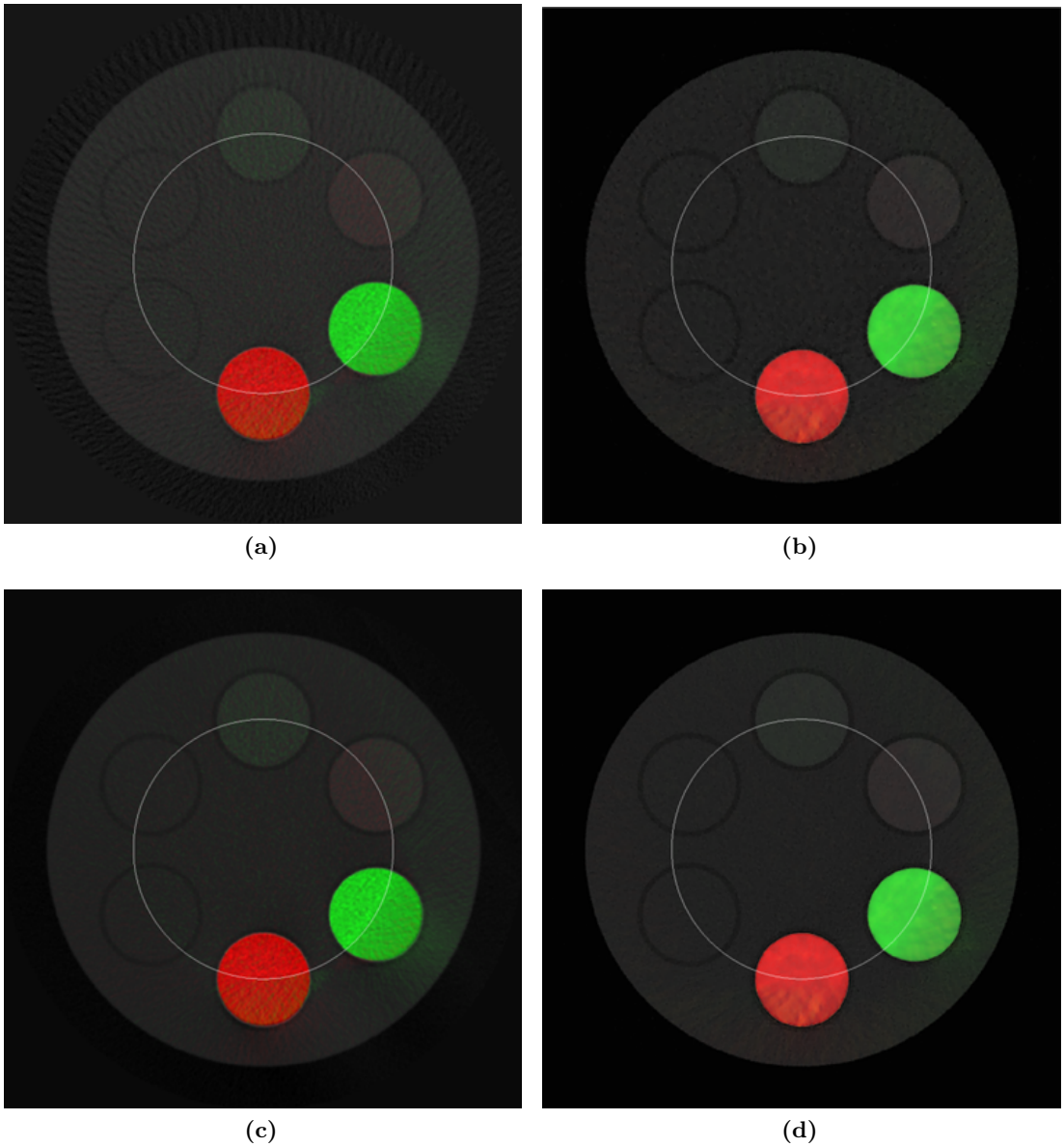

(a) **(b)**

(c) **(d)**

Figure 6.23: Hybrid spectral reconstructions of Phantom B simulation data with FOV of 60%, after ICA and colour-mapping, showing the effect of decreasing the number of global projections. Top row shows 100 global projections, bottom row shows 700 global projections. Left shows FBP, right shows CS-SIT. Observe that (a) contains streaking while (c) does not, and (b) is dappled while (d) is not. The features mentioned can be hard to see on paper, but are more visible on a computer screen.

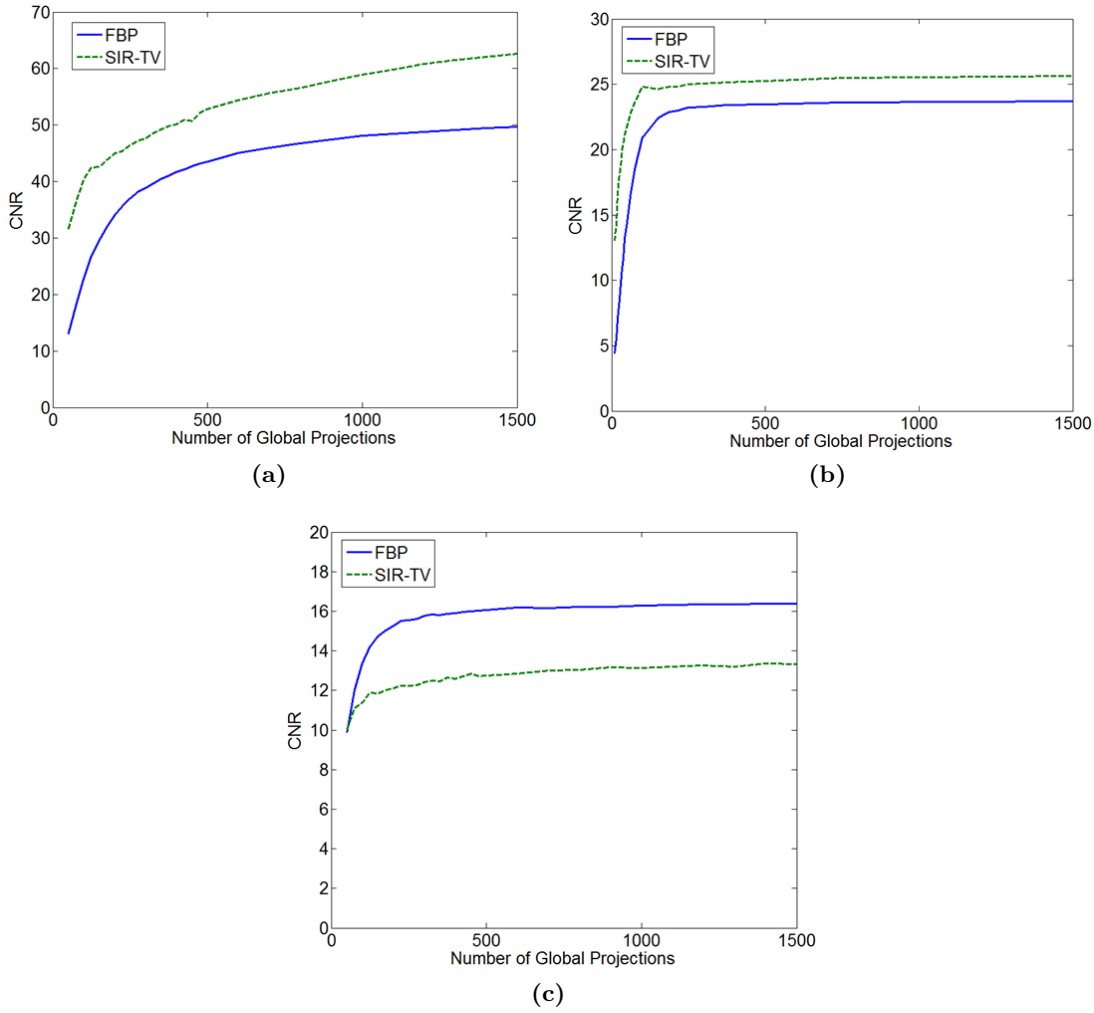

Figure 6.24: CNR of greyscale reconstructions as a function of the number of global projections for the (a) simulated Phantom B, (b) real Phantom B, and (c) simulated thorax phantom.

the CNR, exhibiting a gentle decline in CNR as the number of projections drops from 1500, then a knee at 100–200 projections below which the CNR drops more rapidly.

6.2.3 Discussion

Reducing exposure generally also reduces either the quantity or quality of data available for reconstruction. The cases studied here all reduced the data quantity, whereas exposure reduction by other means (e.g. decreasing flux or acquisition time) would reduce the data quality since the signal-to-noise ratio (SNR) of an x-ray measurement is proportional to the square-root of the measurement due to its Poisson nature (Buzug, 2008). Reduction of the quantity of data always results in reduced reconstruction quality for a given reconstruction algorithm, so there is always a trade-off between radiation exposure and quality of the reconstructed image, and research is constantly ongoing to develop advanced algorithms for better image reconstruction from a given set of projections. This study did not investigate the effects of scan parameters such as acquisition time or beam flux; hence absolute dose values are not given, only relative exposure values.

The overall finding is that there is further scope for radiation exposure reduction—and hence dose reduction—in the hybrid scan protocol. The number of global projections clearly need not be 1500, a figure close to 300 is more appropriate and corresponds to an exposure reduction of 80% in the global imaging chain relative to the manufacturer recommended protocol. The number of interior spectral projections need not be 360, either; it could be reduced by up to 50% compared with previous hybrid scan protocols. Finally, the spectral FOV need not be larger than the region of interest (ROI). It appears to be feasible to reduce the FOV to be inside the ROI, as spectral information extends beyond the FOV. Acceptable FOV truncation levels depend on the expected concentration of the contrast agent(s) within the sample, leading to a trade-off: a narrower spectral FOV can be achieved if the contrast agent concentration is increased. However, there are practical limits to the permissible contrast agent concentration, principally patient toxicity (Prince et al., 1996). This trade-off also applies to the number of spectral projections to a certain extent. A comprehensive study of the relationship between contrast agent concentration and the combination of spectral FOV and number of spectral projections is warranted.

A probable reason why the CNR of images reconstructed with the iterative techniques is often greater than that of images reconstructed with FBP is that SIR-TV and CS-SIT include a smoothing operation which suppresses the amount of variation in the images. It may be possible to increase the CNR of the FBP images to similar levels by applying a post-reconstruction smoothing filter. However, these results are presented not to compare the absolute CNR values between reconstruction algorithms but to observe the relative behaviour of each plot. The results presented here show

that the two algorithms exhibit a similar behaviour in response to decreasing numbers of global projections. Conversely, the response to decreasing the number of interior projections varied between data sets: in two cases the CNR of the CS-SIT images did not change significantly with a decreasing number of projections, but in a third case the CNR responded to the decrease by itself declining. Thus it is not safe to assume that CS-SIT is unaffected by decreasing numbers of projections.

Comparison of the results presented here suggests that CS-SIT generally outperforms FBP for hybrid reconstruction. The smoother reconstructions appear to slow the deterioration of spectral fidelity with increasing distance from the FOV. An additional consideration is the reconstruction time: a single CS-SIT reconstruction takes nearly 19 minutes while a single FBP reconstruction with comparable optimisation takes only 23 seconds. These routines can be optimised and multiple energy bins can be reconstructed in parallel, but these numbers are indicative of the relative computational expense of the algorithms. This large difference in computational expense may outweigh the slight quality advantage of CS-SIT in some situations and promote the selection of the FBP method instead.

The EFOV is useful as a measure of interior reconstruction quality. It is worth noting that the EFOV does not delineate a boundary beyond which there is no spectral information, rather, spectral information does extend beyond the EFOV but it is less reliable. In this study, the accuracy threshold was set to 90%; an appropriate value for this threshold could differ for other studies, where more or less reliability is desired. 90% was chosen after considering a small set of options: 95% was found to be too conservative compared to visual inspection, and while 85% produced apparently reasonable measurements, it was considered to be too generous. The EFOV has here been defined according to the identification of two contrast agents, as this is an easily calculated quantity and is representative of one possible application of spectral CT. It could be readily redefined to operate with any other quantitative measure of image quality, either spectral or greyscale, to suit other applications of interior reconstruction. The EFOV is evaluated as the radius of a circle for two reasons: it allows straightforward comparison to the circular FOV, and it makes the values simple to interpret, i.e., a larger EFOV is better.

This work has identified several promising areas for follow-up studies. In addition to measuring the relationship between contrast agent concentration and EFOV, optimising the parameters that control the iterative reconstruction techniques would be worthwhile. CS-SIT only uses the global reconstruction as an initial image estimate, hence the influence of the global image diminishes and the image quality outside the FOV deteriorates as the iterations advance. Naturally, performing zero iterations would not incorporate the spectral data into the reconstruction, so an optimal number of iterations that maximises the spectral image quality while minimising interior reconstruction artefacts must exist. The objective TV parameter controls the amount of smoothing

performed by the TV minimisation; this parameter has been kept constant across all reconstructions to allow a fair comparison, but the amount of smoothing that results from a particular value was observed to be dependent on the image being reconstructed. A means to separate this parameter from the image and an optimisation study would enhance the results generated using this relatively new algorithm.

6.2.4 Conclusion

Several promising methods have been investigated for exposure reduction in the hybrid spectral micro-CT architecture. The effects of decreasing the spectral FOV, the number of spectral projections, and the number of global projections have been studied and exposure reductions up to 80% relative to the manufacturer recommendation were found to be achievable. Several further areas have been found that need optimisation. The iterative reconstruction algorithms outperform FBP, although the latter did produce reasonable results with much lower computational cost.

Chapter Seven

Conclusions and future work

This dissertation presents research toward the advancement of spectral CT, in particular Compton scatter estimation and interior tomography. An algorithm for calculating energy-resolved estimates of Compton scatter is developed and verified against Monte Carlo simulations, and an approximation used in its derivation is analysed in more detail. A brief study is made of one interior reconstruction technique, which finds the technique to be quite sensitive to error. A novel scanner architecture is described and prototype system results are analysed. The architecture is further studied from the perspective of radiation exposure reduction, and the effect on the spectral fidelity of the reconstructed images is evaluated. This chapter summarises and briefly discusses the results and conclusions of the research presented in the rest of the dissertation, and suggests directions for further research related to each part.

7.1 Scatter estimation

In Chapter 4, a new algorithm is developed for estimating Compton scatter levels in a spectral micro-CT scan, then one approximation from that algorithm is analysed. The algorithm, "IBLESS", analytically calculates the intensity of single Compton scatter and the final energy of the scattered photons. Comparisons of the output of IBLESS with the output of Monte Carlo simulations showed that IBLESS produced very accurate estimates. One of the findings of the verification study is that the energy lost by a photon in a single Compton scatter interaction is rarely enough to cause that photon to be detected in a different energy bin to that in which it began its life (for practically-sized energy bins). From this result, much of the complexity of IBLESS could be considered redundant for standard scatter correction; however, situations exist where narrow bins are desirable, or alternatively, IBLESS could be incorporated into simulation code, for example that of Algorithm 1. The computational cost of IBLESS is significantly lower than that of the corresponding Monte Carlo simulation using BEAMnrc: 3.5 seconds for IBLESS versus approximately 32 hours for Monte Carlo. However, the model used by IBLESS is limited to micro-CT, for two reasons. First, only single scatter is considered, because the complexity required for modelling multiple scatter in

the same framework is prohibitive, but multiple scatter far exceeds single scatter for objects beyond the micro-CT scale. Second, a "zero angle approximation" is made in the derivation of IBLESS, and the analysis of this approximation in the second part of Chapter 4 indicates that the error introduced by this approximation varies with both the size and the composition of the object. For medically relevant materials, the error introduced at micro-CT scale reaches about 5%, but for human sized objects (such as a human) the error is unacceptably large.

IBLESS is not yet ready for application to real scan data. The model does not currently account for the electron binding effect on Compton scatter, which alters the spatial distribution of scattered photons. The development in Chapter 4 focuses solely on Compton scatter because that variety affects the energy of the photons, but in reality Rayleigh scatter also occurs and causes artefacts similar to those caused by Compton scatter. Calculation of both of these phenomena needs to be added to the model to allow IBLESS to estimate actual scatter intensities. Finally, the present implementation of IBLESS assumes parallel beam geometry. Modern scanners do not use this geometry but rather a fan or cone beam, so the implementation must be updated to operate with these geometries. Upon completion of these improvements, the estimates produced by IBLESS need to be verified against real scan measurements.

7.2 Interior tomography

In Chapter 5, the DBP-POCS interior reconstruction algorithm is tested to determine its sensitivity to error in the prior knowledge. Errors in the mean value of the known region are found to introduce both offset and cupping errors to the reconstruction, while noise in the known region spreads across the whole reconstruction. Overall, the algorithm is not very stable and published results could not be reproduced.

The largest contribution of this dissertation is the work on the hybrid spectral interior architecture, which combines a full field of view (FOV) conventional imaging chain and an interior FOV spectral imaging chain. This design takes advantage of both the high spatial resolution possible with modern conventional x-ray detectors and the energy resolution offered by new spectral detectors. It reduces the size requirement for cutting-edge spectral detector technology by only using an interior FOV for the spectral imaging chain, and enables faster scan time and better image quality in the interior region. Chapter 6 reports two studies on this new architecture, the first analysing data from the first prototype system, to confirm the expected results, and the second evaluating the effect of exposure reduction measures on spectral fidelity. Simulated and experimental data sets are reconstructed with an iterative interior reconstruction algorithm, and analysis with principal components analysis (PCA) demonstrates the results predicted in the original proposal paper by Xu et al. (2012). Separation of two contrast agents, iodine and gadolinium, is found to be possible within the interior

FOV, although only the k-edge of iodine can be observed because the low efficiency of the silicon detector layer at the k-edge of gadolinium (50.2 keV) precluded meaningful measurements around this energy. Based on this study, the hybrid architecture is considered to show promise and warrant further investigation.

The second study in Chapter 6 continues the exploration of the hybrid architecture. Three elements of the scan protocol are reduced for the purpose of radiation exposure reduction and the effect on spectral fidelity is evaluated. The three protocol elements are the width of the interior spectral FOV, the number of interior spectral projections, and the number of conventional projections. In addition, a new FBP-based hybrid reconstruction method is described and its output is compared against that of the iterative method from the first study ("CS-SIT"). Differentiation between iodine and gadolinium is used as a simple measure of spectral fidelity. All three protocol elements are found to have scope for reduction whilst maintaining the quality of the hybrid reconstructions; in particular, the number of conventional projections can be lowered by as much as 80% (compared to previously used protocols based on the recommendations of the equipment manufacturer) without significant loss in image quality. The number of spectral projections can also be reduced, although not by the same proportion. The interior FOV width depends on several factors. The results of the first study suggest that useful spectral information extends beyond the spectral FOV, so this phenomenon is considered further in the second study. Evidence is again found to support this claim, but the extent of the "spectral dispersion" is found to be dependent on both the structure of the object and on the concentration of the contrast agents within it. Greater concentration leads to greater dispersion, however there is insufficient information to fully characterise the effect of object structure. For these reasons a simple description of how far the interior FOV can be truncated could not be made, except that it need not be larger than the area in which contrast agent is expected, and that it may be possible to shrink it further than that. The new FBP-based hybrid reconstruction method is found to be significantly faster than CS-SIT, however the spectral fidelity of the reconstructed images is slightly better with CS-SIT.

The studies on the hybrid scanner have suggested several avenues of future work. The relationship between contrast agent concentration and effective FOV extension ought to be studied further to obtain a more complete understanding of the trade-off between the two. Similarly, the effect of different structures in the object upon spectral dispersion needs to be further explored to provide context for any findings on the dependence on contrast agent concentration. Optimisation of CS-SIT appears to be possible, which should further improve the quality of hybrid images reconstructed with this method. This optimisation should focus on the number of iterations that should be applied, and on a means for identifying a suitable objective value for the total variation step. James and I are presently engaged in studying the optimal width for energy bins for k-edge imaging, and initial results suggest that the optimal width may be larger than

what is published elsewhere and was used in these studies. Thus further improvement to contrast agent resolution may be possible with the results of the present study.

7.3 Concluding thoughts

I believe that spectral imaging is next major advance in CT technology. The technology is advancing rapidly; I have seen notable improvements even during the short period of my studies in the field. However, there is still plenty of scope for detector technology improvement, in terms of both semiconductor layers and processing electronics, and the speed at which this technology matures will have a large impact on how soon spectral imaging is adopted into pre-clinical and clinical use. Image processing techniques are being continually improved, and are well ahead of the physical technology due to many simulation studies. However, many of the techniques are grounded entirely in simulation, thus validation of the techniques as detectors improve is vital in confirming the feasibility of these techniques. I hope that the research reported in this dissertation goes some way to helping the modality along the path to clinical adoption and I look forward to seeing the future progress of the field.

References

Achenbach, S., Ulzheimer, S., Baum, U., Kachelrieß, M., Ropers, D., Giesler, T., Bautz, W., Daniel, W. G., Kalender, W. A., and Moshage, W. (2000), 'Noninvasive coronary angiography by retrospectively ECG-gated multislice spiral CT', *Circulation* **102**(23), 2823–2828.

Als-Nielsen, J. and McMorrow, D. (2011), *Elements of Modern X-ray Physics*, John Wiley & Sons, Hoboken, NJ, USA.

Alvarez, R. E. (2010), 'Near optimal energy selective x-ray imaging system performance with simple detectors', *Medical Physics* **37**(2), 822–841.

Alvarez, R. E. and Macovski, A. (1976), 'Energy-selective reconstructions in x-ray computerized tomography', *Physics in Medicine and Biology* **21**(5), 733–744.

Amsel, G., Bosshard, R., and Zajde, C. (1967), 'Processing of detector signals at very high counting rates for precision pulse-height analysis', *IEEE Transactions on Nuclear Science* **14**(1), 1–48.

Andersen, A. H. and Kak, A. C. (1984), 'Simultaneous algebraic reconstruction technique (SART): a superior implementation of the ART algorithm', *Ultrasonic Imaging* **6**(1), 81–94.

Anderson, N., Butler, A., Scott, N., Cook, N., Butzer, J., Schleich, N., Firsching, M., Grasset, R., de Ruiter, N., Campbell, M., and Butler, P. (2010), 'Spectroscopic (multi-energy) CT distinguishes iodine and barium contrast material in mice', *European Radiology* **20**(9), 2126–2134.

Anton, G., Gebert, U., Michel, T., and Rügheimer, T. K. (2009), 'A hybrid photodetector using the timepix semiconductor assembly for photoelectron detection', *Nuclear Instruments and Methods in Physics Research Section A: Accelerators, Spectrometers, Detectors and Associated Equipment* **602**(1), 205–208.

Ardran, G. M. and Crooks, H. E. (1964), 'The reduction of scatter fog in chest radiography', *British Journal of Radiology* **37**(438), 477–479.

Baba, R., Konno, Y., Ueda, K., and Ikeda, S. (2002), 'Comparison of flat-panel detector and image-intensifier detector for cone-beam CT', *Computerized Medical Imaging and Graphics* **26**(3), 153–158.

Badea, C., Hedlund, L. W., and Johnson, G. A. (2004), 'Micro-CT with respiratory and cardiac gating', *Medical Physics* **31**(12), 3324–3329.

Ball, J., Moore, A. D., and Turner, S. (2012), *Ball and Moore's Essential Physics for Radiographers*, John Wiley & Sons, Chichester, UK.

Ballabriga, R., Campbell, M., Heijne, E., Llopart, X., and Tlustos, L. (2007), 'The Medipix3 prototype, a pixel readout chip working in single photon counting mode with improved spectrometric performance', *IEEE Transactions on Nuclear Science* **54**(5), 1824–1829.

Ballabriga, R., Campbell, M., Heijne, E., Llopart, X., Tlustos, L., and Wong, W. (2011), 'Medipix3: A 64k pixel detector readout chip working in single photon counting mode with improved spectrometric performance', *Nuclear Instruments and Methods in Physics Research Section A: Accelerators, Spectrometers, Detectors and Associated Equipment* **633**(S1), S15–S18.

Barrett, H. H. and Swindell, W. (1981), *Radiological Imaging: The theory of Image Formation, Detection, and Processing*, Academic Press, San Diego, CA, USA.

Basu, S. and De Man, B. (2006), 'Branchless distance driven projection and back-projection', *in* 'Computational Imaging IV', Vol. 6065 of *Proceedings of the SPIE*, p. 60650Y.

Bates, R. H. T. and Peters, T. M. (1971), 'Towards improvements in tomography', *NZ Journal of Science* **14**, 883–896.

Bauschke, H. H. and Borwein, J. M. (1993), 'On the convergence of von Neumann's alternating projection algorithm for two sets', *Set-Valued Analysis* **1**(2), 185–212.

Beer, A. (1852), 'Bestimmung der Absorption des rothen Lichts in farbigen Flüssigkeiten', *Annalen der Physik und Chemie* **86**(5), 78–88.

Bennett, J. R., Opie, A. M. T., Xu, Q., Yu, H., Walsh, M., Butler, A., Butler, P., Cao, G., Mohs, A., and Wang, G. (2013), 'Hybrid spectral micro-CT: System design, implementation and preliminary results', *IEEE Transactions on Biomedical Engineering*.

Bentzen, S. M. (1983), 'Evaluation of the spatial resolution of a CT scanner by direct analysis of the edge response function', *Medical Physics* **10**(5), 579–581.

Berger, M. J., Hubbell, J. H., Seltzer, S. M., Chang, J., Coursey, J. S., Sukumar, R., Zucker, D. S., and Olsen, K. (2010), XCOM: Photon cross sections database (version 1.5), Technical Report 87-3597, National Institute of Standards and Technology, Gaithersburg, MD, USA. Available at `http://physics.nist.gov/xcom`.

Bertram, M., Sattel, T., Hohmann, S., and Wiegert, J. (2008), 'Monte-Carlo scatter correction for cone-beam computed tomography with limited scan field-of-view', *in* 'Medical Imaging 2008: Physics of Medical Imaging', Vol. 6913 of *Proceedings of the SPIE*, p. 69131Y.

Bharath, A. (2009), *Introductory Medical Imaging*, Morgan & Claypool, San Rafael, CA, USA.

Bones, P. J., Butler, A. P. H., Ronaldson, J. P., and Opie, A. M. T. (2010), 'Development of a CT scanner based on the Medipix family of detectors', *in* 'Developments in X-Ray Tomography VII', Vol. 7804 of *Proceedings of the SPIE*.

Boone, J. and Seibert, J. (1988), 'An analytical model of the scattered radiation distribution in diagnostic radiology', *Medical Physics* **15**(5), 721–725.

Bracewell, R. N. (1986), *The Fourier Transform and its Applications*, 2nd edn, McGraw-Hill, Singapore.

Brooks, R. A. and Chiro, G. D. (1976), 'Beam hardening in x-ray reconstructive tomography', *Physics in Medicine and Biology* **21**(3), 390–398.

Brooks, R. A., Di Chiro, G., and Keller, M. R. (1980), 'Explanation of cerebral white-gray contrast in computed tomography', *Journal of Computed Assisted Tomography* **4**(4), 489–491.

Bushberg, J. T., Seibert, J. A., Leidholdt, Jr., E. M., and Boone, J. M. (2012), *The Essential Physics of Medical Imaging*, 3rd edn, Lippincott Williams & Wilkins, Philadelphia, PA, USA.

Butler, A. P. H., Butzer, J., Schleich, N., Cook, N. J., Anderson, N. G., Scott, N., de Ruiter, N., Grasset, R., Tlustos, L., and Butler, P. H. (2011*a*), 'Processing of spectral x-ray data with principal components analysis', *Nuclear Instruments and Methods in Physics Research Section A: Accelerators, Spectrometers, Detectors and Associated Equipment* **633**(S1), S140–S142.

Butler, A., Ronaldson, P., Walsh, M., Aamir, R., Doesburg, R., de Ruiter, N., Scott, N., Zainon, R., Giesig, S., Woodfield, T., Siegert, A., Mohr, J., Anderson, N., and Butler, P. (2011*b*), 'Development of a Medipix3 based spectral (multi-energy) CT for pre-clinical evaluation of biomarkers', *in* 'Royal Australian and New Zealand College of Radiologists Annual Scientific Meeting'.

Butzer, J. S., Butler, A. P. H., Butler, P. H., Bones, P. J., Cook, N., and Tlustos, L. (2008), 'Medipix imaging – evaluation of datasets with PCA', *in* 'Image and Vision Computing New Zealand 2008', pp. 1–6.

Buzug, T. M. (2008), *Computed Tomography: From Photon Statistics to Modern Cone-Beam CT*, Springer-Verlag, Berlin, Heidelberg, Germany.

Cao, G., Lee, Y. Z., Peng, R., Liu, Z., Rajaram, R., Calderon-Colon, X., An, L., Wang, P., Phan, T., Sultana, S., Lalush, D. S., Lu, J. P., and Zhou, O. (2009), 'A dynamic micro-CT scanner based on a carbon nanotube field emission x-ray source', *Physics in Medicine and Biology* **54**(8), 2323–2340.

Clackdoyle, R. and Defrise, M. (2010), 'Tomographic reconstruction in the 21st century', *IEEE Signal Processing Magazine* **27**(4), 60–80.

Clackdoyle, R., Noo, F., Guo, J., and Roberts, J. A. (2004), 'Quantitative reconstruction from truncated projections in classical tomography', *IEEE Transactions on Nuclear Science* **51**(5), 2570–2578.

Colijn, A. and Beekman, F. (2004), 'Accelerated simulation of cone beam x-ray scatter projections', *IEEE Transactions on Medical Imaging* **23**(5), 584–590.

Courdurier, M., Noo, F., Defrise, M., and Kudo, H. (2008), 'Solving the interior problem of computed tomography using *a priori* knowledge', *Inverse Problems* **24**(6), 065001.

Crawford, C. R. (1986), 'Reprojection using a parallel backprojector', *Medical Physics* **13**(4), 480–483.

Cunningham, I. and Philip, J. (2006), *The Biomedical Engineering Handbook*, Vol. 2, 3rd edn, CRC Press, Boca Raton, FL, USA.

De Man, B. and Basu, S. (2002), 'Distance-driven projection and backprojection', *in* '2002 IEEE Nuclear Science Symposium Conference Record', Vol. 3, pp. 1477–1480.

De Man, B. and Basu, S. (2004*a*), 'Distance-driven projection and backprojection in three dimensions', *Physics in Medicine and Biology* **49**(11), 2463–2475.

De Man, B. and Basu, S. (2004*b*), 'A study of noise and spatial resolution for 2D and 3D filtered backprojection reconstruction', *in* '2004 IEEE Nuclear Science Symposium Conference Record', Vol. 6, pp. 3937–3939.

Defrise, M., Noo, F., Clackdoyle, R., and Kudo, H. (2006), 'Truncated Hilbert transform and image reconstruction from limited tomographic data', *Inverse Problems* **22**(3), 1037–1053.

Del Sordo, S., Abbene, L., Caroli, E., Mancini, A., Zappettini, A., and Ubertini, P. (2009), 'Progress in the development of CdTe and CdZnTe semiconductor radiation detectors for astrophysical and medical applications', *Sensors* **9**(5), 3491–3526.

Dubois, P. F., Hinsen, K., and Hugunin, J. (1996), 'Numerical Python', *Computers in Physics* **10**(3).

Eby, P. (2005), 'Python 2.4 decorators', *Dr Dobb's Journal — Software Tools for the Professional Programmer* **30**, 54–57.
URL: *http://www.drdobbs.com/web-development/python-24-decorators/184406073*

Engel, K. J., Bäumer, C., Wiegert, J., and Zeitler, G. (2008), 'Spectral analysis of scattered radiation in CT', *in* 'Medical Imaging 2008: Physics of Medical Imaging', Vol. 6913 of *Proceedings of the SPIE*, p. R9131.

Epstein, C. L. (2008), *Introduction to the Mathematics of Medical Imaging*, 2nd edn, SIAM, Philadelphia, PA, USA.

Erdoğan, H. (1999), Statistical image reconstruction algorithms using paraboloidal surrogates for PET transmission scans, PhD thesis, University of Michigan.

Feldkamp, L. A., Davis, L. C., and Kress, J. W. (1984), 'Practical cone-beam algorithm', *Journal of the Optical Society of America A* **1**(6), 612–619.

Gomer, R. (1993), *Field Emission and Field Ionization*, American Vacuum Society Classics, American Institute of Physics, College Park, MD, USA.

Grass, M., Köhler, T., and Proksa, R. (1999), '3D cone-beam CT reconstruction for circular trajectories', *Physics in Medicine and Biology* **45**(2), 329–347.

Grodstein, G. W. (1957), X-ray attenuation coefficients from 10 keV to 100 MeV, Technical Report ADA278139, Defense Technical Information Center, Ft. Belvoir, VA, USA.

He, P., Wei, B., Cong, W., and Wang, G. (2012), 'Optimization of k-edge imaging with spectral CT', *Medical Physics* **39**(11), 6572–6579.

Hendee, W. R. and Ritenour, E. R. (2002), *Medical Imaging Physics*, 4th edn, Wiley–Liss, New York, NY, USA.

Herman, G. T. (1980), *Image Reconstruction from Projections*, Academic Press, Orlando, FL, USA.

Hofmann, H. G., Keck, B., Rohkohl, C., and Hornegger, J. (2011), 'Comparing performance of many-core CPUs and GPUs for static and motion compensated reconstruction of C-arm CT data', *Medical Physics* **38**(1), 468–473.

Hounsfield, G. N. (1977), 'The E.M.I. scanner', *Proceedings of the Royal Society of London* **195**(1119), 281–289.

Hsieh, J. (2003), *Computed Tomography: Principles, Design, Artifacts, and Recent Advances*, SPIE Press, Bellingham, WA, USA.

Hu, X., Shimizu, A., Kobatake, H., and Nawano, S. (2004), Independent component analysis of four-phase abdominal CT images, *in* C. Barillot, D. Haynor, and P. Hellier, eds, 'Medical Image Computing and Computer-Assisted Intervention 2004', Vol. 3217 of *Lecture Notes in Computer Science*, Springer Berlin Heidelberg, pp. 916–924.

Hubbell, J. H. and Seltzer, S. M. (2004), Tables of x-ray mass attenuation coefficients and mass energy-absorption coefficients (version 1.4), Technical report, National Institute of Standards and Technology, Gaithersburg, MD, USA. Available at `http://physics.nist.gov/xaamdi` [2013-04-07].

Hunter, A. K. and McDavid, W. D. (2012), 'Characterization and correction of cupping effect artefacts in cone beam CT', *Dentomaxillofacial Radiology* **41**(3), 217–223.

Hyvärinen, A. (1999), 'Fast and robust fixed-point algorithms for independent component analysis', *IEEE Transactions on Neural Networks* **10**(3), 626–634.

Hyvärinen, A. and Oja, E. (2000), 'Independent component analysis: algorithms and applications', *Neural Networks* **13**(4–5), 411–430.

Jarry, G., Graham, S., Moseley, D., Jaffray, D., Siewerdsen, J., and Verhaegen, F. (2006), 'Characterization of scattered radiation in kV CBCT images using Monte Carlo simulations', *Medical Physics* **33**(11), 4320–4329.

Jiang, M. and Wang, G. (2003), 'Convergence of the simultaneous algebraic reconstruction technique (SART)', *IEEE Transactions on Image Processing* **12**(8), 957–961.

Johns, H. E. and Cunningham, J. R. (1983), *The Physics of Radiology*, 4th edn, Charles C Thomas, Springfield, Illinois, USA.

Johns, P. and Yaffe, M. (1982), 'Scattered radiation in fan beam imaging systems', *Medical Physics* **9**(2), 231–239.

Joseph, P. and Spital, R. (1982), 'The effects of scatter in x-ray computed tomography', *Medical Physics* **9**(4), 464–472.

Kaczmarz, S. (1937), 'Angenäherte auflösung von systemen linearer gleichungen', *Bulletin International de l'Academie Polonaise des Sciences et des Lettres* **35**, 355–357.

Kaczmarz, S. (1993), 'Approximate solution of systems of linear equations', *International Journal of Control* **57**(6), 1269–1271. English translation of Kaczmarz (1937).

Kak, A. C. and Slaney, M. (1987), *Principles of Computerized Tomographic Imaging*, IEEE Press, New York, NY, USA.

Kalender, W. (1981), 'Monte Carlo calculations of x-ray scatter data for diagnostic radiology', *Physics in Medicine and Biology* **26**(5), 835–849.

Kalender, W. A. (1982), 'Calculation of x-ray grid characteristics by Monte Carlo methods', *Physics in Medicine and Biology* **27**(3), 353–361.

Kalukin, A. R., Van Geet, M., and Swennen, R. (2000), 'Principal components analysis of multienergy x-ray computed tomography of mineral samples', *IEEE Transactions on Nuclear Science* **47**(5), 1729–1736.

Katsevich, A. (2002), 'Analysis of an exact inversion algorithm for spiral cone-beam CT', *Physics in Medicine and Biology* **47**(15), 2583–2597.

Klein, O. and Nishina, Y. (1928), 'The scattering of light by free electrons according to Dirac's new relativistic dynamics', *Nature* **122**(3072), 398–399.

Korn, A., Firsching, M., Anton, G., Hoheisel, M., and Michel, T. (2007), 'Investigation of charge carrier transport and charge sharing in x-ray semiconductor pixel detectors such as Medipix2', *Nuclear Instruments and Methods in Physics Research Section A: Accelerators, Spectrometers, Detectors and Associated Equipment* **576**(1), 239–242.

Kotter, E. and Langer, M. (2002), 'Digital radiography with large-area flat-panel detectors', *European Radiology* **12**(10), 2562–2570.

Kudo, H., Courdurier, M., Noo, F., and Defrise, M. (2008), 'Tiny *a priori* knowledge solves the interior problem in computed tomography', *Physics in Medicine and Biology* **53**(9), 2207–2231.

Kyriakou, Y. and Kalender, W. (2007), 'X-ray scatter data for flat-panel detector CT', *Physica Medica* **23**(1), 3–15.

Lambert, J. H. (1760), *Photometria, sive de mensura et gradibus luminis, colorum et umbrae*, Sumptibus Viduae Eberhardi Klett.

Leipsic, J., LaBounty, T. M., Heilbron, B., Min, J. K., Mancini, G. B., Lin, F. Y., Taylor, C., Dunning, A., and Earls, J. P. (2010), 'Estimated radiation dose reduction using adaptive statistical iterative reconstruction in coronary CT angiography: the ERASIR study', *American Journal of Roentgenology* **195**(3), 655–660.

LeVine III., H. (2010), *Medical Imaging*, ABC-CLIO, Santa Barbara, CA, USA.

Lewitt, R. M. (1983), 'Reconstruction algorithms: Transform methods', *Proceedings of the IEEE* **71**(3), 390–408.

Lewitt, R. M. and Bates, R. H. T. (1978*a*), 'Image reconstruction from projections: I: General theoretical considerations', *Optik* **50**(1), 19–33.

Lewitt, R. M. and Bates, R. H. T. (1978*b*), 'Image-reconstruction from projections: III: Projection completion methods (theory)', *Optik* **50**(3), 189–204.

Llopart, X., Campbell, M., Dinapoli, R., San Segundo, D., and Pernigotti, E. (2002), 'Medipix2: A 64-k pixel readout chip with 55-µm square elements working in single photon counting mode', *IEEE Transactions on Nuclear Science* **49**(5), 2279–2283.

Lo, J. Y., Floyd, Jr., C. E., Baker, J. A., and Ravin, C. E. (1994), 'Scatter compensation in digital chest radiography using the posterior beam stop technique', *Medical Physics* **21**(3), 435–443.

Louis, L., Baud, P., and Wong, T.-F. (2007), 'Characterization of pore-space heterogeneity in sandstone by x-ray computed tomography', *Geological Society, London, Special Publications* **284**, 127–146.

Love, L. A. and Kruger, R. A. (1987), 'Scatter estimation for a digital radiographic system using convolutional filtering', *Medical Physics* **14**(2), 178–185.

Mikhlin, S. G. (1957), *Integral equations and their applications to certain problems in mechanics, mathematical physics, and technology*, Pergamon Press, New York, NY, USA.

Mohr, P. J., Taylor, B. N., and Newell, D. B. (2008), 'CODATA recommended values of the fundamental physical constants: 2006', *Journal of Physical and Chemical Reference Data* **37**(3), 1187–1284.

Natterer, F. (1986), *The Mathematics of Computerized Tomography*, John Wiley & Sons, Chichester, UK.

Neitzel, U. (1992), 'Grids or air gaps for scatter reduction in digital radiography: A model calculation', *Medical Physics* **19**(2), 475–481.

Nelson, R., Feuerlein, S., and Boll, D. (2011), 'New iterative reconstruction techniques for cardiovascular computed tomography: How do they work, and what are the advantages and disadvantages?', *Journal of Cardiovascular Computed Tomography* **5**(5), 286–292.

Niederlohner, D., Karg, J., Giersch, J., Firsching, M., and Anton, G. (2004), 'Practical aspects of energy weighting in x-ray imaging', *in* '2004 IEEE Nuclear Science Symposium Conference Record', pp. 3191–3194.

Ning, R., Tang, X., and Conover, D. (2004), 'X-ray scatter correction algorithm for cone beam CT imaging', *Medical Physics* **31**(5), 1195–1202.

Nishad, P. M. (2013), 'Various colour spaces and colour space conversion', *Journal of Global Research in Computer Science* **4**(1), 44–48.

Noo, F., Clackdoyle, R., and Pack, J. D. (2004), 'A two-step Hilbert transform method for 2D image reconstruction', *Physics in Medicine and Biology* **49**(17), 3903–3923.

Nuyts, J., De Man, B., Dupont, P., Defrise, M., Suetens, P., and Mortelmans, L. (1999), 'Iterative reconstruction for helical CT: a simulation study', *Physics in Medicine and Biology* **43**(4), 729–737.

Nuyts, J., Michel, C., and Dupont, P. (2001), 'Maximum-likelihood expectation-maximization reconstruction of sinograms with arbitrary noise distribution using NEC-transformations', *IEEE Transactions on Medical Imaging* **20**(5), 365–375.

Ohnesorge, B., Flohr, T., and Klingenbeck-Regn, K. (1999), 'Efficient object scatter correction algorithm for third and fourth generation CT scanners', *European Radiology* **9**(3), 563–569.

Oliphant, T. E. (2007), 'Python for scientific computing', *Computing in Science & Engineering* **9**(3), 10–20.

Opie, A. M. T. and Bones, P. J. (2011), 'Sensitivity to error of the truncated Hilbert transform technique for interior reconstruction', *in* 'IEEE International Conference on Image Processing 2011', pp. 421–424.

Opie, A. M. T., Butler, A. P. H., and Bones, P. J. (2012), 'Energy-resolved Compton scatter estimation for micro-CT', *in* 'Developments in X-Ray Tomography VIII', Vol. 8506 of *Proceedings of the SPIE*, p. 850616.

Pan, Y., Whitaker, R., Cheryauka, A., and Ferguson, D. (2010), 'TV-regularized iterative image reconstruction on a mobile C-arm CT', *in* 'Medical Imaging 2010: Physics of Medical Imaging', Vol. 7622 of *Proceedings of the SPIE*, p. 76222L.

Panta, R. K., Walsh, M. F., Bell, S. T., Anderson, N. G., Butler, A. P. H., and Butler, P. H. (2013), 'Characterisation of energy response of a hybrid energy resolving photon counting detectors in charge summing mode with MARS-readout and software', *In preparation.*

Parker, D. L. (1982), 'Optimal short scan convolution reconstruction for fan beam CT', *Medical Physics* **9**(2), 254–257.

Peters, T. M. (1981), 'Algorithms for fast back- and re-projection in computed tomography', *IEEE Transactions on Nuclear Science* **28**(4), 3641–3647.

Primak, A. N., Giraldo, J. C. R., Liu, X., Yu, L., and McCollough, C. H. (2009), 'Improved dual-energy material discrimination for dual-source CT by means of additional spectral filtration', *Medical Physics* **36**(4), 1359–1369.

Prince, M. R., Arnoldus, C., and Frisoli, J. K. (1996), 'Nephrotoxicity of high-dose gadolinium compared with iodinated contrast', *Journal of Magnetic Resonance Imaging* **6**(1), 162–166.

Qian, X., Tucker, A., Gidcumb, E., Shan, J., Yang, G., Calderon-Colon, X., Sultana, S., Lu, J., Zhou, O., Spronk, D., Sprenger, F., Zhang, Y., Kennedy, D., Farbizio, T., and Jing, Z. (2012), 'High resolution stationary digital breast tomosynthesis using distributed carbon nanotube x-ray source array', *Medical Physics* **39**(4), 2090–2099.

Radon, J. (1986), 'On the determination of functions from their integral values along certain manifolds', *IEEE Transactions on Medical Imaging* **5**(4), 170–176. Translation of the original German, by P. C. Parks.

Redus, B. (2002), Efficiency of Amptek XR-100T-CdTe and CZT detectors, Technical report, Amptek, Inc.

Rinkel, J., Gerfault, L., Estève, F., and Dinten, J.-M. (2007), 'A new method for x-ray scatter correction: first assessment on a cone-beam CT experimental setup', *Physics in Medicine and Biology* **52**(15), 4633–4652.

Roessl, E. and Proksa, R. (2007), 'K-edge imaging in x-ray computed tomography using multi-bin photon counting detectors', *Physics in Medicine and Biology* **52**(15), 4679–4696.

Rogers, D. W. O., Walters, B., and Kawrakow, I. (2006), BEAMnrc users manual, Technical Report 509(A), National Research Council of Canada.

Röntgen, W. C. (1896), 'On a new kind of rays', *Science* **3**(59), 227–231.

Ross, F. (2008), Alignment system for MARS scanner, Honours project report, University of Canterbury.

Rührnschopf, E.-P. and Klingenbeck, K. (2011), 'A general framework and review of scatter correction methods in x-ray cone-beam computerized tomography. Part 1: Scatter compensation approaches', *Medical Physics* **38**(7), 4296–4311.

Sauer, K. and Bouman, C. (1993), 'A local update strategy for iterative reconstruction from projections', *IEEE Transactions on Signal Processing* **41**(2), 534–548.

Schlomka, J. P., Roessl, E., Dorscheid, R., Dill, S., Martens, G., Istel, T., Bäumer, C., Herrmann, C., Steadman, R., Zeitler, G., Livne, A., and Proska, R. (2008), 'Experimental feasibility of multi-energy photon-counting K-edge imaging in pre-clinical computed tomography', *Physics in Medicine and Biology* **53**(15), 4031–4047.

Schmidt, T. G. and Pektas, F. (2011), 'Region-of-interest material decomposition from truncated energy-resolved CT', *Medical Physics* **38**(10), 5657–5666.

Schneider, U., Pedroni, E., and Lomax, A. (1996), 'The calibration of CT hounsfield units for radiotherapy treatment planning', *Physics in Medicine and Biology* **41**(1), 111–124.

Scudder, H. J. (1978), 'Introduction to computer aided tomography', *Proceedings of the IEEE* **66**(6), 628–637.

Seeram, E. (2009), *Computed Tomography: Physical Principles, Clinical Applications and Quality Control*, 3rd edn, Saunders Elsevier, Philadelphia, PA, USA.

Seibert, J. and Boone, J. (1988), 'X-ray scatter removal by deconvolution', *Medical Physics* **15**(4), 567–575.

Shepp, L. A. and Logan, B. F. (1974), 'Reconstructing interior head tissue from x-ray transmissions', *IEEE Transactions on Nuclear Science* **21**(1), 228–236.

Shung, K. K., Smith, M. B., and Tsui, B. (1992), *Principles of Medical Imaging*, Academic Press, San Diego, CA, USA.

Siddon, R. L. (1985), 'Fast calculation of the exact radiological path for a three-dimensional CT array', *Medical Physics* **12**(2), 252–255.

Siewerdsen, J., Daly, M., Bakhtiar, B., Moseley, D., Richard, S., Keller, H., and Jaffray, D. (2006), 'A simple, direct method for x-ray scatter estimation and correction in digital radiography and cone-beam CT', *Medical Physics* **33**(1), 187–197.

Siewerdsen, J. H., Waese, A. M., Moseley, D. J., Richard, S., and Jaffray, D. A. (2004), 'Spektr: A computational tool for x-ray spectral analysis and imaging system optimization', *Medical Physics* **31**(11), 3057–3067.

Siewerdsen, J. and Jaffray, D. (2001), 'Cone-beam computed tomography with a flat-panel imager: magnitude and effects of x-ray scatter', *Medical Physics* **28**(2), 220–231.

Siffert, P. (1994), 'Cadmium telluride and related materials as x-ray and gamma-ray detectors: a review of recent progress', *in* 'Gamma-Ray Detector Physics and Applications', Vol. 2305 of *Proceedings of the SPIE*, pp. 98–109.

Smith-Bindman, R., Lipson, J., Marcus, R., Kim, K.-P., Mahesh, M., Gould, R., de González, A. B., and Miglioretti, D. L. (2009), 'Radiation dose associated with common computed tomography examinations and the associated lifetime attributable risk of cancer', *Archives of Internal Medicine* **169**(22), 2078–2086.

Smith, S. and Kruger, R. (1986), 'A signal processing model of diagnostic x-ray scatter', *Medical Physics* **13**(6), 831–835.

Stirling, G. and Cotterill, A. (2009), Computed tomography in diagnostic radiology: a survey of use and patient doses for New Zealand, 2007, Technical Report 2009/1, National Radiation Laboratory (NZ Ministry of Health).

Taguchi, K. (2003), 'Temporal resolution and the evaluation of candidate algorithms for four-dimensional CT', *Medical Physics* **30**(4), 640–650.

Taguchi, K., Srivastava, S., Kudo, H., and Barber, W. C. (2009), 'Enabling photon counting clinical x-ray CT', *in* '2009 IEEE Nuclear Science Symposium Conference Record', pp. 3581–3585.

Takahashi, T. and Watanabe, S. (2001), 'Recent progress in CdTe and CdZnTe detectors', *IEEE Transactions on Nuclear Science* **48**(4), 950–959.

Tapiovaara, M. and Wagner, R. F. (1985), 'SNR and DQE analysis of broad spectrum x-ray imaging', *Physics in Medicine and Biology* **30**(6), 519–529.

Thibault, J.-B., Sauer, K. D., Bouman, C. A., and Hsieh, J. (2007), 'A three-dimensional statistical approach to improved image quality for multislice helical CT', *Medical Physics* **34**(11), 4526–4544.

Tlustos, L., Shelkov, G., and Tolbanov, O. (2011), 'Characterisation of a GaAs (Cr) Medipix2 hybrid pixel detector', *Nuclear Instruments and Methods in Physics Research Section A: Accelerators, Spectrometers, Detectors and Associated Equipment* **633**(S1), S103–S107.

Trapp, J. V. and Kron, T., eds (2008), *An Introduction to Radiation Protection in Medicine*, CRC Press, Boca Raton, FL, USA.

Wagner, F., Macovski, A., and Nishimura, D. (1989), 'Two interpolating filters for scatter estimation', *Medical Physics* **16**(5), 747–757.

Walsh, M. F., Opie, A. M. T., Ronaldson, J. P., Doesburg, R. M. N., Nik, S. J., Mohr, J. L., Ballabriga, R., Butler, A. P. H., and Butler, P. H. (2011), 'First CT using Medipix3 and the MARS-CT-3 spectral scanner', *Journal of Instrumentation* **6**, C01095.

Wang, G. and Jiang, M. (2004), 'Ordered-subset simultaneous algebraic reconstruction techniques (OS-SART)', *Journal of X-ray Science and Technology* **12**(3), 169–177.

Wang, G., Snyder, D. L., and Vannier, M. W. (1996), 'Local computed tomography via iterative deblurring', *Scanning* **18**(8), 582–588.

Wang, S., Calderon, X., Peng, R., Schreiber, E. C., Zhou, O., and Chang, S. (2011), 'A carbon nanotube field emission multipixel x-ray array source for microradiotherapy application', *Applied Physics Letters* **98**(21), 213701–213701–3.

Wiegert, J., Bertram, M., Schafer, D., Conrads, N., Timmer, J., Aach, T., and Rose, G. (2004), 'Performance of standard fluoroscopy anti-scatter grids in flat detector based cone beam CT', *in* 'Medical Imaging 2004: Physics of Medical Imaging', Vol. 5368 of *Proceedings of the SPIE*, pp. 67–68.

Xu, Q., Mou, X., Wang, G., Sieren, J., Hoffman, E. A., and Yu, H. (2011), 'Statistical interior tomography', *IEEE Transactions on Medical Imaging* **30**(5), 1116–1128.

Xu, Q., Yu, H., Bennett, J., He, P., Zainon, R., Doesburg, R., Opie, A., Walsh, M., Shen, H., Butler, A., Butler, P., Mou, X., and Wang, G. (2012), 'Image reconstruction for hybrid true-color micro-CT', *IEEE Transactions on Biomedical Engineering* **59**(6), 1711–1719.

Yaffe, M. J. and Rowlands, J. A. (1997), 'X-ray detectors for digital radiography', *Physics in Medicine and Biology* **42**(1), 1–39.

Ye, Y., Yu, H., Wei, Y., and Wang, G. (2007), 'A general local reconstruction approach based on a truncated hilbert transform', *Journal of Biomedical Imaging* **2007**(63634), 1–8.

Yu, H. and Wang, G. (2009), 'Compressed sensing based interior tomography', *Physics in Medicine and Biology* **54**(9), 2791–2805.

Yu, H. and Wang, G. (2010), 'A soft-threshold filtering approach for reconstruction from a limited number of projections', *Physics in Medicine and Biology* **55**(13), 3905–3916.

Yu, H., Ye, Y., and Wang, G. (2008), 'Interior reconstruction using the truncated Hilbert transform via singular value decomposition', *Journal of X-ray Science and Technology* **16**(4), 243–251.

Zeng, K. (2007), *Development and Applications of Cone-beam Imaging Techniques*, ProQuest, Ann Arbor, MI, USA.

Zhang, J., Yang, G., Cheng, Y., Gao, B., Qiu, Q., Lee, Y. Z., Lu, J. P., and Zhou, O. (2005), 'Stationary scanning x-ray source based on carbon nanotube field emitters', *Applied Physics Letters* **86**(18), 184104–184104–3.

Zhu, L., Bennett, N., and Fahrig, R. (2006), 'Scatter correction method for x-ray CT using primary modulation: Theory and preliminary results', *IEEE Transactions on Medical Imaging* **25**(12), 1573–1587.

We apologise for the inconvenience.